Growth of obliquely deposited metallic thin films

Von der Fakultät für Physik und Geowissenschaften

der Universität Leipzig

genehmigte

DISSERTATION

zur Erlangung des akademischen Grades

Doctor rerum naturalium

Dr. rer. nat.

vorgelegt

von M.Sc. Susann Liedtke-Grüner

geboren am 31.07.1989 in Neu Kaliß

Gutachter: Prof. Dr. Dr. h. c. Bernd Rauschenbach

Prof. Dr. Ibrahim Abdulhalim

Tag der Verleihung: 18.03.2019

For my family, wondering what I've been doing all the time.

Für meine Familie, die sich darüber wundert,
was ich die ganze Zeit getan habe.

Bibliographische Beschreibung

Liedtke-Grüner, Susann
Growth of obliquely deposited metallic thin films
Universität Leipzig, Dissertation
143 S., 190 Lit., 71 Abb., 33 Formeln, 2 Tabellen

Referat (abstract):

The present work represents a systematical study of the growth of columnar, metallic thin films deposited under highly oblique vapor incidence on planar substrates. Oblique angle deposition is a physical vapor deposition technique that is based on the self-shadowing effect. This enables the fabrication of highly porous thin films that are composed of three-dimensionally separated, micro-, and nano-sized columns.

For this study, metals that cover a wide range of melting points and crystal structures have been chosen, and the observed growth characteristics are compared with each other to gain information about the growth of obliquely deposited metallic thin films in general. Among the various parameters that have an influence on the growth of columnar thin films, in the focus of this work are the angle of the incoming particle flux, substrate rotation frequency, and substrate temperature as well as the influence of the residual gas atmosphere.

The first part deals with a morphological analysis of the columnar, metallic thin films by scanning electron microscopy (SEM). The columnar shape, the columnar tilt angle, and the thin film porosity are investigated depending on the incidence flux direction as well as substrate temperature and rotation. It is examined how a reduction of the substrate temperature down to 77 K - realized by a liquid nitrogen cooled sample holder - influences the growth of the columnar thin films. Further, it is analyzed how substrate rotation influences the local deposition geometry and accordingly the growth behavior of tilted columns, spirals, screws, and upright columns. Based on geometrical considerations, a theoretical model is proposed and compared with the made observations.

The second part focusses on the high-resolution local structure analysis of individual columns via (scanning) transmission electron microscopy (TEM). On the one hand, the columnar structure is analyzed depending on the substrate temperature and substrate rotation via high resolution TEM. On the other hand, the crystallinity of individual columns is studied along the entire column by nanobeam electron diffraction. This technique is also applied to gain information about the orientation of the crystallites at the substrates surface and to investigate the selection processes of crystalline orientations during the growth. Moreover, the presented studies reveal under which conditions single crystalline columns are forming.

In the final part, the texture of the columnar, metallic thin films is analyzed depending on the film thickness, the angle of the incoming particle flux as well as on the substrate temperature. X-ray diffraction (XRD) measurements, such as pole figures, are applied to determine the orientation of the lattice planes in the columns depending on the incident flux direction and on the substrate temperature. The observations are backed by reflection high-energy electron diffraction (RHEED) investigations. A model is developed that enables to explain why the tilt of the lattice directions in the columns is not equal to the tilt angle of the columns. A further theoretical model is introduced that enables to roughly estimate the tilt angle of the lattice direction that ensures the fastest vertical columnar growth.

CONTENTS

1 MOTIVATION 7

2 BASICS OF OBLIQUE ANGLE DEPOSITION 9

2.1 Thin film growth by oblique deposition 9
  - 2.1.1 Physical vapor deposition 9
  - 2.1.2 Nucleation 10
  - 2.1.3 Shadowing 11
  - 2.1.4 Structure of individual columns 12

2.2 Sculpturing thin films on the nanometer scale 13
  - 2.2.1 Angle of the incoming particle flux 13
  - 2.2.2 Substrate rotation 16
  - 2.2.3 Substrate temperature 17

2.3 Application areas for metallic nanostructured thin films 20

3 EXPERIMENTAL DETAILS 23

3.1 Sample fabrication 23
  - 3.1.1 General deposition system setup and evaporation process 23
  - 3.1.2 Crucibles, substrates, and sample holders 25
  - 3.1.3 Controlling substrate movement and temperature 26
  - 3.1.4 Controlling film thickness and deposition rate 29

3.2 Sample characterization 30
  - 3.2.1 Scanning electron microscope (SEM) 30
  - 3.2.2 Transmission electron microscopy (TEM) 31
  - 3.2.3 X-Ray Diffraction (XRD) and In-Plane Pole Figure measurements (IPPF) 33
  - 3.2.4 Reflection high-energy electron diffraction (RHEED) 36
  - 3.2.5 Raman scattering spectroscopy 36

4 MORPHOLOGICAL ANALYSIS OF COLUMNAR THIN FILMS 39

4.1 Oblique angle deposition 40
  - 4.1.1 Deposition at room temperature 40
  - 4.1.2 Deposition at different temperatures 43

4.2 Glancing angle deposition 61
  - 4.2.1 Continuous substrate rotation 61
  - 4.2.2 Discrete substrate rotation 66

4.3 Summary of results 69

5 STRUCTURAL ANALYSIS OF INDIVIDUAL COLUMNS 71

5.1 Oblique angle deposition 71
  5.1.1 Tilted columns grown at room temperature 71
  5.1.2 Tilted columns grown at different substrate temperatures 78

5.2 Glancing angle deposition 82
  5.2.1 Vertical columns grown by continuous substrate rotation 82
  5.2.2 Zigzag columns grown by discrete substrate rotation 85

5.3 Discussion 87
5.4 Summary of results 89

6 TEXTURE ANALYSIS OF COLUMNAR THIN FILMS 91

6.1 Influence of the film thickness 91
6.2 Influence of the incoming flux direction 99
6.3 Influence of the substrate temperature 110
6.4 Summary of results 116

7 SUMMARY AND CONCLUSIONS 119

8 LIST OF LITERATURE 123
9 LIST OF ABBREVIATIONS 134
10 LIST OF VARIABLES AND CONSTANTS 136
11 ACKNOWLEDGEMENTS 139

PUBLICATION LIST 140

SELBSTSTÄNDIGKEITSERKLÄRUNG 143

1 Motivation

Since decades, considerable research activities have focused on the miniaturization of technological devices with the aim to increase the device performance by simultaneous reduction of the required space, material, and energy demands. Nanostructured thin films play a key role in this process, since the ability to precisely tailor surface topography down to the nanometer range opens the opportunity to generate thin films that exhibit properties that are usually not obtained for bulk materials. However, the controlled fabrication of three-dimensionally separated nanostructures remains as an ambiguous challenge.

Powerful methods to sculpture thin films composed of individual nanostructures are oblique and glancing angle deposition (OAD and GLAD). Characteristic for these methods is that the substrate is tilted to highly oblique angles with respect to the incoming particle flux so that shadowing is induced during the growth process. This enables the self-assembled growth of separated, micro-and nano-sized columns with manifold shapes such as screws, spirals as well as tilted and vertical columns over large substrate areas. OAD and GLAD represent both physical vapor deposition (PVD) processes, meaning that all materials that can be used for common PVD processes are principally utilizable to sculpture such columnar thin films. As a matter of fact, much research has been performed to study the oblique deposition of insulating and semi-conducting thin films, whereas the growth of columnar, metallic thin films is only fragmentarily understood. A profound knowledge of the growth process is of vital importance to finally modify, tune, and optimize the properties of the resulting thin film. Especially metallic columnar thin films have recently shown to be promising candidates for fabricating highly precise Raman active sensors for environmental and bio-medical applications [1-4], for example.

The aim of the present work is to investigate the fundamental growth process of metallic, columnar thin films grown by electron beam evaporation under highly oblique deposition conditions. For this purpose, the following approach is chosen:

(i) Selection of metals that cover a wide range of melting points and crystal structures.
(ii) Fabrication of metallic, columnar thin films with varying deposition parameters.
(iii) Comparison of the observed growth characteristics.
(iv) Deduction of more general information concerning the growth process of columnar metallic thin films.

After a short introduction about OAD and GLAD in chapter 2, and a concise description of the experimental setup, the sample fabrication as well as the characterization methods in chapter 3, the experimental findings are described and discussed in chapters 4 – 6. Chapter 4 focusses on the morphological analysis of metallic thin films grown by oblique deposition. The columnar shape, columnar diameters, as well as the thin film porosity are studied depending of the incoming particle flux direction, the substrate temperature, and the substrate rotation frequency. In this chapter is shown that a reduction of the substrate temperature down to 77 K by an in-house built and designed liquid nitrogen cooled sample holder can be used to counteract the influence of surface self-diffusion, thereby maximizing the shadowing effect. A further issue of this chapter is to analyze the influence of the local deposition geometry on the growth of thin films fabricated by OAD compared to GLAD. A high-resolution structural analysis of individual metallic columns, which can be found in chapter 5, reveals under which deposition parameters the columns exhibit a crystalline structure. The structure is investigated along the columns, starting from the beginning of the growth at the substrate surface up to the very topmost parts of the columns. In chapter 6 is demonstrated how the texture of those metallic thin films can be controlled by varying the film thickness, the incoming flux direction, and the substrate temperature. Finally, in chapter 7 the found results are summarized and the main conclusions of this thesis are outlined.

2 Basics of Oblique Angle Deposition

2.1 Thin film growth by oblique deposition

2.1.1 Physical vapor deposition

For the preparation of thin films, physical vapor deposition (PVD) under ultra-high vacuum conditions is a widely used approach. Atomistic vapor condensates on a substrate surface, which is known as the “vapor-to-solid condensation”. In conventional thin film growth, the incident particle flux strikes and condenses upon a perpendicular substrate. In contrast, oblique angle deposition (OAD) represents a PVD process in which the incoming particles reach the substrate surface under a highly oblique incidence angle ($\theta_{OAD} > 70°$) with respect to the substrate normal, where the microscopic nuclei develop into separated nanostructures (see Figure 2.1). Whereas normal particle incidence leads in general to the formation of a nearly compact, dense thin film, OAD enables to grow highly porous thin films composed of individual nano- and microsized columns inclined towards the incidence vapor. For OAD, no catalysts are required. The first observation that the angle of the incident particle flux influences the film properties has been made by Kundt in 1886 [5].

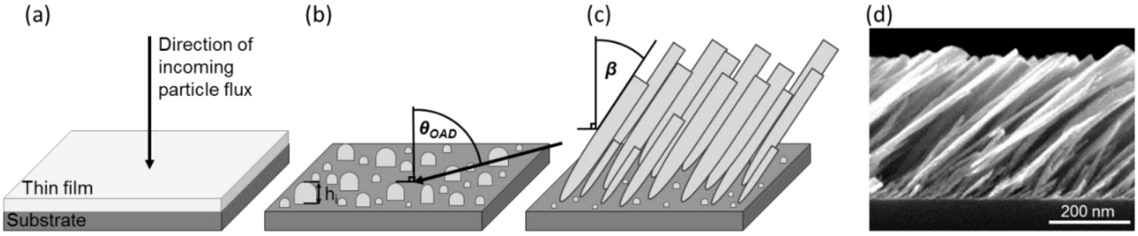

Figure 2.1: Schematic illustration of the deposition geometry for (a) vertical particle incidence compared to (b) oblique particle incidence. The angle of the incoming particle flux with respect to the substrate normal is θ_{OAD}. The height of the nuclei is denoted by h_i. (c) For later growth stages of oblique deposition, tilted columns are forming that are inclined towards the incoming particle flux by the columnar tilt angle β. (d) Cross-sectional scanning electron microscopy image of a columnar Mo thin film deposited obliquely ($\theta_{OAD} = 76°$) at room temperature on a natively oxidized Si(100) substrate.

In principle, all materials that can be evaporated by the PVD-process (all inorganic materials including compounds as well as some organic molecules) can also be used for the oblique deposition approach. An overview can be found in [6].

Depositing a thin film by using the OAD can be realized by various methods. Evaporative deposition is characterized by a thermal vaporization of the source material. This can be realized by either resistive heating (thermal evaporation) or electron bombardment (electron-beam (EB-) evaporation). The angular flux distribution can roughly be approximated by the cosine type [7] so that the particle trajectories are mainly along the particle source normal. Evaporation is a widely used PVD-method, since there are rare inter-particle collisions and consequently linear trajectories even at long distances between particle source and sample surface. This results in a highly linear, locally collimated vapor flux favoring ballistic shadowing that is of major importance for GLAD (see subsection 2.1.3). High deposition rates in the order of nm/s can be realized by evaporative deposition. Process gases are not required so that the probability for inter-particle collisions is further minimized. Evaporative deposition requires high vacuum conditions (< 10^{-6} mbar), which are related to high expenses if the thin films should be fabricated in industry.

For industrial applications, sputtering can be an interesting approach, since the vacuum pressures are much higher (> 10^{-4} mbar). However, higher pressure environment increases the vapor flux scattering rate. Sputtering is characterized by vaporization induced by energetic particle bombardment. Typically, such particles are ions originating from a plasma or an ion beam gun. As the ions collide with the surface atoms, momentum is transferred so that there is a probability that surface atoms are ejected. The gas composition, pressure, and energetics have a significant influence on the film properties. Additionally, there are numerous geometries available, for instance, DC diode sputtering, radio frequency (RF) sputtering, DC and RF magnetron sputtering, hollow cathode sputtering, high - power impulse magnetron sputtering (HIPIMS) or ion beam sputtering. All these geometries have different electrode and magnet properties for plasma generation and configuration, resulting in different process parameters such as energy angular distribution, effective source size, and deposition rate. The resulting film properties are influenced by all these process parameters.

Another, but less common method for GLAD is the pulsed laser deposition (PLD). Stoichiometric films from a single target can be produced by this method. The angular flux distribution is strongly located along the target normal. The vapor flux created by the interaction between laser pulse and target usually consists of compounds instead of atoms and the vapor has commonly high energies when arriving at the sample surface or is cooled during the transport phase by interaction with a process gas, which leads to a loss of the flux collimation.

2.1.2 Nucleation

According to Kashchiev [8], thin film “nucleation is the process of random generation of such nanoscopically small formations of the new phase that have the ability for irreversible growth to macroscopically large sizes”. An atom from the vapor phase that bonds to the substrate surface in a way that this atom can still migrate on the surface is an adatom. By surface self-diffusion, the adatom will aspire to move to its thermodynamically favored equilibrium position. Once the adatom is incorporated in the surface, or if the adatom desorbs back to vapor, it ceases to be an adatom. The condensation of material on a planar substrate results in the intrinsically random formation of nuclei if no epitaxial relation is realized. Depending on the surface energy of the system, three growth modes can be distinguished [9].

(i) For Volmer-Weber growth, the atoms are strongly bound to one another, but the adhesion to the substrate surface is low, resulting in three-dimensional island formation.

(ii) Frank-van-der-Merwe growth is characterized by a two-dimensional layer-by-layer growth.

(iii) Stranski-Krastanov growth is a combination of layer and island growth. After the first monolayer is grown on the substrate surface, the adhesion on this monolayer is stronger than on the substrate surface, leading to the growth of three-dimensional islands on the monolayer.

For OAD, the most relevant growth modes are Volmer-Weber growth and Stranski-Krastanov growth, since the formation of stable clusters that assemble finally to three-dimensional crystallites induces roughness to the surface, which is a prerequisite for shadowing to occur.

2.1.3 Shadowing

The self-shadowing effect originates from a highly collimated, oblique incoming particle flux that creates shadowed regions behind the developing nuclei or columns, and has been first recognized by König and Helwig in 1950 [10]. As shown in Figure 2.2 (a), the nuclei (or columns) at the substrate surface have a certain height h_i so that the ballistic shadowing length l_{Shadow} for oblique deposition at θ_{OAD} can be determined by:

$$l_{Shadow} = h_i \cdot \tan \theta_{OAD}. \tag{2.1.1}$$

Shadowing impedes the later arriving particles condense in the shadowed areas. As a result, nuclei are forced to develop into columns that are inclined towards the direction of the incoming particle flux. Among the initially random oriented crystallites, those with the fastest vertical growth component will overgrow crystallites that grow slower [11]. This competitive growth process leads to the self-assembled formation of thin films composed of three-dimensionally separated tilted columns with different columnar length, as depicted in Figure 2.2 (b). On planar substrates, the columns are arranged randomly, which originates from the stochastic nucleation phase of the film growth. Substrates with periodic structure arrays facilitate to pre-define the position at which a column grows, thus enabling the fabrication of highly uniform, periodic arrays of columns over a large substrate area [12]. Notice that the shadowing effect has not an influence vertically to the incidence plane so that tilted columns grow broader in this direction. In the progress of this broadening, separated columns can agglomerate and finally form chains [13].

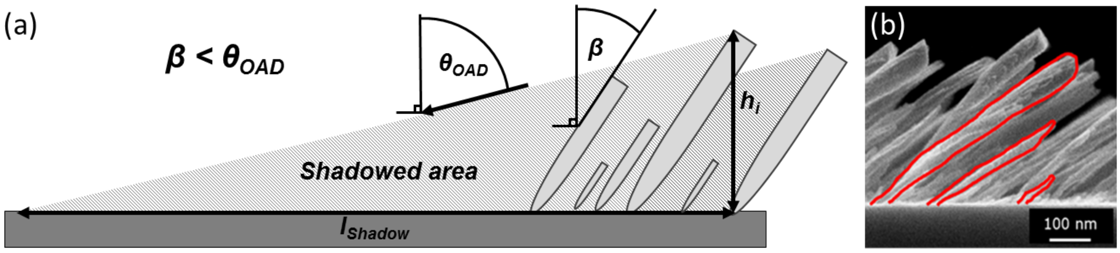

Figure 2.2: (a) Sketch to illustrate the self-shadowing effect. The angle of the incoming particle flux θ_{OAD} and the columnar tilt angle β are both measured with respect to the substrate normal. The height of the columns is denoted by h_i and l_{Shadow} is the shadow length. (b) Tilted Mo columns deposited at room temperature on an natively oxidized Si(100) substrate by an oblique angle $\theta_{OAD} = 84°$. Exemplarily, three columns are surrounded in red color to illustrate that the thin film is composed of separated columns of different length as a result of the competitive growth process.

2.1.4 Structure of individual columns

The formation of OAD and GLAD thin films can be accompanied by crystallization. Such crystallization processes already occur as nuclei have formed at the substrate surface, and further impact the shape of the developing column. A common method to determine the equilibrium shape of a crystal of a fixed volume is the Wulff construction [14]. In thermodynamic equilibrium, a crystal of a fixed volume has the smallest free enthalpy G. In a crystal, the free surface energy $\Sigma = \delta G / \delta A$ (with A denoting the surface area) is anisotropic, and the equilibrium shape is a polyhedron, whose planes have the smallest free surface energy for the respective lattice direction. According to the Gibbs-Wulff theorem, in equilibrium the distances of the planes from the center of the crystal are proportional to their free surface energies per unit area. Planes with small growth speed (Σ small) become larger during growth, but planes with high growth speed (Σ large) become smaller until they vanish. Finally, the crystal shape is confined by planes with minimized surface free energy, which are the planes with minimized growth speed. Those "equilibrium planes" are (111) for crystals with face-centered cubic (fcc) crystal structure and (110) for crystals with body-centered cubic (bcc) crystal structure. A proof of the Gibbs-Wulff theorem has been given by Herring in 1953 [15], for instance.

Several publications have demonstrated the occurrence of crystalline columns by OAD and GLAD. For instance, Sadeghi-Khosravieh and Robbie [16] found polycrystalline tilted Ti columns in thin films grown under highly oblique deposition geometries by electron beam evaporation. Further, Khudhayer *et al.* [17] reported about the formation of single crystalline, vertical Pt columns by magnetron sputtering GLAD.

Moreover, Messier *et al.* [18] have proposed an “evolutionary columnar growth model”, which states that an individual column is a bundled structure that is hierarchically composed of several sub-units such as macrocolumns, microcolumns, and nanocolumns. Nanocolumns with a size of 1 – 3 nm form for film thicknesses in the order of ~ 15 nm. With increasing film thickness, transitions between the nano/micro/macrocolumns take place. This means that several nanocolumns bundle together to a microcolumn, which can further arrange to a macrocolumn as deposition proceeds. These sub-units are separated by interstitial voids. High surface mobility is reported to cause a denser internal columnar structure by reducing the size of those voids. Bundled structures in individual columns have been found, e.g., for TiO_2 and Al_2O_3 thin films [18].

2.2 Sculpturing thin films on the nanometer scale

2.2.1 Angle of the incoming particle flux

A common observation in OAD is that the tilt angle β of the columns is in general smaller than the angle of the incidence flux direction θ_{OAD}, both measured with respect to the substrate normal. The relation between these angles has been under discussion since decades. In 1966, Nieuwenhuizen and Haanstra [19] have suggested the tangent rule that describes the β–θ_{OAD} relation for angles of incidence below approximately 70°:

$$\tan\theta_{OAD} = 2 \cdot \tan\beta. \tag{2.2.1}$$

For more oblique angles ($\theta_{OAD} > 70°$), the cosine rule reported by Tait *et al.* [7] reflects the β–θ_{OAD} relation more appropriately:

$$\beta = \theta_{OAD} - \arcsin\left(\frac{1 - \cos\theta_{OAD}}{2}\right). \tag{2.2.2}$$

However, according to the cosine rule, the columnar tilt angle cannot become larger than $\beta = 60°$. Tangent and cosine rule are based on geometrical considerations, neglecting further factors that influence the columnar growth such as surface diffusion, conversation of parallel momentum, residual gas pressure, etc. Additionally, the research put forward by Zhao *et al.* [20] indicates that the formation of the columnar tilt angle depends on the material property and composition. For those reasons, numerous experimental results cannot be described successfully by those empirical rules.

Hara *et al.* [21] have proposed a model that includes the conversation of parallel momentum of the incoming adatoms. This results in a directional surface diffusion of the incoming adatoms parallel to the film plane so that the columns tend to incline towards the film surface. This model points out that it is important to distinguish between the directional surface diffusion and the thermally activated random surface diffusion. The self-diffusion length Λ of an adatom can be estimated by:

$$\Lambda \approx \sqrt{exp\left(\frac{-E_A}{k_B T_{Sub}}\right)}. \tag{2.2.3}$$

E_A is the surface diffusion activation energy and k_B is the Boltzmann constant. Following Hara´s model, an increase in substrate temperature T_{Sub} leads to an enlarged columnar tilt angle β for a given θ_{OAD}.

Moreover, several continuum models can be found in literature. In such a model, the finite size of the atoms is not considered, since the diameter of a columns is much larger compared to the diameter of the atoms. Instead, the film surface is approximated by a continuous function of the coordinates along the surface and the deposition time [22]. For example, a continuum model has been proposed by Lichter and Chen [23], including random surface diffusion:

$$\tan\beta = \frac{2}{3}\frac{\tan\theta_{OAD}}{(1+\varphi\tan\theta_{OAD}\sin\theta_{OAD})}. \tag{2.2.4}$$

The variable φ can be expressed by:

$$\varphi = \frac{4}{27}\frac{h_i \cdot J}{D_S} \approx {D_S}^{-1}. \tag{2.2.5}$$

The initial surface perturbation (roughness) where the column starts growing from is given by h_i, J is the incident vapor flux deposition rate, and D_S denotes the adatom surface diffusion coefficient. The model includes the influence of the substrate temperature T_{Sub} on the columnar tilt angle β, since:

$$\mathrm{D}_S = \mathrm{D}_0\, exp\left(\frac{-E_A}{k_B T_{Sub}}\right). \tag{2.2.6}$$

D_0 is a proportionality factor. Lichter and Chen conclude that an enlarged random surface diffusion results in columns that grow more towards the incidence flux direction. The model does not consider shadowing and permits only small surface slopes.

A semi-empirical model based on the shadowing effect has been introduced by Tanto *et al.* [24]. In this model, all deposition and material parameters are summarized in on single parameter, the fan angle Φ_{Fan}. This is the angle by which a freestanding fan or overhang structure grows away from the incidence flux. The fan angle can be determined experimentally and used to predict film properties, but this model does not provide information about how the deposition and material parameters influence this fan angle. For periodically arranged columns, Tanto *et al.* have derived the expression:

$$\beta = \begin{cases} \theta_{OAD} - \arctan\left[\frac{\sin(\Phi_{Fan}) - \sin(\Phi_{Fan} - 2\theta_{OAD})}{\cos(\Phi_{Fan} - 2\theta_{OAD}) + \cos(\Phi_{Fan}) + 2}\right], & \theta_{OAD} \leq \Phi_{Fan} \\ \theta_{OAD} - \frac{\Phi_{Fan}}{2} & ,\theta_{OAD} \geq \Phi_{Fan} \end{cases} \tag{2.2.7}$$

Zhu *et al.* [25] have extended Tanto´s model and found out that the fan angle depends closely on the materials melting point for single element materials, the standard heat formation for compound materials, the crystal structure as well as the complexity of the materials. As outlined in chapter 4, we have recently found a β–θ_{OAD} relation based on the fan angle model by Tanto *et al.* that enables to predict the columnar tilt angle over the entire range of the incoming particle flux direction $0° \leq \theta_{OAD} \leq 90°$ [26].

Besides influencing the columnar tilt angle β, the angle of the incoming particle flux θ_{OAD} represents a powerful tool for fabricating textured columnar thin films [27]. According to Wassermann *et al.* [28], texture is defined as "distribution of all crystallographic orientations of a polycrystalline sample". Figure 2.3 gives an overview of different types of texture that can be present in a thin film. A random texture means that that the crystallites in the sample are oriented randomly with respect to each other. For a fiber texture, one crystallographic axis of the crystallites is aligned along the fiber axis, while the remaining axes are oriented randomly around the fiber axis. If there is additionally a confinement around the texture axis in azimuthal direction between the crystallites, the film is biaxially textured [29-31]. During recent years, a growing interest has been devoted to grow textured thin films on amorphous and non-single crystalline substrates [32]. The ability to tailor the texture of nanostructured thin films is a key issue for controlling the optical, magnetic, and electrical properties of such a film, and promising application could already be derived. Some

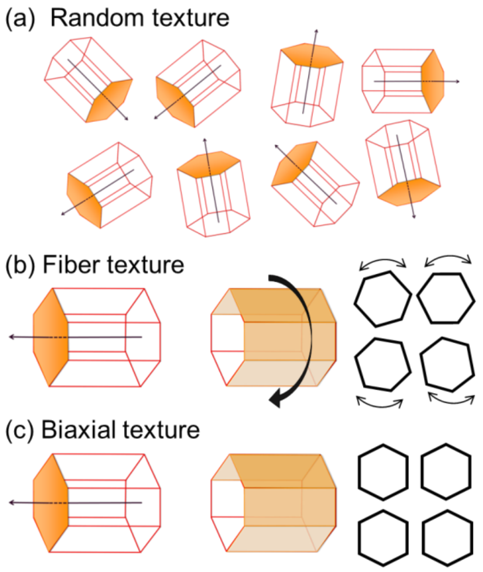

Figure 2.3: Schematic illustration of different types of texture that can be obtained in a thin film: (a) random texture, (b) fiber texture, and (c) biaxial texture.

examples are buffer layers for high temperature superconductor wires based on yttrium barium copper oxide (YBCO) [33, 34], biaxially textured CaF_2 buffer layers for the fabrication of single crystalline Ge wires at low temperatures (~ 673 K) [35], and biaxially textured Si thin films with a high carrier-mobility at room temperature (RT) without the usage of lattice-matched single crystal substrates [36, 37].

2.2.2 Substrate rotation

Combining oblique deposition geometry with azimuthal substrate rotation has first been performed by Young and Kowal in 1959 to create optically active fluorite films based on an otherwise isotropic material [38]. Until structural analysis techniques such as scanning electron microscopy (SEM) became widely available in the 1990s, further experimental research in this field has not been reported. Robbie *et al.* [39, 40] have been the first who then applied the SEM to directly investigate the influence of the substrate rotation on the evolving morphology of obliquely deposited thin films. Since Robbie *et al.* increased θ_{OAD} to a "glancing angle", "Glancing angle deposition (GLAD)" has been suggested as term for the technique of combining oblique particle incidence with substrate rotation. In Figure 2.4, the difference between OAD and GLAD is shown. As both OAD and GLAD films are composed of individual columns, such films exhibit an open-pore structure, meaning that between those columns there is nothing but space.

Substrate rotation around its normal changes the apparent direction of the incoming particle flux from the perspective of the developing columns, which in turn influences the shadowed areas on the substrate. The developing columns aim to follow the direction of the incoming particle flux, which can be used to create manifold columnar morphologies. In general, two types of substrate rotation can be distinguished.

Continuous substrate rotation means that the substrate is rotated continuously around its normal with a fixed substrate rotation frequency ω. This enables the growth of spirals, screws, and vertical columns. The ratio υ of deposition rate r and substrate rotation frequency ω determines which columnar morphology is realized ($\upsilon = r / \omega$). If υ is large (slow substrate rotation frequency), the evolving columns try to follow the continuously changing direction of the incident flux direction, thereby spiral-like columns are formed. Such spirals have an open core, meaning that the height the spiral gains per one complete substrate revolution ("pitch") is smaller than the spiral´s diameter. Intermediate υ – values result in the formation of screw-like columns with compact core. For low υ – values (fast substrate rotation frequency), the particle flux appears omni-azimuthal from the perspective of the growing columns so that the formation of vertical columns is triggered. Exemplarily, Figure 2.4 shows cross-sectional SEM images of spirals, screws, and vertical columns deposited with different substrate rotation frequencies, but similar deposition rate $r = 1$ nm/s.

Discrete substrate rotation combines deposition on a stationary substrate with rapid continuous substrate rotations. For example, a tilted column ("arm") is grown without substrate rotation, then the substrate is rapidly rotated around the desired angle, and a second column ("arm") is deposited directly atop of the other arm, etc. This facilitates to generate manifold, customized *n*-fold columnar morphologies, with *n* denoting the number of deposited arms per one complete substrate revolution. For instance, a 2-fold columnar structure (zigzag structure) realized by discrete substrate rotation can be seen in Figure 2.4.

Besides, it is also possible to change the deposition angle θ_{OAD} during azimuthal substrate rotation, which represents an additional degree of freedom for modifying the columnar morphology [41].

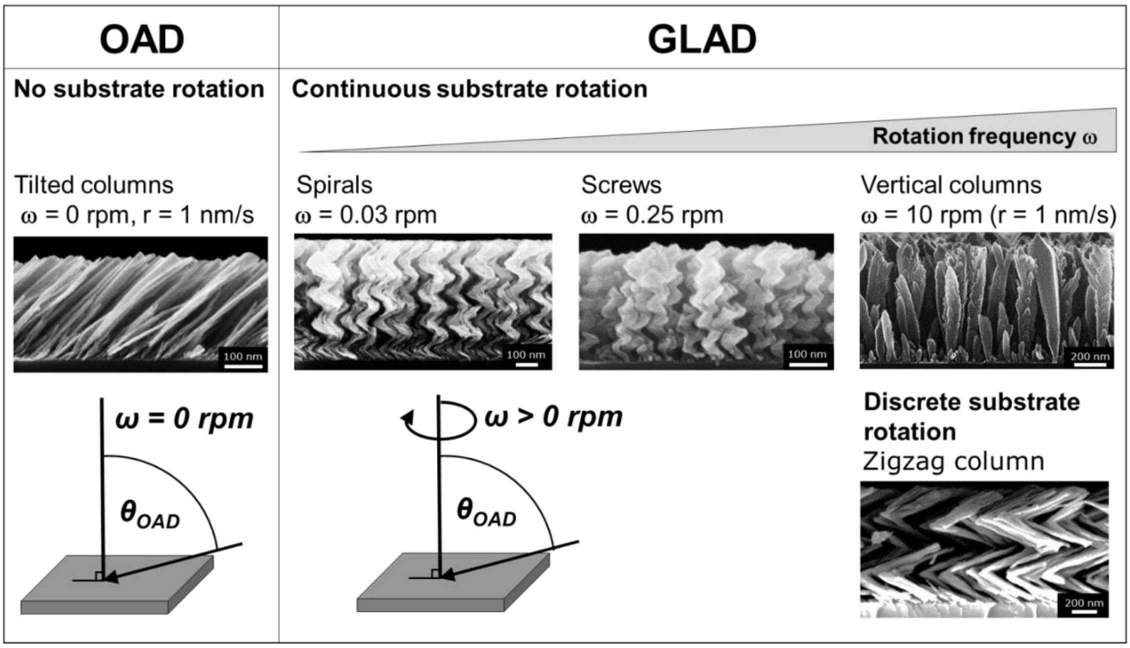

Figure 2.4: Schematic overview to show the difference between OAD and GLAD. The cross-sectional SEM images all depict metallic thin films deposited at room temperature on a natively oxidized Si(100) substrate by an oblique angle $\theta_{OAD} = 84°$ with deposition rate $r = 1$nm/s. ω is the substrate rotation frequency.

2.2.3 Substrate temperature

Changing the substrate temperature directly influences the mobility of the adatoms on the columnar thin films and therefore the entire columnar growth process. For this reason, this subsection starts with some general information concerning diffusion, which will be important to understand the growth of the thin films.

Diffusion is the movement of particles in a solid along the concentration gradient, resulting in a flux J_N from an area of higher particle concentration C to an area of lower concentration leading to a uniform particle distribution. If the system does not change with time, steady state diffusion occurs, meaning that the net flow of atoms is equal to the diffusivity (diffusion coefficient) D_S times the concentration gradient (dC / dx). This is known as Fick´s first law of diffusion:

$$J_N = -D_S \cdot \frac{dC}{dx}. \tag{2.2.8}$$

Notice that the diffusion is driven by a gradient in the chemical potential. Fick´s second law of diffusion applies if the concentration of atoms at any point of material changes with time (non-steady state diffusion):

$$\frac{dC_x}{dt} = \frac{d}{dx} D_S \left(\frac{dC_x}{dx}\right) = D_S \frac{\delta^2 C}{\delta x^2}. \tag{2.2.9}$$

This means that the accumulation or depletion of concentration within the material´s volume is proportional to the local curvature of the concentration gradient. The diffusivity or diffusion constant D_S is temperature T dependent: $D_S = D_0 \cdot \exp(-E_A / k_B T)$ (see equation (2.2.6)). The activation energy is the energy that an atom needs to overcome a potential barrier of the height E_A. Only a fraction of atoms in the system have enough thermal energy to overcome the potential barrier. The probability p_J that an atom has such an energy is given by:

$$p_J \approx \psi \cdot e^{\left(-\frac{E_A}{k_B T}\right)}. \tag{2.2.10}$$

ψ denotes the characteristic atomic oscillation frequency. The atom collides ψ-times against the barrier, and for each collision the probability to jump over the barrier is equal to $\exp(-E_A / k_B T)$. Therefore, p_J is also known as jump frequency (usually between $\approx 10^{11}$ s^{-1} and 10^{13} s^{-1} [42, 43]). Tunneling through the barrier can also take place for light elements such as hydrogen. The diffusivity does not only depend on temperature, but also on the diffusion mechanism, the type of crystal structure, crystal imperfections and the concentration of the diffusing species. The self-diffusion length Λ of an adatom is given by the diffusivity D_S and the mobility lifetime τ_M:

$$\Lambda = 2\sqrt{D_S \cdot \tau_M}\,. \tag{2.2.11}$$

Among the various types of diffusion, surface-self diffusion of adatoms is of major interest for this study, because the columnar thin films are only composed of one single metal. Self-diffusion is the diffusion of atoms of the metal itself, not of impurity atoms. Many possible mechanisms for surface self-diffusion are known, such as jumping or hopping, vacancy diffusion or atomic exchange. Additionally, anisotropy effects for surface self-diffusion must be considered. Those are different diffusion rates and mechanisms depending on the surface orientation so that different planes of the same crystal can exhibit different diffusion coefficients.

Although OAD is typically carried out at low temperatures to ensure maximized shadowing conditions, several research reports indicate that an enlarged substrate temperature combined with highly oblique deposition geometries represents an additional degree of freedom for tailoring the columnar shape and the properties of the columnar thin films, e.g., by providing better control of the crystallinity and electronic mobility of the columns compared to deposition at room temperature [44-50].

To understand the thin film growth at highly oblique deposition angles and elevated substrate temperatures, the competition between shadowing length and adatom diffusion length must be considered. Conventional structure zone models (SZM) such as the SZM by Movchan and Demchishin [51] do not take the shadowing effect into account, but Mukherjee and Gall [52] put forward a SZM for oblique deposition at high temperatures including the resulting competition. In general, the SZM by Mukherjee and Gall distinguishes between high aspect ratio rods, broadened columns, protrusions that extend above the surrounding film, dense equiaxed grain layers, and whisker structures. The formation of such structures can be related to the homologous temperature T_H, which is the actual substrate temperature T_{Sub} scaled to the melting point of the material T_{Melt} ($T_H = T_{Sub} / T_{Melt}$) [53]. High aspect ratio rods are obtained for low homologous temperatures ($T_H < 0.2$), where the structures form according to maximized shadowing conditions. With increasing homologous temperature, the adatom diffusion length increases, thereby counteracting the shadowing effect. This triggers a transition from high aspect ratio rods to broadened columns ($0.2 \leq T_H \leq 0.4$), to protrusions ($0.4 \leq T_H \leq 0.6$) as well as to dense equiaxed grain layers and whiskers ($T_H \geq 0.5$). Protrusions form at high temperatures due to the enlarged adatom mobility, which can cause an enhanced vertical and lateral growth compared to the surrounding structures. Equiaxed grain layers do not exhibit the typically observed columnar thin film structure anymore, because surface and bulk diffusion dominate the shadowing effect. Besides, high aspect ratio structures called “whiskers” can be present at high homologous temperatures, but the origin of their formation has still not been understood. Such whiskers can exhibit remarkable lengths on the µm-scale [44, 45] and are typically single crystalline. In conclusion, the SZM by Mukherjee and Gall enables qualitative predictions concerning the thin film formation at highly oblique angles for varying substrate temperatures.

However, a more precise description of the columnar thin film growth requires detailed information of the adatom surface self-diffusion, for instance. The mass transport on a surface is represented by a large number of individual processes. Adatom surface self-diffusion can depend on various parameters such as the material´s crystal structure, the crystal plane, the surface curvature, actual temperature of the crystal, the surrounding gas pressure, grain boundaries etc. In the literature, several theories have been proposed to explain the surface self-diffusion of adatoms on metallic surfaces [42, 54-66] (to list just a few publications). Most of those studies experimentally examine the diffusivity for high substrate temperatures (> 800 K), indicating that very few information concerning the diffusivity for lower temperatures, which are more relevant for OAD and GLAD, can be found.

2.3 Application areas for metallic nanostructured thin films

Columnar metallic thin films are promising candidates for various fields of applications [31]. A recent application for such films can be found for fuel cells, in which chemical energy provided by a chemical reaction of a fuel, such as H_2, with oxygen or other oxidizing agents is converted into electrical energy. Khudhayer *et al.* [17, 67-69] reported about columnar Pt thin films acting as electrode that increases the efficiency of the oxygen reduction reactions compared to conventional Pt/C electrodes.

Metallic thin films have also the potential to increase the performance of lithium ion batteries. For instance, Sharma *et al.* [70] demonstrated that columnar Al thin films grown on titanium/glass substrates that act as anode electrode in such batteries. The Al columnar thin film has shown an average columbic efficiency of 91% and a specific capacity close to the theoretical maximum.

Moreover, thin films composed of tilted or zigzag Cr columns can be used as nanospring sensors to monitor mechanical forces and pressure [71]. Compressing such nanosprings affects the pathways of the electrical current, thus inducing a change in electrical resistivity of these films. For the zigzag columns, a reversible change of resistivity upon loading and unloading of 50% could be found, but for tilted columns this change is only 5%.

Further, there are several studies dealing with influencing the microfluidic properties of columnar metallic thin films. Superhydrophobic surfaces can be generated by depositing Teflon on columnar tungsten thin films, thereby affecting the chemistry of the surface as well as the morphology and the roughness [72]. Fujii *et al.* [73, 74] have shown that columnar Al thin films show omni-phobic properties concerning water, oils, and hexadecane, if these films are anodized and decorated with fluorinate alkyl phosphate.

The integration of thin films composed of tilted Al columns or SiO_2/Ag multilayers in a capillary electrophoresis microdevice has shown to be useful for the separation and detection of amino acids [75].

For columnar Ag and Au thin films with tuned, narrow particle size distributions immersed in liquids with different refractive indexes, a linear relationship between plasmon resonance wavelength and refractive index of the surrounding media could be found [76].

Highly precise, efficient plasmonic biosensors [2, 4] for the detection of neutravidin [77], streptavidin [78], endocrine disruptors [1], and long-term blood sugar levels [3], for instance, have been realized by anchoring specific receptor molecules on the metallic columns of the thin films. The Raman signal has shown to be enlarged remarkably due to the local excitation of surface plasmons on the metallic columns. Surface-enhanced Raman scattering (SERS) enhancement factors up to 12 orders of magnitude are under debate, enabling the highly-sensitive detection of molecules down to a concentration of some pg/ml [1]. The fact that metallic columnar thin films are suitable as substrates for SERS sensing applications is mainly attributed to their structural characteristics. For instance, sharp tips of the individual columns cause a significant local enhancement of the electrical field, which increases the probability that a SERS event takes place and thus amplifies the SERS signal. The performance of the metallic columnar thin films as SERS substrates can be tuned by tailoring the columnar tilt angles or the columnar diameter [79, 80], for example. Another method to improve the SERS performance is the incorporation of “hot-spots” in the columns [81]. Such regions with an enhanced electromagnetic field have been reported, e.g., for square helical Ag columns [82].

Additionally, a fluorophore molecule located near columnar metallic thin films can show an enhanced emission intensity caused by metal-enhanced fluorescence [79, 83, 84]. This is used as detection and sensing tool for single molecules especially in medical diagnostics and biotechnology [85].

In recent years, columnar TiO_2 thin films have become interesting for coatings of implants. The biocompatibility of Ti originates from the chemically passive oxide layer naturally forming on the Ti surface [86]. Previous research indicates that the surface properties such as composition, hydrophilicity and texture of the oxide on the Ti affect the cellular response [87, 88]. The micro- and nanoscale surface morphology has shown to be a highly-sensitive parameter that influences for instance the cell adherence, proliferation, migration, gene expression, and differentiation [89-93]. Therefore, modifying the implants surface on the micro- and nanometer scale appears to be a promising approach for improving the interaction between tissue and the implants surface [93-96]. For instance, Dolatshahi-Pirouz *et al.* [97] and Pennisi *et al.* [98] have reported that nanostructured platinum surfaces have a profound impact on the proliferation of primary human fibroblasts, suggesting that nanostructured surfaces affect cellular responses.

3 Experimental Details

3.1 Sample fabrication

3.1.1 General deposition system setup and evaporation process

All metallic columnar thin films for the present work have been fabricated in the ultra-high vacuum (UHV) chamber (base pressure $p_{Base} \sim 1 \cdot 10^{-9}$ mbar) with attached load-lock and an electron beam evaporator (up to 10 kV / 500 mA) as described in the following (for illustration see Figure 3.1).

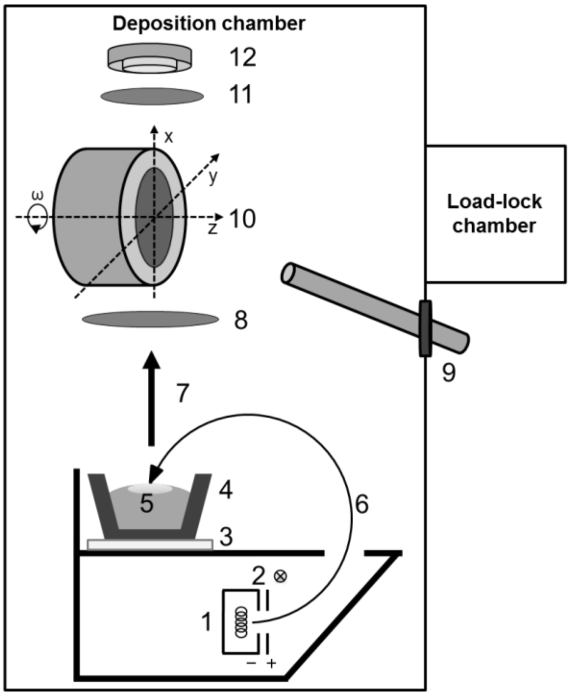

Figure 3.1: Schematic of the deposition system (not to scale). 1: filament, 2: magnetic field, 3: water-cooled crucible holder, 4: crucible, 5: molten spot, 6: path of electrons, 7: flux direction of evaporated material, 8: computer-controlled shutter, 9: tube to insert process gases, 10: substrate manipulator with sample holder, computer-controlled heating system, substrate tilting in the xz-plane and substrate rotation around the z-direction, 11: manually operated shutter, 12: quartz crystal microbalance.

The tungsten filament (1) of the electron beam evaporator is held at negative potential. The electron beam is extracted from the filament by thermionic emission. To direct the path of the electrons from the filament (1) to the material in the crucible (5), a magnetic field (2) is applied. The electrons are accelerated by applying the acceleration voltage U_B so that a high kinetic energy E is reached: $E = e \cdot U_B$. e is the elementary charge. As the electrons interact with the material in the crucible, this kinetic energy is transformed rapidly to other forms of energy, for instance, thermal energy that results in the melting / sublimation and evaporation of the material in the crucible. The resulting vapor flux consists of atoms (7). The substrate manipulator (10) contains the sample holder and enables a computer-controlled substrate movement and heating. A computer-controlled shutter (8) is located between crucible (5) and substrate manipulator (10). Film thickness and deposition rate are controlled by a quartz crystal microbalance (QCM) (12). A further manually operated shutter (11) is located between QCM (12) and substrate manipulator (10). Additionally, there is a tube (9) pointing directly towards the sample holder that allows process gases to flow directly to the substrate, if desired. The chamber is also equipped with different effusion cells (not shown), but those are not applied for the sample preparation.

Mean free path

The average path that a particle can travel without the collision with another particle in the residual gas is given by the mean free path L, which can be estimated by:

$$L = \frac{k_B T}{\pi\sqrt{2}\, d_{Col}^2\, p}. \tag{3.1.1}$$

Thereby, k_B denotes the Boltzmann constant, T is the temperature in the residual gas, d_{Col} is the collision radius between the evaporated particle and the residual gas atom, and p is the pressure in the deposition chamber. Assuming $T = 300$ K, $d_{Col} = 300$ pm, and $p = 1 \cdot 10^{-8}$ mbar results in a mean free path of approximately $L \sim 10.000$ m, which is significantly larger than the distance between crucible and sample holder $s = 30$ cm, indicating that the probability for scattering of the evaporated particles with residual gas atoms is low. Notice that equation (3.1.1) applies for conditions near the thermodynamically equilibrium, which is not fulfilled here. Nevertheless, the equation facilitates a rough estimation the mean free path of the particles. Further, in general a polar angular distribution of the cosine type and a Maxwell-Boltzmann energy distribution of the evaporated particles are assumed. However, as equilibrium conditions are not present, deviations are expected for both distributions.

Influence of residual gas atmosphere

The residual gas atmosphere is mainly composed of carbon monoxide, hydrocarbons, and molecular hydrogen. The proportion of molecular oxygen on the residual gas is merely in the order of magnitude of 1%. For the following estimation is assumed that the residual gas is composed entirely of O_2, since O_2 is more reactive compared to the other residual gas species. The number of oxygen molecules that hit the surface of the deposited material per second and unit area is given by the impingement rate R, which can be estimated by:

$$R = \frac{p}{\sqrt{2\pi\, m_{Mol}\, k_B T}}. \tag{3.1.2}$$

p denotes the pressure in the vacuum chamber, m_{Mol} is the mass of the residual gas particles, k_B is the Boltzmann constant, and T is the temperature. Under the assumption that the residual gas consists completely of molecular oxygen ($m_{Mol} = 32\ u$, with u being the unified atomic mass unit), deposition at RT ($T = 300$ K), and a pressure $p = 10^{-8}$ mbar, the impingement rate R yields $R = 2.7 \cdot 10^{12}$ cm^{-2}s^{-1} for oxygen molecules, and accordingly $5.4 \cdot 10^{12}$ cm^{-2}s^{-1} for oxygen atoms. The volume V of deposited material (for instance, Ti) per cm^2 with a deposition rate $r = 1$ nm/s is $V_{Ti} = 1$ cm$^2 \cdot 1$ nm $= 10^{-7}$ cm^3 per second. This corresponds to a number of Ti atoms of $(D_{Ti} \cdot V_{Ti} / m_{Ti}) = 5.66 \cdot 10^{15}$, with the mass

$m_{Ti} = 7.95 \cdot 10^{-23}$ g, and the bulk density $D_{Ti} = 4.5 \cdot \text{g/cm}^3$. If all the oxygen atoms would be incorporated in the deposited Ti film, this would yield $5.4 \cdot 10^{12} / 5.66 \cdot 10^{15}$ cm = 0.00095 ~ 0.1%. As a result, the influence of oxygen on the growth of the metallic thin films can be neglected.

3.1.2 Crucibles, substrates, and sample holders

For evaporation of Al, Ti, Co, Ni, Mo, and Ta, cylindrical metal pellets are used. These pellets are molten in the crucible before the deposition process started. For Cr, a Cr powder is applied, which is directly sublimated by the electron beam. All metals are evaporated from a crucible with 12 cm^3 filling volume each. The electron beam evaporator enables to insert in total four crucibles, but only one crucible can be accessed during the deposition process. Fabmate®-crucibles (made of high-strength graphite, 99.9995% elemental carbon) are used to evaporate Al, Ni, Ti, Mo, and Ta. Co is evaporated from a Cu-crucible and Cr from a C-crucible.

The maximum sample diameter that can be transferred via load lock to the deposition chamber is approximately 5 cm, but for deposition the Si-wafers are usually broken into pieces of approximately $1 \cdot 1$ cm^2. Thermally oxidized Si(100) pieces with an 800 nm thick oxide layer as well as natively oxidized Si(100) pieces with an oxide layer of typically a few nanometers thickness are used as substrates. Natively oxidized Si(100) pieces are only used for deposition at RT. For elevated substrate temperatures exclusively thermally oxidized Si pieces are used to avoid silicide formation [99-101].

For deposition at room temperature and at elevated temperatures, two different types of sample holders are available. (i) The customized Mo sample holder has a planar surface, meaning that the angle between substrate normal and incoming flux direction is nearly similar (deviation ± 1°) for all samples glued on this holder, but typically only one sample is glued in the middle of this sample holder per deposition process. This sample holder could be used in the range $300\text{ K} \leq T_{Sub} \leq 1100\text{ K}$. (ii) The steal sample holder that we have designed and fabricated in house is appropriate for $300\text{ K} \leq T_{Sub} \leq 600\text{ K}$. In this sample holder, in total three milled planes with different inclinations each are inserted so that different angles of the incoming particle flux could be realized during a single deposition process (same principle used for the liquid nitrogen (LN_2) cooled sample holder depicted in Figure 3.5). Those milled planes are arranged in vertical order one atop the other on the sample holder with respect to the incoming particle flux. Consequently, during deposition more material reaches the milled planes that are located nearer to the crucible. To balance this difference, additionally two Si pieces are glued on the very top and very low part of the planar parts of this steal sample holder, and the obtained difference in deposited film heights is used to adapt the film heights of the remaining samples.

The Si pieces are connected to the sample holders by carbon tape if the deposition is performed at 300 K ≤ T_{Sub} ≤ 400 K. For deposition at T_{Sub} > 400 K, a thin film of liquid carbon glue is applied. The glued samples are let dry overnight. After the desired substrate temperature has been reached, a minimum of five minutes waiting time is held before the deposition process started. This time ensures that the sample has the same temperature as the sample holder.

3.1.3 Controlling substrate movement and temperature

Substrate movement

The substrate manipulator arm can be moved in x-, y-, and z-direction (compare Figure 3.1). Tilting around the y-direction enables to tailor the direction of the incoming particle flux with respect to the substrate normal in the range 0° ≤ θ_{OAD} ≤ 90°. Further, continuous substrate rotation around the z-axis can be applied in the range 0.25 rpm ≤ ω ≤ 60 rpm. To realize even lower rotation frequencies, e.g., for the growth of spirals (see, for instance, Figure 3.2 (c), (f)), the stepper motor of the substrate manipulator arm is used via macro. Thereby, a certain film thickness is grown at stationary substrate, then the substrate is rotated rapidly by a desired small revolution angle ε (e.g., $\varepsilon = 36°$), and again the desired film thickness is grown at stationary substrate. This process of discrete substrate rotation is repeated as often as needed to create a spiral structure with a certain number of loops. For larger ε, other columnar shapes can be realized as well. For example, if $\varepsilon = 180°$, zigzag columns as depicted in Figure 3.2 (a), (e) can be grown.

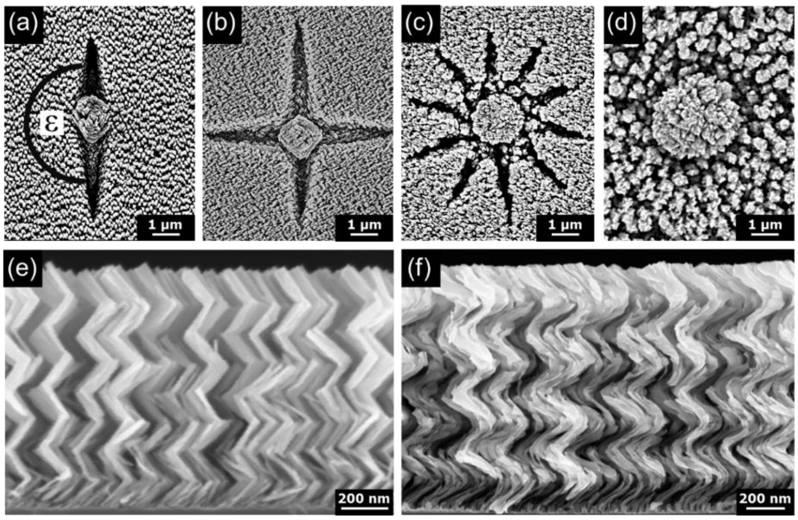

Figure 3.2: Top-view SEM images of (a) 2-fold (zigzag, $\varepsilon = 180°$), (b) 4-fold ($\varepsilon = 90°$), (c) 10-fold ($\varepsilon = 36°$), and (d) 60-fold ($\varepsilon = 6°$) Mo chevron structures deposited at $\theta_{OAD} = 84°$ and at RT on natively oxidized Si(100) substrates. ε is the revolution angle. The shadowed areas are caused from the dust particle in the center of each SEM image. In (d), the shadowed areas are not visible, because of the small revolution angle. (e) and (f) show cross-sectional SEM images corresponding to (a) and (c), respectively.

Substrate heating

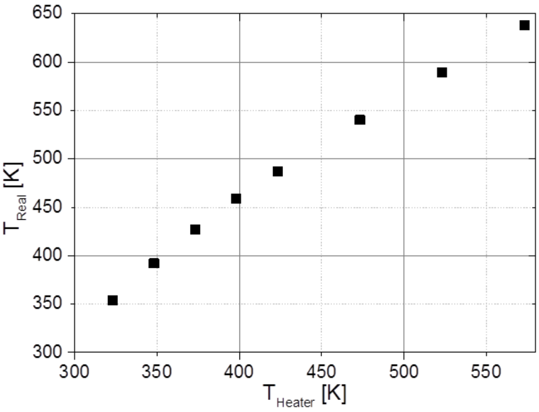

Figure 3.3: Temperature measured by the thermocouple mounted on the substrate holder (T_{Real}) versus the heater temperature T_{Heater}.

The substrate manipulator contains a computer-controlled tungsten wire resistance heater that enables to increase the substrate temperature from RT up to 1100 K. The temperature is controlled by a K type thermocouple (TC). Temperature calibration up to temperatures of 573 K is carried out by mounting another K type thermocouple directly at the substrate holder and then heating the substrate. The temperature given from the heater (T_{Heater}) and the corresponding temperature measured by the TC on the substrate holder (T_{Real}) are depicted in Figure 3.3. For temperatures larger than 573 K, the TC does not deliver reliable results anymore, which is likely due to heat losses in the cables of the TC. Thus, another method, using the eutectic point of the Al-Si system, is applied for calibration in the high temperature regime [102]. For this purpose, a natively oxidized Si(100) substrate is coated first with a 500 nm thick Si layer and then with a 50 nm thick Al film by vertical deposition ($\theta_{OAD} = 0°$). Then, the substrate temperature is increased successively by using the substrate heater in the manipulator arm, and the thermal radiation that the sample surface emits is detected by a pyrometer. The temperature measured by the pyrometer changes remarkably by $\Delta T = 49$ K as the heater temperature increases from 793 K to 803 K, as shown in Figure 3.4. This occurs at the eutectic point, at which Al and Si form a homogenous mixture by melting, although each of the two materials individually exhibit a larger melting point. As the eutectic point for the Al-Si system is known to be at 850 K, this can be used to calibrate the substrate temperature. Precisely, the temperature is interpolated linearly between 573 K and 850 K, resulting in the following extrapolation curve for that temperature range:

$$T_{Real} = 0.986 \cdot T_{Heater} + 69\ K. \tag{3.1.3}$$

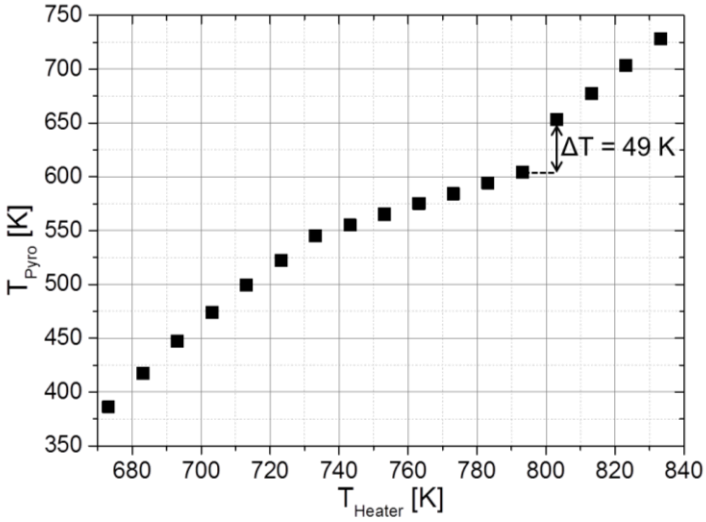

Figure 3.4: Temperature measured by the pyrometer T_{Pyro} depending on the heater temperature T_{Heater}.

Substrate cooling

Lowering the substrate temperature down to 77 K is realized by a continuous flow of liquid nitrogen (LN_2) through an in-house designed and built sample holder, as can be seen in Figure 3.5. This sample holder is composed of two copper blocks. The liquid nitrogen flows through the "body" copper block, while the "front" copper block is the sample holder. The sample holder contains five milled planes with different inclinations each, thereby realizing five different local incidence angles (θ_{OAD} = 0°, 74°, 78°, 82°, 86°) during a single deposition process.

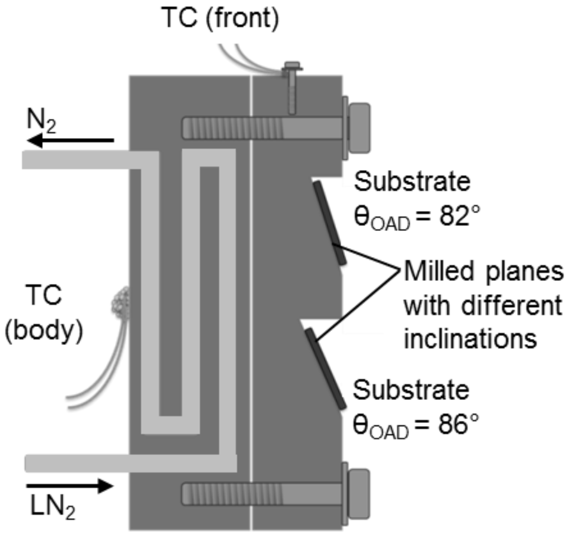

Figure 3.5: Schematic illustration of liquid nitrogen (LN_2) cooled sample holder from side-view (not to scale). TC are thermocouples, and θ_{OAD} is the angle of the incoming particle flux with respect to the substrate normal.

Both blocks are connected by screwing. The distance between LN_2 sample holder and crucible is approximately 35 cm. For controlling the substrate temperature, two independent K type thermocouples are applied, which are mounted directly on the surface of the copper blocks. To ensure a precise calibration, a third thermocouple of the same type is put directly in liquid nitrogen. Notice that the TC voltage is not linear for temperatures lower than 223 K. To calibrate the thermoelectric voltage for low temperatures (range 273 K to 73 K), correction coefficients d_n according to the National Institute of Standards and Technology (NIST) data homepage are applied [103]. The temperature T (in °C) can then be determined by using the thermoelectric voltage U and the correction coefficients d_n:

$$T = d_0 + d_1 U + d_2 U^2 + \cdots + d_n U^n . \tag{3.1.4}$$

As can be seen in Figure 3.6, lowering the substrate temperature from RT to 77 K takes approximately 45 min. During deposition, the substrate temperature is kept constant at 77 K with a fluctuation of ± 1 K. Heating the sample holder after deposition to RT requires about 4 hours and can be realized passively by only stopping the liquid nitrogen supply, as well as actively by letting molecular nitrogen gas flow through the body copper block (as in the heating regions with steeper slope in Figure 3.6). As the temperature of the LN_2 sample holder is over dew point, the chamber can be vented.

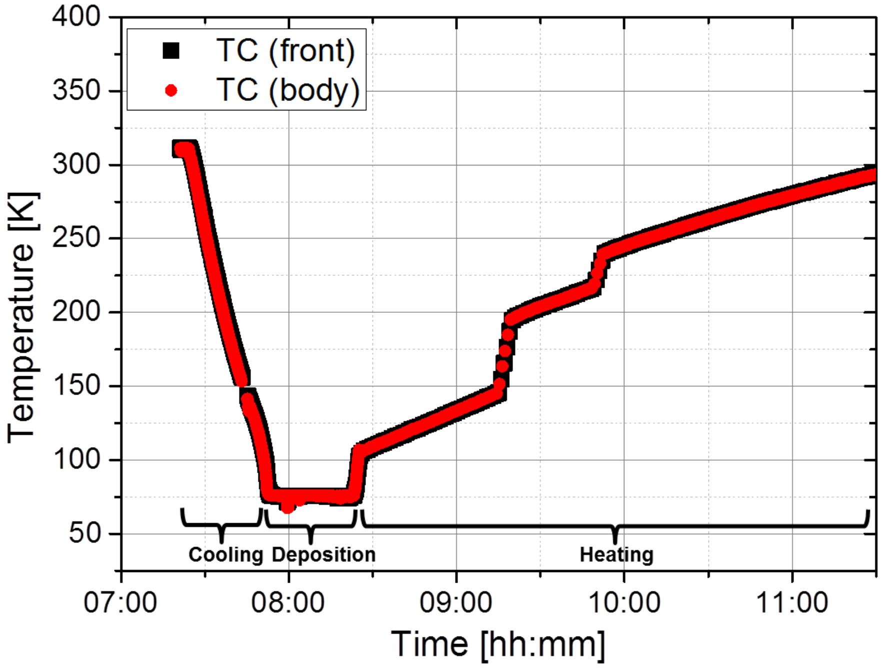

Figure 3.6: Temperature of the thermocouples TC (front) and (body) depending on time.

3.1.4 Controlling film thickness and deposition rate

The deposition rate and the film thickness are controlled by a quartz crystal microbalance (QCM) that is mounted atop the substrate manipulator arm so that principally more material is deposited at the substrate surface than on the QCM. To balance this difference, the tooling factor (TF) is calculated: $TF = TF_{initial} \cdot (t_{measured} / t_{preset})$. Thereby, $TF_{initial}$ is the initially applied tooling factor, $t_{measured}$ is the measured film thickness obtained directly from cross-sectional SEM images, and t_{preset} is the preset film thickness created by the instrument. Both film thicknesses apply for vertical particle incidence ($\theta_{OAD} = 0°$). For example, a tooling factor of 600% means that six times more material has been deposited on the substrate than on the QCM. So, with the TF, the QCM can control the film thickness on the substrate for vertical particle incidence, and all deposition rates denoted in the present work apply always at the substrate. As the substrate is tilted to an oblique angle, the effective substrate area from the perspective of the incoming particles is lowered, resulting in a reduced film thickness than expected for vertical deposition. This film thickness has then to be determined directly from cross-sectional SEM images.

3.2 Sample characterization

3.2.1 Scanning electron microscopy (SEM)

A scanning electron microscope enables to produce images of a sample by scanning the sample surface with a focused primary electron beam. The electrons are emitted out of a cathode and are accelerated towards the sample surface by a voltage in the range of 0.1 kV to 30 kV. As the primary electrons reach the sample surface, they interact with the specimen in a volume that reaches approximately 100 nm underneath the sample surface. Depending on the beam voltage, the sample material, and the excitation volume, different secondary signals are generated. For imaging, the SEM typically collects secondary (SE) and backscattered electrons (BSE), but Auger electrons, continuum and characteristic X-rays, visible light (cathodoluminescence) as well as transmitted electrons can also be emitted. Secondary electrons are generated near the sample surface (~ 50 nm) by inelastic scattering of the primary electrons at the electron shell of the atoms in the specimen. The SEs have an energy lower than 50 eV and contain information about the surface topography up to nanometer resolution. In contrast, the BSEs exhibit an energy larger than 50 eV and are generated deeper in the interaction volume (~ 100 nm underneath the surface) by elastic scattering of the primary electrons. The intensity of the BSE signal depends on the atomic mass of the elements of the specimen and can therefore be used to gain qualitative information about the distribution of different elements in the sample. Most commonly used detectors for collecting the SE and BSE signals are the Everhard-Thornley detector (scintillator-photomultiplier system) [104] and semiconductor detectors.

All SEM images in the present work have been produced by using a Carl Zeiss SMT AG Ultra 55 GEMINI® SEM. The electrons are emitted out of a ZrO_2-coated tungsten tip by field emission and are accelerated by a voltage in the range between 0.5 kV to 50 kV through an electron tube equipped with several electromagnetic lenses to the sample surface where the secondary signals are excited. The limit for topographical resolution is approximately 3 nm. The SEM includes a ring-shaped SE detector within the electron lens system (InLens detector) and another SE detector outside the electron column that points towards the sample stage. Additionally, a BSE detector and an energy and angle selective backscattered electron (EsB) detector are available. For the samples in this study, the beam voltages are adjusted in the range of 3 kV to 10 kV, depending on charging effects on the sample surface. The work distance is always between 2 mm and 5 mm. For the SEM images shown in this study, the InLens detector is used exclusively. Cross-sectional SEM images are obtained by manual cleaving the sample prior to investigation. From these cross-sectional images, the tilt angles of the columns (measured with respect to the substrate normal) as well as the film thickness (measured parallel to the substrates normal) are determined manually [105]. A considerable large set of measurements is carried out to ensure the statistical reliability. The error bars for the determined columnar tilt angles β, film thickness t, and film porosity P are based on the standard deviation, which is automatically calculated by evaluating the SEM images by ImageJ [105].

The size of the smallest features that can be obtained in a microscope is in general determined by the used wavelength. The De Broglie wavelength λ_B [106] of an electron is given by the Planck constant h and the relativistic momentum of the electron p:

$$\lambda_B = \frac{h}{p}. \tag{3.2.1}$$

The relativistic relation between energy and momentum is $E = p^2c^2 + E_0^2$ with $E = E_0 + eU_B$ and $E_0 = m_0c^2$ so that the relativistic formula for the De Broglie wavelength is:

$$\lambda_B = \frac{h}{\sqrt{2m_0eU_B}} \frac{1}{\sqrt{1 + \frac{eU_B}{2m_0c^2}}}. \tag{3.2.2}$$

m_0 is the electron mass, e is the elementary charge, U_B is the acceleration voltage, and c is the speed of light. For example, for electrons accelerated with a voltage of 3 kV, this leads to a wavelength of the electrons of approximately 22 pm, which is smaller than the lattice distances in the investigated columnar Mo thin films ($d_{hkl} \leq 314$ pm).

3.2.2 Transmission electron microscopy (TEM)

Transmission electron microscopy (TEM) is used for high-resolution, local structural analysis of the metallic, columnar thin films. To perform TEM, a stable electron beam is generated out of an electron source. For instance, heated tungsten wires or LaB_6 crystals can be used as cathodes that provide electrons by thermal emission. However, thermal electrons show a broad energy distribution of up to several eV, leading to a lowered resolution. To reduce the energy distribution, field emission cathodes made of ZrO_2/W are applied more recently, which emit electrons by strong electrostatic fields. After emission, the electrons are accelerated and enter a system of several condenser lenses, thereby decreasing the beam divergence. Additional reduction of divergence can be realized by condenser apertures, but this leads to lowered beam intensity. The specimen is located between the lenses of the objective lens system. As the specimen is penetrated by the electron beam, the electrons interact with the atoms of the specimen. The resulting scattering events of the electrons depend on the atomic number, thickness of the specimen as well as on the orientation of the crystalline material. Elastic scattering (such as diffraction) on the lattice results in the local modulation of amplitude and phase of the primary electron wave. Inelastic scattering contains no local information and must be avoided, e.g., by reducing the specimen thickness down to the nm-range. The transmitted and scattered electrons exhibit an angular distribution. With objective apertures, electrons of a certain angular range can be extracted so that diffraction patterns of selected areas of the specimen can be detected (selective area electron diffraction, SAED).

In general, two different imaging modes can be distinguished. (i) In transmission electron microscopy (TEM), a parallel and coherent beam geometry is used, and the specimen is homogenously penetrated with the parallel beam. The objective (contrast) aperture enables to select variously scattered electrons so that bight- and dark-field TEM images can be generated. For projecting these images, a fluorescent screen or a CCD camera are applied. (ii) Scanning transmission electron microscopy (STEM) utilizes a focused, convergent electron beam that is scanned over the specimen. An equal beam geometry is provided over the entire area of the investigated specimen. Several detectors are available to observe transmitted electrons with different angular distributions. For detecting heavily scattered electrons, the high angle angular dark field detector (HAADF) is applied. The scattered electron beam intensity is proportional to the square of the average atomic number in the investigated material ($I \sim Z^2$), which enables to adjust the Z-contrast of the image [107] and can be used to identify chemical elements in the specimen. For dark-field imaging, two annular dark field detectors (DF) are available for different angular ranges each [108]. In contrast to dark field imaging that is based on the diffracted electrons, bright-field TEM images are constructed from the non-diffracted electrons (bright-field detector (BF)). Additionally, lighter elements can be imaged by an annular bright-field detector (ABF).

In the present study, a structural TEM analysis of the metallic columns is carried out by utilizing an aberration corrected Titan^3 G2 60-300 microscope that is optimized for acceleration voltages between 80 kV and 300 kV [109]. The Titan^3 G2 60-300 microscope is located on a vibration-decoupled foundation in a soundproofed and air-conditioned room that is equipped with active magnetic field compensation. The microscope is equipped with an energy dispersive X-ray spectroscopy (EDX) detector (Bruker, Superior X) for chemical analysis as well as with a spectrometer (GIF Quantum 963/P) for electron energy loss (EELS) spectroscopy. All samples shown in this work are analyzed with Titan^3 G2 60-300 microscope working at 300 kV either in TEM or µP-STEM (micro probe STEM) mode. TEM specimens are produced by two different methods. For the first method, TEM specimens are collected by scratching lacey carbon coated Cu grids over the columnar thin films. Solvents are not used. With the second method, cross-sectional specimen for TEM analysis are fabricated by using a focused high energy Ga-ion beam (FIB) and subsequent milling with low-energy Ar-ions (NanoMill) [110]. The final thickness of the FIB lamellae is the range of 80 nm. High-resolution (HR) TEM as well as nanobeam and selected area electron diffraction (NBED and SAED, respectively) are applied to study the local structure and the texture of the samples. Image analysis is performed by using GatanDigitalMicrograph software [111]. The shown diffraction patterns are contrast enhanced.

3.2.3 X-ray diffraction (XRD) and in-plane pole figure measurements (IPPF)

X-Ray Diffraction (XRD) measurements enable to gain information of the crystal structure of the columnar, metallic thin films over a macroscopic substrate area. In the diffractometer, the X-ray radiation is generated by electrons from a cathode that are accelerated to a copper anode, where on the one hand the electrons are strongly decelerated (bremsstrahlung) and on the other hand electrons from the shells of the atoms of the specimen material are removed, thereby creating characteristic X-rays. The X-ray radiation is parallelized by a multilayer gradient mirror. The selection of the Cu $K_{\alpha 1}$ radiation (wavelength $\lambda = 0.15405$ nm) is performed by a dual crystal monochromator. The parallel, monochromatic X-ray beam reaches the lattice plane of the sample under a Bragg angle θ. For parallel planes of atoms with a space distance d_{hkl} between the planes (hkl are the Miller indices), constructive interference occurs if the Bragg condition is fulfilled:

$$2d_{hkl} \sin\theta \; = n\lambda, \tag{3.2.3}$$

where n is a positive integer and λ is the wavelength of the incident wave. The diffracted beam enters an aperture system that limits the beam divergence. Afterwards, the beam is detected by a scintillation detector. For the θ-2θ measurement, the sample moves by the angle θ and the detector simultaneously moves by the angle 2θ, while the X-ray tube is stationary. A fulfilled Bragg condition results in a characteristic diffraction maximum ("Bragg peak"). The position of the Bragg peak in the θ-2θ diffraction diagram depends on the lattice spacing. Such a peak is only observed if the lattice plane normal is parallel to the diffraction vector u, which is the vector that bisects the angle between the incident and diffracted beam. Thus, a θ-2θ measurement only contains information about one family of

Bragg peaks. A SEIFERT XRD 3003 PTS diffractometer is applied for the θ-2θ measurements presented in this study, because it enables to align the position of sample and detector (and accordingly the diffraction vector u) so that the other families of Bragg peaks in the sample can also be detected.

The texture of the samples is investigated by in-plane pole figure (IPPF) measurements. For this purpose, a certain Bragg reflection is chosen from a powder diffraction file database. During the IPPF measurement, the half-sphere above the sample is scanned with a fixed Bragg reflection geometry by varying two geometrical parameters. Firstly, the sample rotates around its normal by the azimuthal angle Φ [0°; 360°]. Secondly, the diffraction plane is tilted with respect to the sample normal by the polar angle χ [0°; 90°]. The step sizes for both motions are 2°. If the Bragg condition (equation (3.2.3)) is fulfilled, a pole density maximum can be obtained. Eventually, the resulting diffracted intensity distribution, measured as a function of these two angles Φ and χ, is plotted in stereographic projection to obtain the pole figure of the chosen Bragg reflection. The projection center is the south pole of the pole sphere as illustrated in Figure 3.7. The center of the pole figure is defined as $\chi = 0°$, while $\chi = 90°$ denotes the outer edge of the pole figure. A pole density maximum at $\chi = 0°$ means that the lattice direction is parallel to the substrate normal, and a pole density maximum located at $\chi = 90°$ indicates that the lattice direction is perpendicular to the substrate normal. The azimuthal angle $\Phi = 0°$ is located at the top of the pole figure (12 o´clock), and is circularly coordinated clockwise, meaning that $\Phi = 90°$ corresponds to 3 o´clock, $\Phi = 180°$ corresponds to 6 o´clock, etc. The position of the pole density maxima of a crystallite oriented perpendicular to the sample surface (reference plane) differs from those crystallites that are tilted with respect to the substrate surface, as indicated in Figure 3.7 (a) and (b), respectively.

The IPPF measurements are performed in an Ultima IV X-ray diffractometer (RIGAKU), because this diffractometer enables XRD measurements with more intensity compared to the SEIFERT diffractometer since there is no monochromator on the incident optics side. The incorporated cross beam optics technology facilitates to select between the permanently mounted and aligned parallel and focusing geometries. In the RIGAKU diffractometer, a copper anode is utilized for X-ray radiation as well. The X-ray generator has a maximum rated output of 3 kW, a rated tube voltage between 20 – 60 kV, and a rated tube current between 2 – 60 mA. The RIGAKU diffractometer is equipped with an automatic alignment of tube height, goniometer, optics, and detector. The horizontal beam divergence is controlled by a Soller slit inserted in X-ray beam path. The in-plane parallel slit collimator (PSC) on the incidence optics side and the in-plane parallel slit analyzer (PSA) on the receiving optics side control the vertical beam divergence and define the covering 2θ-range. In contrast to the Soller slits, the PSC and the PSA determine the

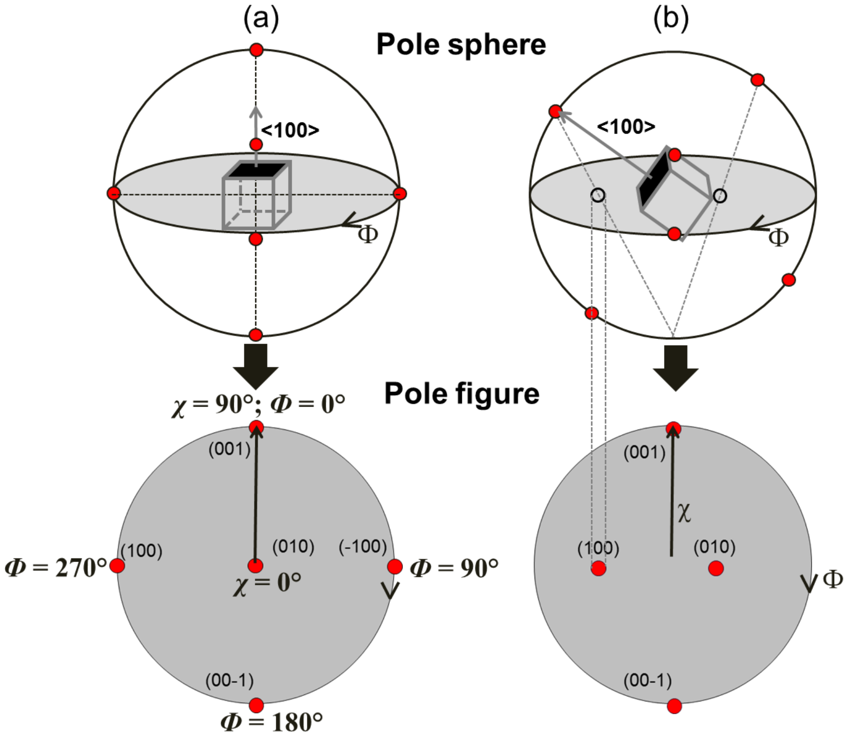

Figure 3.7: Schematic illustration of the pole figure measurement exemplarily for the <100> direction in a bcc crystal oriented perpendicular to the substrate surface (a) and tilted with respect to the substrate surface (b). The red dots illustrate the pole density maxima and the grey plane is the reference plane. χ denotes the polar angle and the Φ is the azimuthal angle.

measurement resolution and reduce the measurement intensity. The PSA collects only the parallel component of the diffraction signal from the sample surface. If the diffraction peak of interest is close to another diffraction peak, a PSA with sufficiently small aperture should be used to avoid detecting intensity from the other diffraction peak. Optionally, a dual position graphite diffracted beam monochromator for Cu can be inserted on the incident beam side, but this reduces the measured intensity significantly. The detector is a scintillation counter.

For all IPPF measurements in this study, the parallel beam geometry produced by a multilayer gradient mirror and collimated primary Cu K_α X-ray radiation (wavelength $\lambda = 0.15405$ nm) is used. Further, a Soller slit of 2.5°, PSC = 2.5°, and a slit that limits the horizontal footprint of the sample (divergence height limiting slit DHL = 5 mm) are applied. As the intensity of the IPPF measurements in the present work is typically lower than 10^3 cps, neither a monochromator nor a PSA are used. Each IPPF is measured for at least 24 h up to several days. Notice that a quantitative analysis of the IPPF measurements requires various corrections such as absorption-, background-, and defocusing-corrections [112]. However, because all IPPF measurements in the present work are evaluated exclusively on a qualitative basis, such corrections are not applied, meaning that all shown IPPFs appear as-measured.

3.2.4 Reflection high-energy electron diffraction (RHEED)

The texture of the thin films surface is additionally analyzed *ex situ* in an ultra-high vacuum chamber that is equipped with a reflection high-energy electron diffraction (RHEED) electron source (30 kV, STAIB Instruments). The electrons strike the sample surface under a gracing incidence angle of approximately 2°, resulting in a low penetration depth of two to three monolayers where diffraction can occur. If the Bragg condition (see equation (3.2.3)) is satisfied, constructive interference and thus diffraction maxima can be obtained. A phosphor screen is used for projecting the resulting RHEED patterns, which are finally recorded by a CCD camera.

3.2.5 Raman scattering spectroscopy

Raman scattering spectroscopy [113] represents a light scattering technique based on the interaction of a monochromatic laser beam with the sample material so that scattered radiation of different wavelengths is generated. Depending on the wavelength (energy) change $\Delta\lambda$, three different categories of light scattering can be distinguished [114]. A wavelength change smaller than 10^{-5} cm^{-1} is known as Rayleigh scattering, a wavelength change of $\Delta\lambda \sim 0.1$ cm^{-1} is known as Brillouin scattering [115], and $\Delta\lambda > 1$ cm^{-1} is known as Raman scattering. While Rayleigh scattering is elastic, both Brillouin and Raman scattering are inelastic, meaning that the wavelength of the scattered light is not equal to the wavelength of the incident light. For Raman shifted photons of light, the frequency difference of the scattered and the incident light can be negative or positive. For the Stokes Raman scattering, an energy transfer from the incident photon to the scattering material takes place, resulting in a lowered energy and frequency of the scattered compared to the incident photon. In contrast, for the anti-Stokes Raman scattering an energy transfer from the scattering material to the incident photon leads to an enlarged energy and frequency of the scattered photon compared to the incident photon. The energy difference between incident and scattered photon corresponds to the energy difference between two resonant states of the material. For molecules, this energy difference is characteristic for the vibrations (bonds) present in the scattering molecule. For crystals, the energy difference corresponds to the excited phonons, and the resulting phonon spectrum contains information about the phase of the elements present in the sample, for example. Energy difference ΔE_{Raman} and Raman frequency shift Δf_{Raman} are linearly correlated by the Planck constant h:

$$\Delta E_{Raman} = h \cdot \Delta f_{Raman}. \tag{3.2.4}$$

The intensity of the scattered light versus the frequency shift Δf of the photons can be presented in a Raman spectrum. Because the Stokes and corresponding anti-Stokes peaks arise from the energy difference of the same resonant states, such peaks are symmetrically arranged around $\Delta f = 0$. The intensity of the peaks is determined by the temperature, which directly influences the populations of the initial states of the material. Lower temperature means that the lower (ground) state is more populated than the excited states so that transitions from the lower to the upper states (Stokes transitions) will occur more properly (stronger peak) compared to anti-Stokes transitions (weaker peak). As this peak ratio is temperature dependent, it can be used to determine the local temperature on the sample. Thereby, it should be considered that irradiating the sample with laser light might cause a locally increased temperature on the sample. For the Raman measurements in this study, a Horiba LabRam HR Evolution spectrometer (Horiba GmbH), equipped with 473 nm, 532 nm, and 633 nm lasers and an Olympus MPlan N 100x/0.90 objective is utilized.

4 Morphological Analysis of Columnar Thin Films

The experimental findings represented in this dissertation have already partly been published or are under review in peer-reviewed journals. In the introduction part of chapters 4 – 6 is noted which of the author´s publication applies to the corresponding chapter. To highlight these first-author publications from other co-author references, the notation [LIE01 – LIE05] is introduced. The corresponding list of publications has been enclosed.

The first part of this chapter focusses on the growth of obliquely deposited Al, Ti, Cr, and Mo thin films. These metals are chosen in a way that a wide range of melting points (from T_{Melt}(Al) = 933 K to T_{Melt}(Mo) = 2890 K) as well as a wide range of crystal structures (Al (fcc), Ti (hexagonal closed packed, hcp), Cr and Mo (bcc)) is covered. The columnar shape, columnar tilt angles β and porosities P of these metallic thin films are studied depending on the angle of the incoming particle flux θ_{OAD} and on the substrate temperature T_{Sub}. Finally, the experimental findings of the columnar metallic thin films are compared with each other to draw more general conclusions concerning the growth process [LIE01, LIE02].

In the second part, the oblique deposition geometry is combined with substrate rotation, which is known as glancing angle deposition (GLAD). The growth process is analyzed in terms of continuous and stepwise substrate rotation in the highly oblique deposition regime at RT (300 K). The observed results are compared with the growth mechanisms found for oblique deposition without substrate rotation [LIE01].

Al, Ti, Cr, and Mo are deposited obliquely at RT on natively and thermally oxidized Si(100) substrates (latter with 800 nm thick oxide layer). The deposition rate is $r = 1$ nm/s for Al, Ti, and Cr and $r = 0.5$ nm/s for Mo, unless otherwise stated. Indeed, every deposition parameter is expected to have a large impact, for instance, considering the shape of the developing structures at the substrate surface. For this reason, the influence of the deposition rate on the morphology of obliquely deposited Mo thin films has been analyzed (see subsection 4.2.1). This analysis reveals that no morphological differences between obliquely deposited Mo thin films deposited with $r = 1$ nm/s and $r = 0.5$ nm/s could be found. Thus, the Mo thin films are deposited with $r = 0.5$ nm/s to preserve the experimental equipment, and these samples are expected to be comparable with Al, Ti, and Cr thin films grown with $r = 1$ nm/s.

4.1 Oblique angle deposition

4.1.1 Deposition at room temperature

In this subsection, the influence of the direction of the incoming particle flux θ_{OAD} on the columnar shape, columnar tilt angles, and on the thin film porosity is analyzed. The substrate temperature is kept constant at RT.

Columnar shape

Al, Ti, Cr, and Mo thin films are grown at RT on natively oxidized Si(100) substrates with varying angles of the incoming particle flux $76° \leq \theta_{OAD} \leq 88°$. Depositing under such highly oblique angles results in the self-assembly of nanostructured thin films that are composed of separated tilted columns inclined towards the direction of the incoming particle flux (see Figure 4.1). The growth of the separated columns is driven by the shadowing effect [10, 13]. According to van der Drift [11], only the columns with the fastest vertical growth component will be successful in the competitive growth, as those columns will overgrow the slower growing columns. As a result of this competitive growth process, the obliquely deposited metallic thin films consist of columns with different sizes. This means that during film growth, a transition from nano- to microsized columns occurs. Once separated columns can also coalesce to larger bundle features (i) as the film growth proceeds (see, e.g., Figure 6.1 (a – d)), or (ii) as the deposition geometry becomes less oblique, thereby reducing the shadowing length (see, e.g., Figure 6.8). This process is known as the frequently observed bundling effect [18, 22, 31, 116].

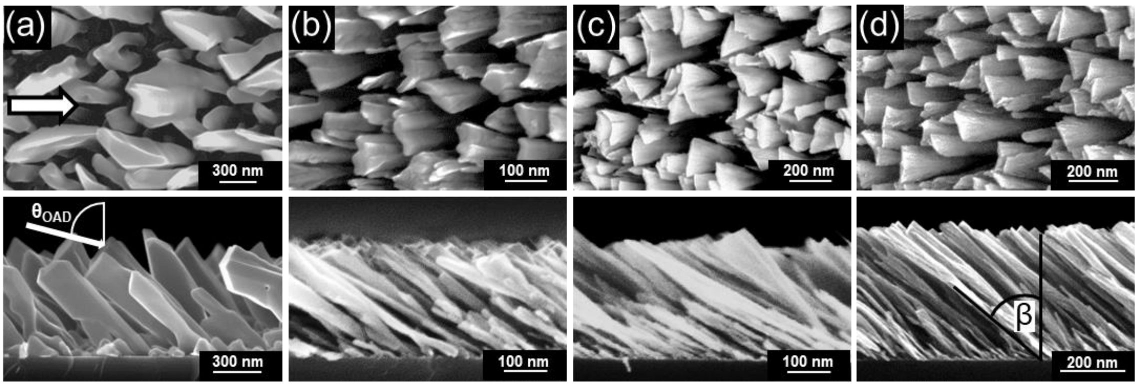

Figure 4.1: Top-view and corresponding cross-sectional SEM images of (a) Al, (b) Ti, (c) Cr, and (d) Mo thin films deposited at an oblique incidence angle θ_{OAD} = 84°at room temperature on natively oxidized Si(100) substrates. The white arrow indicates the direction of the incoming particle flux. The columnar tilt angle is denoted by β. All angles are measured with respect to the substrate normal.

Columnar tilt angles

The columnar tilt angle β for Al, Ti, Cr, and Mo thin films grown at RT on natively oxidized Si(100) substrates is determined depending on the angle of the incoming particle flux θ_{OAD}. Figure 4.2 (a) presents the found relations between both angles β and θ_{OAD}. Three general observations can be made: (i) The tilt angles are smaller than the incidence angle, (ii) the tilt angles tend to increase for more oblique incident angles, and (iii) all observed graphs can be approximated by a linear fit. However, the slope m of these graphs varies significantly for each investigated metal, although all metals have been deposited under similar experimental conditions. The slopes are $m_{Al} = 0.3$, $m_{Ti} = 1.4$, $m_{Cr} = 1.5$, and $m_{Mo} = 0.9$.

The most commonly accepted rules to describe the β–θ_{OAD} relations are the cosine (for $\theta_{OAD} > 70°$) [7] and the tangent rule (for $\theta_{OAD} < 70°$) [19], which are both shown in Figure 4.2 (a). Yet, these rules are not suited to describe the found β–θ_{OAD} relations for Al, Ti, Cr, and Mo adequately. The reason for this is that these rules are based on semi-empirical considerations, meaning that the particular material properties as well as deposition parameters are not considered [23]. To overcome this, numerous models have been suggested in the last decades [7, 23-25, 117] (see also subsection 2.2.1).

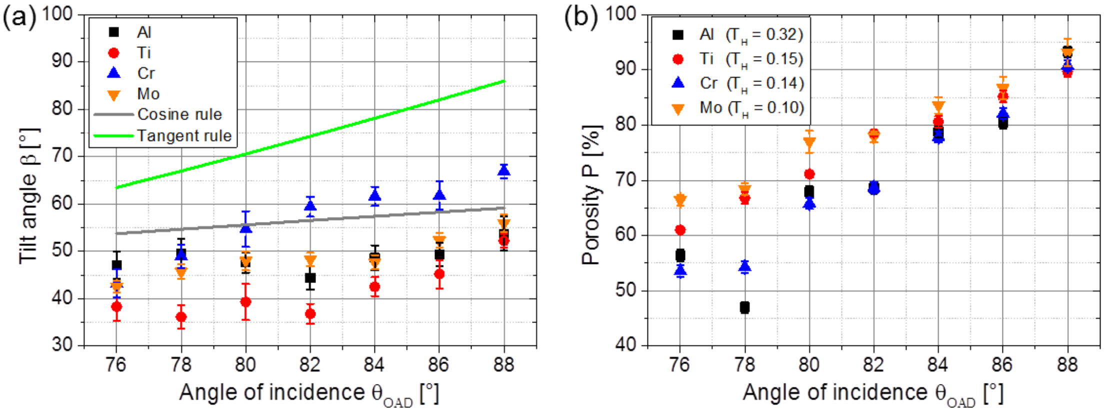

Figure 4.2: (a) Tilt angles β and (b) film porosity P of metallic thin films grown with different oblique incidence angles θ_{OAD} at room temperature on natively oxidized Si(100) substrates.

Recently, we have developed a model that enables the prediction of the tilt angle for the complete range of incidence angles $0° \leq \theta_{OAD} \leq 90°$ that has also been verified for Mo [26], for instance (see Figure 4.3). This model is based on one single parameter, the fan angle Φ_{Fan}, which combines the material properties (e.g. surface-diffusion coefficient) as well as deposition conditions (such as substrate temperature or beam divergence). The fan angle is the angle by which a freestanding fan or overhang structure grows away from the incidence direction. This angle can be determined experimentally before the desired samples are fabricated and can be applied to predict film properties for each deposition angle.

For further investigations of the growth of obliquely deposited metallic thin films, the homologous temperature T_H is used, because this is a well-proven and tested parameter to compare materials with different melting points [53]. The homologous temperature is determined by scaling the actual substrate temperature T_{Sub} to the melting point T_{Melt} of the evaporated metal at standard conditions: $T_H = T_{Sub} / T_{Melt}$ (both in K). As the substrate temperature is kept constant at 300 K, the homologous temperatures for the investigated metals can be determined to $T_H(\mathrm{Al}) = 0.32$, $T_H(\mathrm{Ti}) = 0.15$, $T_H(\mathrm{Cr}) = 0.14$, and $T_H(\mathrm{Mo}) = 0.10$. The homologous temperature enables to compare the activation of the surface self-diffusion for the different metals. As the homologous temperature varies between $0.10 \leq T_H \leq 0.32$, it can be concluded that the surface self-diffusion varies significantly for the metals deposited at RT. For instance, the high T_H for Al suggests an enlarged adatom mobility, which allows incoming atoms to move also in the shadowed regions between the Al columns. This reduces the shadowing effect as well as the influence of the incidence angle on the tilt angle, so that a relatively small slope m_{Al} is obtained. In contrast, the slopes for Ti, Cr, and Mo are steeper due to the more limited surface self-diffusion and in turn more dominant shadowing effect. For further investigations, the homologous temperature is applied to ensure a better compatibility of the deposited metals.

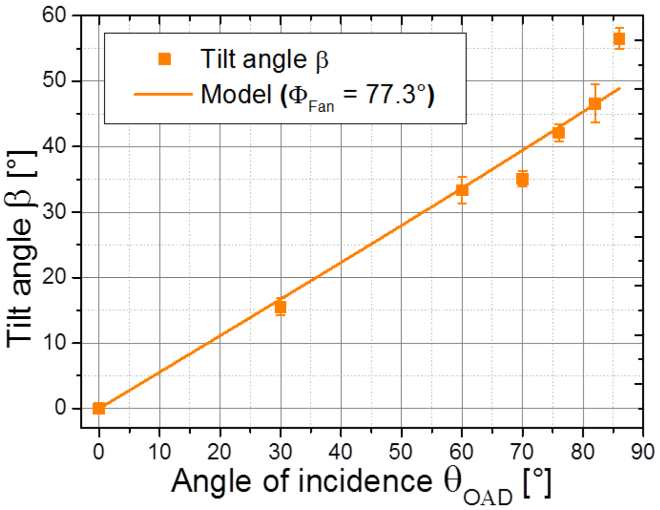

Figure 4.3: Tilt angles β of Mo thin films grown with different oblique incidence angles θ_{OAD} at RT on natively oxidized Si(100) substrates. Φ_{Fan} denotes the fan angle.

Thin film porosity

In addition, the film porosity P versus the incidence angle θ_{OAD} is determined. For vertical deposition ($\theta_{OAD} = 0°$), a nearly compact layer with a film density $\rho_{\theta=0°}$ and a film thickness $t_{\theta=0°}$ (measured parallel to the substrate normal) of the deposited material is forming. Since such a compact layer can contain inner voids, grain boundaries, etc. [118], $\rho_{\theta=0°}$ does not necessarily equal the bulk density of the material. As the substrate is tilted to $0° < \theta_{OAD} < 90°$, the oblique deposition geometry is realized. Thereby, the effective area of the substrate is reduced by a factor cos (θ_{OAD}) from the perspective of the incoming atoms so that only a fraction of the incoming atoms can condense on the substrate. Consequently, the film thickness $t_{\theta>0°}$ is lower than for vertical deposition. However, $t_{\theta>0°}$ is larger than expected, because shadowing is induced during the growth process resulting in a decreased film density $\rho_{\theta>0^\circ}$. The correlation between film porosity P and film density $\rho_{\theta>0^\circ}$ is

$$P = 1 - \frac{\rho_{\theta>0^\circ}}{\rho_{\theta=0^\circ}}. \tag{4.1.1}$$

According to Poxson [119], the film porosity P can then be determined by

$$P = 1 - \frac{t_{\theta=0^\circ}}{t_{\theta>0^\circ}} \cos\theta_{OAD}. \tag{4.1.2}$$

Figure 4.2 (b) gives an overview for the determined film porosities depending on the incidence angle for Al, Ti, Cr, and Mo thin films grown at various highly oblique deposition angles. Due to the enlarged shadowing length, the porosity is increased for flatter incidence angles. Moreover, the Al thin films tend to grow more compact, whereas the Mo thin films exhibit the largest porosity. This observation can also be explained by the different surface self-diffusion for the studied metals at room temperature. For $\theta_{OAD} = 88^\circ$, all thin films show nearly the same film porosity of 90%, which indicates that at such highly oblique deposition angles the extreme shadowing conditions dominate over the surface self-diffusion.

To conclude, surface self-diffusion has a significant impact on the shape, columnar tilt angles as well as on the film porosity of obliquely deposited metallic thin films at room temperature.

4.1.2 Deposition at different temperatures

In this subsection, the influence of the substrate temperature on the columnar shape, the columnar tilt angles, and on the porosity of columnar metallic thin films grown under highly oblique deposition geometry is investigated. As outlined above and as reported in literature [120, 121], especially Al columnar thin films show an enlarged surface self-diffusion already at RT. This smears out the shadowing effect, which impedes the control of shaping the columns precisely. To overcome this, the effect of surface diffusion must be reduced, e.g., by lowering the substrate temperature. So far, the growth of obliquely deposited metallic thin films at low substrate temperatures has only been studied by Jen *et al.* [122-124] for obliquely deposited Ag and Au at $T_{Sub} = 133$ K.

In the present study, seven different metals (Al, Ni, Co, Ti, Cr, Mo, and Ta) are obliquely deposited at $T_{Sub} = 77$ K by using the LN_2-cooled sample holder. Additionally, metallic columnar thin films are deposited at elevated substrate temperatures. Finally, the found experimental results concerning columnar shape, columnar tilt angles and thin film porosity for the different substrate temperatures are discussed and compared with each other.

Columnar shape

For all deposited metallic thin films so far, the deposition has been carried out at constant substrate temperature (RT). A change of substrate temperature has direct impact on the adatom mobility. Notice that the film growth process is composed of several sub-processes such as nucleation, island growth, coalescence, and column formation [116]. The adatom mobility influences each of these sub-processes. Consequently, the nucleation (growth of the first 10 nm) should be performed at the same temperature for all samples (e.g. RT), while the variation of substrate temperature should only be performed during the later columnar growth. This might ensure a better comparability of the deposited films compared to those films that have been deposited at constant T_{Sub} for the entire deposition process. To investigate this in more detail, exemplarily Ti thin films are deposited obliquely on thermally oxidized Si(100) substrates with a deposition rate $r = 1$ nm/s. For the first set of samples, the beginning of the deposition (first 10 nm) is carried out at RT. Then, the samples are cooled down to 77 K before deposition is continued. For the second set of samples, the substrate temperature is 77 K for the entire deposition process. Top-view and cross-sectional SEM images of such Ti thin films deposited at $\theta_{OAD} = 86°$ are shown in Figure 4.4. A comparison of these images reveals columns with high aspect ratio that are inclined towards the direction of the incoming flux for both deposited thin films. Both samples exhibit similar columnar tilt angles ($\beta = 62°$) and film porosities ($P = 87\%$). Therefore, it is concluded that the substrate temperature can be kept constant for the entire period of deposition, and that the thin films are still assumed to be comparable with each other.

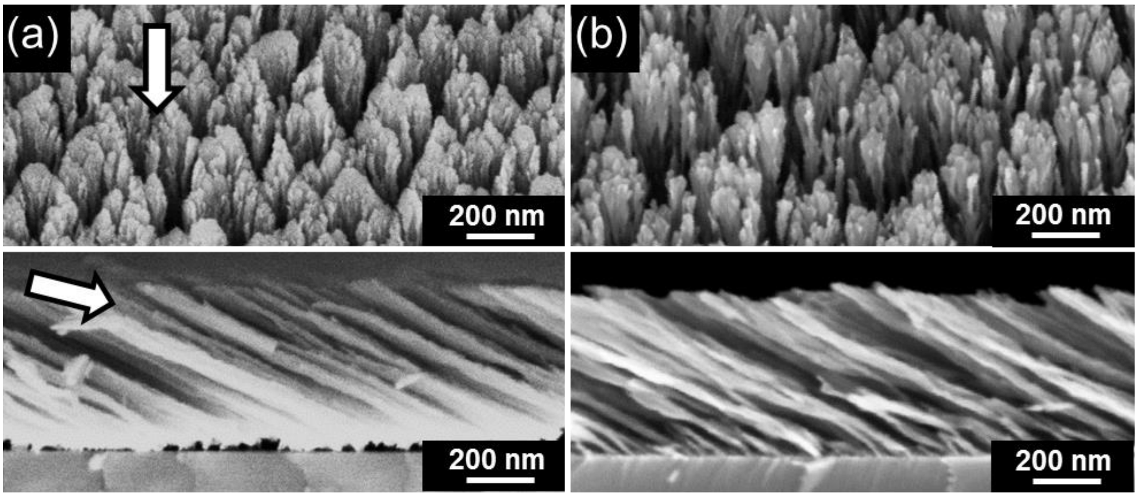

Figure 4.4: Top-view and cross-sectional SEM images of Ti thin films deposited at an incidence angle $\theta_{OAD} = 86°$ on thermally oxidized Si(100) substrates. (a) Deposition of the first 10 nm at room temperature, then cooling of the substrate down to 77 K and continuing deposition. (b) Deposition at 77 K for the entire period of thin film growth. The white arrow indicates the direction of the incoming particle flux.

Figure 4.5 shows cross-sectional and top-view SEM images of tilted Al columns deposited with $r = 0.5$ nm/s at $\theta_{OAD} = 82°$ on thermally oxidized Si(100) substrates at (a) 300 K and (b) 77 K substrate temperature. These SEM images reveal significant morphological differences. The largest columns in a thin Al film fabricated at 300 K have a columnar diameter $d = 126 \pm 25$ nm, but for deposition at 77 K this diameter is reduced by a factor of approximately three to $d = 36 \pm 10$ nm. The diameters of the columns remain approximately constant for the entire length of the columns. Because Al exhibits high surface adatom mobility already at room temperature [42], which counteracts the shadowing effect, the entire column grows broader in diameter. Lowering the substrate temperature down to 77 K leads to a reduction of Al adatom mobility so that the columns grow with high aspect ratios. It can be noted that the substrate temperature and accordingly surface self-diffusion have a remarkable influence on the shape of tilted Al columns.

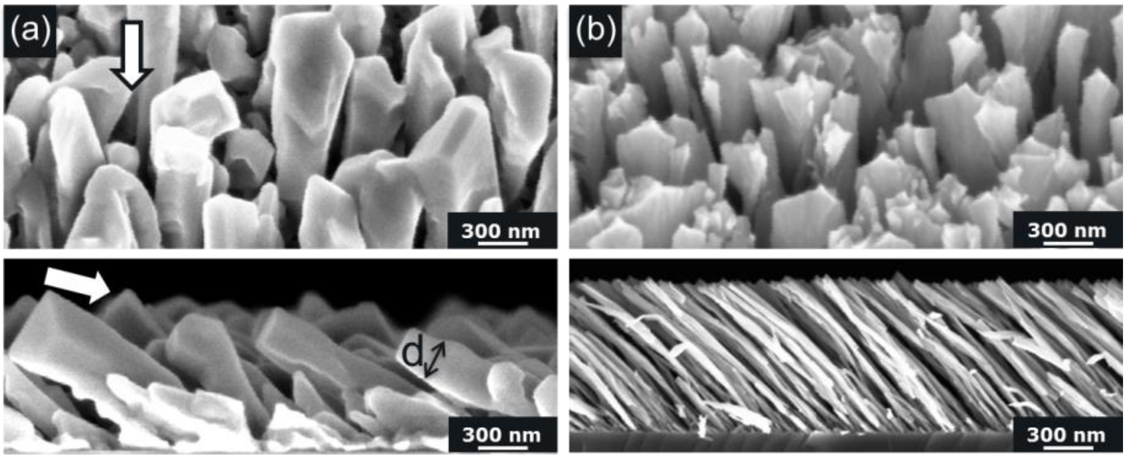

Figure 4.5: Cross-sectional (top) and top-view (bottom) SEM images of tilted Al columns deposited at an incidence angle $\theta_{OAD} = 82°$ on thermally oxidized Si substrates and at a substrate temperature of (a) 300 K and (b) 77 K. The white arrow indicates the direction of the incoming particle flux.

Further metallic (Ta, Mo, Cr, Ti, Ni, and Co) columns are fabricated under similar experimental conditions ($r = 0.5$ nm/s, $\theta_{OAD} = 82°$, $T_{Sub} = 77$ K). An overview is given in Figure 4.6. In general, all columns show a high aspect ratio, and therefore have the same overall shape. To understand the reason for this similar shape, the homologous temperature T_H is used, as has already been done previously. As $T_{Sub} = 77$ K, the homologous temperature can be calculated to vary between $T_H = 0.02$ for Ta and $T_H = 0.08$ for Al. This corresponds to zone 1 in the structure zone model introduced by Movchan and Demchishin [51]. At such low substrate temperatures, only very few adatoms will have sufficient thermal energy to overcome the potential barrier, meaning that surface self-diffusion is strictly limited. As a consequence, the adatoms tend to stick at the surface where they hit [125], meaning that shadowing is the expected dominant effect in the columnar growth process. As the mobility of the adatoms is restricted, it is unlikely that diffusion from one column to another column occurs. Due to the limited adatom mobility, the formation of amorphous columns is expected. In subsection 5.1.2, a high-resolution structural analysis of such individual columns is shown exemplarily for Ti. Under the assumption that an amorphous column is formed, the columns can only compete by shadowing. Thereby, the columns with the geometrically fastest vertical growth component will shadow slower growing columns, which stop to develop at a certain columnar length. This explains why all columnar thin films deposited at 77 K consist of separated columns with different columnar length *l*. In conclusion, the generally similar columnar morphologies obtained at 77 K substrate temperature can be attributed to the dominating shadowing effect.

However, a closer look at Figure 4.6 reveals differences in the columnar diameter. For high melting point materials Ta, Mo, and Cr ($T_{Melt} > 2000$ K) smaller diameters ($d \sim 10$ nm) than for the remaining metals (e.g. up to $d \sim 46$ nm for Al) can be obtained. The detailed dependence of the adatom self-diffusion is unknown for most metals, but an increase of temperature is expected to result in an enlarged adatom surface mobility, because this is a thermally activated process and therefore exponentially related to temperature. Consistently, a temperature rise from 77 K to 300 K induces a significant enlarged in surface self-diffusion for low-melting metals, whereas such a temperature rise leads only to a small increase in surface mobility for high-melting metals.

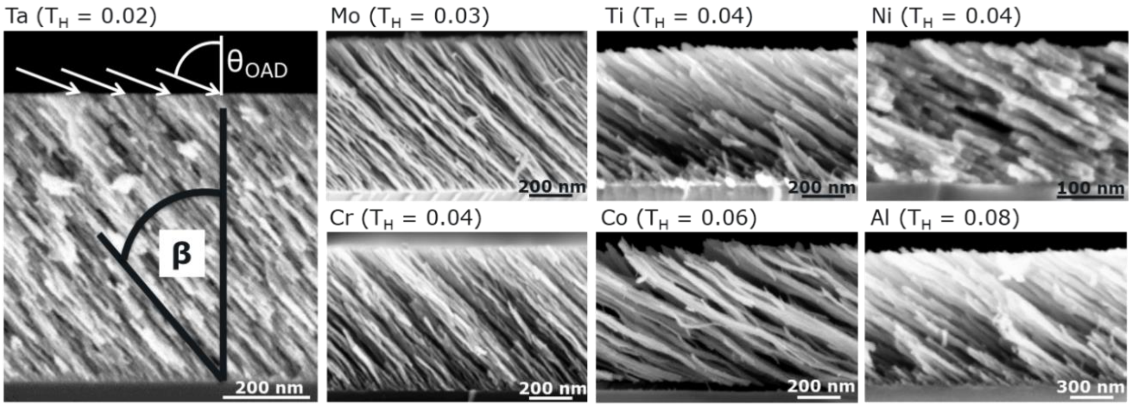

Figure 4.6: Cross-sectional SEM images of tilted metallic columns deposited at an incidence angle of 82° on thermally oxidized Si substrates with $r = 0.5$ nm/s and at a substrate temperature of 77 K. The tilt angle of the columns is β and θ_{OAD} depicts the incidence angle, both with respect to the substrate normal. T_H is the homologous temperature.

Oblique angle deposition is typically performed at low substrate temperatures to ensure maximized shadowing conditions, but recent research reported about combining oblique deposition geometry with a high surface mobility induced by enlarged substrate temperatures [46-50]. This approach enables an improved control of intrinsic material parameters such as crystallinity and electronic mobility. Consequently, oblique angle deposition performed at high temperatures provides an additional degree of freedom to tailor such material properties, e.g., for later device application [116].

Figure 4.7 gives an overview of the observed columnar morphologies for obliquely deposited Al, Ti, Cr, and Mo thin films grown on thermally oxidized Si(100) substrates (800 nm thick oxide layer) at various substrate temperatures. The incidence angle is in the range of 82° ≤ θ_{OAD} ≤ 84°. The first row depicts cross-sectional SEM images of samples grown at T_{Sub} = 77 K, in the second row is T_{Sub} = 300 K and the third row shows samples deposited at elevated substrate temperatures: Mo (T_H = 0.35, T_{Sub} = 1011 K), Cr (T_H = 0.45, T_{Sub} = 981 K), Ti (T_H = 0.45, T_{Sub} = 873 K), and Al (T_H = 0.50, T_{Sub} = 466 K). A comparison of these SEM images reveals again that all metallic columns tend to grow broader in diameter as the substrate temperature is enlarged. Hence, oblique deposition at different substrate temperatures enables the growth of different columnar morphologies.

For deposition at 77 K (first row in Figure 4.7), columns with high aspect ratio (“rods”) can be observed, which have been discussed previously.

For increased substrate temperatures (second row), columns evolve that broaden with increasing columnar length (see Cr (T_H = 0.14) and Ti (T_H = 0.15) in Figure 4.7). Increasing the substrate temperature to RT leads to an enlarged thermal energy of the adatoms so that crystalline nuclei (columns) can be formed during the growth. The increased substrate temperature also enlarges the probability for an adatom to reach the edge of a crystal lattice and migrate to other crystallographic planes by overcoming the Ehrlich-Schwoebel barrier. Adatoms that have overcome the Ehrlich-Schwoebel barrier will contribute more to the lateral growth of the crystal, thereby increasing the columnar diameter *d*. In contrast, adatoms that cannot cross this barrier will contribute more to the length growth of the crystal, which would explain the formation of high aspect ratio columns for lower temperatures. Notice that Fink and Ehrlich [126] found for single W adatoms migrating across a W(211) plane a remarkably higher occupation at the edge of the planes, indicating a stronger binding to these sites (“edge effect”). Such a stronger binding is also assumed to be caused by the chemical identity of the adatom.

As the substrate temperature is further enlarged (second to third row), the columns grow broader directly from the beginning of the growth, as the SEM images for Al (T_H = 0.32) and Mo (T_H = 0.35) unveil. The adatom mobility is so high that the number of nuclei on the substrate surface is reduced. This process is known as coarsening. Moreover, as the number of nuclei is lowered, the number of columns in the film (per unit area) is also decreased compared to lower substrate temperatures. Further, the mobility of the adatoms is so large that shadowing has only a minor influence of the column growth. Thus, the typically observed columnar thin films cannot be obtained anymore for a certain substrate temperature. Instead, the crystalline nuclei develop to larger crystallites according to their crystal habit (see Cr and Ti (T_H = 0.45)). A deeper discussion concerning the substrate temperature and the crystal habit can be found in section 6.3. The high adatom mobility can also induce a rapid vertical and lateral growth of substrate features, which causes the formation of protrusions extending the surrounding film (not shown here). Especially for

Al thin films, whisker growth is detected for elevated substrate temperatures, while the columnar structures completely disappear. The length of such whiskers can reach several µm, as demonstrated for Al ($T_H = 0.50$) in Figure 4.7. Such whisker growth has been observed by Suzuki *et al.* [44, 45] for the first time, but a concise explanation for its origin is still not found jet.

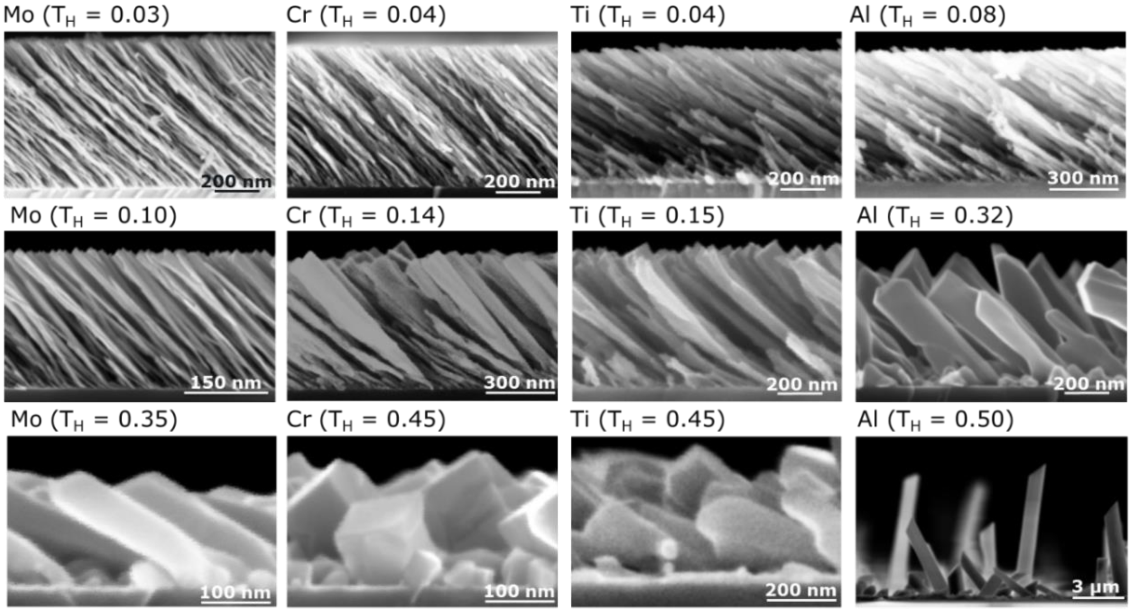

Figure 4.7: Cross-sectional SEM images for metallic thin films deposited obliquely at $82° \leq \theta_{OAD} \leq 84°$ on thermally oxidized Si(100) substrates for varying homologous temperatures T_H. The samples in the first row are all fabricated with the liquid-nitrogen cooled sample holder ($T_{Sub} = 77$ K), and the samples in the second row are deposited at RT. For the samples in the third row, the following substrate temperatures are used: Mo ($T_H = 0.35$, $T_{Sub} = 1011$ K), Cr ($T_H = 0.45$, $T_{Sub} = 981$ K), Ti ($T_H = 0.45$, $T_{Sub} = 873$ K), and Al ($T_H = 0.50$, $T_{Sub} = 466$ K).

Figure 4.8 summarizes the observed morphologies for Al, Ti, Cr, and Mo thin films obliquely deposited ($82° \leq \theta_{OAD} \leq 84°$) at different homologous temperatures, which basically follow the structure zone model introduced by Mukherjee and Gall [52]. Up to $T_H = 0.15$, a rod shape could be detected. Columnar morphologies occur for $0.15 \leq T_H \leq 0.3$, and for $T_H > 0.3$ additionally protrusions are forming. In the case of Al thin films, whiskers are growing for $T_H > 0.45$. Following Mahieu *et al.* [32], it should be mentioned that the substrate temperature does not entirely control the process of diffusion and of structure formation. For example, as the incoming particle flux reaches the substrate, each of the incoming particles will transfer a fraction of their kinetic energy to the growing surface. Accordingly, the total energy flux to the growing surface must be considered, so quantitative values for T_H should be taken with care. Nevertheless, Figure 4.8 reveals that for the investigated metallic thin films similar morphologies are obtained for similar homologous temperatures. Thus, the homologous temperature is found to be a suitable tool to compare the overall morphology of obliquely deposited thin films made of metals with different melting points.

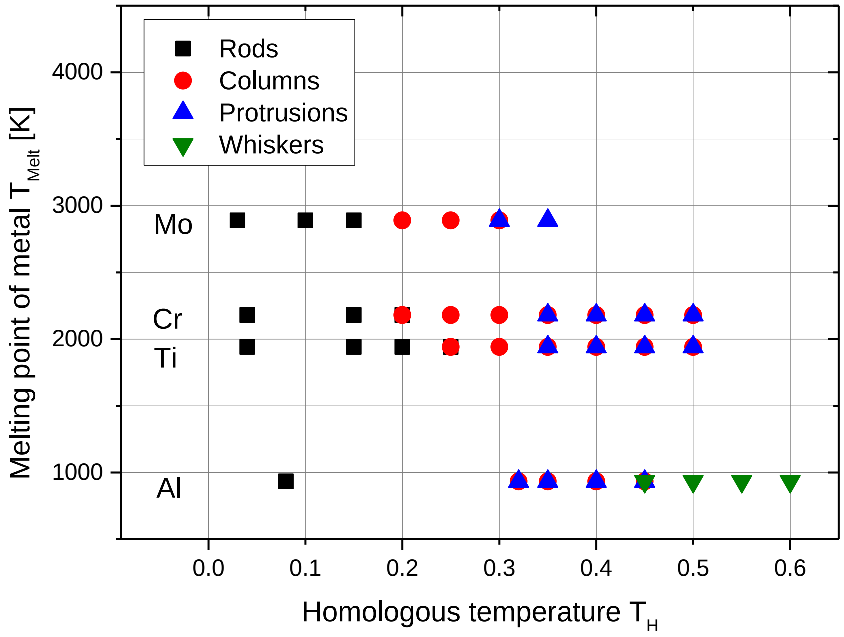

Figure 4.8: Overview of the observed morphologies for Al, Ti, Cr, and Mo thin films obliquely deposited at 82° ≤ θ_{OAD} ≤ 84° for various homologous temperatures T_H.

Columnar tilt angles

Besides the shape, the tilt angles β are studied depending on the substrate temperature. A closer inspection of Figure 4.6 indicates that the columns have different tilt angles, although all metals have been deposited under identical experimental conditions (T_{Sub} = 77 K, θ_{OAD} = 82°, r = 0.5 nm/s). For example, Ta columns show a much steeper tilt angle than Al and Ni columns, whereas the tilt angles for Ta, Mo, and Cr columns are almost identical. Figure 4.9 (a, b, c) depict the dependence of the tilt angle β on the angle of the incoming particle flux θ_{OAD} for Al and Ni columns, for Ti and Co columns as well as for Ta, Mo, and Cr columns, respectively.

The substrate temperature is changed from 77 K (blue data points) to 300 K (red data points). Three observations can be made. Firstly, the tilt angles of Mo, Cr, and Ni columns do not change for a fixed angle of the incoming particle flux if deposited at 77 K or at 300 K. Secondly, the tilt angles of the Ta, Mo, Cr, Ti, and Co columns increase significantly as θ_{OAD} is enlarged, but the tilt angles of the Al, and Ni columns are not influenced by θ_{OAD}. Thirdly, Ti and Co columns exhibit larger tilt angles if deposited at lower substrate temperatures, which contrasts with all other investigated metals. To sum up, between 77 K and 300 K influences of the incidence angle as well as of the substrate temperature on the columnar tilt angle are detected.

To understand in more detail how the substrate temperature affects the columnar tilt angles, Mo is deposited exemplarily up to a homologous temperature $T_H = 0.3$ ($T_{Sub} = 869$ K) for varying incidence angles (see Figure 4.10). The $\beta\text{–}\theta_{OAD}$ relations do not change for deposition between $T_H = 0.03$ to $T_H = 0.15$. For $0.20 \leq T_H \leq 0.30$, a significant increase for the tilt angles is obtained, while the slope for all investigated $\beta\text{–}\theta_{OAD}$ relations remains approximately constant.

For comparison, Ta and Al are deposited up to $T_H = 0.3$ ($T_{Sub} = 987$ K) and $T_H = 0.3$ ($T_{Sub} = 280$ K), respectively. For each homologous temperature, the angle of the incoming particle flux is varied between $74° \leq \theta_{OAD} \leq 86°$ so that a $\beta\text{–}\theta_{OAD}$ relation is found for each T_H. This relation is fitted linearly and then extrapolated to $\theta_{OAD} = 90°$. The corresponding extrapolated tilt angle is called "$\beta_{\theta=90°}$" (see Figure 4.9 (c) for illustration).

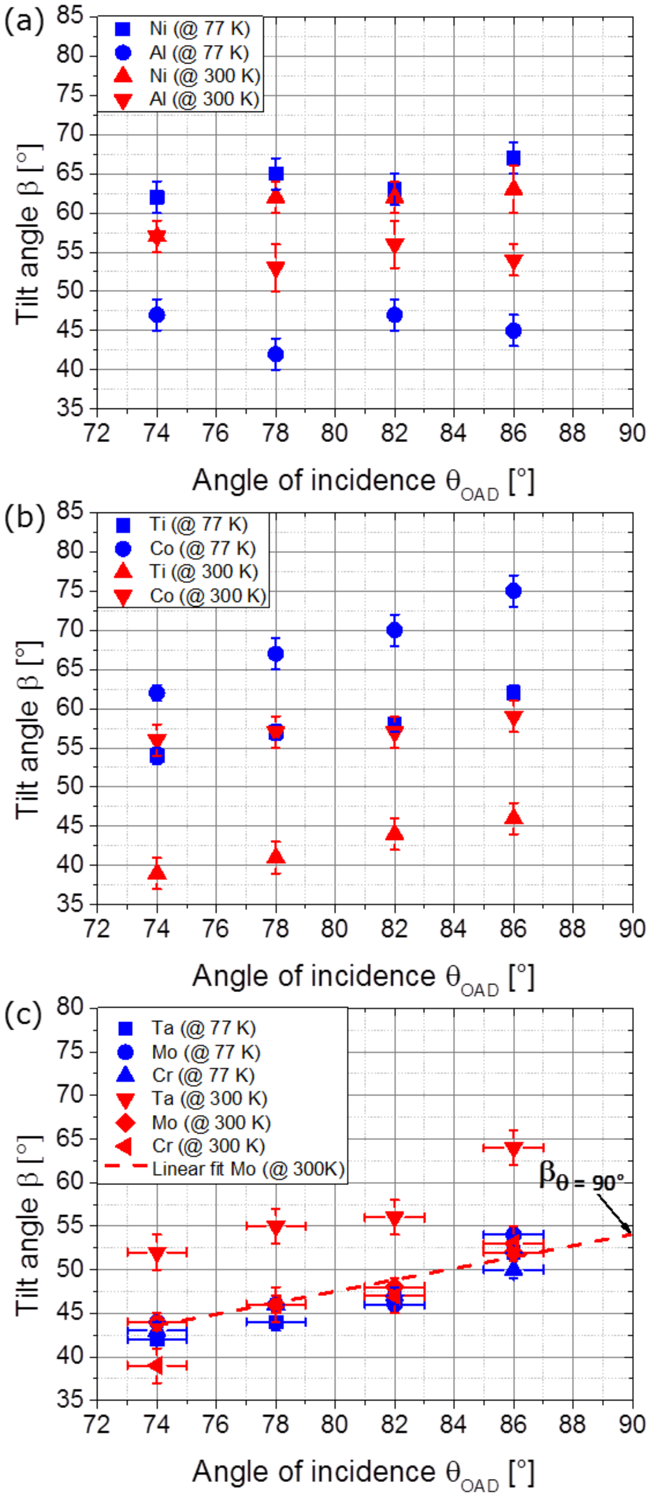

Figure 4.9: Columnar tilt angles β depending on varying angles of incidence θ_{OAD} at 77 K and 300 K substrate temperature for columnar thin films made of (a) the fcc metals Al, and Ni, (b) hcp metals Ti, and Co (c) the bcc metals Cr, Mo, and Ta.

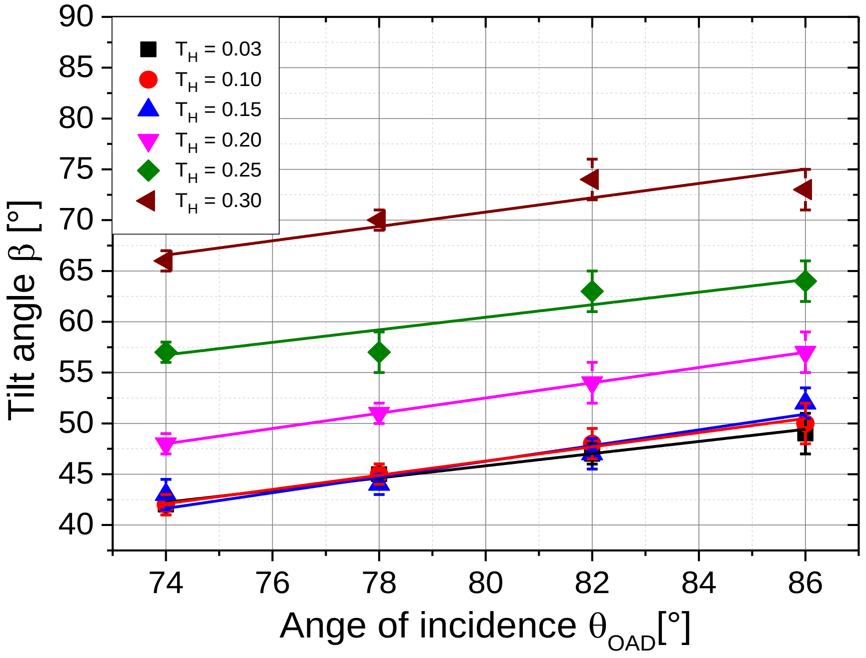

Figure 4.10: Tilt angles β versus angles of incidence θ_{OAD} for tilted Mo columns deposited on thermally oxidized Si(100) substrates with different homologous temperatures T_H.

The parametrization of the relations between the angles β and θ_{OAD} for varying T_H facilitates to detect at which T_H these relations change remarkably. Moreover, the extrapolation is carried out to balance statistical fluctuations.

Figure 4.11 shows the $\beta_{\theta=90°}$-values for Ta, Mo, and Al obtained for varying homologous temperatures. Up to $T_H = 0.15$ ($T_{Sub} = 300$ K), the plot for Mo shows a small slope, while for larger T_H the $\beta_{\theta=90°}$-values increase remarkably. A reason for this is that below $T_H = 0.15$ the Mo adatoms do not exhibit adequate energy to overcome the diffusion activation barrier. As a result, surface diffusion would be suppressed until $T_H > 0.15$, providing adequate activation energy. Thus, columnar Mo thin films deposited at $T_H = 0.03$ and $T_H = 0.10$ are assumed to exhibit similar columnar tilt angles β, but for $T_H > 0.15$ a significant change in β is expected. Indeed, the cross-sectional SEM images of Mo thin films in Figure 4.11 (inlet) reveal a larger tilt angle β for $T_H = 0.25$ compared to $T_H = 0.03$ and $T_H = 0.15$.

A comparison of the tilt angles for Al and Ta deposited at 300 K indicates a difference of approximately 15°. Moreover, there is a significant increase for both slopes already for 77 K ($T_H > 0.08$ and $T_H > 0.02$, respectively). This is in contrast to Mo, whose slope rises significantly not until $T_H > 0.15$ ($T_{Sub} = 300$ K). Consequently, for Al and Ta surface diffusion is already dominant at 300 K, but for Mo higher T_{Sub} are required. The previous results have shown that an argumentation exclusively based on the homologous

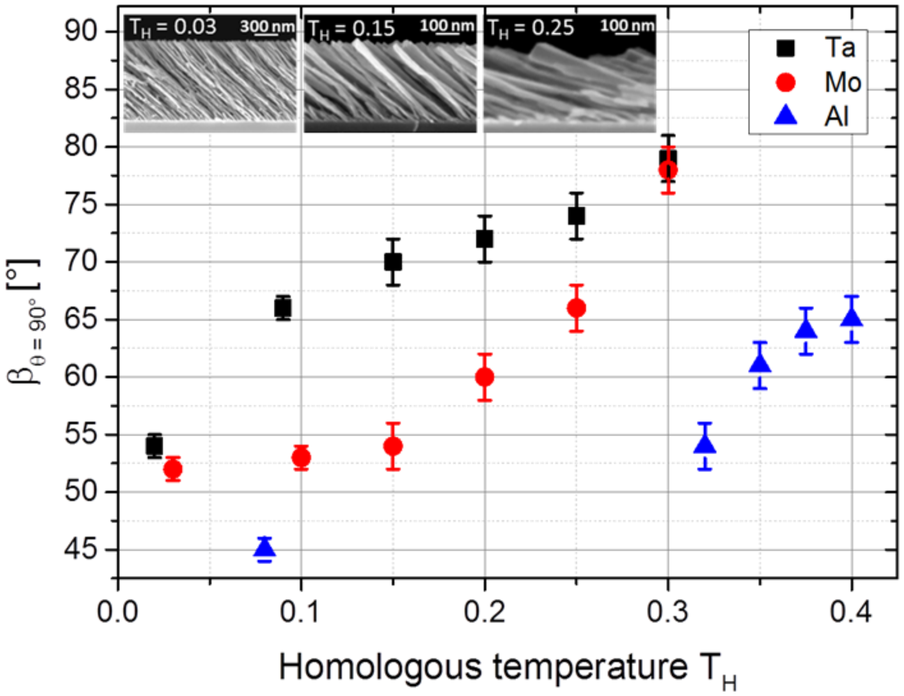

Figure 4.11: $\beta_{\theta=90°}$-values for Ta, Mo and Al columns depending on the homologous temperature T_H (for explanation see text). Inlet: Cross-sectional SEM images of tilted Mo columns grown at an incidence angle of 82° on thermally oxidized Si substrates at $T_H = 0.03$ (left), $T_H = 0.15$ (middle) and $T_H = 0.25$ (right).

temperature is not sufficient to describe the tilt angles adequately. A deeper understanding should include surface self-diffusion.

Under the assumption that crystalline columns can form (as will be demonstrated in chapter 5), the diffusivity D_S for adatom surface self-diffusion varies remarkably depending on the actual temperature of the crystal, the diffusion mechanism, the type of crystal structure, the particular crystal plane (anisotropy effects), etc. (see subsection 2.2.3). Although numerous publications can be found that focus on the surface self-diffusion of adatoms on metallic surfaces [42, 54-66], the adequate description of adatom movements on the actual surface of a growing column still remains as an ambiguous task. The experimental studies in literature have determined diffusion coefficients for high substrate temperatures (> 800 K). However, OAD and GLAD are typically performed at lower temperatures where surface self-diffusion dominates over bulk self-diffusion. Thus, the diffusion coefficients D_S cannot be simply extrapolated to those low temperatures. Nevertheless, the activation energy for surface self-diffusion E_A does not depend on the temperature and is therefore considered for this discussion. In the following, the activation energies of the metals used in the present work are examined and compared with each other with the aim to derive a qualitative correlation between activation energies E_A for surface self-diffusion and the experimentally observed columnar tilt angles β.

Hok and Drechsler [56] found an activation energy of 2.767 eV for the surface self-diffusion of Ta, but there is no information about the corresponding crystal plane.

Flahive and Graham [55] reported on pair potential calculations to model single atom self-diffusion of Ta, for instance. This study shows that (i) the activation energies vary significantly for different surface orientations, and (ii) that the lattice relaxation has a profound impact on the activation energies. They found activation energies (without relaxation) of 0.3 eV for Ta(110), 1.7 eV for Ta(111), and 1.2 eV for Ta(100). In contrast, the activation energies for Mo (without relaxation), are 0.4 eV for Mo(110), 1.9 eV for Mo(111), and 1.4 eV for Mo(100). So, the activation energies for Ta are smaller than for Mo. This is also the case for the activation energies after full relaxation. Smaller activation energies correspond to a larger surface-self diffusion, which might be an explanation for the larger tilt angles of the Ta columns compared to the Mo columns as shown in Figure 4.11.

The activation energies for Al have been studied more extensively compared to Ta. Depending on the diffusion mechanism (hopping or exchange) and the surface, the reported activation energies scatter between 0.02 eV and 0.8 eV [59, 60, 62, 127]. Hence, the activation energies for Al are smaller than for Mo, which leads on the one hand to an enlarged surface self-diffusion and, accordingly, to a reduced shadowing effect for Al thin films. This also decreases the influence of the angle of the incoming particle flux θ_{OAD} on the tilt angle β (see Figure 4.9 (a)). In addition, this smaller activation energy and accordingly larger surface self-diffusion can be a reason why the tilt angles for Al columns are enlarged by approximately 15° if deposited at 300 K compared to 77 K. On the other hand, although the activation energies for Al are smaller than for Mo, the Al tilt angles tend to be smaller than the Mo tilt angles (compare Figure 4.11). A reason for this can be the different crystal structures (Mo is bcc and Al is fcc).

Further, Figure 4.11 reveals that the $\beta_{\theta=90°}$-values for Ta, Mo, and Cr at 77 K are nearly identical. A reason for this is the fact that all these metals have a high melting point so that surface diffusion can be considered as negligible at 77 K. However, Cr has a comparable melting point as Ti ($T_{Melt}(Cr) = 2180$ K, $T_{Melt}(Ti) = 1941$ K), but for the Cr columns different tilt angles compared to the Ti columns are obtained (compare Figure 4.9 (b) and (c)). It is expected that there are different diffusion paths depending on the crystal structure of the metals. Ta, Cr, and Mo all represent bcc metals, but Ti exhibits an hcp crystal structure. In conclusion, the fact that Ta, Mo, and Cr have the same crystal structure can be another reason that contributes to the nearly identical $\beta_{\theta=90°}$-values at 77 K. Moreover, the fact that Ti and Co exhibit an hcp crystal structure, while the remaining investigated metals have a cubic crystal structure, might be a reason for the larger tilt angles of Ti and Co if deposited at 77 K compared to 300 K (see Figure 4.12). The activation energy for surface self-diffusion of Co is, for instance, reported to be 0.14 eV by Prasad *et al.* [58]. Dabrowski *et al.* [61] found an activation energy for Ti of 1.31 eV. The small activation energy of 0.14 eV for Co indicates a larger surface self-diffusion compared to Ti with

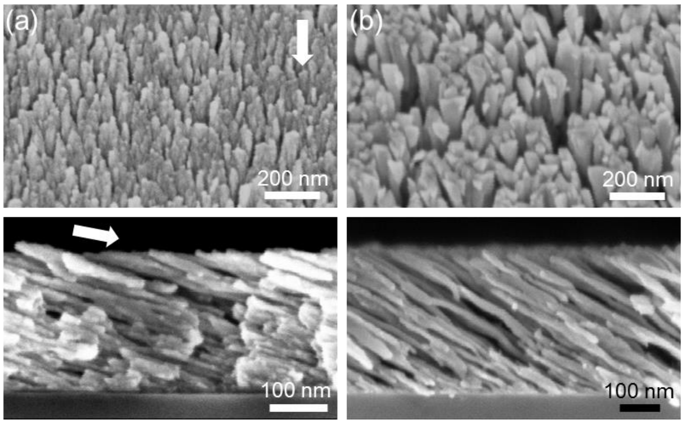

Figure 4.12: Top-view and corresponding cross-sectional SEM images of tilted Co columns deposited on thermally oxidized Si(100) substrates with $r = 0.5$ nm/s, θ_{OAD} = 82°, and (a) $T_{Sub} = 77$ K, (b) $T_{Sub} = 300$ K. The white arrow indicates the direction of the incoming particle flux.

activation energy of 1.31 eV. This could be an explanation why for Co columns larger tilt angles are obtained than for Ti columns (see Figure 4.9 (b)).

Furthermore, several reports in literature refer to the conservation of parallel momentum that directs the movement of adatoms according to the incident flux direction [21, 128, 129] (compare also subsection 2.2.1). For the present study such a mechanism does not seem to be likely. For instance, as Ta is evaporated, the Ta atoms exhibit a kinetic energy close to the thermal energy $E_{therm} = k_B T = (8.617 \cdot 10^{-5}\ \text{eV/K}) \cdot (3270\ \text{K} + 100\ \text{K}) \sim 0.29$ eV. T denotes the melting temperature plus some additional energy, because the material is not just melted, the Ta atoms are evaporated. k_B is the Boltzmann constant. When the Ta atoms reach the surface of the developing columns, a momentum transfer occurs so that the thermal energy is nearly completely transferred to the crystal lattice of the Ta column. Since the columns are inclined towards the incident flux direction, the local deposition geometry for growth zone of such a column becomes less oblique from the perspective of the incident particle flux (see also section 4.2). Such a less oblique deposition is argued to favor a nearly complete transfer of momentum of the arriving atoms to the crystal lattice of the column, thereby impeding a directed diffusion of adatoms defined by the incidence flux direction. Consequently, the Ta adatoms have then a low thermal energy of approximately $E_{therm} = k_B T \sim (8.617 \cdot 10^{-5}\ \text{eV/K}) \cdot (T_{Sub}) \sim 0.03$ eV, if the substrate temperature is 300 K.

To conclude, the activation energies for surface self-diffusion vary significantly depending on the crystal plane, the crystal structure, the diffusion mechanism, and the lattice relaxation, etc. [59, 60, 62, 127]. A selection of activation energies for surface self-diffusion can be found in Table 1, and in Figure 4.13 these activation energies are shown as a function of the melting point of the metals. Liu *et al.* listed activation energies for different fcc metals depending on the crystal plane [42]. In addition, the activation energies are still under discussion in literature [65]. For example, Davydov [130] reported about a barrier of 1.2 eV for Mo(110), which is a three times higher value compared to the study by Flahive and Graham [55]. A comprehensive study of single-atom surface diffusion on metal surfaces has also been performed by Kellogg *et al.* [131]. Summarizing, Table 1 and Figure 4.13 reveal that the activation energies for surface self-diffusion for different planes of the same crystallite scatter significantly.

Table 1 Activation energies E_A for surface self-diffusion of particular crystal planes.

Metal	Melting point [K]	Activation energy [eV]	Self-diffusion	Source
Al(111)	933	0.05	Surface	[42]
Al(100)	933	0.69	Surface	[42]
Al(111)	933	0.04	Surface	[60]
Al(100)	933	0.35	Surface	[60]
Ag(111)	1235	0.04	Surface	[42]
Ag(100)	1235	0.75	Surface	[42]
Cu(111)	1357	0.03	Surface	[42]
Cu(100)	1357	0.79	Surface	[42]
Ni(111)	1726	0.06	Surface	[42]
Ni(100)	1726	1.15	Surface	[42]
Pd(111)	1827	0.03	Surface	[42]
Pd(100)	1827	0.74	Surface	[42]
Pt(111)	2045	0.01	Surface	[42]
Pt(100)	2045	1.25	Surface	[42]
Pt(100)	2045	0.47	Surface	[132]
Mo(110)	2890	1.20	Surface	[130]
Mo(110)	2890	0.40	Surface	[55]

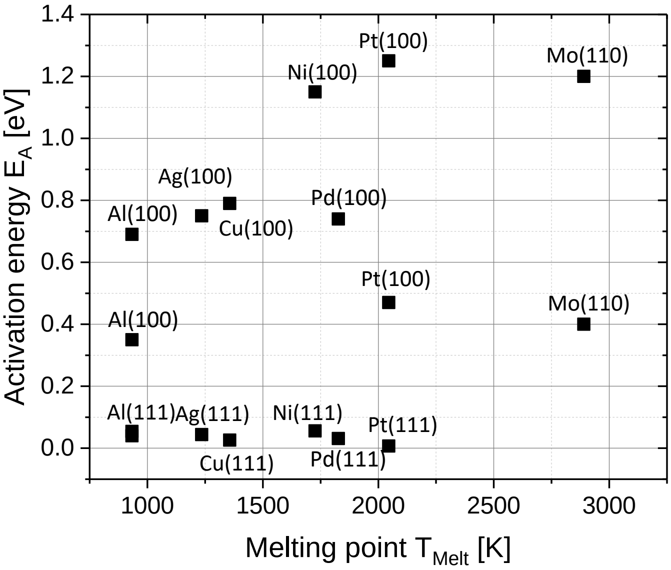

Figure 4.13: Activation energies E_A for surface self-diffusion of particular crystal planes versus the material melting point T_{Melt} (same values as shown in Table 1).

For bulk self-diffusion some authors [63, 133, 134] argue that there is a linear dependence between activation energy and melting point. A selection of activation energies E_A for bulk self-diffusion reported in literature for various metals are summarized in Table 2. In Figure 4.14, the activation energies listed in Table 2 are shown as a function of the melting point of the materials. From Figure 4.14 can be deduced that the activation energies for bulk self-diffusion show indeed a linear dependence on the melting point, but there is no physically based explanation found for this empirical observation yet. According to Figure 4.14, the relation between the average activation energies E_A of bulk self-diffusion and the melting temperature T_{Melt} is given by $E_{A,\,Bulk} = 18.9\ k_B T_{Melt}$.

Table 2 Average activation energies E_A of metals for bulk or surface self-diffusion with different melting points T_{Melt} taken from the corresponding sources.

Metal	Melting point [K]	Activation energy [eV]	Self-diffusion	Source
Rb	312	0.40	Bulk	[63, 135]
Na	371	0.44	Bulk	[63, 135]
Li	454	0.57	Bulk	[63, 135]
Sn	505	1.14	Bulk	[63, 135]
Mg	921	1.41	Bulk	[63, 135]
Al	933	0.45	Surface	[131]
Ag	1235	1.98	Bulk	[63, 135]
Au	1337	0.675	Surface	[136]
Cu	1357	2.44	Bulk	[63, 135]
Cu	1357	0.61	Surface	[137]
Ni	1726	3.00	Bulk	[63, 135]
Co	1768	2.70	Bulk	[63, 135]
Pd	1827	2.77	Bulk	[63, 135]
Ti	1941	1.31	Surface	[61]
V	2163	3.87	Bulk	[63, 135]
Cr	2180	3.51	Bulk	[138]
Nb	2740	2.36	Surface	[139]
Mo	2890	2.10	Surface	[140]
Mo	2890	2.28	Surface	[141]
Mo	2890	2.53	Surface	[142]
Ta	3269	2.77	Surface	[56]
W	3683	5.91	Bulk	[63, 135]
W	3683	3.10	Surface	[143]

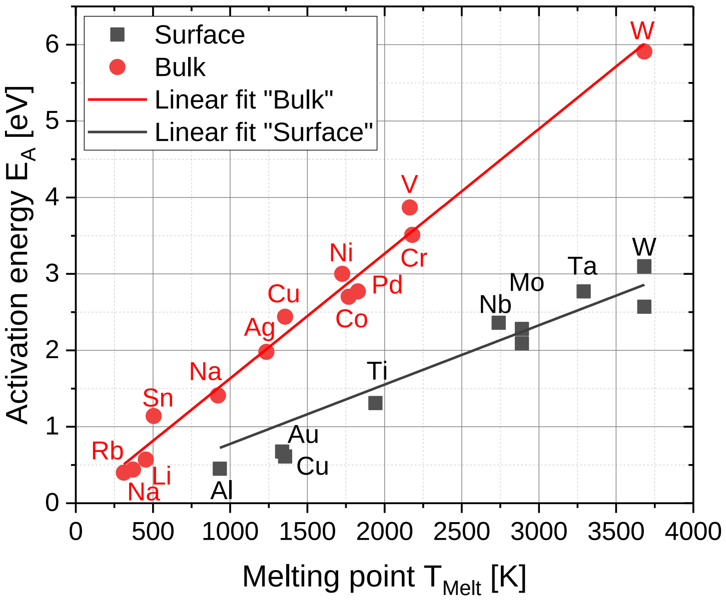

Figure 4.14: Average activation energies E_A of metals for bulk (red circles) and surface self-diffusion (black squares) versus the material melting point T_{Melt} (same values as shown in Table 2).

If a linear dependence between the activation energies for bulk self-diffusion and the melting point exists, it can also be presumed that such a relation might exist for the *average* activation energies for surface self-diffusion (i.e., if the activation energies for all planes of a crystal are averaged). Table 2 includes some of those *average* activation energies for surface self-diffusion, and Figure 4.14 indeed indicates such a linear dependence on the melting point: $E_{A,\ Surface} = 9.1\ k_B T_{Melt}$ with the Boltzmann constant k_B. It can be concluded that:

$$E_A = m \cdot k_B \cdot T_{Melt}. \qquad (4.1.3)$$

Notice that m is the slope of the linear fit for the E_A–T_{Melt} relation scaled with k_B. As already outlined in subsection 2.2.3, the self-diffusion length Λ of an adatom is given by the diffusivity D_S and the mobility lifetime τ_M: $\Lambda = 2\sqrt{D_S \cdot \tau_M}$ (equation (2.2.11)). Here, it is assumed that the mobility lifetime τ_M corresponds to the time interval Δt between the deposition of successive monolayers. This time interval depends on deposition flux J_D, the atomic area density (atoms per unit area in a monolayer) N, and the atomic volume Ω:

$$\Delta t = N \cdot \frac{\Omega}{J_D}. \qquad (4.1.4)$$

The temperature T_{Sub} dependent diffusivity or diffusion constant D_S can be expressed by:

$$D_S = D_0 \cdot e^{\left(-\frac{E_A}{k_B T_{Sub}}\right)}. \tag{4.1.5}$$

D_0 is a proportionality factor. Combining equations (4.1.3) to (4.1.5) yields the following expression for the self-diffusion length Λ:

$$\Lambda = 2\sqrt{\frac{D_0 \cdot N \cdot \Omega}{J_D \cdot e^{\left(\frac{m}{T_H}\right)}}}. \tag{4.1.6}$$

T_H is the homologous temperature ($T_H = T_{Sub} / T_{Melt}$). Exemplarily for Ti, the adatom surface self-diffusion length Λ is estimated. Assuming $D_0 = 3 \cdot 10^{-7}$ m^2/s [130], $N = 1.5 \cdot 10^{19}$ m^{-2}, $J_D = 1 \cdot 10^{-9}$ m, $\Omega = 1.2 \cdot 10^{-29}$ m^3, equation (4.1.6) yields:

$$\Lambda = \sqrt{\frac{2.16 \cdot 10^{-7}\, m^2}{e^{\left(\frac{m}{T_H}\right)}}}. \tag{4.1.7}$$

For $m = 9.1$, this equation gives $\Lambda \sim 3 \cdot 10^{-8}$ nm for $T_H = 0.15$ (T_{Sub} = RT) and $\Lambda \sim 5$ nm for $T_H = 0.4$ (T_{Sub} = 776 K). Those values are supposed to be systematically underestimated, since the surface of the growing columns are expected to exhibit parts with large surface curvature, e. g., which is not considered by equation (4.1.7). Moreover, compared to bulk self-diffusion for surface self-diffusion less data are available, meaning that the slope m is also expected to change as the research activities proceed. Further, it should be pointed out that with increasing T_{Sub} the homologous temperature approaches $T_H \sim 1$, which is correlated with an increasing influence of bulk self-diffusion. However, GLAD and OAD are usually performed for significantly lower temperatures, where the formation of separated columns indicates that shadowing and surface self-diffusion are dominant, whereas bulk self-diffusion is considered as negligible.

In conclusion, the formation of the columnar tilt angle can be viewed as the result of the complex interplay between surface self-diffusion, shadowing as well as possible changes in the crystalline structure of the deposited metals (see chapter 5), which should also be considered.

Thin film porosity

The porosity P of metallic, columnar thin films is investigated depending on the angle of the incoming particle flux and on the homologous temperature.

Figure 4.15 depicts the film porosities versus angle of the incoming particle flux for deposition at 77 K (blue data points) and 300 K (red data points). In general, the porosity is larger for flatter incidence angles, because for more oblique deposition the shadowing length is increased. Thus, more space is created between the columns, thereby the film density is lowered and hence the porosity of the entire film is increased. Besides, the films grown at 77 K exhibit a larger porosity compared to deposition at 300 K, since the increased surface diffusion for higher substrate temperatures favors the growth of more compact thin films.

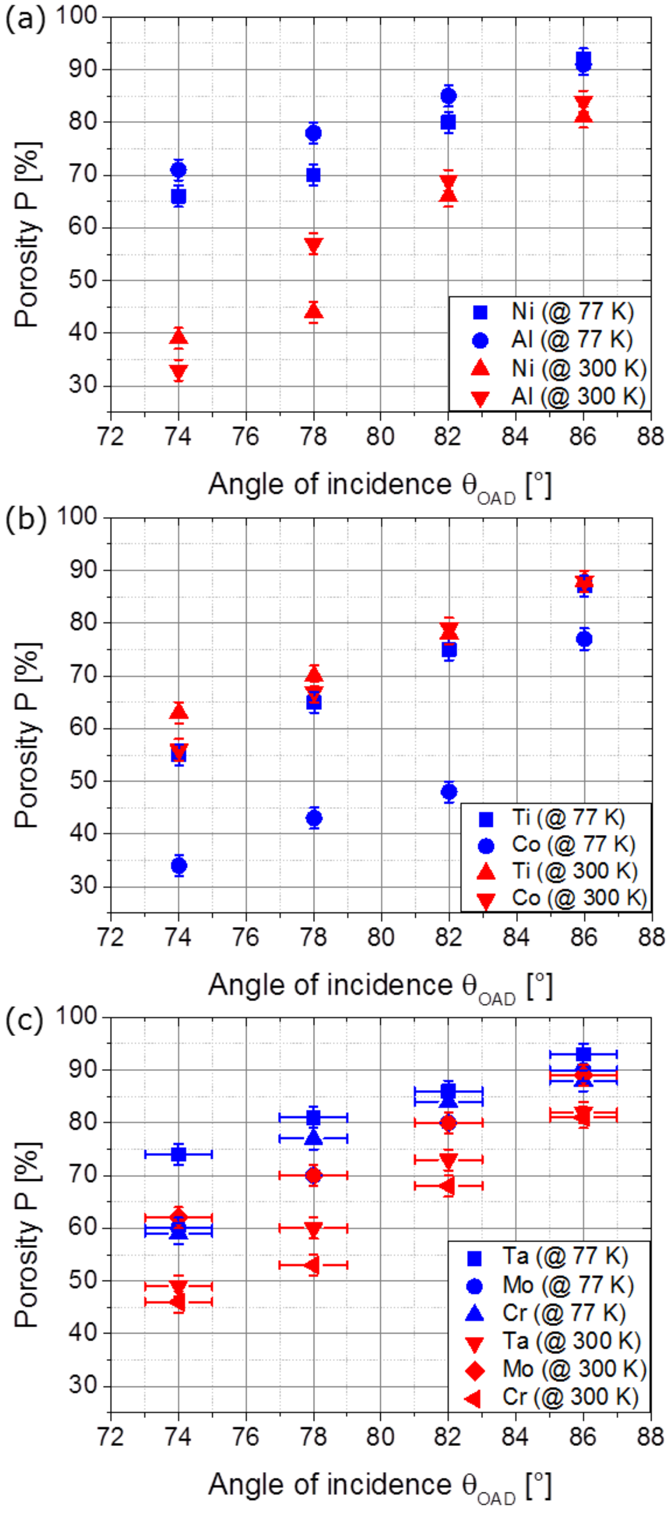

Figure 4.15: Porosity P depending on varying angles of incidence θ_{OAD} at 77 K and 300 K substrate temperature for columnar thin films made of (a) the fcc metals Al, and Ni, (b) hcp metals Ti, and Co (c) the bcc metals Cr, Mo and Ta.

An exception are the obliquely deposited Co thin films, which tend to grow more porous if deposited at 300 K compared to 77 K. This can be understood with view to the Co tilt angles, which have already been discussed above. For deposition at 77 K, larger tilt angles are observed compared to 300 K. A larger tilt angle means that the entire Co thin film has a slower vertical growth component, which results directly in a decreased porosity of the thin film (compare equation (4.1.2)).

The lowest porosity $P = 33\%$ could be obtained for Al deposited at 300 K and $\theta_{OAD} = 74°$. Porosities up to 93% have been detected for Ta fabricated at $T_{Sub} = 77$ K and $\theta_{OAD} = 86°$.

Such high porosities have already been reported for obliquely deposited SiO_2 [119]. Xi *et al.* [144] notify a remarkable low refractive index for obliquely deposited SiO_2, which corresponds to a film porosity of approximately 90%.

An overview of film porosities determined for Al, Ti, Cr, and Mo thin films obliquely deposited at $\theta_{OAD} = 84°$ on thermally oxidized Si(100) substrates for varying T_H is given in Figure 4.16. The film porosities for deposition at 77 K at $\theta_{OAD} = 84°$ (T_H (Al) = 0.08, T_H (Ti) = 0.04, T_H (Cr) = 0.04, T_H (Mo) = 0.03) are interpolated from Figure 4.15, since the liquid nitrogen cooled sample holder did not allow to deposit at $\theta_{OAD} = 84°$ (see subsection 3.1.2). Up to $T_H \sim 0.4$, all thin films show the tendency to grow more compact as the homologous temperature is enlarged, which is a result of the increasing surface diffusion and accordingly the washed-out shadowing effect. For larger T_H, porosity values could not be determined for Al thin films due to the whisker growth and for Mo thin films due to the required, but technically not realizable, high substrate temperature ($T_{Sub} > 1100$ K). For the Ti and Cr thin films, an increased T_H from $T_H > 0.3$ to $T_H = 0.5$ reveals that the film porosity enlarges to $P \sim 70\%$ for Ti and $P \sim 65\%$ for Cr. These porosity values remain approximately constant. As discussed previously, the adatom mobility is large for such high homologous temperatures so that shadowing does not determine the growth of the thin films anymore. The formation of the columns (crystallites) is thermodynamically driven, meaning that the planes with the lowest surface energy will determine the crystallites shape.

In summary, both the angle of the incoming particle flux and the substrate temperature have significant impact on the film porosity. The largest porosities could be realized by combining a highly oblique deposition geometry with a low substrate temperature.

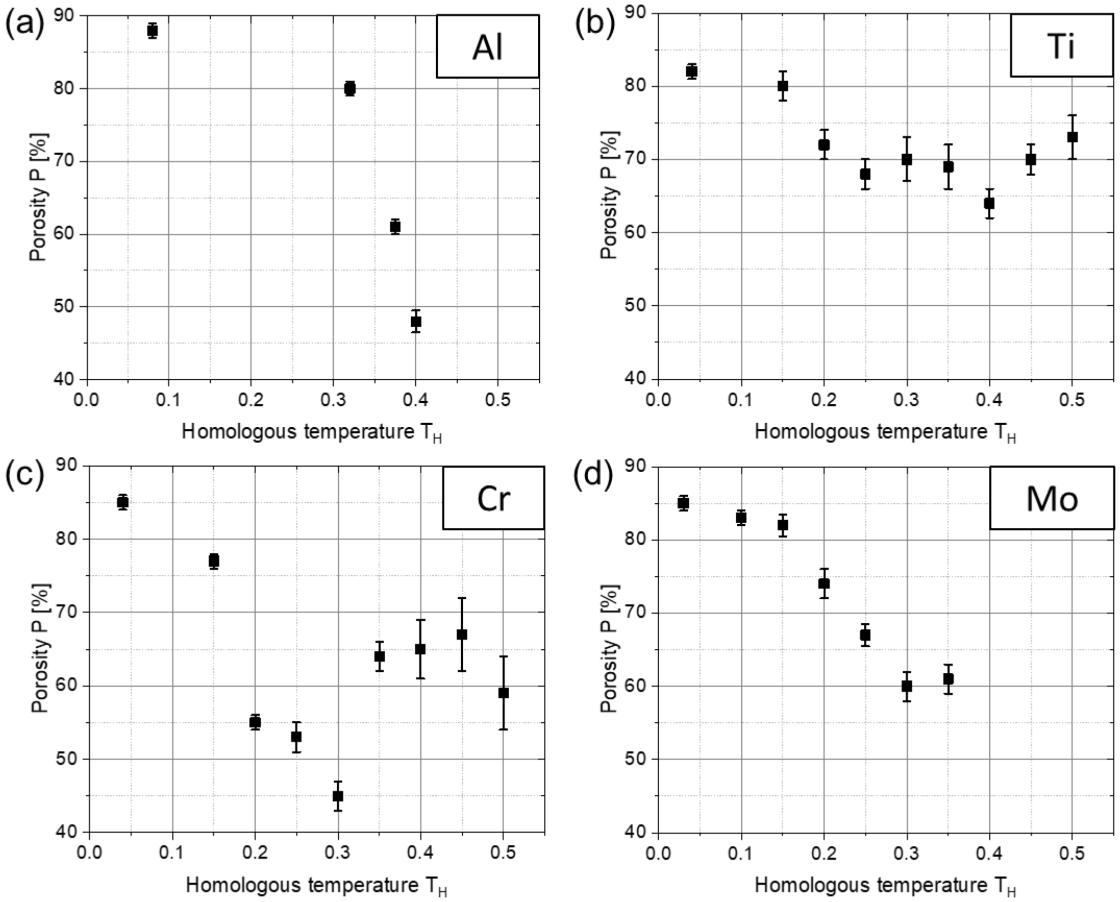

Figure 4.16: Porosity P depending on the homologous temperature T_H for thin films composed of tilted (a) Al, (b) Ti, (c) Cr, and (d) Mo columns deposited at an incidence angle θ_{OAD} = 84° on thermally oxidized Si substrates. The porosity values for deposition at 77 K (T_H (Al) = 0.08, T_H (Ti) = 0.04, T_H (Cr) = 0.04, T_H (Mo) = 0.03) are interpolated from Figure 4.15.

4.2 Glancing angle deposition

4.2.1 Continuous substrate rotation

Al, Ti, Cr, and Mo thin films are grown with an fixed oblique deposition angle $\theta_{OAD} = 84°$ on natively oxidized Si(100) substrates at RT. Combining such an oblique deposition geometry with azimuthal substrate rotation facilitates to change the columnar shape. For example, varying the substrate rotation frequency from $\omega = 0.03$ rpm to $\omega = 10$ rpm enables the growth of Mo spirals, screws, and vertical columns, respectively, as shown in Figure 4.17. The homologous temperature for Mo is $T_H = 0.1$ for deposition at RT. This is the lowest homologous temperature compared to the other metals Al, Ti, and Cr, and indicates a strictly limited surface self-diffusion at RT. Hence, the shadowing effect is maximized, which promotes a precise shaping of the columns by substrate rotation already at RT. In contrast, the homologous temperature is slightly increased for Ti and Cr to $T_H = 0.14$ and $T_H = 0.15$, respectively. This means that the incoming atoms can also move in the shadowed areas, thus reducing the inter-columnar shadowing effect. As a result, the columns grow (i) with a smoothened surface and (ii) broader in diameter as the columnar growth proceeds. For the oblique deposition of Al, the only the growth of vertical columns can be observed, although the substrate rotation frequency is varied between 0.03 rpm ≤ ω ≤ 10 rpm. The reason for this is the high surface self-diffusion that Al adatoms have at RT ($T_H = 0.32$), which washes out the shadowing effect and therefore impedes the formation of spirals and screws. Similar observations have also been reported by Sumigawa *et al.* [145].To conclude, the homologous temperature as well as the substrate rotation frequency have a significant influence on the shape of the OAD and GLAD structures.

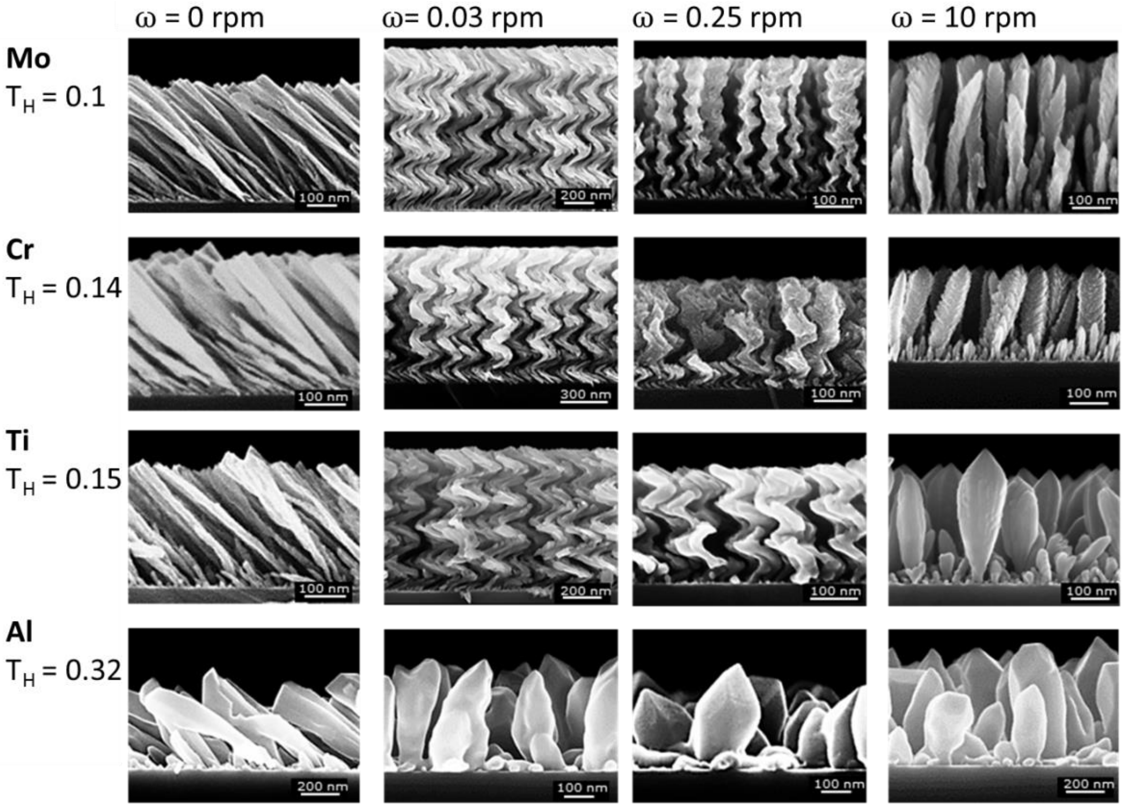

Figure 4.17: Cross-sectional SEM images of Al, Ti, Cr, and Mo thin films deposited obliquely ($\theta_{OAD} = 84°$) at room temperature with varying substrate rotation frequencies ω (T_H is the homologous temperature).

Further, it is analyzed how fast obliquely deposited thin films grow in height depending on the substrate rotation frequency. For this purpose, scaling factors SF are used, which scale the film thickness of an obliquely deposited thin film $t_{\theta=84°}$ with the thickness of a vertically deposited thin film $t_{\theta=0°}$ for equal deposition times and deposition rates: $\mathrm{SF} = t_{\theta=84°} / t_{\theta=0°}$. For vertical deposition ($\theta_{OAD} = 0°$), the scaling factor is SF = 1, but for oblique deposition applies $0 < \mathrm{SF} < 1$. For instance, the scaling factor for Ti thin films grown (i) vertically ($\theta_{OAD} = 0°$, $\omega = 10$ rpm) and (ii) obliquely ($\theta_{OAD} = 84°$, $\omega = 10$ rpm) at

RT with $r = 1$nm/s and with equal deposition times yields $SF_{Ti} = 0.55$. This means that the film thickness for the obliquely deposited thin film is reduced by a factor of 0.55 compared to the vertically deposited thin film.

Figure 4.18 shows the scaling factors obtained for thin films composed of tilted ($\omega = 0$ rpm) and vertical Al, Ti, and Mo columns ($\omega = 10$ rpm). Since all depositions are carried out at RT, the corresponding T_H are: $T_H(\mathrm{Al}) = 0.32$, $T_H(\mathrm{Ti}) = 0.15$, and $T_H(\mathrm{Mo}) = 0.1$. From Figure 4.18 can be seen that the difference between the SF for deposition with and without substrate rotation is increased as the homologous temperature enlarges. Moreover, Figure 4.18 indicates that tilted columns grow faster than vertical columns for equal deposition rates and deposition times.

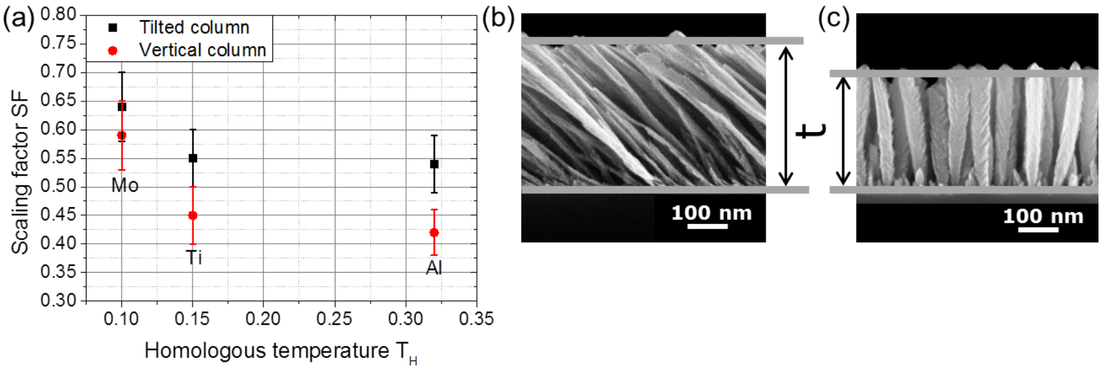

Figure 4.18: (a) Scaling factors SF for varying homologous temperatures T_H. (b) Cross-sectional SEM images of (b) tilted and (c) vertical Mo columns.

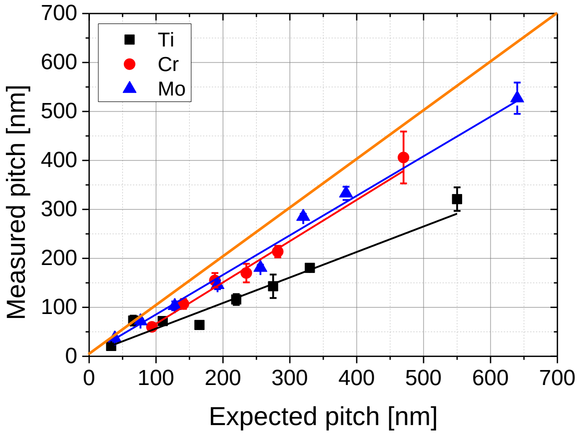

Figure 4.19: Expected versus measured pitch for Ti, Cr, and Mo screws and spirals. The orange line is the bisecting line.

To investigate the growth of spirals and screws in more detail, the pitch is used that is defined as the film thickness deposited per one complete substrate revolution [116]. Scaling factors are applied to calculate which pitch is expected if screws and spirals would grow as fast as tilted columns. For this purpose, the previously determined scaling factors for the tilted columns ($SF_{Ti} = 0.55$, $SF_{Cr} = 0.47$, $SF_{Mo} = 0.64$) are multiplied with the film thickness obtained for the corresponding vertically deposited thin film. This expected pitch can then be compared with the measured pitch taken from the cross-sectional SEM images (see Figure 4.19). The orange graph in Figure 4.19 illustrates the case if spirals and screws would grow as fast as tilted columns. In this case, expected and measured pitch would be equal. However, Figure 4.19 reveals that the measured pitch is smaller than the expected pitch. So, it can be concluded that spirals and screws grow slower than tilted columns as well. Al spirals and screws are not considered in the discussion due to the high surface-self diffusion. In summary, tilted columns grow faster than spirals, screws, and vertical columns.

An explanation for this can be found with view to the preferred growth direction of the columns and thus with view to the columnar growth zone with respect to the substrate. While for vertical columns the columnar growth direction is parallel to the substrate normal, for tilted columns the preferred growth direction is along the column (thus not parallel to substrate normal). These different preferred growth directions affect the local deposition geometry of the columnar growth zone, which is discussed in the following.

According to Knudsen [146], the particle flux Φ_{Flux} is defined as evaporated mass m_{Evap} per unit area A and deposition time t_{Dep}

$$\frac{dm_{Evap}}{A\,dt_{Dep}} = \frac{M}{4\pi\,t_{Dep}}\frac{1}{s} = \Phi_{Flux}\,. \tag{4.2.1}$$

M is the mass of the evaporated element and s is the distance between evaporation source and sample surface (here 30 cm). The grown film thickness t measured parallel to substrate normal per time t_{Dep} is defined by the deposited mass m_{Dep} and the film density ρ of the deposited material, for instance,

$$\frac{dm_{Dep}}{dt_{Dep}} = A \cdot t \cdot \frac{\rho}{t_{Dep}}\,. \tag{4.2.2}$$

The film density ρ of the deposited material is defined by the density ρ_0 of the vertically deposited thin film and the porosity P: $\rho = \rho_0\,(1 - P)$. Remember that ρ_0 is not necessarily equal to the bulk density, since the film can contain inner voids, etc. [118]. Tilting the substrate to an oblique angle leads to a reduction of the effective growth front of the thin film by a factor (cos θ_{OAD}) from the perspective of the incoming atoms so that only a fraction of the evaporated atoms reaches the substrate. The film thickness t_0 can then be calculated to

$$t_0 = \frac{\Phi_{Flux}\ \cdot\ t_{Dep}\cos(\theta_{OAD})}{\rho} = \frac{\Phi_{Flux}\ \cdot\ t_{Dep}\cos(\theta_{OAD})}{\rho_0(1 - P)}\,. \tag{4.2.3}$$

For vertical deposition is $\theta_{OAD} = 0°$ and thus $\cos(\theta_{OAD}) = 1$, but for oblique deposition is $\theta_{OAD} > 0°$ and $\cos(\theta_{OAD}) < 1$. Consequently, the obliquely deposited thin film grows slower in height compared to the corresponding vertically deposited thin film. The difference between both film thicknesses is yet smaller than expected, because the density of the obliquely deposited thin film is decreased significantly as the substrate is inclined to oblique angles. Vertical columns grow parallel to the substrate normal, meaning that the columnar growth zone is oriented parallel to the substrate. Since the substrate normal is tilted by an angle θ_{OAD} with respect to the particle source, the flux of particles reaching the growth zone is $\Phi_{Parallel} = \Phi_{Flux} \cdot \cos(\theta_{OAD})$. Hence, equation (4.2.3) can be applied to calculate the film thickness. In the case of tilted columns, the growth zone is not parallel to the substrate surface, because the growing surface is inclined to ($\beta - 90°$). The tilt angle β is measured between columnar growth direction and substrate normal. The new incidence angle α between incoming particles and normal of the growth zone is $\alpha = \theta - \beta$. Thus, the particle flux reaching the growth zone of the tilted column is given by

$$\Phi_{Tilt} = \Phi_{Flux} \cdot \cos(\alpha) = \Phi_{Flux} \cdot \cos(\theta - \beta). \tag{4.2.4}$$

Additionally, the columns grow in height with a factor ($t / l = \cos\beta$) with film thickness t and length of column l. Finally, the growth in height for a tilted column is given by

$$t_{Tilt} = \frac{\Phi \cdot t_{Dep} \cos(\alpha) \cdot \cos(\beta)}{\rho}. \tag{4.2.5}$$

Rearranging the trigonometrical term in equation (4.2.5) yields

$$\cos(\theta_{OAD}) < \cos(\alpha) \cdot \cos(\beta), \tag{4.2.6}$$

which can be proven for OAD and GLAD conditions and which reflects the tendency of tilted columns to grow faster than spirals, screws, and vertical columns.

Notice that Mo had to be evaporated with a deposition rate $r = 0.5$ nm/s to preserve the experimental equipment, whereas the deposition rate for the remaining metals has been typically at $r = 1$ nm/s. To investigate if a change of the deposition rate in the range of $0.5 \text{ nm/s} \leq r \leq 1 \text{ nm/s}$ has an influence on the columnar morphology, Mo spirals are deposited obliquely ($\theta_{OAD} = 84°$) at room temperature using a macro as described in chapter 3. The deposition rate has been $r = 0.5$ nm/s for the first set of samples and $r = 1$ nm/s for the second set of samples (see Figure 4.20 (a) and (b), respectively.). Comparing cross-sectional SEM images of those samples reveals no morphological differences for the grown Mo spirals. Further, the pitch of the spirals is analyzed quantitatively. This analysis indicates equal measured pitches for both sets of samples. It is concluded that a change of deposition rate from 0.5 nm/s to 1 nm/s does not has an influence on the morphology of the Mo structures. Consequently, it is stated that Mo samples deposited with 0.5 nm/s are comparable with Al, Ti, and Cr samples deposited with 1 nm/s.

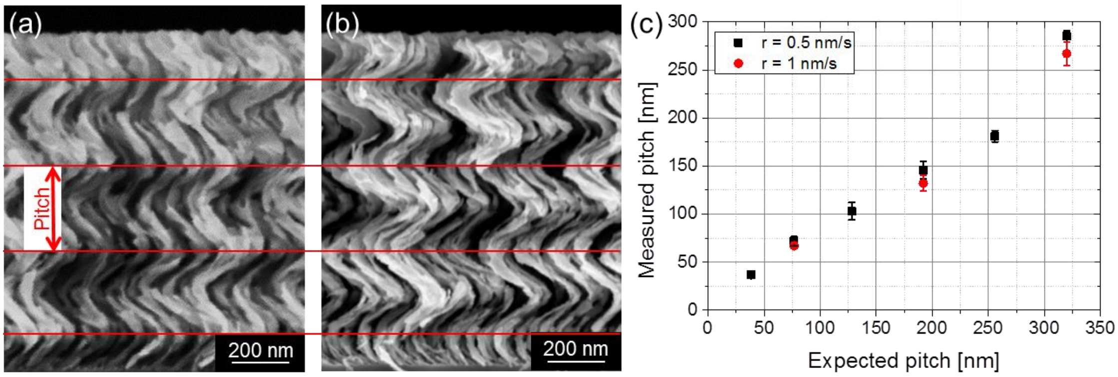

Figure 4.20: Cross-sectional SEM images of Mo spirals grown with a deposition rate (a) $r = 0.5$ nm/s and (b) $r = 1$ nm/s at room temperature on natively oxidized Si(100) substrates. (c) Expected versus measured pitch for Mo spirals grown with different deposition rates r.

4.2.2 Discrete substrate rotation

A rapid step-like substrate movement in combination with a linear growth interval without substrate movement characterizes discrete substrate rotation. This technique can realize manifold columnar shapes on the micro- and nanoscale. For example, growing a tilted columnar arm after every 180° rotation step leads to zigzag structures. Exemplarily, the growth of Mo zigzag columns deposited at a fixed oblique angle $\theta_{OAD} = 84°$ with a constant deposition rate $r = 0.5$ nm/s is be described in detail, because Mo has the lowest T_H compared to the other metals (Al, Ti, Cr) and the influence of surface diffusion can be neglected at RT. Consequently, the influence of discrete substrate rotation on the growth process of Mo zigzag structures can be studied with a minor influence of the surface self-diffusion.

Three sets of zigzag samples are created with different film thicknesses each. The scaling factor SF is used again to determine the expected film thickness (and thus the expected thickness per arm) at a deposition of $\theta_{OAD} = 84°$. For this, the film thickness at $\theta_{OAD} = 0°$ (100 nm, 200 nm, and 400 nm) is multiplied with the previously introduced scaling factor for tilted Mo columns ($SF_{Mo} = 0.64$). This leads to the expected film thickness (or expected thickness per arm measured parallel to substrate normal, for illustration see Figure 4.22) of the obliquely deposited Mo thin films: 64 nm (8 nm), 128 nm (16 nm), and 256 nm (32 nm) per sample, respectively. The corresponding measured film thicknesses are determined directly from the cross-sectional SEM images, as depicted in Figure 4.21.

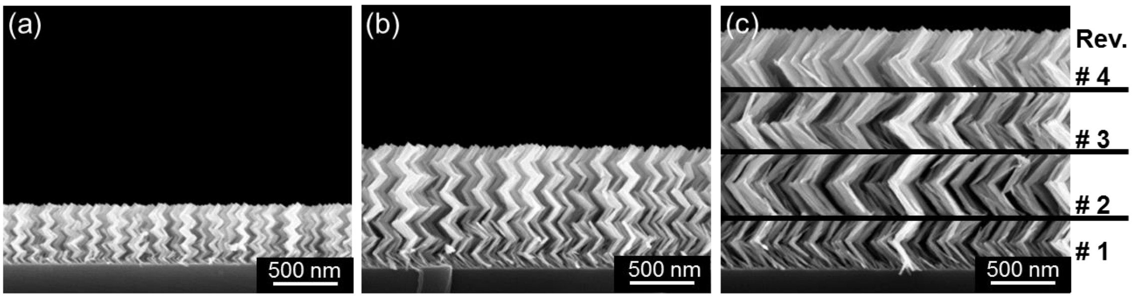

Figure 4.21: Side-view SEM images of Mo zigzag structures deposited at $\theta_{OAD} = 84°$ and at RT on natively oxidized Si(100) substrates with varying film thickness t (measured parallel to substrate normal): (a) $t = 475$ nm, (b) $t = 965$ nm, and (c) $t = 1855$ nm. To grow the Mo zigzag films, in total four substrate revolutions (Rev.) are applied, as indicated in (c).

As illustrated in Figure 4.22, each Mo zigzag structure is composed of eight arms. The numeration of the arms starts with arm 1, which is located directly on the substrate, up to arm 8, which has the largest distance to the substrate. The connection point between two arms stacking one atop the other is called turning point.

The tilt angles of arm 1 to arm 8 are measured with respect to the substrate normal for all three sets of samples. The experimental results are presented in Figure 4.23 (a). Following Harris *et al.* [147], the most significant variation of tilt angles is expected to occur from arm 1 to arm 2. As can be seen in Figure 4.23 (a), there is indeed such a significant variation of tilt angles from arm 1 to arm 2 observed (up to 13° difference). An explanation for this can be found with view to the substrate. For the first arm, the incoming particles condense on a planar substrate. This process is intrinsically random. The recently started nucleation process causes the growth of numerous columnar arms with varying tilt angles, as depicted in the left inlet of Figure 4.23 (b). For all following arms, the incoming particles arrive on top of the previously deposited arms instead of a planar substrate (right inlet of Figure 4.23 (b)). According to Harris *et al.* [147], these previously deposited arms define a new surface, where further incoming particles condense. Consequently, the angle of incidence is redefined to $\theta^* = 90° - \beta$ with respect to the new surface normal. Thus, the new deposition geometry is less oblique and therefore considered to be a reason for the significant change of tilt angles for arm 1 and 2. In contrast to Harris *et al.* [147], who reported about larger becoming tilt angles with increasing number of arms for oxides SiO_2 and ZrO_2 zigzags, for metal Mo zigzags those tilt angles tend to become smaller. The contrasts between the experimental findings for Mo

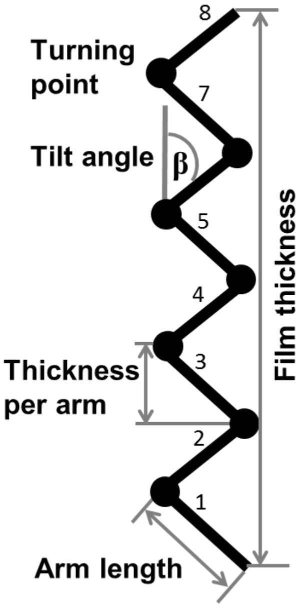

Figure 4.22: Schematic illustration of a single zigzag structure, which is composed of eight arms (corresponding to four substrate revolutions in total). For explanation see text.

zigzags from those ZrO_2 and SiO_2 zigzags reported by Harris *et al.* [147] might be caused by different growth behaviour of oxides compared to single component metals. Moreover, Figure 4.23 (a) indicates that the tilt angles of Mo zigzags tend to converge with increasing number of arms to a tilt angle of approximately $\beta = 37°$. To understand this, the competitive growth process must be discussed in more detail. Following van der Drift [11], the zigzag arms with the fastest vertical growth component shadow the slower growing arms so that the latter stop to develop, which causes a reduction of the total number of evolving zigzag structures during this competitive growth process. Notice that exclusively columnar arms with a tilt angle that is favorable to the direction of the incoming particle flux are selected, because only those arms will be able to capture enough material to finally overgrow the remaining zigzag arms. A combination of the reduction and selection of the growing zigzag structures might account for the observed converging tilt angles of Mo zigzag arms.

As mentioned recently, the zigzag arms are expected to grow faster in height (faster vertical growth component) as the competitive growth proceeds. To quantify how fast the arms are growing, scaling factors are applied again, following the same procedure as described in subsection (4.2.1). These factors are calculated by scaling the measured (obtained by SEM) to the expected thickness per arm. As illustrated in Figure 4.23 (b), arms with a rather short expected thickness of 8 nm (black data points) grow remarkably faster with increasing number of arms as a consequence of competitive growth. For zigzags with an expected thickness of 16 nm and 32 nm per arm, the selection process is basically finished after the growth of the first few arms so that for enlarged numbers of arms the scaling factor remains approximately constant. To sum up, with ongoing film growth the competitive growth process proceeds, and the number of selected zigzag arms becomes smaller.

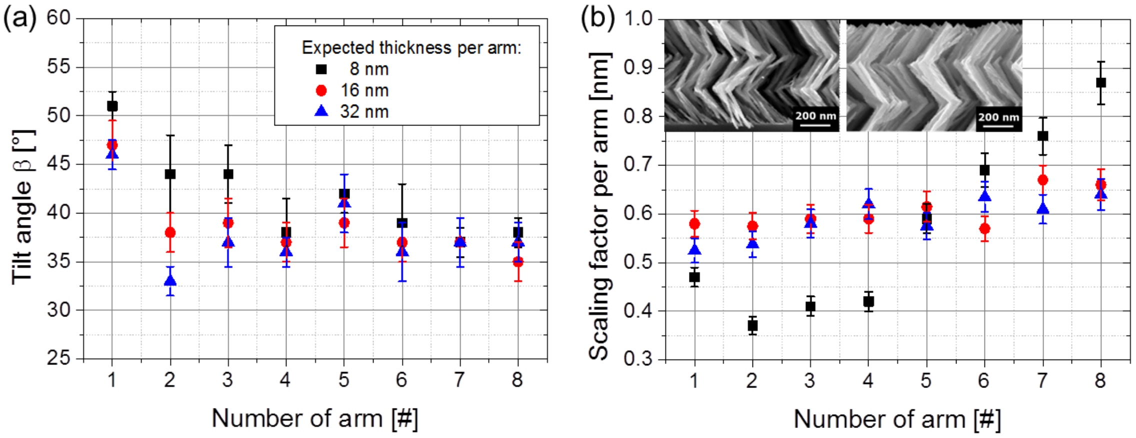

Figure 4.23: (a) Tilt angles β and (b) scaling factors for the columnar arms of Mo zigzag structures are shown for three different samples, where the expected thickness per arm is 8 nm, 16 nm and 32 nm for each sample, respectively. Inlet (b): Cross-sectional SEM images of Mo zigzag structures with arms located near the substrate (left: arm 1, arm 2, arm 3) and distanced to the substrate (right: arm 6, arm 7, arm 8).

4.3 Summary of results

Based on the experimental observations described in this chapter, the following conclusions can be drawn:

Oblique angle deposition:

- Oblique angle deposition enables the growth of metallic tilted columns, but surface diffusion shows already at room temperature a significant influence on the columnar shape, especially for low melting point metals such as Al.
- It could be successfully proven that the homologous temperature is a suitable approach to compare the overall shape of the investigated metallic Al, Ni, Co, Ti, Cr, Mo, and Ta columns. Similar columnar shapes are obtained for similar homologous temperatures. However, a more detailed understanding of the shape, tilt angles, and porosities requires a detailed examination of the adatom surface self-diffusion.
- No differences in the shape, tilt angles, and film porosity could be detected for obliquely deposited Ti thin films fabricated in a way that the first 10 nm are grown at RT and then the samples are cooled down to 77 K before continuing growth, or if the entire growth process is carried out at 77 K. Consequently, if the substrate temperature is varied, the sample is kept constant at the desired substrate temperature for the entire growth process.
- The influence of surface self-diffusion could significantly be reduced by using the liquid nitrogen cooled sample holder, which enables to cool down the substrate to 77 K. The metals deposited obliquely at such low substrate temperatures are all grown with high aspect ratio columns, but the columnar tilt angles as well as the columnar diameters differ from each other.
- The columnar tilt angle as well as the film porosity shows the tendency to become larger for more oblique deposition angles. In general, with increasing substrate temperature, the tilt angles become larger and the films tend to grow more compact. For $T_H \geq 0.3$, the porosity of the Ti and Cr columnar thin films is increased. This is due to the fact that for such high temperatures the columnar growth is no longer dominated by shadowing, since the adatoms have sufficient mobility to more to their favored thermodynamically position.
- An exception from this are obliquely deposited Co thin films, which exhibit larger tilt angles if deposited at 77 K compared to 300 K. Consequently, the film porosity is also decreased for increasing substrate temperatures. An unusually low activation

energy for surface self-diffusion of 0.14 eV according to Prasad *et al.* [58] might contribute to this growth characteristic.

- By adjusting the substrate temperature and the angle of incidence, the film porosity could be varied from $P = 33\%$ for Al deposited at $T_{Sub} = 300$ K to $P = 93\%$ for Ta fabricated at $T_{Sub} = 77$ K and $\theta_{OAD} = 86°$.
- The formation of the columnar tilt angle is the result of the complex interplay between surface self-diffusion, shadowing as well as possible changes in the crystalline structure of the deposited metals.

Glancing angle deposition:

- A variation of the substrate rotation frequency from $\omega = 0.03$ rpm to $\omega = 10$ rpm during oblique deposition ($\theta_{OAD} = 84°$) at RT allows to fabricate spirals, screws, and vertical Ti, Cr, and Mo columns. The high surface self-diffusion of Al at RT impedes the formation of screws and spirals so that only vertical Al columns could be grown with the previously mentioned deposition parameters.
- Tilted columns grow faster in height than spirals, screws, and vertical columns, if deposited under similar experimental conditions. This can be understood by the different preferred growth directions, which are for vertical columns parallel to substrate normal, but for tilted columns not parallel to substrate normal. These different preferred growth directions influence the local deposition geometry of the growth zones of the columns. From theoretical considerations, an inequality could be derived that reflects the tendency for tilted columns to grow faster than spirals, screws, and vertical columns.
- A variation of the deposition rate between $r = 0.5$ nm/s and $r = 1$ nm/s for Mo spirals does not have an influence on the columnar morphology and on the pitch. Therefore, Mo thin films grown obliquely with $r = 0.5$ nm/s are assumed to be comparable with Al, Ti, and Cr thin films obliquely deposited with $r = 1$ nm/s.
- From zigzag arm 1 to zigzag arm 2 the largest difference in the tilt angles of the arms is detected, which could be attributed to the change of the local deposition geometry as the zigzag structure evolves. The local deposition geometry becomes less oblique for the growth of arm 2 compared to arm 1, which grows directly on the planar substrate surface. The less oblique local deposition geometry for arm 2 leads to a decreased tilt angle for this arm.
- The tilt angles of Mo zigzag structures grown obliquely at RT tend to converge with increasing number of arms, caused by the reduction and selection of evolving zigzag structures in the progress of the competitive growth process.

5 Structural Analysis of Individual Columns

In this chapter, the structure of individual metallic columns grown by oblique (section 5.1) and glancing angle deposition (section 5.2) is studied by TEM measurements. For OAD and GLAD is usually not expected that columns with a long range crystalline order are formed, because those are processes performed typically at low temperatures ($T_H < 0.3$) [30]. However, several research groups reported about the growth of crystalline columnar thin films by OAD and GLAD for various materials, for example Al [120], Co [148], CrN [149], Cu [150, 151], Ge [152, 153], Mg [154], Sn [155], Ti-doped Mg [156], Ru [157], β-phase W [158, 159], and ZnO [160]. Although there are many observations concerning the formation of crystalline columnar thin films, an overall understanding has not been achieved up to now. A reason for this is that the growth of crystalline columns depends on various parameters such as the deposited material, the deposition method, the incidence flux direction, etc., indicating that the structural analysis of columnar thin films must be carried out on a case by case basis. For the experiments described in this chapter, the metals Ti (hcp), Cr (bcc), and Mo (bcc) are chosen, because they cover a wide range of melting points and have different crystal structures. The deposition rate is always $r = 1$ nm/s and the angle of the incoming particle flux is $\theta_{OAD} = 84°$, unless otherwise noted. The crystalline structure of single metallic columns is examined along the columnar length l, and depending on the substrate temperature T_{Sub}, as well as on continuous and discrete substrate rotation [LIE01, LIE03-05]. In contrast to chapters 4 and 6, the discussion of the results is presented in a separated section 5.3 for reasons of clarity.

5.1 Oblique angle deposition

5.1.1 Tilted columns grown at room temperature

In the following, the atomic-resolved structure of individual Mo columns grown at RT with an oblique incidence angle $\theta_{OAD} = 84°$ on thermally oxidized Si(100) substrates with 800 nm thick oxide layer is investigated. For this purpose, micro-probe (µP-) STEM nanobeam electron diffraction (NBED) is applied. This enables the investigation of the local crystalline structure along an individual Mo column with nanometer resolution, starting from the beginning of the growth on the substrate up to the topmost part of the column.

Figure 5.1 (a) includes a bright-field TEM overview image of such Mo columns detected in close vicinity to the substrate, and the corresponding diffraction patterns (I) – (V) exemplarily obtained at five different positions of the µP-STEM nanobeam at the interface between substrate and columns. These patterns contain the Bragg reflections related to all Mo crystals located on the substrate that are covered by the nanobeam. For each position, distinct spots can be observed, but their position changes remarkably as the nanobeam is carried along the interface between substrate and columns. This indicates that the Mo crystallites are randomly oriented at the substrate surface. Consequently, a preferentially oriented nucleation seems unlikely. The diffuse diffraction rings that appear on all patterns originate from the 800 nm thick thermal oxide layer atop of the Si(100) substrate.

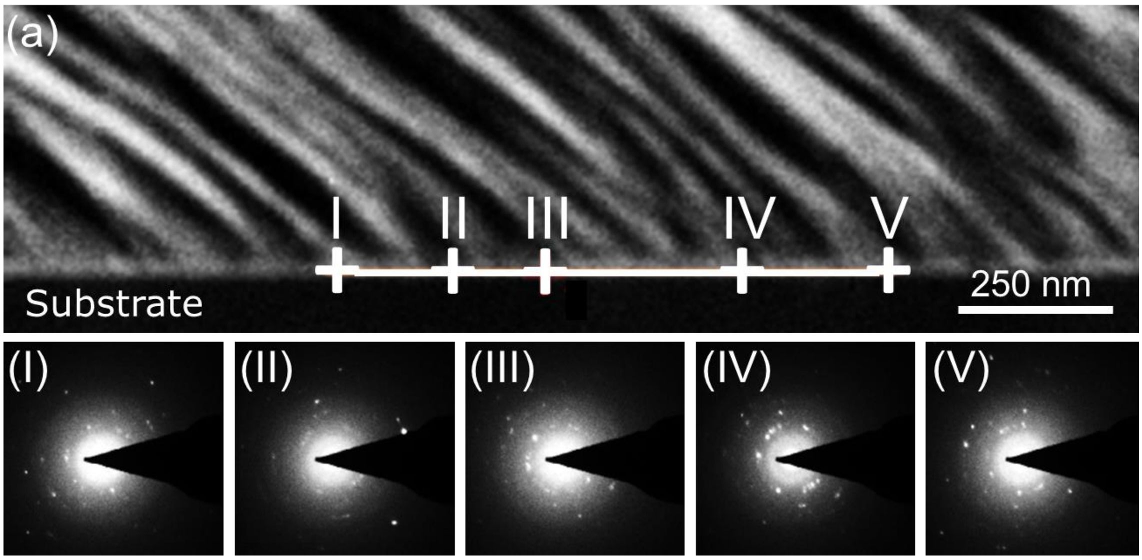

Figure 5.1: Bright-field TEM overview image, and corresponding µP-STEM nanobeam electron diffraction patterns (I) – (V) of Mo columns grown at RT and $\theta_{OAD} = 84°$.

As the nanobeam is moved along an individual Mo column, further diffraction patterns can be obtained (see Figure 5.2 (a), (I) – (IV), and Figure 5.3 (a), (V) – (X)). Near the substrate (Figure 5.2 (I)), many separated reflections as well as diffuse diffraction rings are detected. Since the columnar growth process has just begun, the columnar diameter *d* is in the nanometer range. Hence, the distinct spots in Figure 5.2 (I) are assumed to originate from several Mo columns. As the Mo columns further grow in height, the number of distinct spots in Figure 5.2 (II) is reduced. Further, the reflections in Figure 5.2 (III) can already be identified completely with the diffraction pattern expected for a single crystalline bcc Mo crystal, as a comparison between the experimentally obtained (III) and theoretical calculated pattern (b) in Figure 5.2 [161] confirms.

As can be determined from the bright-field TEM overview image in Figure 5.2, the columns exhibit a length up to 4 µm. Caused by the preparation of the FIB lamella [110], it has not been possible to prepare the lamella in a way that one individual column can be studied from the beginning at the substrate up to the very topmost part of the lamella. Many columns have been cut at a certain length *l* during preparation of the FIB lamella. The diffraction pattern (V) in Figure 5.3 is recorded at such a cutting point. Nevertheless, the patterns (VI) – (X) can again be correlated to the calculated diffraction

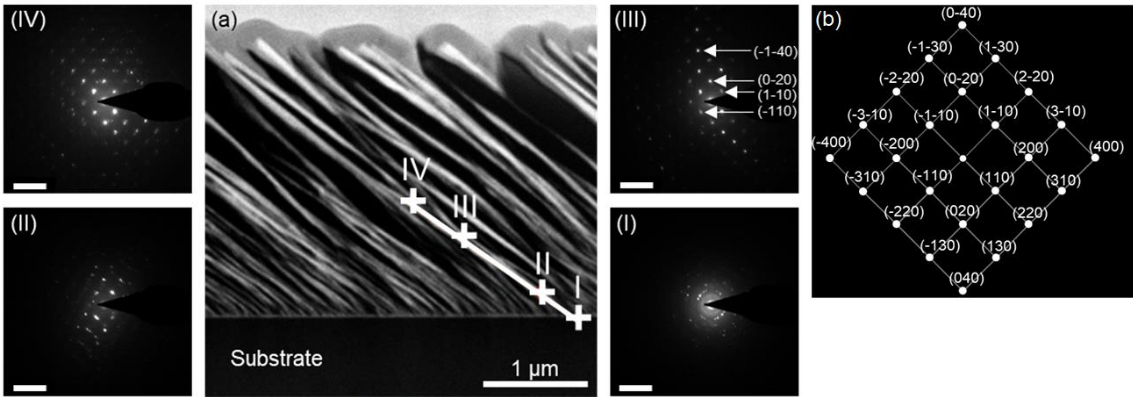

Figure 5.2: (a) Bright-field TEM overview image, and corresponding µP-STEM NBED (I) – (IV) of Mo columns grown at RT and θ_{OAD} = 84°. The scale bars are 10 1/nm. (b) Calculated diffraction pattern of a bcc Mo single crystal [161]. The zone axis is [001].

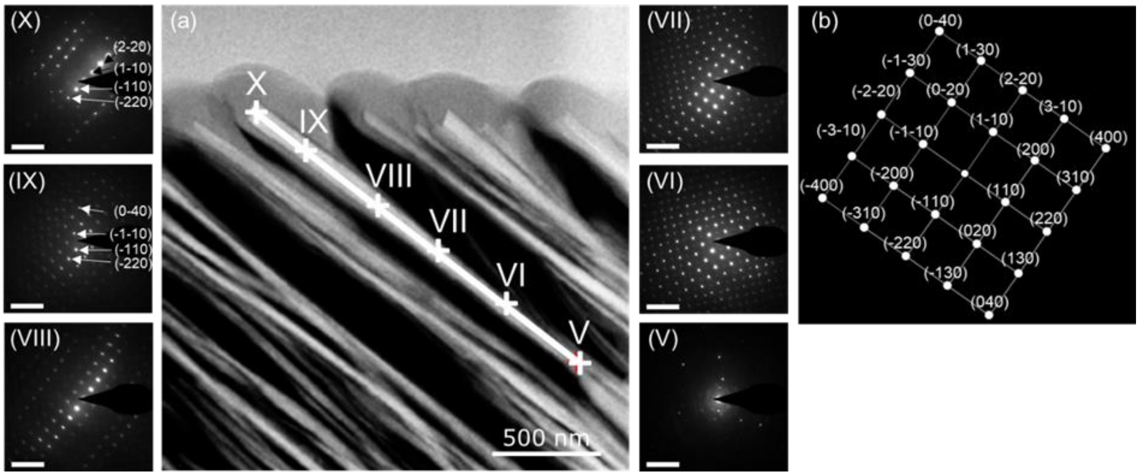

Figure 5.3: (a) Detail of the bright-field TEM overview image in Figure 5.2 (a), and corresponding µP-STEM NBED patterns (V) – (X) of Mo columns grown at RT and θ_{OAD} = 84°. The scale bars are 10 1/nm. (b) Calculated diffraction pattern of a bcc Mo single crystal [161]. The zone axis is [001].

pattern of a single crystalline bcc Mo crystal (see Figure 5.3 (b)) [161]. In summary, the Mo columns grown on obliquely at RT on thermally oxidized Si(100) substrates show the tendency to grow single crystalline. The 800 nm thick oxide layer prevents any epitaxial relationship between the columns and the substrate.

To ensure that the single crystalline structure of the Mo columns is not caused by the preparation of the FIB lamella, additional TEM specimen are prepared by collecting Mo columns on a TEM grid by scratching (as described in subsection 3.2.2). Figure 5.4 (a) is a bright field-TEM overview image of such a Mo column grown at RT on a natively oxidized Si(100) substrate without substrate rotation. The corresponding SAED patterns in Figure 5.4 (b) and (c) reveal clearly separated, distinct spots. For both patterns, the zone axes are calculated to be [-135]. A bright-field TEM overview image of another Mo column deposited with identical experimental conditions is presented in Figure 5.4 (c). The HRTEM images in Figure 5.4 (d) show parallel oriented lattice planes over the entire volume of the column. The crystal lattice spacing is 0.22 nm, corresponding to the Mo{110} planes. To sum up, Mo columns grown obliquely at RT on natively and thermally oxidized Si(100) substrates exhibit a single crystalline structure. It is assumed that there is no epitaxial relation between columns and substrates.

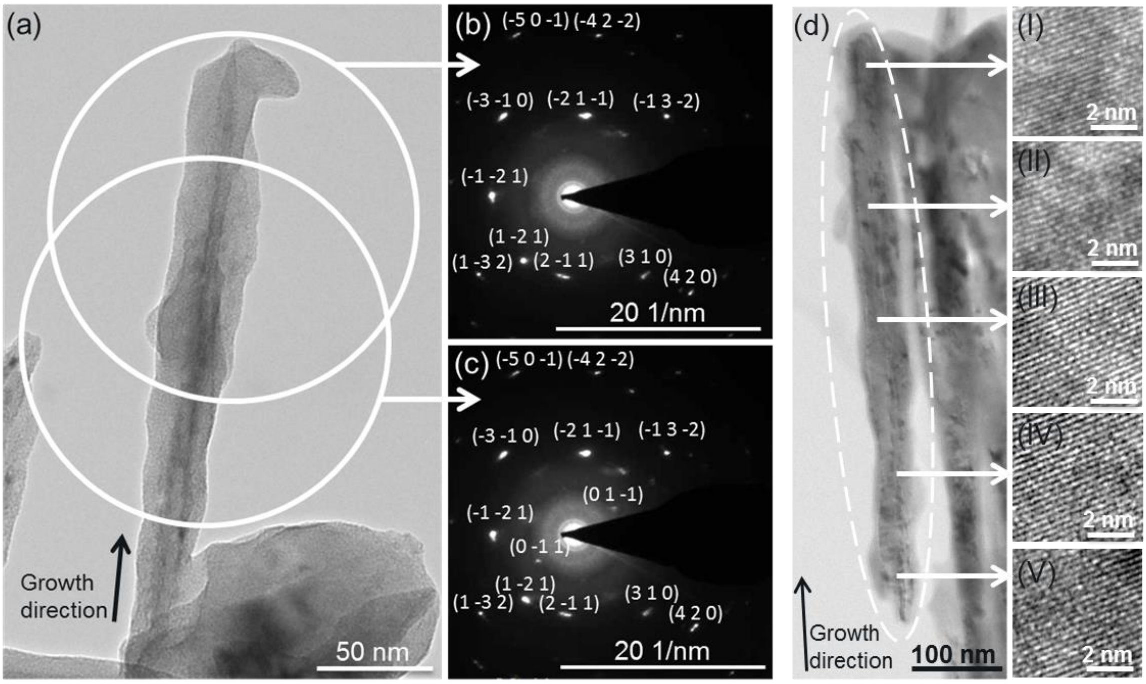

Figure 5.4: (a) Bright-field TEM overview image and (b, c) SAED patterns of a Mo column grown at RT and θ_{OAD} = 84°. (d) Bright-field TEM overview image and ((I) – (V)) HRTEM images of a Mo column grown at RT and θ_{OAD} = 84°. Natively oxidized Si(100) substrates are used.

Additionally, the crystalline structure of individual bcc Cr columns deposited obliquely on natively oxidized Si(100) substrates at RT is studied (see Figure 5.5 (a)). The SAED pattern in Figure 5.5 (b) is detected over the entire area of the column shown in Figure 5.5 (a). The clearly separated reflections imply a single crystalline structure of the individual Cr columns, too.

Moreover, the results of the structural analysis of a tilted hcp Ti column deposited obliquely at RT on a natively oxidized Si(100) substrate are presented in Figure 5.6. The HRTEM images (I – IV) depict lattice planes oriented parallel to each other over a large volume of the Ti column. The lattice spacing is 0.233 nm and corresponds to the Ti c-planes. Further, the SAED patterns in (b, c) show distinct spots. The remaining low-intensity diffraction reflections originate from the TiO_x-layer (see Figure 5.8) that is formed on the Ti column after the sample is removed from the UHV chamber. To conclude, the tilted Ti columns exhibit a single crystalline structure if deposited at RT, which is in accordance with the tilted Cr and Mo columns.

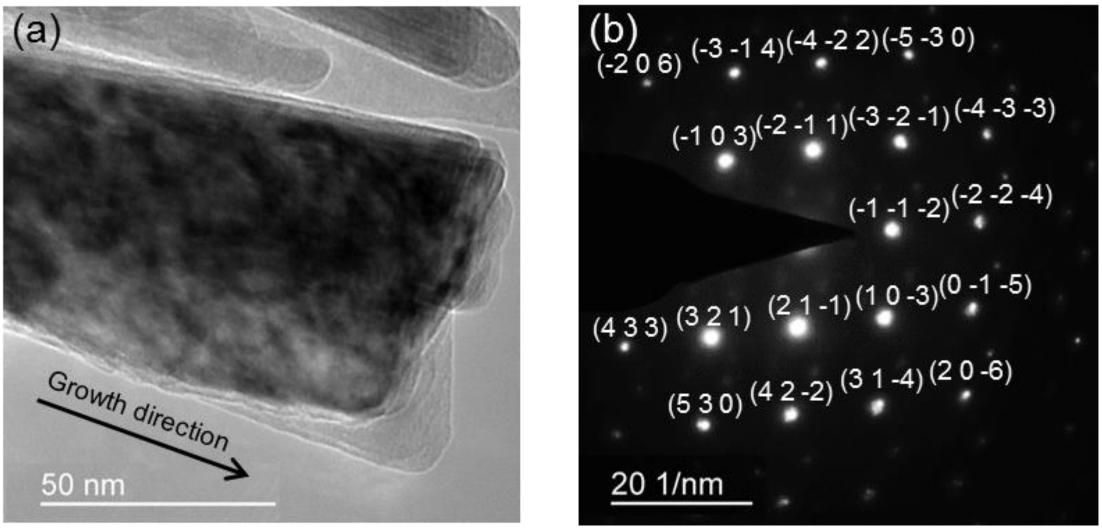

Figure 5.5: (a) Bright-field overview TEM image, and (b) corresponding SAED pattern of a tilted Cr column deposited at RT and θ_{OAD} = 84°.

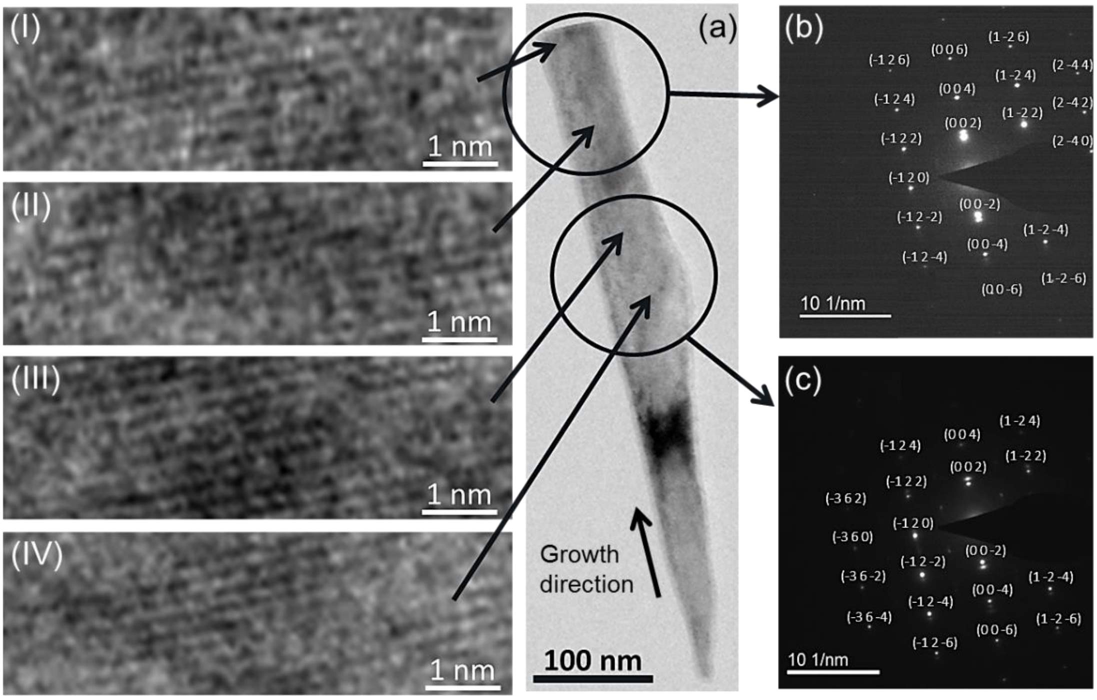

Figure 5.6: (a) Bright-field TEM overview image, (b) corresponding SAED patterns and (I – IV) HRTEM images of a tilted Ti column deposited on a natively oxidized Si(100) substrate at RT with θ_{OAD} = 84°.

The observation that obliquely deposited tilted Ti columns grown at RT on natively oxidized Si(100) substrates show a single crystalline structure is in contrast to Sadeghi-Khosravieh and Robbie [16], who reported on the growth of polycrystalline Ti columns at RT on natively oxidized substrates. An explanation for this can be found concerning the working pressure. Sadeghi-Khosravieh and Robbie [16] used a working pressure of

$p_{Work} \sim 10^{-6}$ mbar (base pressure $p_{Base} \sim 10^{-7}$ mbar), whereas for the deposition of Ti columns as described in this subsection the work pressure is in the range of $p_{Work} \sim 1 \cdot 10^{-8}$ mbar ($p_{Base} \sim 10^{-8}$ mbar). To evaluate the influence of the working pressure on the columnar structure, the following two experiments are conducted: (i) Ti columns are deposited obliquely ($\theta_{OAD} = 88°$) at $p_{Work} \sim 1 \cdot 10^{-8}$ mbar. (ii) Ti columns with similar deposition parameters are grown, but during the growth process 0.3 sccm air from the environment is added in the deposition chamber, leading to an enlarged $p_{Work} \sim 2 \cdot 10^{-7}$ mbar ($p_{Base} \sim 3 \cdot 10^{-6}$ mbar). The air is allowed to flow directly on the substrate. Figure 5.7 depicts the top-view SEM images of the corresponding columnar Ti thin films. In contrast to the first case (Figure 5.7 (a)), numerous branches appear on the column surface as can be obtained in Figure 5.7 (b). A closer inspection of the SEM images implies that these branches are not necessarily oriented in the same direction as the primary crystallite. The formation of such branches is obviously due to the presence of air during the columnar growth, but it has to be clarified which component of the air causes the formation of such branches. Branched columns have already been observed for vertical Cu columns deposited obliquely by magnetron sputter deposition [150]. According to the MD simulations presented in this article, a grain boundary develops at the interface between the branches. For the incoming particles, it is energetically less favorable to condense on the absorption sited provided by the grain boundary, leading to a spatial separation of the branches. The extreme shadowing as induced by the highly oblique deposition geometry further deepens the gap.

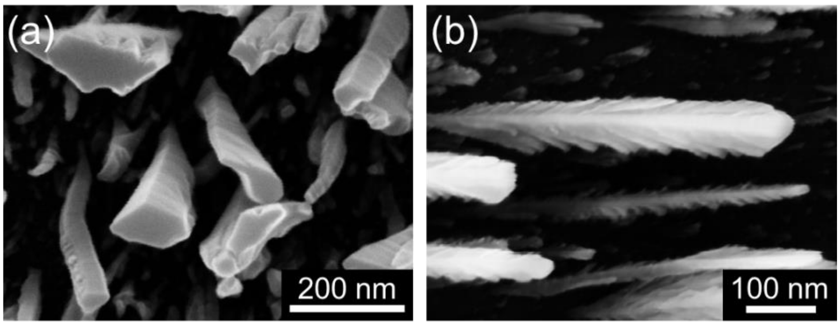

Figure 5.7: Top-view SEM images of tilted Ti columns deposited at $\theta_{OAD} = 88°$ at RT on thermally oxidized Si(100) substrates with (a) $p_{Work} \sim 1 \cdot 10^{-8}$ mbar), and (b) $p_{Work} \sim 2 \cdot 10^{-7}$ mbar (higher pressure realized by inserting 0.3 sccm air from environment during deposition).

However, it should be pointed out that Wang *et al.* [150] investigated vertical Cu columns ($\omega = 60$ rpm), whereas in the present study the tilted Ti columns ($\omega = 0$ rpm) in Figure 5.7 are studied. For deposition on a continuously rotating substrate, the incoming particles reach several crystal facets of the developing column. In contrast to that, for a stationary substrate the particles arrive at one particular crystal facet of the column. Hence, the deposition on rotating substrates is expected to additionally favor the formation of branched columns. Nevertheless, for deposition on stationary substrates branched columns can also be grown if the working pressure is sufficiently low. The formation of single crystalline columns deposited obliquely has already been described in literature. For instance, Karabacak *et al.* [158] reported on the experimental investigation of single crystalline tungsten at a maximal substrate temperature of 358 K and $\theta_{OAD} = 87°$. To conclude, the formation of unbranched single crystalline columns by OAD at RT requires a sufficiently low pressure during deposition and highly oblique angle of the incoming particle flux.

Besides, the HRTEM image in Figure 5.8 (a) contains information about the TiO_x-layer of the Ti columns. This oxide layer is formed naturally on air, when the sample is removed from the UHV deposition chamber. The HRTEM image in Figure 5.8 is recorded from a sample that has been lying on air from the environment for nine months without any substrate heating (RT). The thickness of the oxide layer is approximately 5 nm and surrounds the Ti-column entirely. Even after month, the oxygen does not further penetrate the Ti column. Moreover, the HRTEM image shows parallel oriented lattice planes not only for the Ti column, but also partly for the TiO_x-layer. This suggests that the TiO_x-layer is at least partially crystalline.

The corresponding Raman spectrum depicted in Figure 5.8 (b) is obtained for a laser with $\lambda = 473$ nm and approximately 800 nm spot size that has irradiated the sample two times for 60 s with 5% laser power. Although the wavelength of $\lambda = 532$ nm and 633 nm have been applied as well, the spectra are not shown here, because the peak intensity has been too low. The Raman spectrum reveals four peaks at 150 cm^{-1}, 250 cm^{-1}, 430 cm^{-1}, and 610 cm^{-1} that can be identified to be the B_{1g}, M, E_g, and A_{1g} Raman modes of rutile, respectively [162]. Rutile is the thermodynamically most stable phase of the three TiO_2-phases, and its formation is expected for much higher temperatures. It is assumed that the single crystalline microstructure of the Ti column might contribute to the formation of rutile already at room temperature. To sum up, the oxide layer of Ti columns that forms naturally on air at RT exhibits a partially crystalline rutile structure, and the oxide does not penetrate the Ti columns even after month. The TiO_x-layer is chemically passivating, which is the reason for the biocompatibility of those columnar Ti thin films [86]. Therefore, such films are promising candidates for applications in coatings of implants, for instance [94, 163, 164].

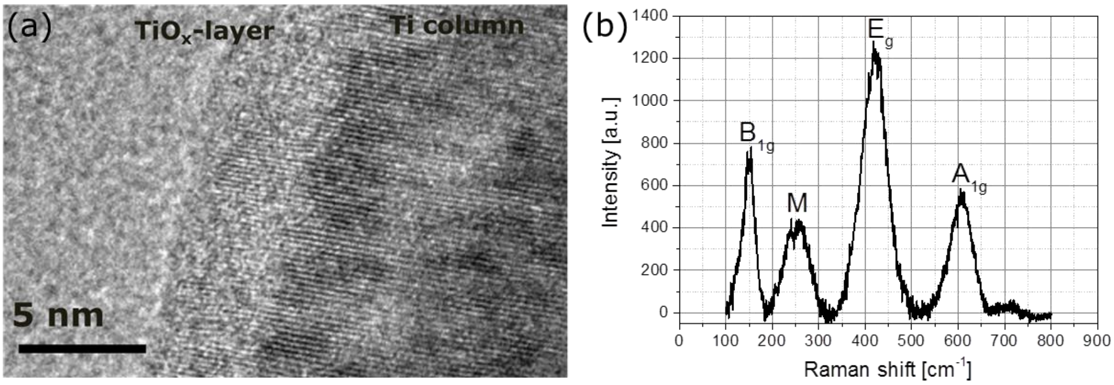

Figure 5.8: (a) HRTEM image of a Ti column grown at RT on natively oxidized Si(100) substrates with $\theta_{OAD} = 84°$. The oxide layer is formed naturally as the sample is removed from the UHV chamber. (b) Corresponding Raman spectrum obtained for $\lambda = 473$ nm at RT.

5.1.2 Tilted columns grown at different substrate temperatures

The previously presented studies have demonstrated that Ti, Cr, and Mo columns deposited obliquely at RT exhibit a single crystalline structure (see subsection 5.1.1). Exemplarily, the influence of the substrate temperature on columnar crystalline structure is investigated exemplarily for individual tilted Ti columns. Two cases are considered: Firstly, the liquid nitrogen cooled sample holder is applied that facilitates to cool down the substrate to $T_{Sub} = 77$ K (T_H(Ti) = 0.04). Secondly, the substrate is heated up to $T_{Sub} = 679$ K (T_H(Ti) = 0.35). Then, the found results are examined with view to the obtained single crystalline structure for Ti columns grown at RT.

Lowered substrate temperature

Tilted Ti columns are fabricated by using thermally oxidized Si(100) substrates, an angle of the incoming particle flux $\theta_{OAD} = 82°$, and a substrate temperature $T_{Sub} = 77$ K ($T_H = 0.04$). Figure 5.9 (a) presents a bright-field TEM overview image of such tilted Ti columns. The corresponding SEAD patterns in Figure 5.9 (b, c) are detected for a large volume of the sample and indicate distinct spots as well as continuous diffraction rings. In addition, the HRTEM images reveal that amorphous regions (Figure 5.9 (I)) as well as crystalline regions with different orientations (Figure 5.9 (II – III)) are present in the sample. To specify where these regions appear in the sample, the HRTEM images are investigated in more detail.

The HRTEM overview image in Figure 5.10 includes details of two Ti columns from Figure 5.9 (a). Each column is surrounded by a TiO_x-layer that is formed naturally as the sample has been removed from the UHV chamber (see, e.g., Figure 5.10 (III)). The Ti columns exhibit a crystalline structure, but the orientation of the crystallites in the column differs. Thus, a single crystalline structure as found for deposition at RT could not be observed. The TiO_x-layer has both partially crystalline and amorphous regions. Between the TiO_x-

layers of two neighboring Ti columns, further partly amorphous regions are located (compare Figure 5.10 (II, V)). These regions are expected to originate from the Pt that is been deposited on the sample during preparation of the FIB lamella [110].

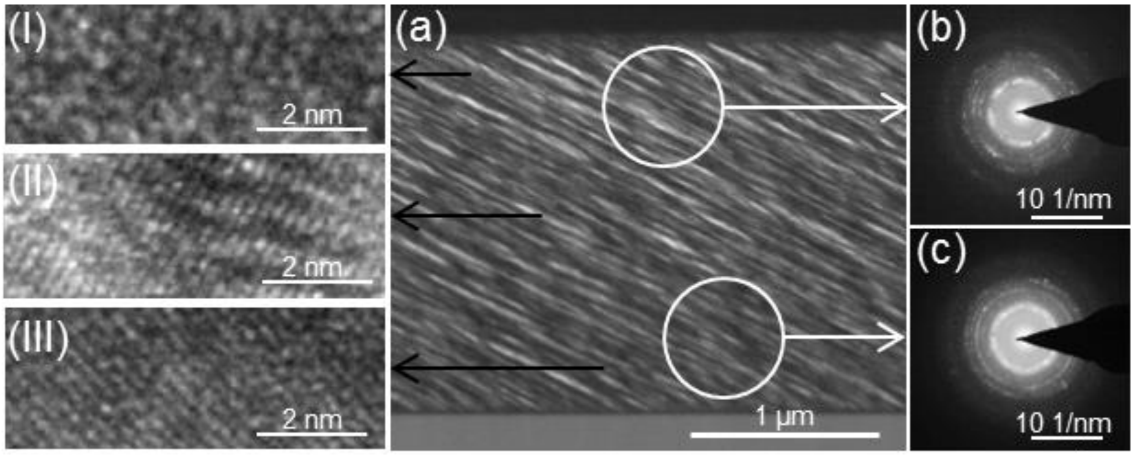

Figure 5.9: (a) Bright-field TEM overview image of Ti tilted columns grown at $T_{Sub} = 77$ K on thermally oxidized Si(100) substrates at $\theta_{OAD} = 82°$. (b, c) Corresponding SEAD patterns and (I – III) HRTEM images.

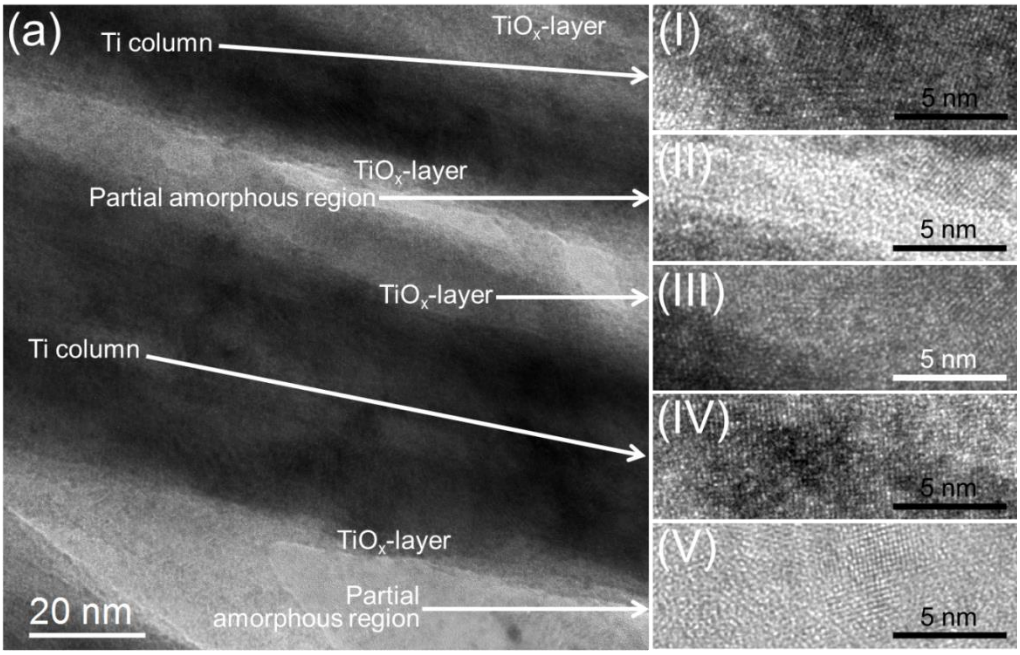

Figure 5.10: (a) HRTEM overview image of Ti columns grown at 77 K on a thermally oxidized Si(100) substrate at $\theta_{OAD} = 82°$. (I – V) Magnified HRTEM images.

Further, NBED is performed to study the crystalline structure of a single Ti column depending on the columnar length *l*. The results are depicted in Figure 5.11 and Figure 5.12. All corresponding NBED patterns (see (I – IV) in Figure 5.11 and (V – VIII) in Figure 5.12) reveal distinct spots, indicating a polycrystalline structure of the Ti columns. Especially the patterns shown in Figure 5.11 (II) and Figure 5.12 (VI) can be identified with those diffraction patterns as calculated for a hcp Ti single crystal. The zone axis is [111] for both patterns. To conclude, shadowing dominates the growth process at 77 K, and the columns exhibit a polycrystalline structure, which is in contrast to the formation of single crystalline columns as observed for deposition at room temperature.

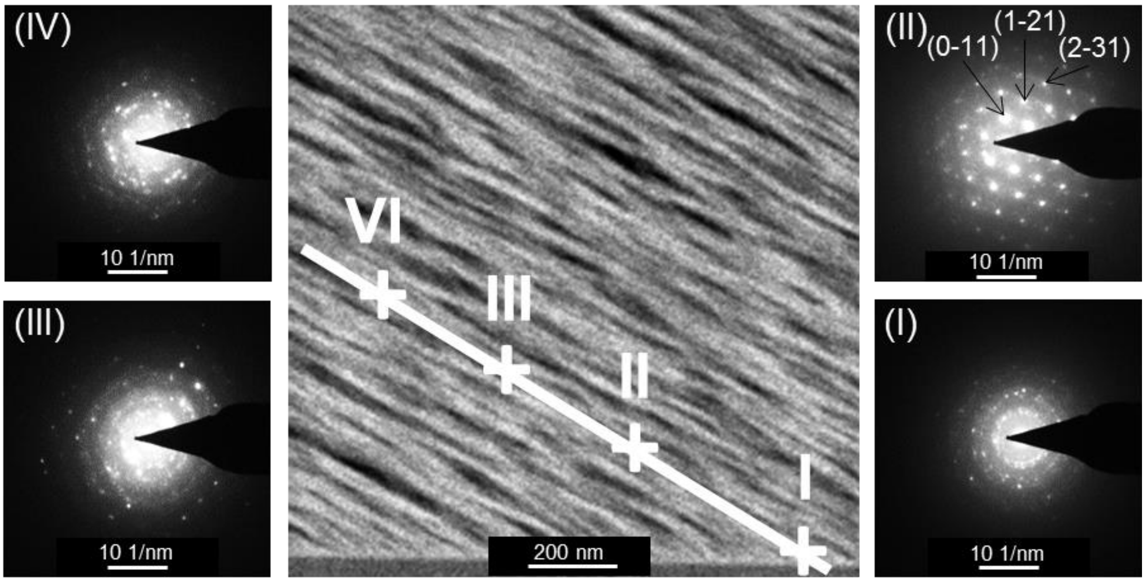

Figure 5.11: Detail of the bright-field TEM overview image in Figure 5.9 (a) for Ti tilted columns grown at T_{Sub} = 77 K on thermally oxidized Si(100) substrates at θ_{OAD} = 82°. (I – IV) Corresponding µP-STEM NBED patterns.

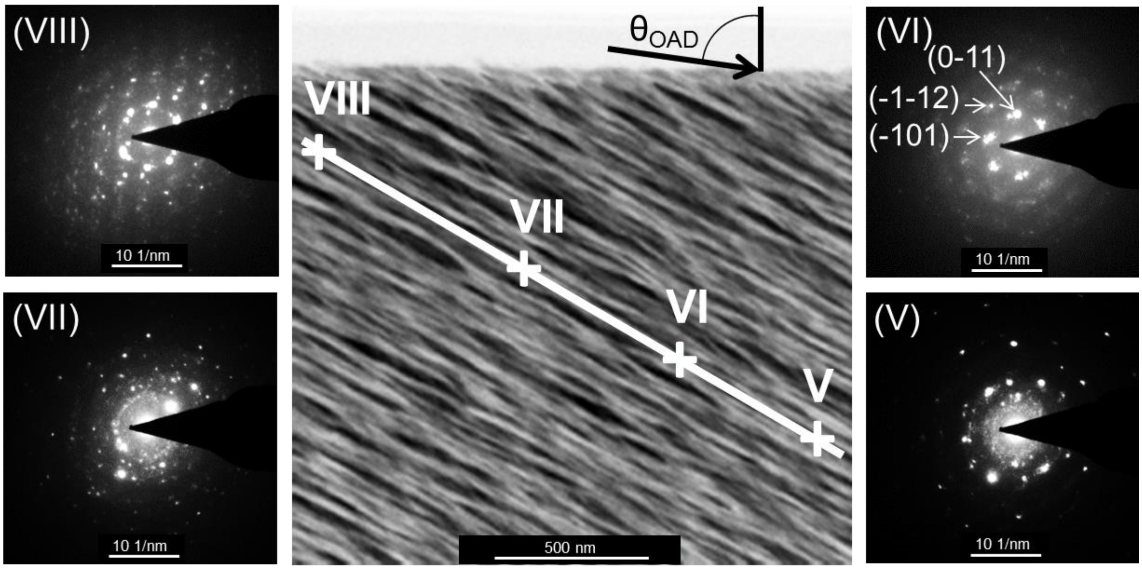

Figure 5.12: Detail of the bright-field TEM overview image in Figure 5.9 (a) for Ti tilted columns grown at T_{Sub} = 77 K on thermally oxidized Si(100) substrates at θ_{OAD} = 82°. (V – VIII) Corresponding µP-STEM NBED patterns.

Elevated substrate temperature

Tilted Ti columns are fabricated by oblique deposition ($\theta_{OAD} = 84°$) using thermally oxidized Si(100) substrates and a substrate temperature $T_{Sub} = 679$ K ($T_H = 0.35$). A bright-field TEM overview image of an agglomeration of smaller and larger Ti columns can be seen in Figure 5.13 (a). This agglomeration occurs, because the columns are collected on the TEM grid by scratching over the sample (see subsection 3.2.2). Nevertheless, the distinct spots in the diffraction patterns of the larger columns in Figure 5.13 (b) and (c) reveal the presence of large crystallites, which is an indication for the tendency of a single crystalline growth of the individual Ti columns. The zone axes are [201] for (b) and [120] for (c). Because the individual columns are collected on the TEM grid by scratching, the individual columns are distributed randomly on the grid. This is the reason for the different zone axes of the SAED patterns in Figure 5.13 (b) and (c).

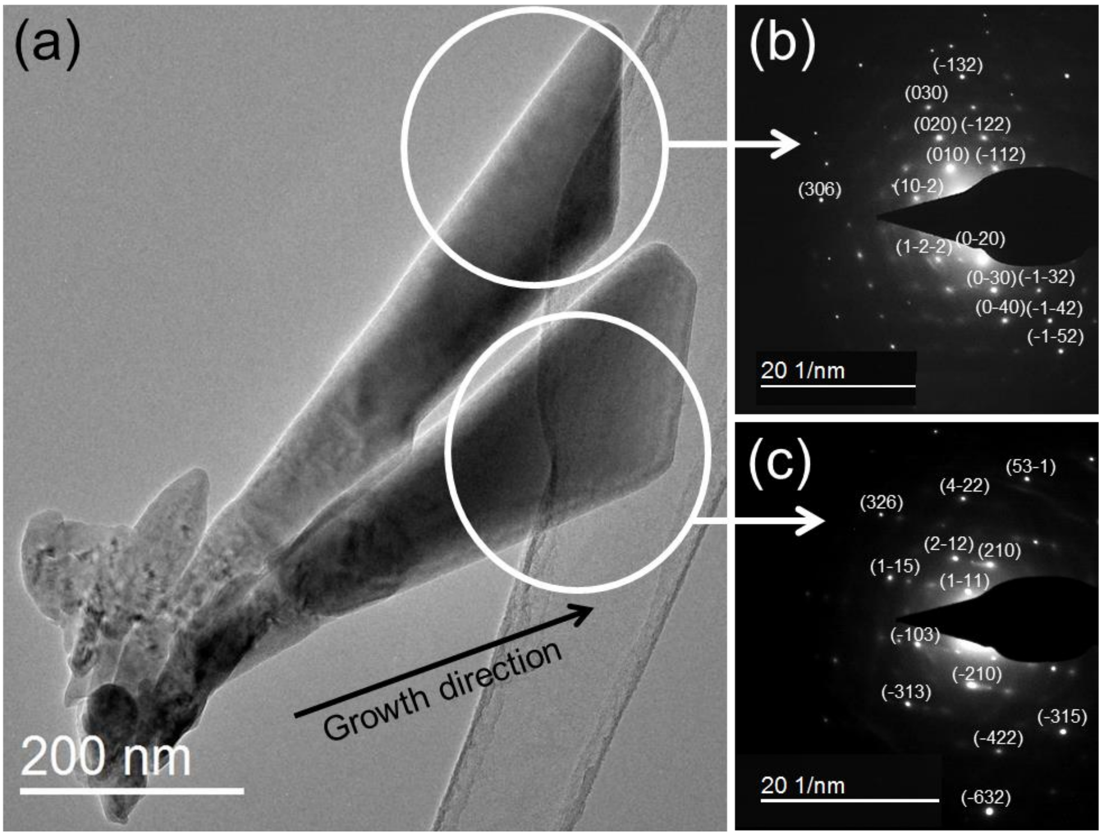

Figure 5.13: (a) Bright-field TEM overview image of an agglomeration of Ti columns deposited with $\theta_{OAD} = 84°$ on a thermally oxidized Si(100) substrate at 679 K substrate temperature ($T_H = 0.35$). (b, c) Corresponding SAED patterns.

5.2 Glancing angle deposition

5.2.1 Vertical columns grown by continuous substrate rotation

Figure 5.14 (a) depicts a bright-field TEM overview image of such a vertical column. The parallel oriented lattice planes in the corresponding HRTEM images (I) – (IV) have a lattice spacing of 0.21 nm, corresponding to the {110} planes of bcc Cr crystals. A comparison between (I) – (IV) unveils that the lattice planes are not oriented parallel to each other over the entire volume of the column. Thus, the Cr column does not exhibit a single crystalline structure. Additionally, all SAED patterns depicted in Figure 5.14 (b – d) show nearly the same, slightly smeared spots. The zone axis for the spots labelled in (b) is [133], but several other spots are present that belong to different crystal orientations. These SAED patterns indicate that the orientation of most the crystallites does not undergo a significant change as the column growth proceeds. Indeed, a closer inspection of the HRTEM images reveals that dominantly the orientation of lattice planes as shown in (I) and (IV) is present, while the orientations depicted in (II) and (III) can only rarely be obtained. In conclusion, the Cr column does not have a single crystalline structure, but the majority of the crystallites exhibits a preferred growth direction along [110].

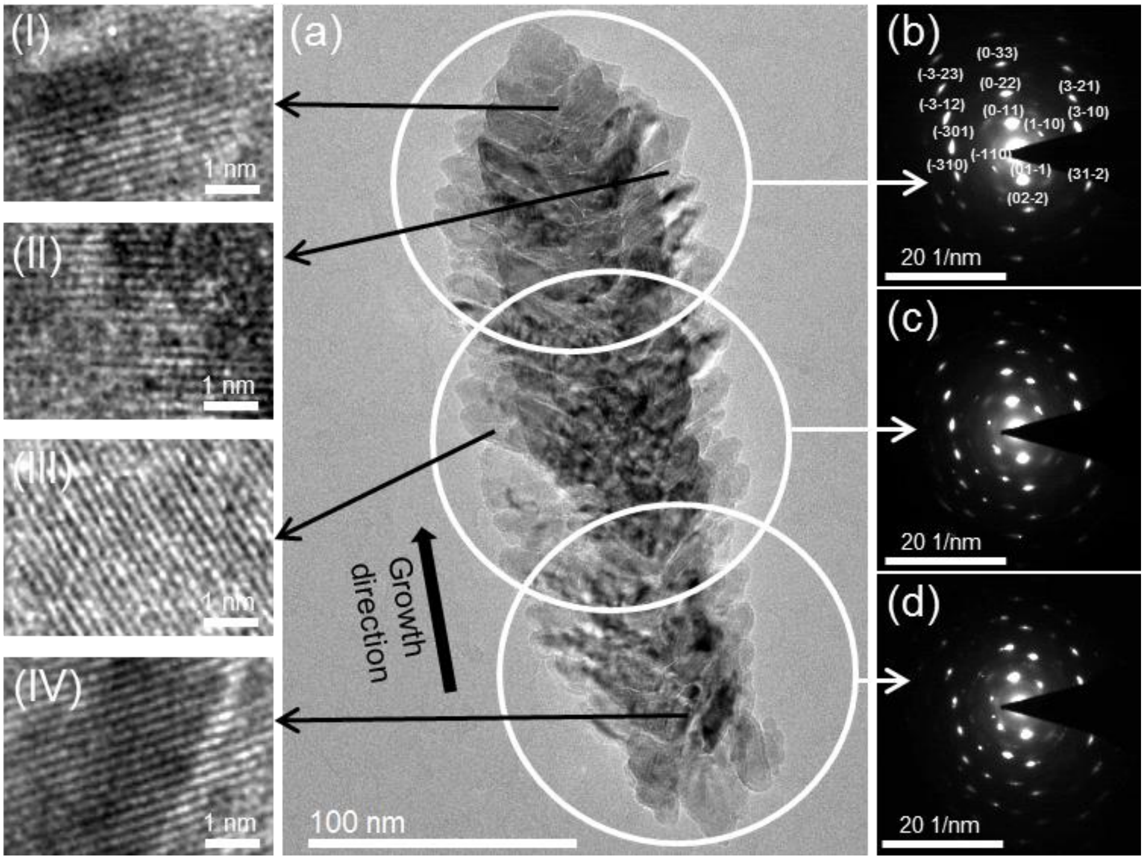

Figure 5.14: (a) Bright-field TEM overview image, and corresponding HRTEM-images (I-IV) as well as SAED patterns (b – d) of a vertical Cr column deposited at RT and at θ_{OAD} = 84° on a natively oxidized Si(100) substrate with ω = 10 rpm.

Besides, vertical Mo columns are grown with an oblique deposition angle $\theta_{OAD} = 84°$ at RT on natively oxidized Si(100) substrates with a deposition rate $r = 0.5$ nm/s and $\omega = 5$ rpm. A bright-field overview TEM image of the upper part of such an individual Mo column is depicted in Figure 5.15 (a). The corresponding HRTEM images (I – III) indicate parallel aligned lattice planes over a large volume of the column with a lattice distance of approximately 0.21 nm, representing the Mo{110} planes. The zone axis is [131]. Further, the SAED pattern in Figure 5.15 (b), which is measured for the entire area of the vertical Mo column as shown in Figure 5.15 (a), shows clear and distinct reflections.

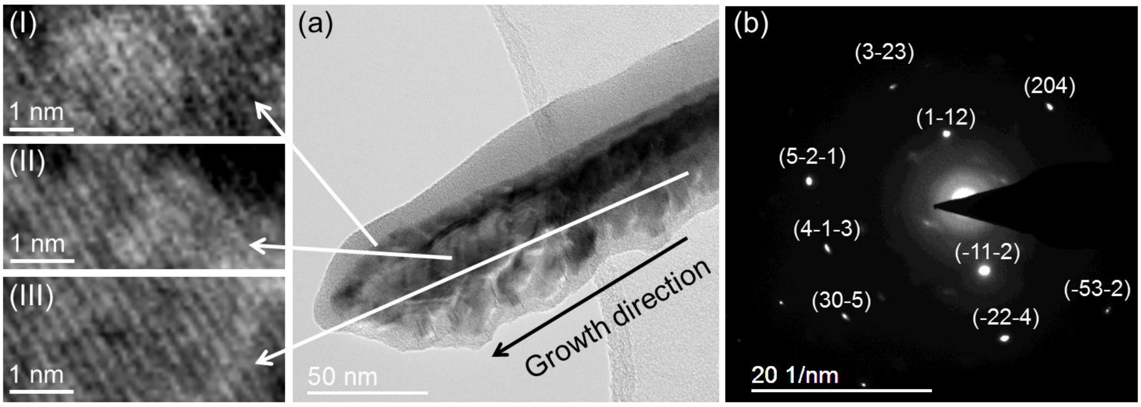

Figure 5.15: (a) Bright-field overview TEM image and corresponding HRTEM-images (I – III) as well as (b) the corresponding SAED pattern of a vertical Mo column deposited at RT and $\theta_{OAD} = 84°$ on a natively oxidized Si(100) substrate with $\omega = 5$ rpm and $r = 0.5$ nm/s.

Another vertical Mo column fabricated with the same experimental conditions as described above (see Figure 5.15) is depicted in the bright-field overview TEM image in Figure 5.16 (a). The corresponding SAED patterns in Figure 5.16 (b – d) contain separated spots. The number of these spots is largest for the SAED pattern in (d), because (at least) two columns are overlapping there (compare Figure 5.16 (a)). Moreover, the spots in (d) could be identified with at least two distinct orientations, which are color-coded in white and green. The zone axis is [511] for the white color-coded reflections and [111] for the green color-coded reflections.

The experimental findings imply that the vertical Mo columns tend to grow with a single crystalline structure. This contrasts with the observed polycrystalline vertical Cr columns. A reason for this might be that Cr is more reactive towards components of the residual gas in the deposition chamber compared to Mo, which can restrain the formation of a single crystalline column. The preferred growth direction for both vertical Cr and Mo columns is along the [110] direction (parallel to substrate normal), which is typical for metals with a bcc crystal structure.

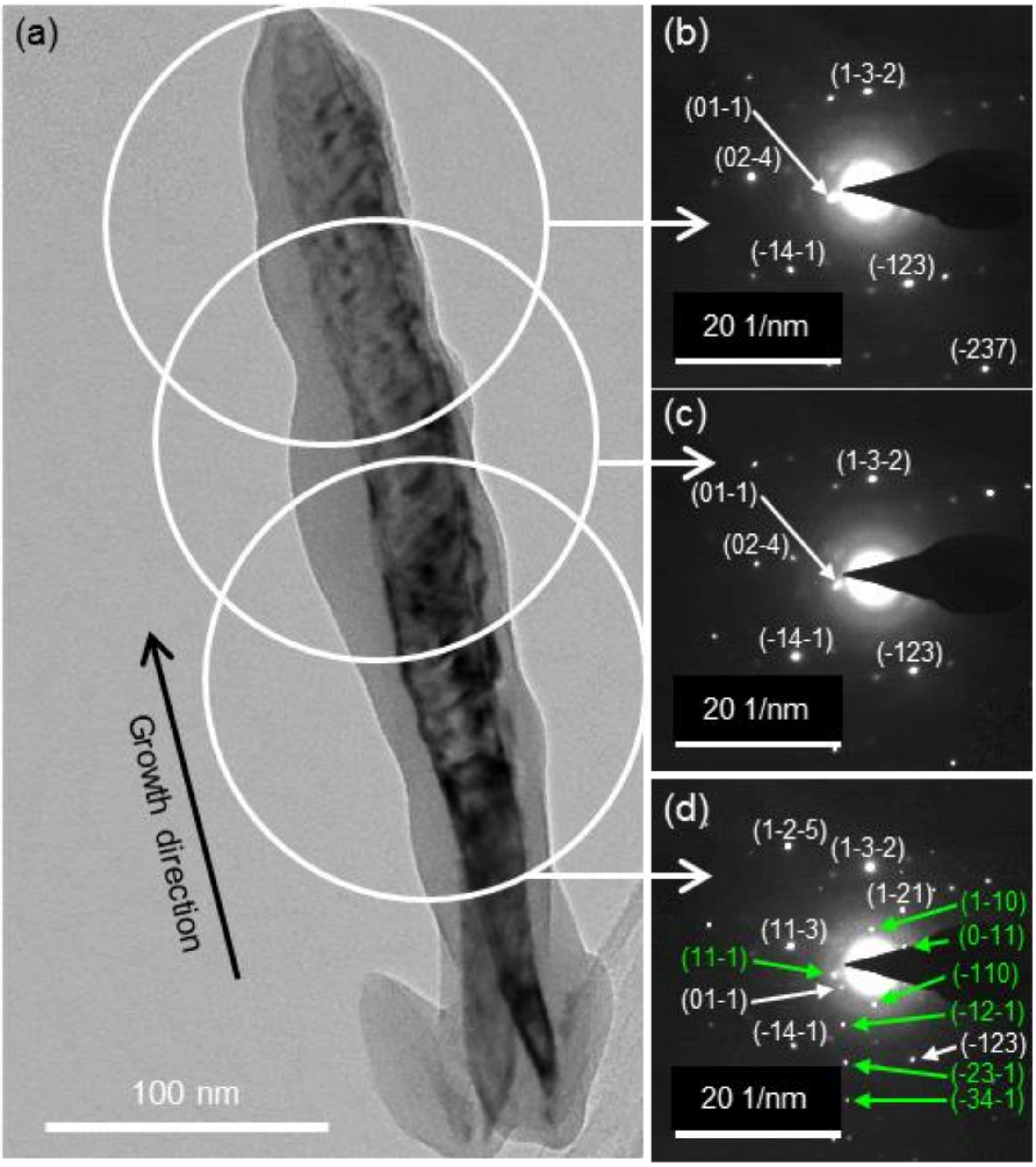

Figure 5.16: (a) Bright-field overview TEM image and (b – d) corresponding SAED patterns of a vertical Mo column deposited at room temperature and at $\theta_{OAD} = 84°$ on a natively oxidized Si(100) substrate with $\omega = 5$ rpm and $r = 0.5$ nm/s.

5.2.2 Zigzag columns grown by discrete substrate rotation

The Mo zigzag columns studied in this subsection are deposited at RT by discrete substrate rotation (as described in subsection 4.2.2) on natively oxidized Si(100) substrates with $\theta_{OAD} = 84°$ and $r = 0.5$ nm/s.

Figure 5.17 (a) is a bright-field TEM overview image of such Mo zigzag columns. Because the zigzag columns are collected on the TEM grid by scratching, the zigzags are agglomerated. Consequently, the SAED patterns in (b, c) represent a superposition of reflections originating from approximately two to four zigzag columns, respectively. Nevertheless, clearly visible distinct spots could be detected in each pattern, indicating a crystalline structure. The zone axes are calculated to [111] for Figure 5.17 (b) and [110] for (c).

To gain further information about the crystalline structure, HRTEM measurements of these Mo zigzag columns are carried out. The results are represented in Figure 5.18 (I – VI). Parallel oriented lattice planes can be distinguished in each of the HRTEM images. For (IV – VI), atomic resolution could be achieved. A comparison between (II) and (III)

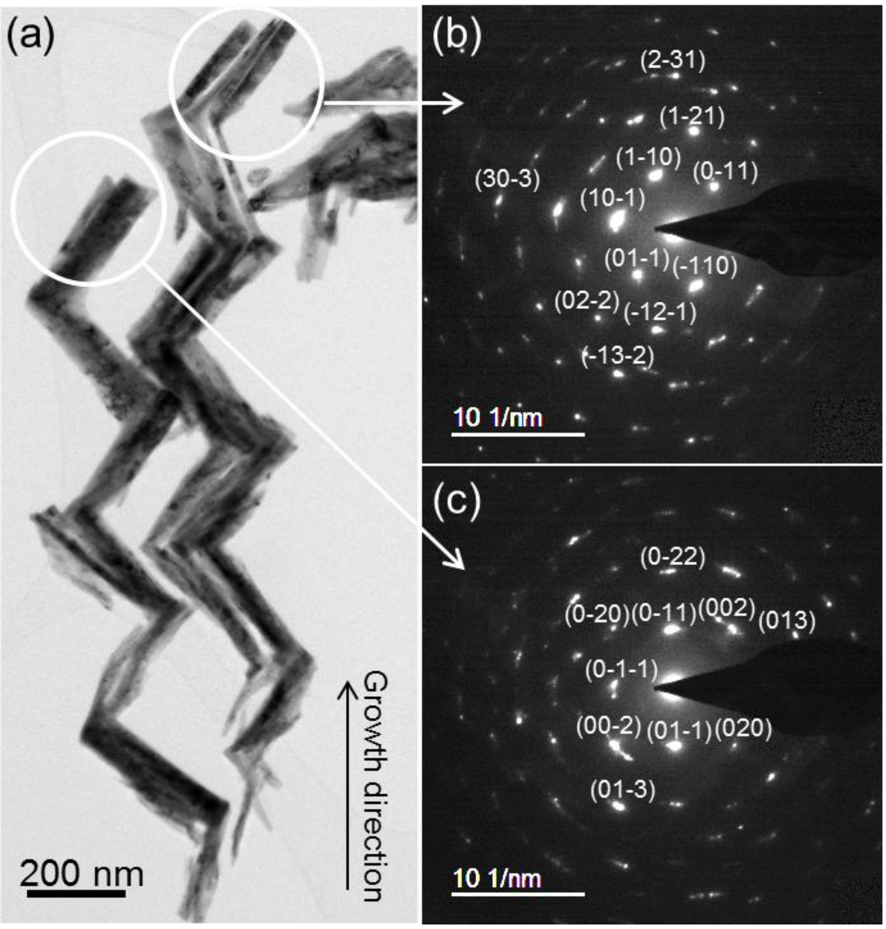

Figure 5.17: (a) Bright-field TEM overview image and (b, c) corresponding SAED patterns of Mo zigzag columns deposited at room temperature with $\theta_{OAD} = 84°$ and $r = 0.5$ nm/s on a natively oxidized Si(100) substrate.

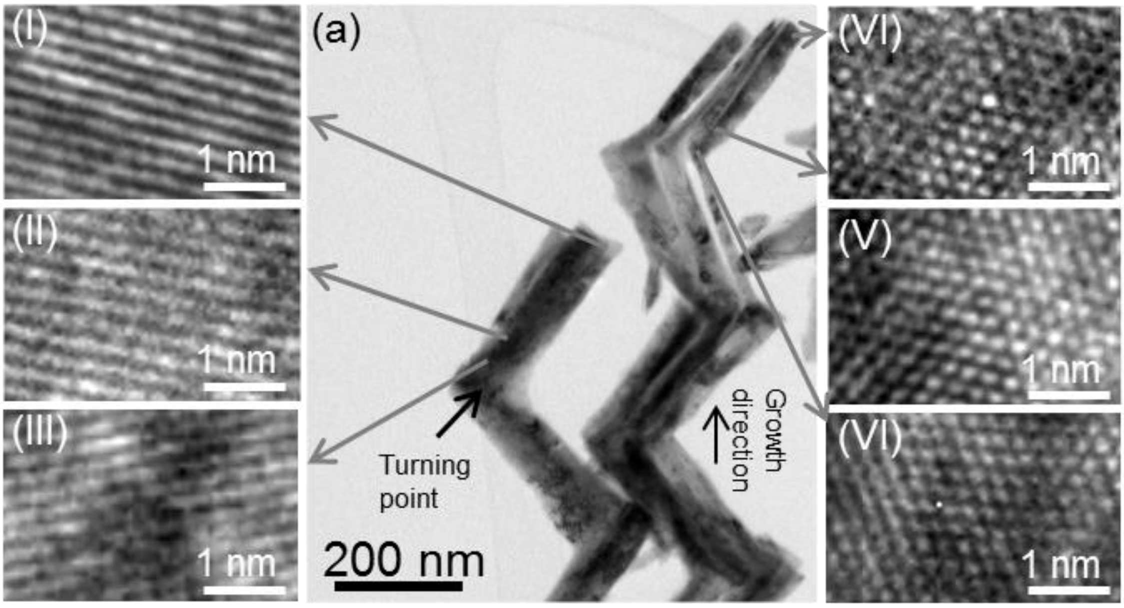

Figure 5.18: (a) Bright-field TEM overview image and corresponding HRTEM-images (I – VI) of Mo zigzag columns deposited at RT with θ_{OAD} = 84° and r = 0.5 nm/s on a natively oxidized Si(100) substrate.

indicates that the lattice planes are not oriented parallel over the entire volume of the column.

Figure 5.19 (a) depicts a bright-field TEM overview image of a turning point of a Mo zigzag column. The corresponding HRTEM images (I – V) reveal parallel aligned lattice planes over the entire volume of the turning point. The lattice distance is 0.22 nm, corresponding to the {110} planes of a Mo bcc crystal. Further turning points have also been studied, but a change of the orientation of the crystalline lattice planes could not be detected. Hence, the conclusion is drawn that such a change does not occur directly at the turning point, but at a certain position between two turning points. A closer inspection of the HRTEM images (II) and (III) in Figure 5.18 suggests that the change of the crystalline orientation occurs in closer vicinity above the turning point. Based on the TEM measurements can be concluded that the Mo zigzag columns deposited at RT exhibit a high crystalline quality, but a single crystalline structure could not be observed.

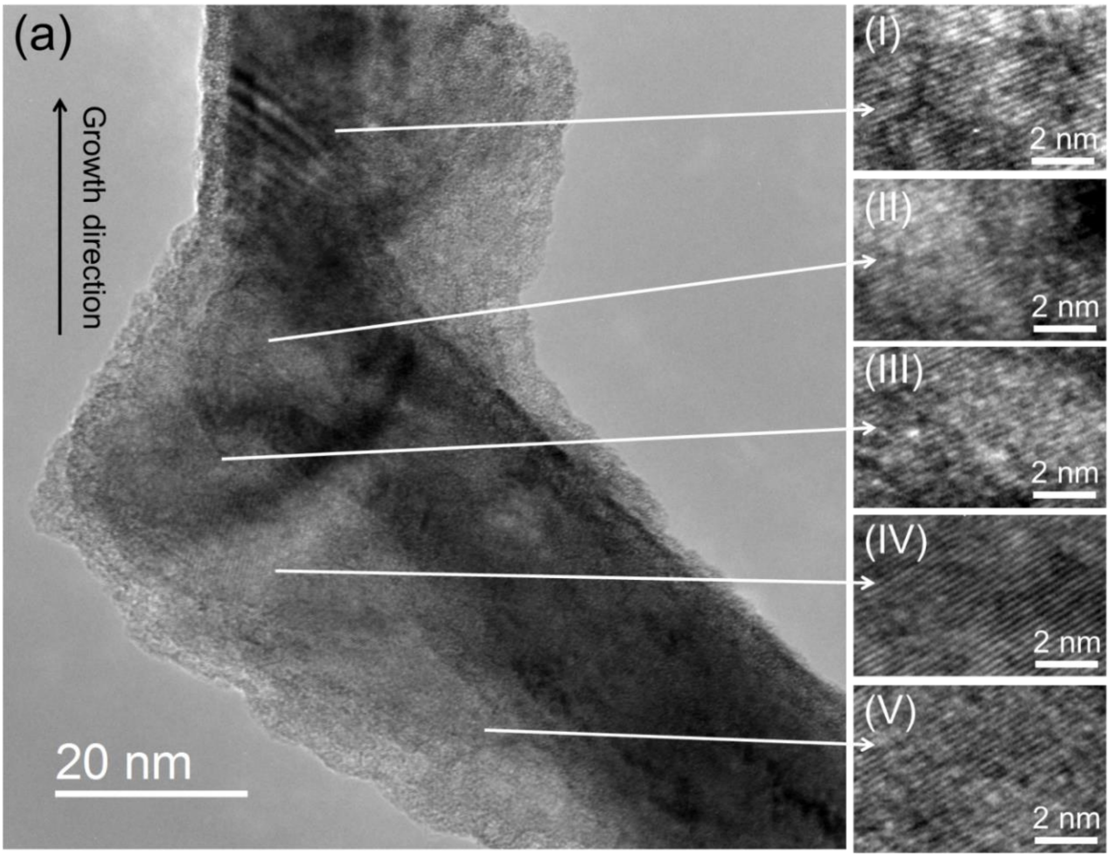

Figure 5.19: (a) HRTEM image and corresponding magnified HRTEM-images (I – V) of a turning point of a Mo zigzag column deposited at RT with $\theta_{OAD} = 84°$ and $r = 0.5$ nm/s on a natively oxidized Si(100) substrate.

5.3 Discussion

In the electron diffraction patterns detected at the interface between substrate surface and tilted Ti and Mo columns deposited at 77 K (see Figure 5.11) and 300 K (see Figure 5.1), (i) randomly oriented spots and (ii) diffuse diffraction rings could obtained. (i) The occurrence of distinct spots originates from crystalline nuclei forming at the substrate surface. Such a formation requires that the adatoms have enough thermal energy to overcome the diffusion barrier so that surface self-diffusion can occur. The resulting shape of those nuclei is determined by the planes with the lowest surface energy (slowest growing planes). During nucleation, crystallites with random orientations towards the incoming particle flux are forming. (ii) The diffuse diffraction rings are expected to come from the 800 nm thick oxide layer on the Si(100) substrate. In the case of Ti deposited at 77 K, those might originate also from some amorphous nuclei that might have been formed due to the highly restricted adatom surface self-diffusion.

For deposition at 77 K, the Ti columns are partly crystalline and partly amorphous. The presence of crystalline parts indicates that there is a fraction of adatoms that have enough energy to overcome the diffusion barrier. However, the adatom mobility is strictly limited so that they cannot move to other planes or even columns. For the other fraction of adatoms, the mobility is expected to be suppressed so that the adatoms stick where they hit the surface. This causes the growth of the amorphous parts of the column. Due to the strictly limited surface self-diffusion, the columns can only compete by shadowing, and not due to crystallographic reasons. Thereby, the columns that capture the largest amount of material during growth shadow those columns that capture less material, which requires an anisotropy of the incoming particle flux. It can be noted that single crystalline Ti columns at 77 K are not observed, because the adatom mobility is too low.

For deposition at RT, the adatom mobility is enlarged, meaning that the adatoms will be able to diffuse on the crystal plane or will be able to reach underlying planes of the same orientation by overcoming the Ehrlich-Schwoebel barrier. Once the adatom is incorporated in the crystal lattice, it is immobilized and cannot be activated again. The nuclei that form on the substrate are expected to be single crystalline, but the adatom mobility does not allow the movement from one nucleus to other nuclei. If shadowing is the dominating effect during the growth process, the initial orientation of the crystallites will be preserved so that single crystalline nuclei develop to single crystalline columns, as has been observed for tilted Ti, Cr, and Mo columns grown at $\theta_{OAD} = 84°$ at RT. For less oblique deposition geometry, for instance, the shadowing length would be decreased, causing a bundling of the columns to a larger column, which would then not be single crystalline anymore. Additionally, if the vacuum requirements are not sufficient, impurities can be incorporated in the crystal lattice. Hence, the initial orientation of the nuclei is not preserved, favoring the growth of a polycrystalline column. This argumentation could be proven for tilted Ti columns deposited at RT with different working pressures.

As the substrate temperature is further increased, adatoms might be able to diffuse between nuclei to find their most thermodynamically stable position. Thereby, once incorporated adatoms can be activated again so that nuclei can dissolve and the adatoms might migrate to other nuclei so that the total number of nuclei per unit area is reduced. This process is called coarsening. For later stages of growth, the adatoms might be able to move from one column to another column. In general, a higher adatom mobility is expected to favor the growth of single crystalline columns, because then the probability is higher that the adatom can move to a more thermodynamically favored position. Indeed, for deposition at 679 K, tilted Ti columns with large single crystalline crystallites could be observed. Although adatom mobility is already high, shadowing is present, indicated by the observed growth of tilted columns.

Besides, vertical Mo columns deposited at RT have a single crystalline structure as well. At RT, the adatom mobility is high enough so that single crystalline nuclei with different orientations at the substrate are created. As the substrate is rotated continuously, the direction of the incoming particle flux with respect to the developing nuclei / columns is changed. This means that the adatoms can reach different facets of the same crystal, thus inducing crystal growth, while the initial orientation of the crystallite is still preserved. That the vertical Cr columns have not been single crystalline might be caused by the higher reactivity of Cr towards residual gas components than Mo.

Moreover, the HRTEM images reveal that for deposition at RT the tilted hcp Ti columns grow along the [0002] direction, and the tilted and vertical bcc Cr as well as bcc Mo columns grow preferably along the [110] direction. These are the thermodynamically most favored planes for the corresponding crystal structures. As a matter of fact, the TEM measurements do not allow to determine the tilt angle of the direction of these planes with respect to the substrate normal. Therefore, it is also not possible to compare the tilt angle of these crystal planes with the columnar tilt angles. To address these questions, and to gain in general more information about the distribution of the crystal orientations in the columnar thin films, XRD-pole figure measurements are applied (see chapter 6).

In conclusion, the growth of single crystalline metal columns at RT could be proven for a highly oblique deposition geometry ($\theta_{OAD} > 80°$), low working pressure ($p_{Work} \sim 10^{-8}$ mbar), and a substrate temperature high enough to provide adatom mobility ($T_{Sub} \geq 300$ K).

5.4 Summary of results

Concerning the high-resolution structural analysis of individual metallic columns grown by OAD and GLAD, the following conclusions can be drawn:

Oblique deposition:

- Tilted Ti, Cr, and Mo columns deposited obliquely ($\theta_{OAD} = 84°$) at RT tend to grow single crystalline.
- Tilted Mo columns with single crystalline structure are observed for both natively and thermally oxidized Si(100) substrates. For the latter, the 800 nm thick oxide layer impedes any epitaxial relation between the substrate and the columns. An epitaxial relation is also not expected for deposition on natively oxidized Si(100) substrates.
- Besides highly oblique deposition geometry ($\theta_{OAD} > 80°$) and an adequate substrate temperature to provide adatom mobility ($T_{Sub} \geq 300$ K), the formation of single crystalline metallic columns at RT requires high vacuum conditions (working pressure $p_{Work} \leq \sim 10^{-8}$ mbar). An increased working pressure favors the formation of branched and polycrystalline columns.
- An oxide layer is forming naturally on the metallic columns after locking the samples out of the UHV chamber. For Ti columns, the oxide layer is approximately

5 nm thick. The partially observed rutile structure of the oxide might be caused by an epitaxial transformation of the Ti column surface to the TiO_x-layer.

- For deposition at higher substrate temperatures (T_H(Ti) = 0.35), individual Ti columns tend to be single crystalline, but for lower substrate temperatures (T_{Sub} = 77 K) a polycrystalline structure due to the restricted adatom mobility is observed. In particular, a columnar bundle structure as described by Messier *et al.* [18] (see subsection 2.1.4) is not obtained.

Glancing angle deposition:

- Vertical Cr columns grown obliquely on natively oxidized Si(100) substrates at RT are not single crystalline, but the majority of the crystallites exhibits a preferred orientation along the [110] direction (parallel to substrate normal).
- In contrast to vertical Cr columns, vertical Mo columns tend to grow single crystalline if deposited with similar experimental conditions. A possible explanation for this is that Cr is more reactive towards residual gas components than Mo.
- Mo zigzag columns obliquely deposited at RT on natively oxidized Si(100) substrates are polycrystalline, but show a high crystalline quality. The change of the crystal orientation could not be detected directly at the turning point, but in closer vicinity above such a turning point.

6 Texture Analysis of Columnar Thin Films

The high-resolution TEM and electron diffraction measurements shown in the previous chapter have given information about the local structure of the metallic columns. However, some questions remain unanswered, such as the orientation of the crystal planes obtained in the HRTEM images with respect to the substrate normal or to the growth direction of the tilted columns. To address these questions, texture analysis is carried out by using XRD pole figure measurements. A profound understanding of the texture formation in metallic thin films is of vital importance, because the ability to precisely tailor the texture represents a key issue for controlling the optical, magnetic, and electrical properties of these films. Although considerable research activities have been carried out to study the conditions under which columnar thin films become textured [16, 27, 30, 157, 158, 165-180], contradictory statements persist so that a general trend is missing so far. Consequently, the texture formation of columnar thin films must be analyzed on a case-by-case basis. In the first part of this chapter, the texture evolution depending on the film thickness is analyzed exemplarily for columnar Mo thin films [LIE04]. The second part focusses on the influence of the incidence flux direction θ_{OAD} on the texture of Ti thin films. [LIE03]. Further, the dependence of the substrate temperature T_{Sub} on the texture of obliquely deposited Ti, Al, and Cr thin films is described and discussed in section 6.3 [LIE02, LIE05].

6.1 Influence of the film thickness

For the experiments in this section Mo has been chosen, because this metal has a high melting point $T_{melt} = 2896$ K, and therefore a relatively low homologous temperature $T_H = 0.1$ at RT. This facilitates the detection of structural changes of the columnar thin film. Additionally, Mo thin films show a good response to RHEED and XRD measurements, which relieves the analysis of texture evolution with increasing film thickness. A high thermal stability of the columnar Mo thin films may be expected due to the high melting point of the material.

Columnar Mo thin films are fabricated by oblique deposition at $\theta_{OAD} = 84°$ at RT and with a constant deposition rate $r = 1$ nm/s. The film thickness is varied in the range between $10 \text{ nm} \leq t \leq 2.5\ \mu\text{m}$. Si(100) pieces with a 800 nm thick oxide layer are used as substrates. During the experiments, the working pressure in the ultra-high vacuum chamber is constant at 10^{-8} mbar (base pressure 10^{-9} mbar).

Figure 6.1 (a) – (d) represent top-view SEM images of columnar Mo films with film thicknesses varying from 10 nm to 2.5 µm. Due to the oblique deposition geometry, shadowing is induced during the growth process so that separated columns are forming, which are inclined towards the direction of the incident particle flux. In the progress of the evolutionary selection process [11], the columns with the fastest vertical growth direction will overgrow columns that grow slower in height. Thus, as the film grows thicker, the total number of growing columns per unit area is reduced, as a comparison between Figure 6.1 (d) and Figure 6.1 (a) implies. In addition, Figure 6.1 (i) depicts a cross-sectional SEM image exemplarily for a 2.5 µm thick Mo film consisting of separated columns with different aspect ratios. The columns are inclined by an angle $\beta = 52° \pm 2°$ with respect to the substrate normal.

The corresponding RHEED patterns are presented in Figure 6.1 (e) – (h). For the film thicknesses $t = 10$ nm (Figure 6.1 (h)) and $t = 30$ nm (not shown here), the patterns show continuous diffraction rings, denoting a random orientation of Mo crystallites on the substrate. Breaks in the diffraction rings are observed for 40 nm thick films (Figure 6.1 (g)) for the first time, indicating that the orientation of the crystallites is not random anymore. The symmetric breaks in the middle of the rings emerge further as the film thickness is increased from 70 nm (Figure 6.1 (f)) up to 2.5 µm (Figure 6.1 (e)) as a result of the ongoing selection process among the developing columns. Besides, film thicknesses of 110 nm and 250 nm have been investigated as well, but those are not shown here, because the observations have been analogue to those obtained for the 70 nm thick films. The symmetry of the RHEED patterns originates from the parallel alignment of the electron beam to the projected tilt direction of the columns. From Figure 6.1 (e), the ratio of the radii from the inner to the outer rings is determined to 1:1.22:1.58:1.73. Based on this ratio, the conclusion is drawn that the {211}, {310}, and {312} bcc Mo planes correspond to these rings [161]. Moreover, the RHEED patterns include additional diffuse rings, whose number is largest for the films with thicknesses from $t = 10$ nm to $t = 70$ nm. Notice that the RHEED measurements had to be performed *ex situ* so that a Mo oxide layer has been formed prior to the measurements. RHEED is characterized by the limitation of penetration and escape depths of electrons, which enables the study of the surface. Because the electron beam reaches the surface under a grazing angle, the RHEED patterns include information of the Mo oxide layer. For the Mo films with 10 nm, 40 nm, and 70 nm, a large number of small columns can be observed, providing a large area covered by an oxide. For the 2.5 µm thick film, the diffraction rings from the Mo oxide is expected to be present as well, but not visible due to the low intensity. It can be noted that the RHEED measurements are a first indication for the texture formation of the columnar Mo thin films.

In contrast to RHEED measurements, which provide information about the texture of the surface-near volume [181], pole figure measurements contain the texture information of the complete or considerable part of the film due to the large penetration depths of the X-rays (several microns) [182]. To perform the IPPF measurements, the samples are positioned in the XRD goniometer so that the azimuthal angle $\Phi = 270°$ in the stereographic projection of the pole figure corresponds to the direction of the incoming particle flux (as indicated by the grey arrows in Figure 6.2 (g), (h)). Mo{110} and Mo{200}

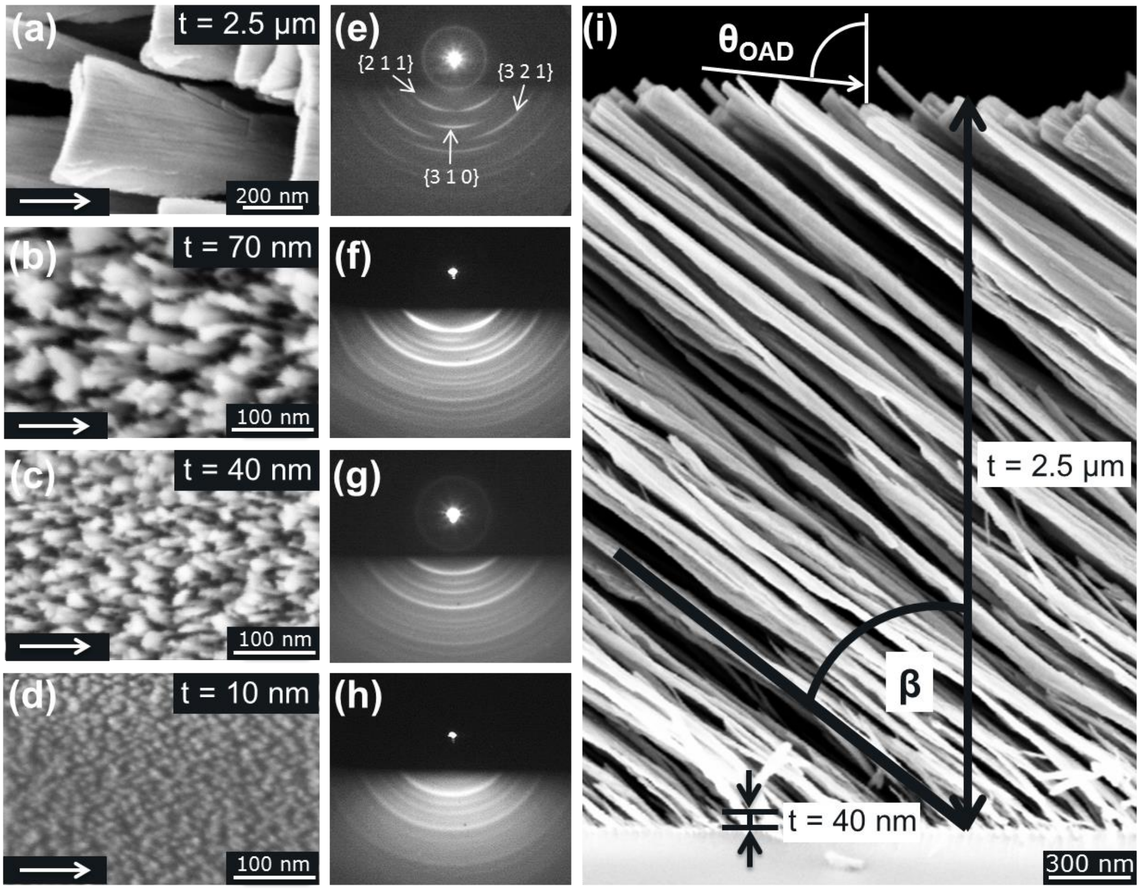

Figure 6.1: (a) – (d) Top-view SEM images of Mo thin films deposited at an incidence angle θ_{OAD} = 84° and 300 K for varying film thicknesses t = 2.5 µm, 70 nm, 40 nm, and 10 nm, respectively. The white arrows indicate the direction of the incoming particle flux. (e) – (h) Corresponding RHEED patterns of the Mo thin films. (i) Cross-sectional SEM image of the 2.5 µm thick Mo film. The incidence angle θ_{OAD}, the tilt angle of the column β, and the film thickness t are measured with respect to the substrate normal.

IPPFs are measured exemplarily for columnar Mo films with t = 70 nm, 250 nm, and 2.5 µm by using the Bragg reflections 2θ = 40.515° and 2θ = 58.608° [183], respectively. It should be mentioned that for the θ-2θ scans carried out with common measurement geometry no peaks could be detected. The reason for this is that the planes of the bcc Mo crystals are tilted with respect to the substrate normal so constructive interference does not occur. Consequently, the Bragg reflections had to be taken from a database [183]. The diffracted intensity in Figure 6.2 is scaled linear and applies for all measured pole figures (see subsection 3.2.3). For film thicknesses less than 70 nm, the diffracted intensity is too low to detect any pole density maximum. The first, weak intensity maximum can be obtained at Φ = 270° and χ = 10° for the Mo{110} IPPF shown in Figure 6.2 (a), but further pole density maxima can hardly be distinguished. Nevertheless, this IPPF reveals that the crystallites show preferably arbitrary orientations on the surface, but the selection of crystal orientations has already begun, which is in accordance which the previously discussed

RHEED patterns. The sharp and intense pole density maxima in Figure 6.2 (b), (d), (f) originate from the Si(100) substrate below the oxide layer.

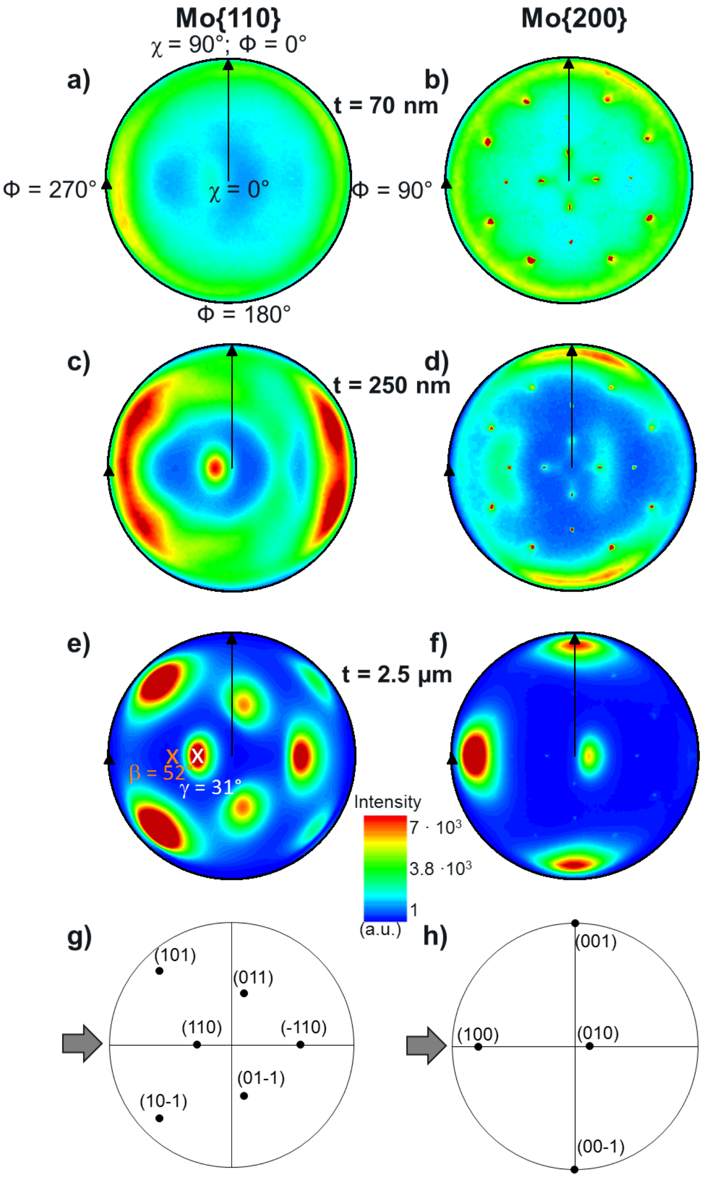

Figure 6.2: Measured in-plane pole figures for the bcc Mo{110} and Mo{200} reflections in a Mo thin film obliquely deposited at $\theta_{OAD} = 84°$ and at RT: (a) and (b) $t = 70$ nm, (c) and (d) $t = 250$ nm, (e) and (f) $t = 2.5$ µm. $\gamma_{[110]}$ (white cross) is the tilt angle of the [110] direction of the bcc Mo crystal and β (orange cross) is the tilt angle of the Mo column, both measured with respect to the substrate normal. The intensity is depicted on a linear scale and applies for all measured pole figures. (g) and (h) Theoretical expected pole figures for the bcc Mo{110} and Mo{200} planes for a single crystal, tilted by $\gamma_{[110]} = 31°$. The grey arrows indicate the direction of the incoming particle flux.

The IPPFs for the 250 nm thick Mo film are presented in Figure 6.2 (c) and (d). The intensity maximum at $\Phi = 270°$ and $\chi = 10°$ in Figure 6.2 (c) is remarkably more pronounced compared to Figure 6.2 (a), and additional pole density maxima occur at $\Phi = 68°, 112°, 240°, 300°$ and $\chi = 84°$. Notice that these pole density maxima are located near the edge of the pole figure. Due to the reduced mass sensitivity at the edge of the IPPF, the pole density maxima appear to be moved inwards. A homogeneous density ring connects pairs of neighboring pole density maxima, indicating a fiber texture contribution. In Figure 6.2 (d), four pole density maxima can be distinguished at ($\Phi = 0°$, $\chi = 87°$), ($\Phi = 90°$, $\chi = 27°$), ($\Phi = 180°$, $\chi = 87°$), and ($\Phi = 270°$, $\chi = 62°$), which are separated by an angle of $\Phi = 90°$ as expected for the adjacent <100> directions in a bcc crystal. The pole density maxima indicate a confinement of the crystallites in azimuthal and polar direction, meaning that there is an evolving biaxial texture. Moreover, a fiber texture component could be identified, since some crystallites are exclusively confined in polar direction.

In Figure 6.2 (e), (f), the IPPFs for a 2.5 μm thick columnar Mo film are illustrated. The pole density maxima at (101), (011), (110), (-110), (01-1), and (10-1) are broad, clearly separated (see Figure 6.2 (e)), and correspond to the six {110} planes of a bcc crystal. In Figure 6.2 (f), four pole density maxima (001), (100), (010), and (00-1) can be identified, which coincide with four of the in total six {100} bcc planes. The remaining two pole density maxima do not appear in the IPPF, because the [100] direction of the crystallites is tilted by an angle $\gamma_{[100]}$ with respect to the substrates normal so that these two pole density maxima are not in the upper half sphere above the sample anymore. A comparison between the four pole density maxima in Figure 6.2 (d), (f) indicates that the pole density maxima become significantly more pronounced as the film thickness is enlarged from $t = 250$ nm to $t = 2.5$ μm. The pole density maxima in Figure 6.2 (e), (f) are not connected by a pole density ring, meaning that there is a nearly full biaxial texture with no or only a minor fiber texture contribution. There is a good match with the calculated IPPFs [161] in Figure 6.2 (g), (h). The 800 nm thick oxide layer atop the Si(100) substrate inhibits an epitaxial relationship between the Mo columns and the substrate. To sum up, the texture changes as the film grows from a not-well oriented texture for $t = 70$ nm to a biaxial textured thin film with fiber contribution ($t = 250$ nm) and finally to a nearly complete biaxial texture ($t = 2.5$ μm).

From the pole density maxima (110) in Figure 6.2 (e) (see white cross), the tilt angle $\gamma_{[110]} = 31°$ of the [110] direction of the bcc crystallites with respect to the substrate normal can be determined (see Figure 6.6 for illustration). The cross-sectional SEM image in Figure 6.1 (i) reveals a columnar tilt angle $\beta = 52° \pm 2°$, but this does not coincide with any of the pole density maxima in Figure 6.2 (e) (see orange cross). The difference between both angles is 21°, meaning that the columns grow along a crystal direction that is tilted by 21° with respect to the substrate normal.

Furthermore, a cross-sectional TEM specimen is prepared from a 2.5 μm thick columnar Mo film, as shown in Figure 6.3 (a). The direction of the incoming particle flux is indicated by the thick white arrow. The corresponding SAED patterns are presented in Figure 6.3 (b) – (e). At an early growth stage, nearly continuous diffraction rings can be observed, which indicate a random crystal orientation on the substrate. As the columns develop, smeared reflections can be seen (Figure 6.3 (d)), and distinct reflections evolve (Figure 6.3 (c)). These observations confirm again that the evolutionary growth process leads to a reduction of the distribution of crystal orientations of the growing film. A comparison between Figure 6.3 (b) and (c) shows that the number of distinct reflections is lowered for the topmost part of the TEM specimen. In detail, the four distinct reflections in Figure 6.3 (b) correspond to the {101} planes. Second order reflections can also be observed. The remaining week reflections originate from other crystal orientations, but those are expected to vanish with enlarged film thickness. The diffuse rings are caused by the Pt that had to be deposited atop the Mo film for preparing the FIB lamella [110].

In conclusion, the competitive growth process is basically ceased for $t = 2.5$ µm, and the finally established crystal orientation is a result of this process.

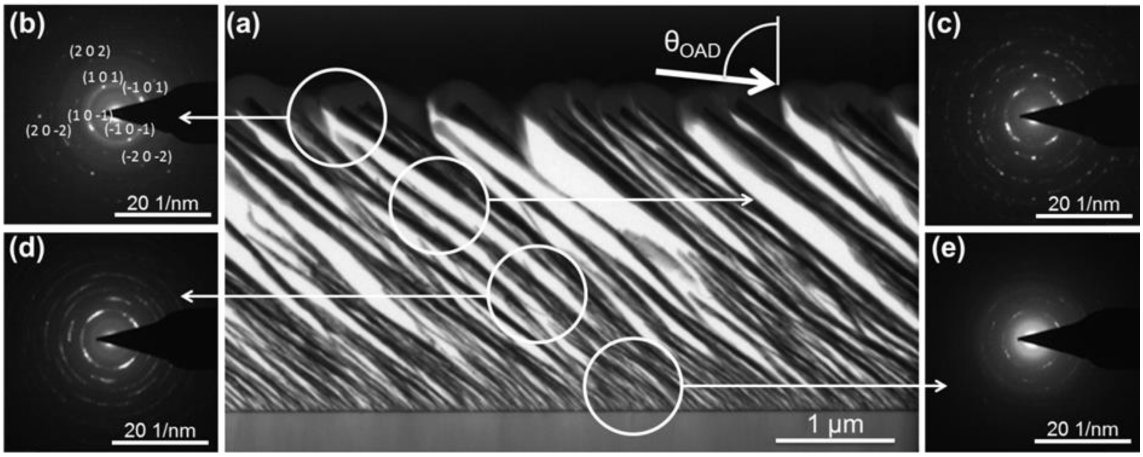

Figure 6.3: (a) Image of a cross-sectional TEM specimen of the columnar Mo film with $t = 2.5$ µm deposited at $\theta_{OAD} = 84°$. (b) – (e) Corresponding SAED patterns. The thick white arrow indicates the direction of the incoming particle flux.

A biaxial texture could further be detected for obliquely deposited Cr thin films, grown with the same experimental conditions as the above discussed columnar Mo thin films. The Cr{110} and Cr{200} IPPFs are measured by using the Bragg reflections $2\theta = 44.390°$ and $2\theta = 64.578°$ [184], respectively (see Figure 6.4 (a) and (b)). The intensity is depicted on a linear scale. The film thickness of the columnar Cr thin film is 1540 nm, determined from cross-sectional SEM images. Both pole figures show separated pole density maxima connected by a low-density ring, indicating a biaxial texture with fiber texture components.

The calculated pole figures are in good agreement with the measured pole figures. The [110] direction of the bcc Cr crystallites is tilted by an angle $\gamma_{[110]} = 27°$ away from the substrates normal (see Figure 6.4 (a)), which is nearly the angle that has been observed for the bcc Mo crystallites ($\gamma_{[110]} = 31°$). In contrast, the Cr columnar tilt angle measured from the cross-sectional SEM images is $\beta = 52 \pm 2°$, which is identical with the Mo columnar tilt angle (compare Figure 6.1). In conclusion, the tilt angle β is again not equal to the tilt of the crystallites [110] direction.

Additionally, the crystallographic alignment in the columnar thin films is expected to be influenced by the direction of the incoming particle flux [32] as well as by the surface self-diffusion [11, 32, 168], which are discussed in sections 6.2 and 6.3.

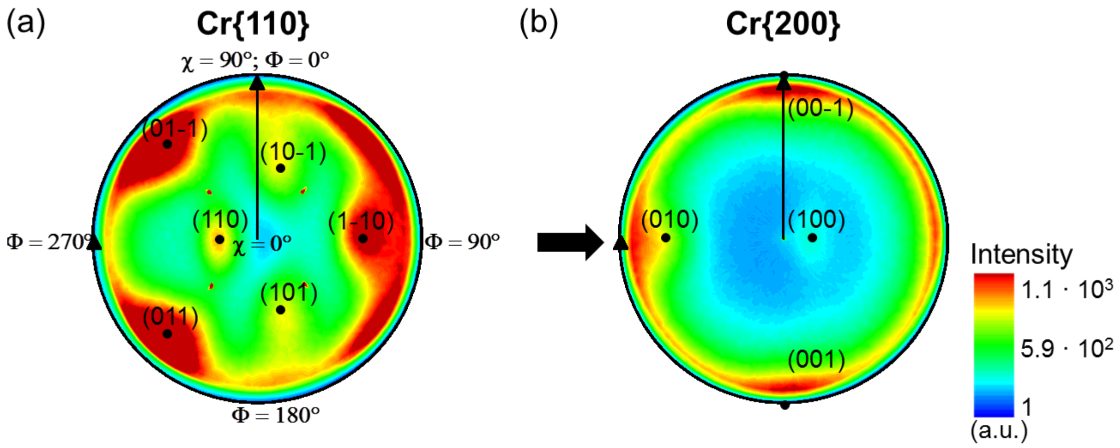

Figure 6.4: Overlay of measured and calculated in-plane pole figures for the bcc (a) Cr{110} and (b) Cr{200} reflections in a Cr thin film obliquely deposited at θ_{OAD} = 84° and 300 K. The intensity is depicted on a linear scale and applies for all measured pole figures. The black arrow in (b) indicates the direction of the incoming particle flux.

According to van der Drift [11], there are three factors that may introduce texture in a thin film: (i) preferentially oriented nucleation, (ii) post-deposition crystallization, and (iii) evolutionary or competitive selection of initially random oriented nuclei. As known from the SAED measurements in subsection 5.1.1, the nucleation on the planar Si substrates is random. Post-deposition crystallization is also not appropriate, since post-deposition sample heating (annealing) has not been applied. Hence, the evolutionary selection process between initially randomly oriented crystallites on the substrates surface is assumed to be a major factor that causes the formation of the observed texture in the deposited columnar Mo thin films. The deposition has been carried out at RT ($T_H = 0.1$), indicating a limited surface self-diffusion. The adatoms will not be able to move to other crystal planes or nuclei, for instance, but the mobility is sufficient so that single crystalline nuclei can form. From subsection 5.1.1 is known that due to the dominating shadowing effect, the single crystalline structure is preserved as the nuclei develop further. During the competitive growth process, those nuclei / crystallites are selected that exhibit planes with a favorable angle γ towards the incoming particle flux. In this case, “favorable” means that the planes are tilted towards the incoming flux so that they can capture a maximal amount of material. Consequently, among the initially random oriented crystallites some will grow faster in height than other crystallites for equal deposition times and deposition rates. A simplified, qualitative illustration of this process can be found in Figure 6.5. The growing plane of the right crystallite captures less material so that this crystallite continuously becomes shadowed by the left crystallite. This results in the formation of a V-shaped form, before the right crystallite is completely in the shadow of the left crystallite and stops growing. Consequently, there is an anisotropy of growth rates of the crystallites caused by the different alignment (γ-angles) of the planes towards the incoming particle flux. This anisotropy leads to a selection of crystal orientations that ensures a maximal vertical growth component. The selection process intrinsically proceeds with increasing film thickness so that the distribution of crystal orientations in the growing film becomes continuously narrowed down, which has previously been observed as the evolving biaxial texture of columnar Mo thin films.

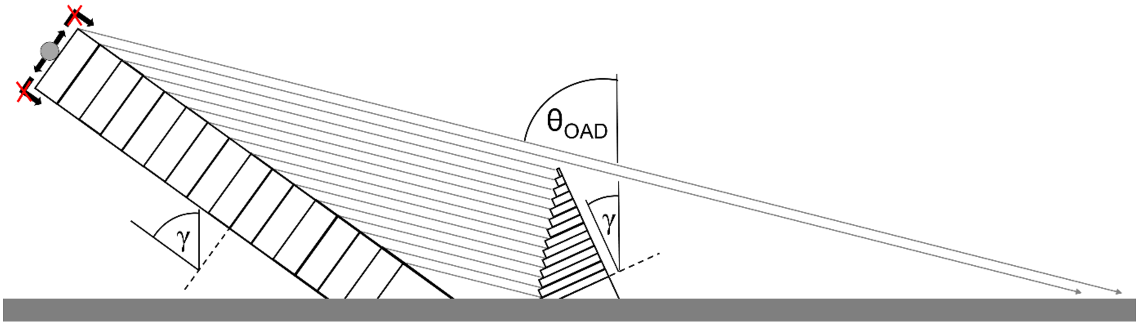

Figure 6.5: Schematic illustration of tilted metallic crystallites grown on an amorphous SiO_2 substrate at a highly oblique angle θ_{OAD}. The adatom mobility is restricted to a particular lattice plane. The crystallites are tilted by an angle γ. All angles are measured with respect to the substrate normal. The shadowed areas are shaded.

In the following, a rough estimation is derived that allows to approximate the γ-angles that lead to a maximal vertical growth. As discussed in section 5.3, the mobility of the Mo adatoms is sufficiently high for deposition at RT so that the shape (facets) of all these nuclei is defined by the planes with the lowest surface energy. In bcc crystals such as Mo and Cr, the {110} plane is the thermodynamically favored crystal plane. For vertical deposition ($\theta_{OAD} = 0°$), a crystalline layer with growth direction along a <110> direction is forming. From the IPPFs is known that the [110] direction is tilted by an angle $\gamma_{[110]}$ with respect

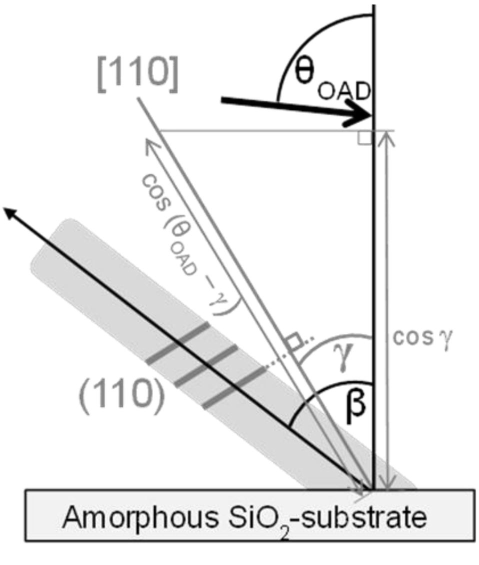

Figure 6.6: Schematic illustration of a tilted Mo column grown on an amorphous SiO_2 substrate at an oblique angle $\theta_{OAD} = 84°$. The column is tilted by an angle β and the [110] direction of the bcc Mo crystallites is inclined by an angle $\gamma_{[110]}$. All angles are measured with respect to the substrate normal.

to the substrate normal. Since $\gamma_{[110]} \neq \theta_{OAD}$, the amount of material flux (particles per unit area) reaching the (110) plane is reduced by the factor cos ($\theta_{OAD} - \gamma_{[110]}$). The crystal growth along [110] is accompanied by a growth along the substrate normal, which results in a further reduction by the factor cos ($\gamma_{[110]}$). These geometrical considerations are illustrated in Figure 6.6. According to the evolutionary selection process introduced by van der Drift [11], only the crystallites with the fastest vertical growth component will be successful in the competitive growth process. This would be realized if the product (cos (γ) · cos ($\theta_{OAD} - \gamma$)) becomes maximal, indicating that $\gamma = ½ \cdot \theta_{OAD}$ [11].

For $\theta_{OAD} = 84°$ this leads to a prediction of $\gamma_{[110]} = 42°$, which is in the same order of magnitude as the measured value of $\gamma_{[110]} = 31°$ for the tilted Mo columns and $\gamma_{[110]} = 27°$ for the tilted Cr columns. Indeed, there is a difference between the predicted and measured angle of 11° (Mo) and 15° (Cr). This difference is assumed to be due to the fact that the prediction is exclusively based on geometrical considerations. To conclude, the Mo and Cr bcc crystallites grow along the thermodynamically favored [110] direction, but only those with an tilt angle $\gamma_{[110]}$ that results in a maximized vertical growth will be successful in the competitive growth.

This is in contrast to Chen *et al.* [176], who reported about a biaxially textured Mo thin film grown by DC magnetron sputter deposition at RT and $\theta_{OAD} = 85°$. The largest Mo columns are reported to have the {111} plane oriented towards the incoming particle flux. This might be due to the magnetron sputtering process, since sputtered particles have much higher kinetic energies compared to evaporated particles and sputtered particles might collide with each other or with particles in the plasma, which can cause a change in momentum vector of the incident particles [185, 186].

Concluding, the highly oblique particle incidence (shadowing) as well as the substrate temperature (adatom mobility) are key parameters if columnar thin films with a biaxial texture are to be realized. The influence of those two parameters on the texture formation is therefore investigated in more detail in sections 6.2 and 6.3 exemplarily for columnar Ti thin films. Besides, the observation that the tilt angle $\gamma_{[110]}$ of the [110] direction is not equal to the tilt angle β of the Mo columns is further investigated and discussed in section 6.2.

6.2 Influence of the incoming flux direction

In the previous chapter 5 has been outlined that Ti columns deposited with an incidence angle $\theta_{OAD} = 84°$ at RT on natively oxidized Si(100) substrates exhibit a single crystalline structure (see Figure 6.7, for example). As can be determined from the HRTEM images (I, II) in Figure 6.7, the parallel oriented lattice planes exhibit a lattice spacing of 0.233 nm, thus indicating a c-axis oriented column. From the TEM measurements it is not possible to determine the tilt $\gamma_{[0001]}$ of the Ti c-planes with respect to the substrates normal (see Figure 6.7 (b) for visualization), but XRD measurements such as IPPFs have been shown to be a

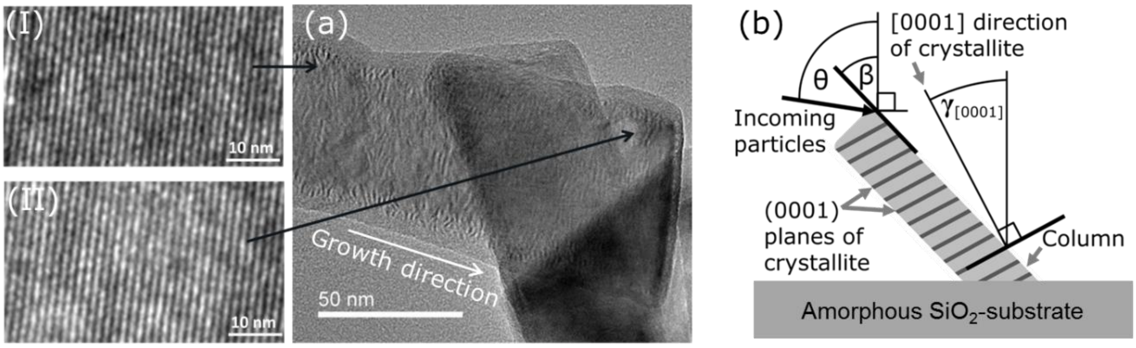

Figure 6.7: (a) HRTEM overview image, and (I, II) magnified HRTEM images of tilted Ti columns deposited at $\theta_{OAD} = 84°$ and at RT. (b) Illustration of an obliquely deposited tilted Ti column on an amorphous substrate at RT. The angle of incidence θ_{OAD}, the columnar tilt angle β and the tilt angle of the [0001] lattice planes $\gamma_{[0001]}$ are all measured with respect to the substrate normal.

suitable tool to gain information about this γ-angle (compare section 6.1). Based on XRD measurements, the influence of the incidence flux direction on the tilt angle $\gamma_{[0001]}$ is investigated in this section.

Ti thin films are deposited at RT with a constant deposition rate $r = 1$ nm/s. Thermally oxidized Si(100) pieces with 800 nm thick oxide layer are used as substrates. The direction of the incoming particle flux is varied between $\theta_{OAD} = 70°$ and $\theta_{OAD} = 84°$. The film thickness expected for vertical deposition ($\theta_{OAD} = 0°$) is 4 µm for all films (measured by the quartz crystal micro balance), meaning that the same amount of material is evaporated to grow each of the investigated columnar Ti thin films. The experimentally achieved film thicknesses for the incidence angle $70° \leq \theta_{OAD} \leq 84°$ could then be determined directly from the cross-sectional SEM images and are found to vary between approximately 1700 nm to 2500 nm (compare Figure 6.8). During deposition, the work pressure has been $p_{Work} \sim 1 \cdot 10^{-8}$ mbar. Due to getter effects, this pressure is lower than the base pressure of $p_{Base} \sim 3 \cdot 10^{-8}$ mbar.

The cross-sectional and top-view SEM images in Figure 6.8 show the columnar Ti thin films grown at $70° \leq \theta_{OAD} \leq 84°$. All deposited thin films consist of separated columns that are inclined towards the incoming particle flux direction. For less oblique deposition angles, the shadowing length is decreased, resulting in the bundling of several columns [18, 22, 31, 116] as well as in an enlarged total number of growing columns per unit area.

IPPF measurements are carried out to determine the texture of the columnar Ti thin films. The samples are aligned in the XRD goniometer so that $\Phi = 270°$ corresponds to the direction of the incoming particle flux (see black arrows in Figure 6.9 (g) and (h)). The calculated pole figures for a Ti single crystal tilted by $\gamma_{[0001]} = 36°$ are presented in Figure 6.9 (a) and (b) [161]. The Ti{0002} and Ti{10-10} IPPFs are measured by using the Bragg reflections $2\theta = 38.421°$ and $2\theta = 35.093°$, respectively [187]. The diffracted intensity of the measured pole figures is depicted on a linear scale and applies for all measured pole figures (Figure 6.9 (c) – (h)).

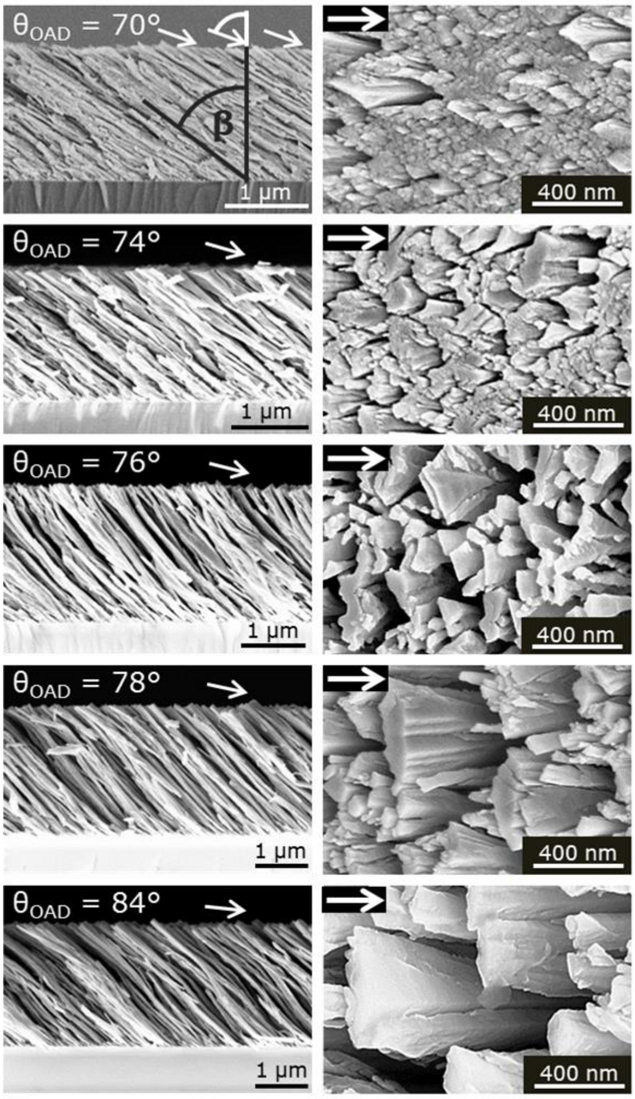

Figure 6.8: Cross-sectional and corresponding top-view SEM images of tilted Ti columns deposited at room temperature on thermally oxidized Si(100) substrates. The angle of the incoming particle flux θ_{OAD} is varied between 70° and 84°. The white arrows illustrate the direction of the incoming particle flux. The tilt angle of the column is represented by β. Both angles are measured with respect to the substrate normal.

Figure 6.9 (c) and (d) present the pole figures of the Ti{0002} and Ti{10-10} Bragg reflections for a Ti thin film deposited at θ_{OAD} = 78°, respectively. In Figure 6.9 (c), a pole density maximum at Φ = 270° and χ = 40° can be obtained. This indicates that the c-axes of the hcp Ti crystallites are oriented towards the direction of the incoming particle flux and thus towards the growth direction of the columns, which is typical for hcp crystals. In addition, four pole density maxima (0-110), (1-100), (10-10), and (01-10) can clearly be distinguished in Figure 6.9 (d). These four pole density maxima represent four of the in total six m-planes of the hcp unit cell. The remaining two pole density maxima cannot be seen, because the crystallites are tilted by an angle γ away from the substrate normal so that these two reflections are not in the upper hemisphere above the sample during IPPF measurements. The broad, but clearly separated pole figure measurements in Figure 6.9 (c) and (d) reveal that the orientation of the c-axes of the hcp crystals is constrained in polar direction and that the m-planes are additionally constrained in azimuthal direction. Thus, the Ti thin film exhibits a biaxial texture. Further, a homogenous low-density ring connection of the four pole density maxima can be seen in Figure 6.9 (d). This means that there is a fraction of crystallites that are randomly oriented around the c-axes. In summary, a biaxial texture with minor fiber contribution is observed for the Ti thin film grown at θ_{OAD} = 78°.

Comparing calculated (Figure 6.9 (a) and (b)) and measured (Figure 6.9 (c) and (d)) pole figures shows that there is a good match. Pole figure measurements have also been performed for Ti thin films deposited at $\theta_{OAD} = 84°$ (not shown here). For those films, a biaxial texture with fiber contribution could be obtained as well.

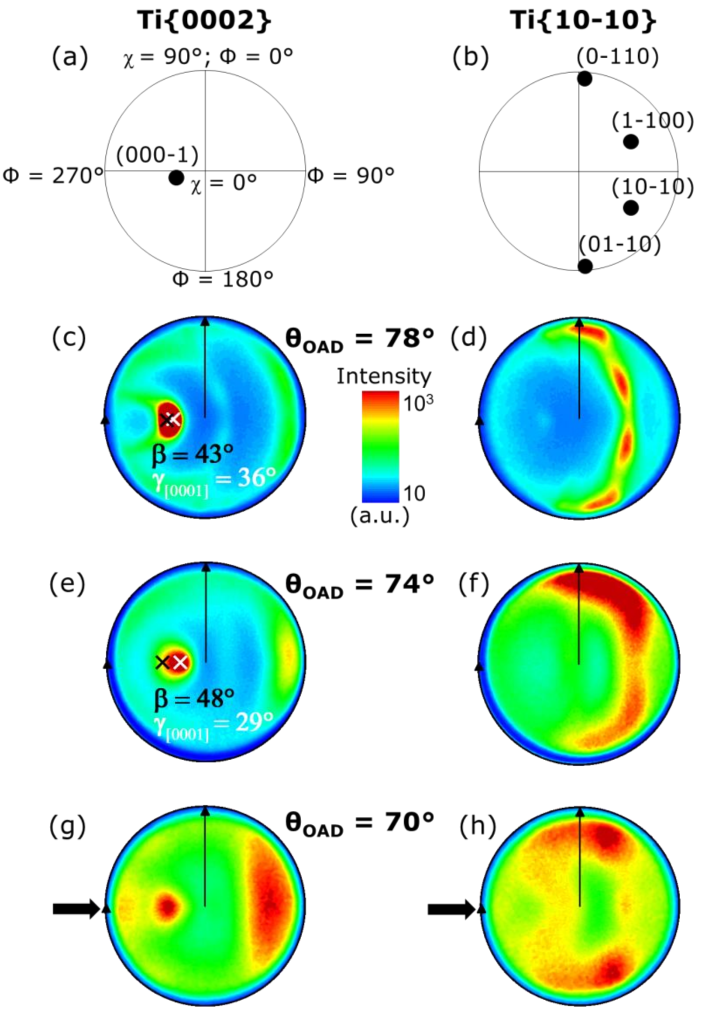

Figure 6.9: Theoretical expected pole figures for the hcp (a) Ti{0002} and (b) Ti{10-10} planes for a single crystal, tilted by $\gamma = 36°$ [161]. Measured in-plane pole figures for the hcp Ti{0002} and Ti{10-10} planes in an obliquely deposited Ti thin film at 300 K: (c, d) $\theta_{OAD} = 78°$; (e, f) $\theta_{OAD} = 74°$; (g, h) $\theta_{OAD} = 70°$. The black and the white cross in (c, e) correspond to the tilt angle β of the column and the tilt angle of the crystallite planes $\gamma_{[0001]}$ in the column, respectively. Both angles are measured with respect to the substrate normal. The black arrows in (g, h) indicate the direction of the incoming particle flux.

The pole figures for the Ti{0002} and Ti{10-10} Bragg reflections for a Ti thin film deposited at $\theta_{OAD} = 74°$ and $\theta_{OAD} = 70°$ are illustrated in Figure 6.9 (e) and (f) as well as in Figure 6.9 (g) and (h), respectively. As can be seen from Figure 6.9 (e), two pole density maxima at ($\Phi = 270°$, $\chi = 30°$) and ($\Phi = 90°$, $\chi = 80°$) can be distinguished. The occurrence of two pole density maxima indicates that there are two texture components, meaning that there are two fractions of crystallites with similar orientation each. For the first component ($\Phi = 270°$, $\chi = 30°$), the crystallites c-axis is aligned towards the particle flux direction. In contrast, for the second component ($\Phi = 90°$, $\chi = 80°$), the c-axis points away from the incident flux direction. Figure 6.9 (f) shows a broad density ring with smeared pole density maxima, revealing a decreased confinement of the m-planes in azimuthal direction. Thus, for the Ti thin film deposited at $\theta_{OAD} = 74°$, mainly a fiber texture can be observed. Nevertheless, the confinement of the hcp crystallites in azimuthal direction has already begun and is intensified with more oblique deposition angles.

Two pole density maxima at ($\Phi = 270°$, $\chi = 42°$) and ($\Phi = 90°$, $\chi = 67°$) can also be distinguished in Figure 6.9 (g). Thus, there is a crystal component with the c-axis tilted away from the particle flux in addition to a crystal component with the c-axis pointing in the incident flux direction. However, the SEM images indicate that the columns still grow towards the particle flux. As the growth direction of the columns is not preferably along the c-axis anymore, other growth directions must be present. Moreover, Figure 6.9 (h) shows broad intensity rings, but pole density maxima cannot be identified. This suggests that for deposition at $\theta_{OAD} = 70°$, the m-planes are even more randomly oriented in azimuthal direction compared to $\theta_{OAD} = 74°$. This is also in contrast for deposition at $\theta_{OAD} = 78°$, where a biaxial texture could be observed. In summary, for deposition at $\theta_{OAD} \geq 78°$, a biaxial texture with preferred growth direction along the c-axis is observed, while for $\theta_{OAD} < 78°$ fiber texture contributions become more dominate and the orientation of the c-axes of the crystallites towards the incoming particle flux vanishes. The 800 nm thick thermal oxide layer on the Si(100) substrate avoids any epitaxial relationship between the Ti columns and the substrate. This is in contrast to Sagedhi-Khosravieh and Robbie [16], who used natively oxidized Si-substrates for their experiments and who found an biaxial texture already for an incidence angle of $\theta_{OAD} = 60°$. Reasons for this might be caused by differences concerning the deposition rate, the working pressure, the used types of substrates, or the composition of the residual gas, for instance.

The pole density maxima in Figure 6.9 (c), (e), (g) are separated, but also broadened, meaning that there is an extension in polar and azimuthal direction. Such a broadening in polar direction indicates that the orientation of the c-axes of the hcp crystallites is distributed in polar direction. This distribution is investigated in more detail by χ-scans for the Ti(0002) reflection. For this purpose, χ is varied between –90° to +90°, while keeping Φ constant. Hence, such χ-scans can be viewed as a “cut” through the pole figures (see Figure 6.9 (c), (e), (g)).

Figure 6.10 (a) depicts the χ-scans for Ti thin films grown at $\theta_{OAD} = 70°$, 74°, 76°, and 78°, respectively. Gaussian functions are applied to approximate the maxima of the χ-scans. The maxima correspond to the tilt of the c-axis $\gamma_{[0001]}$ with respect to the substrate normal. The full width at half maximum (FWHM) indicate the distribution of the c-axes orientations in χ-direction. As the angle of the incoming particle flux becomes more oblique, (i) the maximum of the peaks ($\gamma_{[0001]}$) is shifted, and (ii) the FWHM is lowered from FWHM = 32° for $\theta_{OAD} = 74°$ to FWHM = 14° for $\theta_{OAD} = 78°$. This reveals that the confinement of the c-axes is increased with more oblique deposition angles. For steeper incident angles, this confinement vanishes, and other growth directions become more dominant.

To study this further, θ-2θ X-ray diffraction patterns are measured for particular χ-angles ($\gamma_{[0001]}$), i.e. in the center of the dominant pole density maximum of the corresponding Ti{0002} pole figure. The resulting θ-2θ X-ray diffraction patterns for Ti thin films deposited at $\theta_{OAD} = 70°$, 74°, 76°, and 78° are depicted in Figure 6.10 (b). For $\theta_{OAD} = 76°$ and 78°, only two sharp peaks at $2\theta = 38.4°$ and $2\theta = 82.5°$ can be detected,

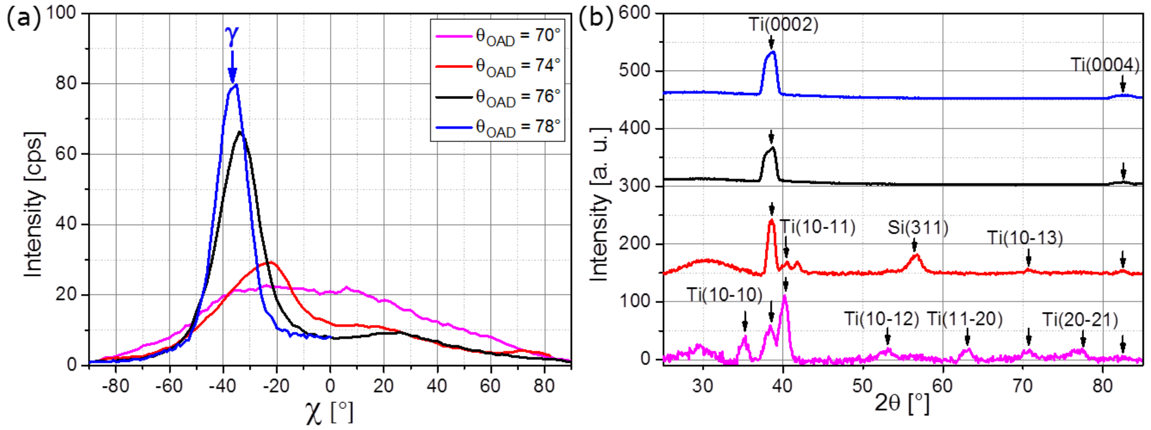

Figure 6.10: (a) χ-scans of the Ti(0002) reflections of thin films deposited at θ_{OAD} = 70°, 74°, 76°, and 78° at RT on thermally oxidized Si(100) substrates, respectively, and (b) θ-2θ X-ray diffraction patterns measured at the obtained maximum position ($\gamma_{[0001]}$) of each χ-scan.

corresponding to the first and second order Ti(0002) reflections. For less oblique deposition (θ_{OAD} = 74°), the reflections Ti(0002), Ti(10-11), and Ti(10-13) can be distinguished. Additionally to these reflections, Ti(10-10), Ti(10-12), Ti(11-20), and Ti(20-21) can be observed for deposition at θ_{OAD} = 70°. The intensity distribution of this θ-2θ X-ray diffraction pattern is similar to the intensity distribution that is expected for a Ti powder diffraction pattern [187]. The broad peak at 2θ = 30.2° originates from the oxide layers on the Ti columns and on the Si(100) substrate. It can be noted that the θ-2θ X-ray diffraction patterns confirm the decreased confinement of the $\gamma_{[0001]}$-angles with less oblique deposition geometry.

From the pole density maxima in Figure 6.9 (c), the angle between the c-direction of the hcp-crystallites and the substrates normal $\gamma_{[0001]} = 36°$ for $\theta_{OAD} = 78°$ can be derived. The corresponding tilt angle β of the Ti column with respect to the substrate normal is determined from the cross-sectional SEM images $\beta = 43° \pm 2°$. Thus, there is a difference between both angles $\Delta = \beta - \gamma = 7°$ for a Ti thin film grown at θ_{OAD} = 78°. In contrast, this difference is $\Delta = 48° - 29° = 19°$ for deposition at θ_{OAD} = 74°, which is approximately a three times higher value.

The influence of the angle of the incoming particle flux ($76° \leq \theta_{OAD} \leq 88°$) on the tilt angle $\gamma_{[0001]}$ and on the tilt angle β of the Ti column is studied in more detail in Figure 6.11. Three observations can be made. Firstly, the tilt angle of the columns β is not equal to the $\gamma_{[0001]}$ angle, and secondly, both angles are enlarged as the incoming particle flux becomes more oblique. Finally, the measured $\gamma_{[0001]}$-angles in Figure 6.11 (a) are in good agreement with the predicted $\gamma_{[0001]}$-angles for maximized vertical growth: $\gamma = ½ \cdot \theta_{OAD}$ (see dotted blue line), which has been deduced in the previous section.

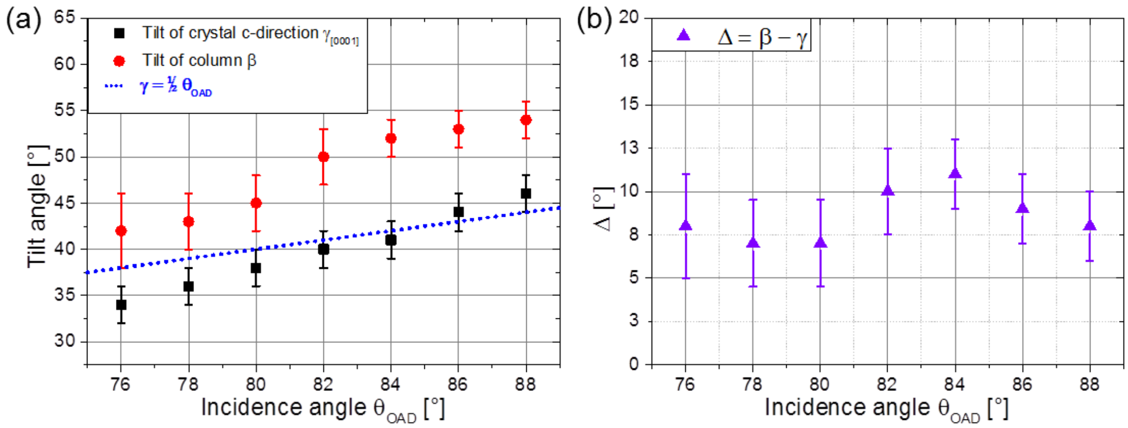

Figure 6.11: (a) Tilt angle of the c-axis of the hcp crystallites $\gamma_{[0001]}$ and tilt angle β of a Ti column obliquely deposited at RT for varying angles of the incoming particle flux θ_{OAD}. All angles are measured with respect to the substrate normal. (b) Difference Δ between β and $\gamma_{[0001]}$ depending on θ_{OAD}.

This observation provides additional evidence for the argumentation that during growth those crystallites are selected that tend to grow with an angle $\gamma_{[0001]}$ so that their vertical growth component is maximized. Since deposition is carried out at RT (T_H(Ti) = 0.15), adatom mobility is on the one hand sufficiently high so that randomly oriented crystalline nuclei can form at the beginning of the growth. On the other hand, the mobility is limited, meaning that the Ti adatoms are not expected to be able to move to other nuclei or columns. Hence, those crystal planes will grow fastest in height compared to all other orientations that are inclined towards the incoming particle flux so that the amount of captured material is maximized (compare also Figure 6.5). Accordingly, a more oblique incidence angle will favor the growth of crystallites with c-axes tilted more towards the incoming flux direction (larger tilt angles $\gamma_{[0001]}$). Thus, the incident particle flux direction triggers the selection of crystallites with preferably $\gamma_{[0001]}$-angles among initially randomly oriented crystallites (nuclei). Furthermore, this selection process proceeds faster for more oblique deposition angles due to the enlarged shadowing length. For the investigated Ti samples deposited each with the same amount of material during the same period of time, the evolutionary selection process is more advanced for more oblique angles. Accordingly, a narrowed distribution of $\gamma_{[0001]}$-angles is present for more oblique angles, explaining the decreased FWHM of the χ-scans and the exclusive occurrence of the Ti(0002) reflection in Figure 6.10. As the incident angle becomes less oblique, the shadowing length is reduced, leading to a larger variety of $\gamma_{[0001]}$-angles, and consistently to a decreased azimuthal alignment of the c-axes of the hcp crystallites. This decreased azimuthal alignment is the reason for the observed fiber texture of the columnar Ti thin films. For more oblique incident angles the $\gamma_{[0001]}$-angles become more confined as a result of the competitive growth process, resulting in a biaxial texture. In summary, exemplarily for columnar Ti thin films deposited at RT has been demonstrated that for such a constant substrate temperature the variation of the incidence particle flux direction can be used to influence the texture.

In the following, it is discussed why the tilt angle of the column β is not equal to (larger than) the $\gamma_{[0001]}$-angle. Due to the shadowing effect, the atoms on the layers in the column become shadowed as the growth process proceeds, which is schematically illustrated in Figure 6.12 (a) and (b). The layers are shown in grey, and the shadowed areas are shaded. As deposition is performed at highly oblique angles, a particle arriving at the growing crystal plane (growth zone) cause the creation of a shadowed area. In Figure 6.12 (a), the particle in blue color prevents the condensation of later arriving particles in the shadowed area projected behind this particle. Thereby, the layer grows shortened compared to the underlying layer in the direction of the incoming particle flux so that a step-like structure evolves. Towards the incoming particle flux direction, the growth of the layer is completed by the particle in red, which forms an overhang structure. This overhang stops to develop as the shadowed region created by the blue particle of the before standing crystallite is reached (compare (II) and (III)). Finally, a tilted column composed of layers is formed (see Figure 6.12 (b)). Notice that the effect will not be as regular as suggested by Figure 6.12. Moreover, if surface diffusion is strong enough, a single particle cannot prohibit that another particle will move in its shadow, because the new particle might diffuse around the already deposited particle. However, the probability of becoming deposited in a shadowed area is decreased with the same consequences. Besides, the shadowing of the layers in the column is a process based on a large number of particles. Each of those processes is expect to be individual regarding the particle divergence and the resulting shadowing effect, but on average it is assumed that the shadowing of the layers in the column will follow the principle indicated in Figure 6.12.

From Figure 6.11 (b) can further be deduced that the difference Δ between both angles is $\Delta = \beta - \gamma_{[0001]} \sim 9°$, so Δ is kept approximately constant as the incidence angle is varied between $76° \leq \theta_{OAD} \leq 88°$. As the IPPF measurements in Figure 6.9 have shown, for $\theta_{OAD} < 76°$, this difference becomes larger, e.g. $\Delta = 19°$ for $\theta_{OAD} = 74°$ and $\Delta = 18°$ for $\theta_{OAD} = 72°$, which can be attributed to the larger variation of the $\gamma_{[0001]}$-angles caused by the reduced shadowing effect obtained for steeper deposition geometries.

The observation that the lattice planes in the columns are not necessarily aligned with the tilt angle of the columns has already been shown for Co/Pt multilayer thin films, for instance [167]. In addition, the investigations of Morrow *et al.* [157] as well as Alouach and Mankey [188, 189] indicate that varying the angle of the incoming particle flux can be used to influence the crystallographic orientation of individual columns. In contrast to that, Hagemeyer [166] reported that the c-axis of Co-Cr magnetic thin films is always aligned with the columnar growth direction, indicating a strong material dependent component for the texture formation.

To sum up, among initially randomly oriented Ti crystallites those are selected that grow with an angle $\gamma_{[0001]}$ that ensures the maximal vertical growth component, but shadowing finally defines the tilt angle β of the column. Consistently, the β-angle is always larger than the $\gamma_{[0001]}$-angle, which has also been observed in section 6.1 for tilted Mo and Cr columns.

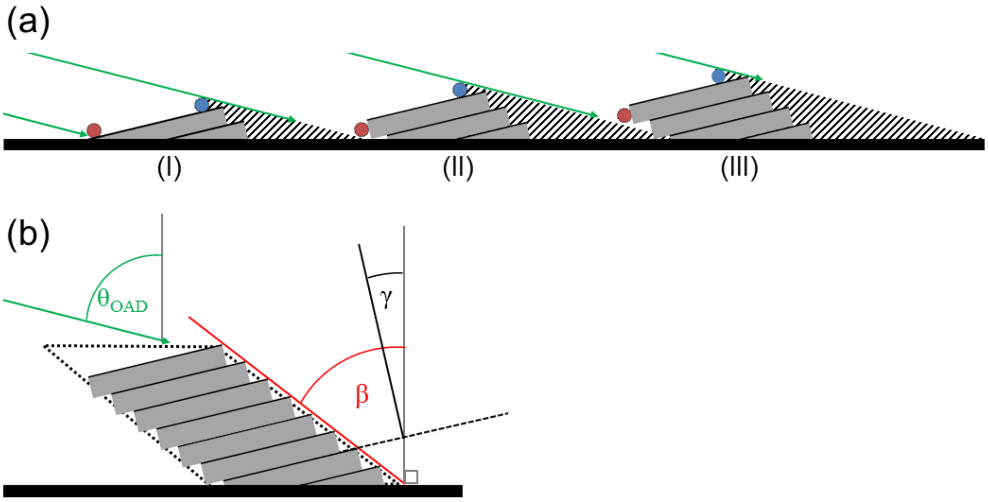

Figure 6.12: (a) Schematic to illustrate the shadowing of the layers in a column and the resulting formation of the columnar tilt angle β for highly oblique incidence angles θ_{OAD} (green arrow, I – III). Shadowed areas are shaded. Behind the particle in blue color, the following particles cannot condense caused by shadowing. The red particle denotes the particle that completes a growing layer, thereby forming an overhang structure. For more explanation see text. (b) Schematic to illustrate the geometric relations of the tilt angle β, tilt of the crystallites direction γ, and incidence angle θ_{OAD} on a tilted column composed of lattice planes. All angles are measured with respect to the substrate normal. The resulting shape of the column is indicated by the dotted envelope.

If the substrate is rotated continuously around its normal, the direction of the incoming particle flux from the perspective of the growing columns changes, which provides an additional degree of freedom for influencing the texture of the resulting columnar thin film. This is demonstrated exemplarily for columnar Ti and Cr thin films that are grown on thermally oxidized Si(100) substrates with a 800 nm thick oxide layer at RT. The angle of the incoming particle flux is $\theta_{OAD} = 84°$ and the deposition rate is constant at $r = 1$ nm/s. During deposition, the substrate is rotated continuously with $\omega = 10$ rpm. The incident flux directions are indicated by the black arrows in the IPPF shown in Figure 6.13 (d). Top-view and cross-sectional SEM images are depicted exemplarily for vertical Ti columns in Figure 6.13 (a) and (b). The film thickness is 1850 nm for the Ti thin films, and 750 nm for the Cr thin film. IPPFs are carried out by using the Bragg reflections $2\theta = 38.421°$ and $2\theta = 35.093°$ for the Ti{0002} and Ti{10-10} IPPFs [187] as well as $2\theta = 44.390°$ and $2\theta = 64.578°$ for the Cr{110} and Cr{200} IPPFs [184], respectively. Notice that there is no central pole density maximum in the IPPFs shown in Figure 6.13 (c) – (f). The sharp peaks in Figure 6.13 (e) originate from the Si(100) substrate. In all measured IPPFs, several concentric density rings can be detected, indicating that the azimuthal confinement of the crystallographic directions is lost. Because deposition is carried out at RT, it is again assumed that randomly oriented, crystalline nuclei are formed at the substrate surface.

During growth, those planes that capture the largest amount of material will exhibit the fastest vertical growth component and are selected. Since the incident flux direction is not fixed, there is no selection and thus no alignment of the crystallites in azimuthal direction. In conclusion, a fiber texture can be expected. This is in contrast to deposition on stationary substrates, which results a biaxial texture as outlined previously. The discussion is analogous for vertical Cr columns, which grow along the [110] direction (see subsection 5.2.1). Concluding, substrate rotation provides an additional parameter that influences the texture of a columnar thin film.

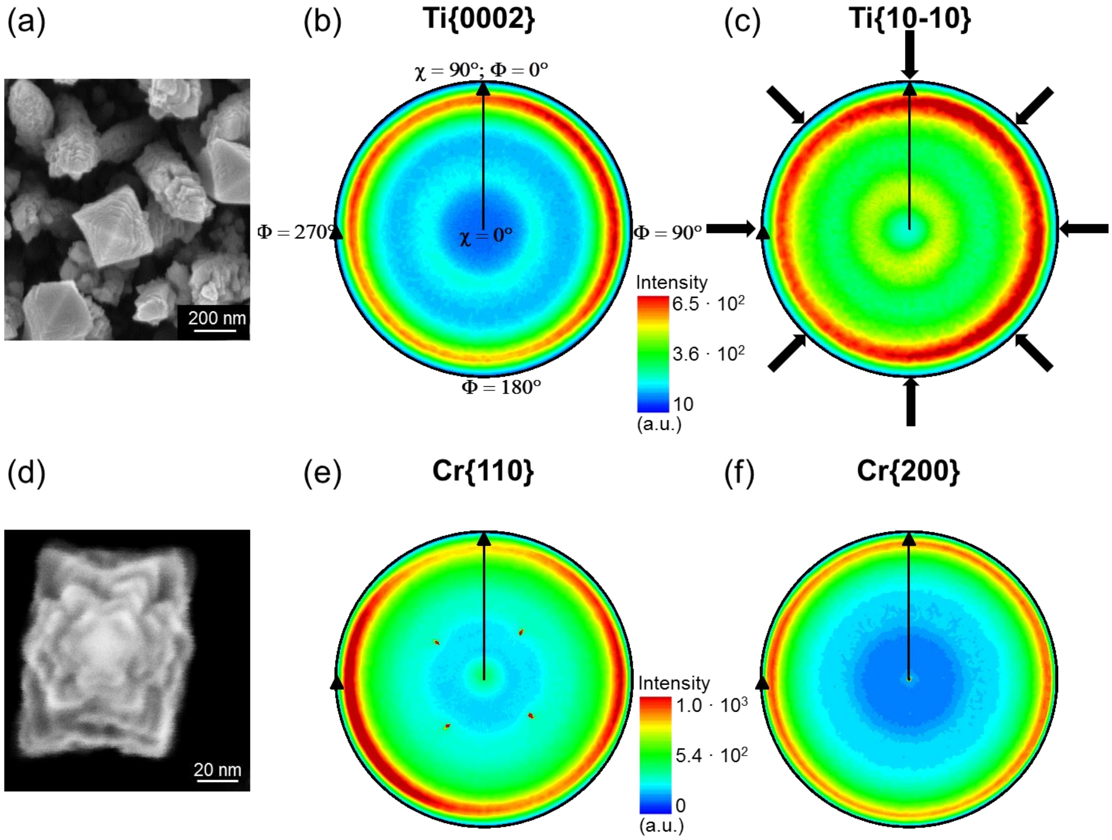

Figure 6.13: (a) Top-view SEM image of a columnar Ti thin film deposited at $\theta_{OAD} = 84°$ with continuous substrate rotation of $\omega = 10$ rpm at RT on thermally oxidized Si(100) substrate. (b) and (c) Corresponding measured IPPFs for the hcp Ti{0002} and Ti{10-10} planes, respectively. The direction of the incoming particle flux is represented by the black arrows in (c). (d) Top-view SEM image of a columnar Cr thin film deposited at $\theta_{OAD} = 84°$ with continuous substrate rotation of $\omega = 10$ rpm at RT on thermally oxidized Si(100) substrate. (e) and (f) Corresponding measured IPPFs for the bcc Cr{110} and Cr{200} planes, respectively. The intensity is on a linear scale.

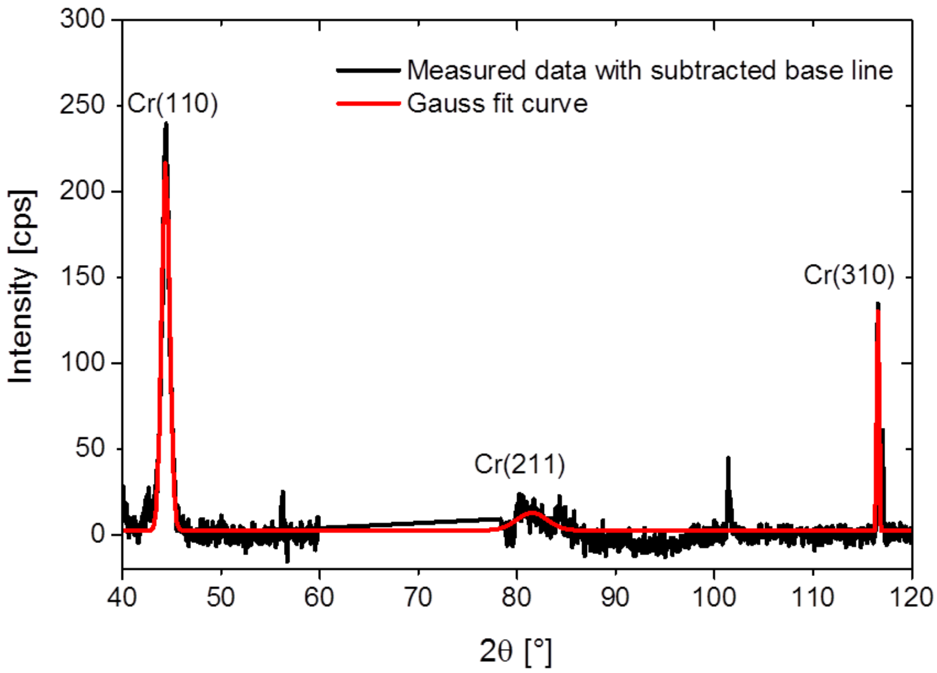

Figure 6.14: (a) θ-2θ X-ray diffraction pattern of a columnar Cr thin film deposited at θ_{OAD} = 84° with ω = 10 rpm and RT on thermally oxidized Si(100) substrates.

Exemplarily for the thin film composed of vertical Cr columns, a θ-2θ X-ray diffraction pattern can be seen in Figure 6.14. Measured data are not depicted for $60° \leq 2\theta \leq 78°$, because the high-intensity reflections from the substrate appear in this range. The area covered by the Cr(110), Cr(211), and Cr(310) reflections is calculated by Gaussian approximation and yield 217.15 cps·°, 39.96 cps·°, and 22.05 cps·°, respectively. This corresponds to an intensity distribution of 100:18.4:10.15, which is in contrast to the intensity distribution expected for a powder 100:30:20 [184]. As a result, a slightly preferred growth along the [110] direction is expected, which is in accordance with the HRTEM and SAED measurements carried out for vertical Cr columns as shown in subsection 5.2.1. Additionally, the θ-2θ X-ray diffraction pattern indicates the presence of further growth directions of the bcc crystallites in the vertical Cr columns. The occurrence of these directions might be explained by the evolutionary selection process that has not been proceeded sufficiently for a film thickness of 750 nm. As the selection process is correlated with the film thickness, further increasing film thickness is expected to select the columns that grow along [110], while the remaining columns stop developing. In summary, the direction of the incoming particle flux has profound impact on the texture of the investigated metallic thin films.

6.3 Influence of the substrate temperature

In section 4.1 has been demonstrated that surface self-diffusion has significant impact on the columnar shape, the columnar tilt angles as well as on the porosity of the obliquely deposited, metallic thin films. In this section, the influence of surface self-diffusion is analyzed with view to the texture of the obliquely deposited thin films [LIE05]. The texture is studied exemplarily for columnar Ti thin films grown at substrate temperatures varying between 77 K $\leq T_{Sub} \leq$ 873 K. Further, the impact of substrate temperature on the orientation of the Al crystallites in columnar Al thin films grown at 77 K and 300 K is investigated. For all experiments in this section, the angle of the incoming particle flux is kept constant at $\theta_{OAD} = 82°$ and thermally oxidized Si(100) pieces with a 800 nm thick oxide layer are used as substrates.

Columnar Ti thin films are grown at substrate temperatures varying between 77 K ($T_H = 0.04$) and 873 K ($T_H = 0.45$). The deposition rate is set to $r = 1$ nm/s. The film thickness calibrated for vertical particle incidence is 4000 nm for all samples so that for each sample the same amount of material is evaporated. The actual film thicknesses are determined by SEM (compare Figure 6.15).

To gain information about the texture of the columnar Ti thin films grown at different substrate temperatures, IPPF measurements are performed. As indicated by the black arrows in Figure 6.16 (g, h), the samples are aligned in the XRD goniometer so that $\Phi = 270°$ corresponds to the incident flux direction. The Bragg reflections $2\theta = 38.421°$ and $2\theta = 35.093°$ are used to detect the Ti{0002} and Ti{10-10} IPPFs, respectively [187]. The diffracted intensity of the measured pole figures is on a linear scale and applies for all measured pole figures (Figure 6.16 (a) – (h)). Figure 6.16 reveals that the IPPFs obtained for Ti thin films fabricated by the liquid nitrogen cooled sample holder (at T_{Sub} = 77 K) and those grown at elevated substrate temperatures (T_{Sub} = 485 K, 679 K, 873 K) differ

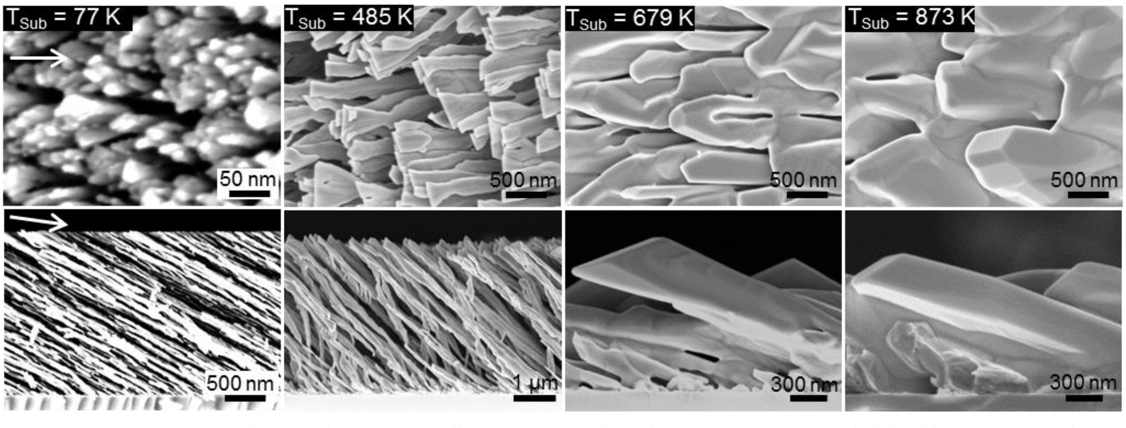

Figure 6.15: Top-view and corresponding cross-sectional SEM images of Ti thin films grown with an oblique angle of incidence $\theta_{OAD} = 82°$ and with substrate temperatures varying between 77 K and 873 K. The white arrows indicate the direction of the incoming particle flux.

significantly from the IPPFs obtained for Ti thin films grown at RT (compare Figure 6.9 (c, d)). Remember that a biaxial texture could clearly be detected for highly oblique incidence angles (θ_{OAD} = 78°, 84°) and deposition at RT.

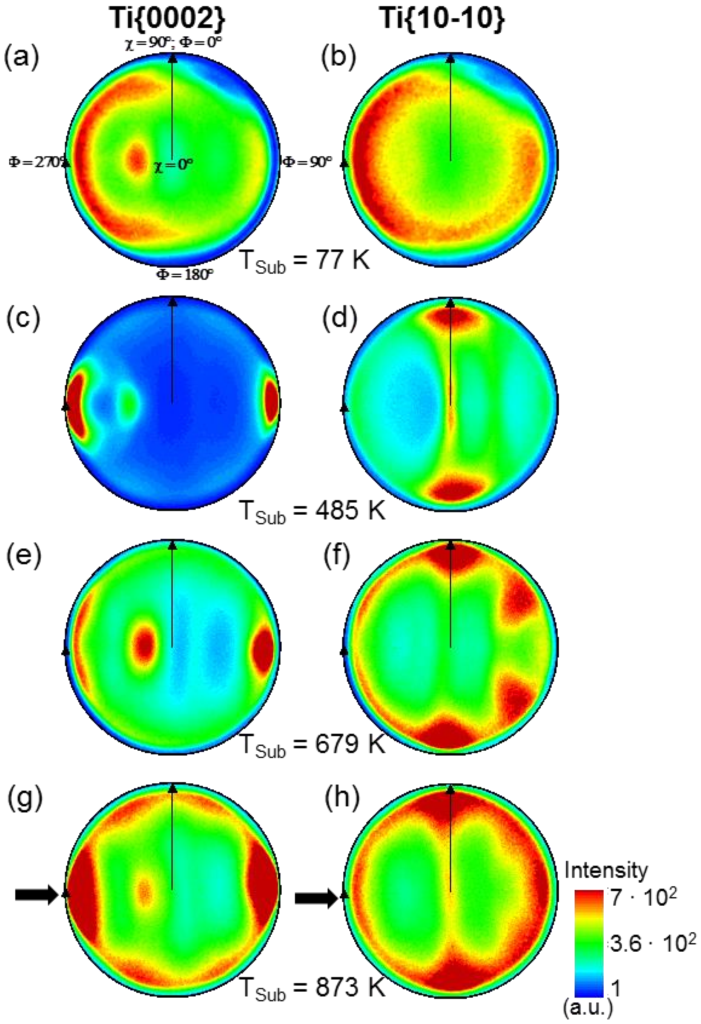

Figure 6.16: Measured in-plane pole figures for the hcp Ti{0002} and Ti{10-10} reflections in an obliquely deposited Ti thin film at θ_{OAD} = 82° and with varying substrate temperatures: (a) and (b) T_{Sub} = 77 K, (c) and (d) T_{Sub} = 485 K , (e) and (f) T_{Sub} = 679 K , (g) and (h) T_{Sub} = 873 K. The intensity is depicted on a linear scale and applies for all measured pole figures. The black arrows in (g) and (h) indicate the direction of the incoming particle flux.

However, this is not the case anymore as the substrate temperature is lowered to 77 K, as Figure 6.16 (a) and (b) indicate. Figure 6.16 (a) shows a pole density maximum at ($\Phi = 270°$, $\chi = 37°$), and additionally a density-ring can be obtained at (Φ = [65°, 0°], $\chi = 83°$). Hence, there are two components of crystallites present. For the first component, the hcp crystallites exhibit a c-axis pointing towards the direction of the incoming particle flux. Precisely, the crystallites c-axes are inclined by an angle of $\gamma_{[0001]} = 37°$ with respect to the substrate normal. Consequently, a confinement in polar direction exists, but the density ring in the pole figure depicted in Figure 6.16 (b) suggests that there is no confinement in azimuthal direction. So, the first component of crystallites is characterized by a fiber texture. For the second texture component, a fiber texture is given as well, because the crystallites c-axes are confined on a fixed polar angle $\chi = 83°$ around another virtual center. In conclusion, two fiber textures could be observed in the columnar Ti thin film deposited at 77 K.

At elevated substrate temperatures, density rings become less pronounced. Instead, well-separated pole density maxima are observed. For deposition at 485 K (Figure 6.16 (c)), three pole density maxima can be detected: ($\Phi = 270°$, $\chi = 45°$),

($\Phi = 270°$, $\chi = 88°$), and ($\Phi = 90°$, $\chi = 88°$). The crystallites represented by the first pole density maximum have a c-axis that is tilted by an angle of $\gamma_{[0001]} = 45°$ with respect to the substrate normal. In contrast, for the crystallites represented by the latter two pole density maxima, the c-axes can be viewed as aligned horizontally with respect to the substrate surface. The clearly visible pole density maxima connected by a low-density ring in Figure 6.16 (d) confirm the azimuthal confinement of the m-axes of the hcp crystallites.

Three pole density maxima can also be distinguished in Figure 6.16 (e) for deposition at 679 K: ($\Phi = 270°$, $\chi = 28°$,), ($\Phi = 270°$, $\chi = 88°$), and ($\Phi = 90°$, $\chi = 88°$). A comparison between these pole density maxima with the pole density maxima in Figure 6.16 (c) leads to the following observations. Firstly, the tilt of the crystallites c-axes for the first crystal component changes from $\gamma_{[0001]} = 45°$ to $\gamma_{[0001]} = 28°$ as the substrate temperature is increased. Secondly, the c-axes of the second and third crystal component are aligned parallel to the substrate surface, but the angular distribution in azimuthal direction becomes broader with increasing substrate temperature. This azimuthal distribution is not random, since four separated pole density maxima can clearly be distinguished in Figure 6.16 (f) at ($\Phi = 0°, 55°, 125°, 180°$; $\chi = 88°$). Additionally, these pole density maxima are connected by a low-density ring. In conclusion, a biaxial texture with fiber contribution is observed for deposition at 485 K and 679 K.

The IPPFs obtained for deposition at 873 K substrate temperature are shown in Figure 6.16 (g, h). The pole density maximum at ($\Phi = 270°$, $\chi = 29°$) represents the component of crystallites whose c-axes are inclined by an angle of $\gamma_{[0001]} = 29°$ away from the substrate normal. The remaining six pole density maxima at ($\Phi = 20°, 90°, 149°, 200°, 270°, 332°$; $\chi = 88°$) represent c-axes that are aligned nearly parallel to the substrate surface. Notice that the pole density maxima in Figure 6.16 (h) are remarkably extended in azimuthal direction,

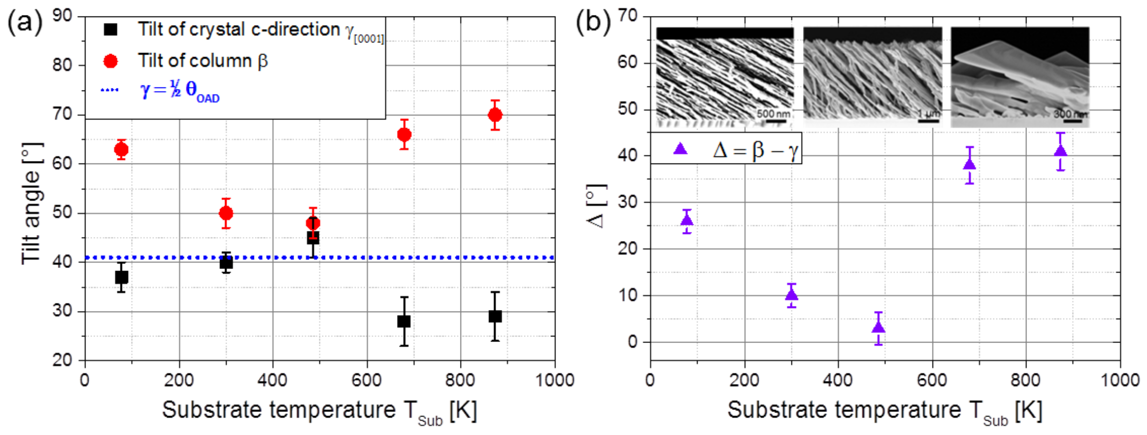

Figure 6.17: (a) Tilt angle of the c-axis of the hcp crystallites $\gamma_{[0001]}$ and tilt angle β of Ti columns obliquely deposited at an angle of the incoming particle flux $\theta_{OAD} = 82°$ for varying substrate temperatures T_{Sub}. All angles are measured with respect to the substrate normal. (b) Difference Δ between β and $\gamma_{[0001]}$ depending on T_{Sub}. Inlet: Cross-sectional SEM images for (left) $T_{Sub} = 77$ K, (middle) $T_{Sub} = 485$ K, and (right) $T_{Sub} = 679$ K. The scale bars are 500 nm (left), 1µm (middle), and 300 nm (right).

suggesting a vanishing confinement of the m-axes in that direction. Concluding, a fiber texture is observed.

To sum up, a biaxial texture with minor fiber contributions could be detected for columnar Ti thin films grown at 485 K (T_H(Ti) = 0.25) and 679 K (T_H(Ti) = 0.35). In contrast, for low substrate temperatures (T_{Sub} = 77 K, T_H(Ti) = 0.04) and for high substrate temperatures (T_{Sub} = 873 K, T_H(Ti) = 0.45), fiber texture components become more pronounced.

Moreover, the orientation of the c-axis is significantly influenced by the substrate temperature. For the investigated substrate temperatures, two crystal components could be observed: (i) components with the c-axes tilted away by an angle $28° \leq \gamma_{[0001]} \leq 45°$ with respect to the substrate normal, and (ii) components with the c-axes aligned nearly parallel to the substrate surface. For the component (i), the dependence of the angles $\gamma_{[0001]}$ and β on the substrate temperature are summarized in Figure 6.17 (a), (b). The following observations can be made. First of all, the tilt angle β is in general larger than the tilt angle of the crystallites c-direction $\gamma_{[0001]}$, which is in accordance with the observations reported in sections 6.1 and 6.2. Secondly, the obtained $\gamma_{[0001]}$-angles scatter around the arithmetic mean value $\gamma_{[0001]} \sim 36°$, which is near the predicted angle for a maximized vertical growth $\gamma = ½\, \theta_{OAD} = 41°$. In contrast, the β-angles scatter around the arithmetic mean value $\beta \sim 60°$. Thirdly, the difference between both angles Δ changes with substrate temperature. According to Figure 6.17 (a) and (b), the difference between the tilt of the crystal direction and tilt of the column is $\Delta = 26°$ for 77 K ($T_H = 0.04$). For temperatures up to 485 K ($T_H = 0.25$), β becomes smaller and $\gamma_{[0001]}$ larger again, until both angles are nearly equal ($\Delta = 3°$). It can be stated that a temperature change from 77 K to 485 K results in a larger change of the columnar tilt angles ($48° \leq \beta \leq 63°$) than for the tilt of the crystal c-direction ($37° \leq \gamma_{[0001]} \leq 45°$). As the temperature is further increased, β becomes larger and γ smaller again, thereby increasing the difference between both angles up to $\Delta = 41°$ for 873 K ($T_H = 0.45$). At such high temperatures, the surface self-diffusion might be large enough so that incoming particles can move to other crystal planes of the same crystal or even to other crystals. This might contribute to the enlarged Δ for $T_H > 0.25$. Comparing Figure 6.16 and Figure 6.17 indicates that the occurrence of a biaxial texture for columnar Ti thin films might be correlated with a small difference ($3° \leq \Delta \leq 10°$) between both tilt angle β and $\gamma_{[0001]}$, and a fiber texture might be correlated with a larger difference ($\Delta \geq 26°$) between both tilt angles β and $\gamma_{[0001]}$. However, such a correlation could not be verified for columnar Cr and Mo (see section 6.1) as well as Al thin films (see below, section 6.3).

The observed differences in texture of the columnar Ti thin films are a result of the competition between the shadowing effect induced by the highly oblique deposition angle of $\theta_{OAD} = 82°$ and the adatom mobility, which increases with substrate temperature. To understand why fiber and biaxial textures are only observed for certain ranges of temperature, the adatom mobility has to be taken into account. Deposition at 77 K is associated with a strictly limited adatom mobility. Only a fraction of adatoms will have sufficient energy to overcome the diffusion barrier, causing the formation of partly crystalline, partly amorphous columns (see subsection 5.1.2). The competitive growth process is on the one hand determined by an anisotropy of the incoming particle flux. This leads to the selection of the columns that capture randomly a maximal amount of material, resulting in a maximized geometrically fastest vertical growth. Those texture components with random orientation cannot be seen in the IPPFs. On the other hand, the IPPFs in Figure 6.16 (a, b) reveal two density rings, indicating that the adatom mobility has been sufficient for the development of at least two fiber texture components with preferred crystal orientations. Increasing the substrate temperature to 300 K leads to an adatom mobility high enough for the formation of randomly oriented, single crystalline nuclei that develop to single crystalline columns. Those planes will be selected that are inclined towards the incoming flux direction so that a maximal amount of material is captured. This selection process is based on the assumptions that, firstly, the adatom mobility is so low that the adatoms cannot reach other nuclei or columns. Secondly, shadowing occurs so that columns with faster vertical growth will be able to overgrow slower developing columns, thereby reducing the distribution of crystal orientations of the growing film. As a result, a biaxial texture is observed. Further increasing the substrate temperature results in an adatom mobility that allows the adatoms to move from one nuclei (column) to other nuclei (columns) (see subsection 4.1.2 and section 5.3). Thus, the influence of the incoming particle flux direction and accordingly the shadowing effect is reduced, since the adatoms are sufficiently mobile to move to their thermodynamically favored position. As a result, a fiber texture is observed.

In conclusion, the formation of a biaxial texture requires to balance both adatom diffusion length and the shadowing length to realize a crystal confinement in both polar and azimuthal direction. A fiber texture will develop if this balance is either shifted to shadowing (by lowering the substrate temperature) or to adatom mobility (by increasing the substrate temperature).

Additionally, the texture formation depending on the substrate temperature is examined for columnar Al thin films deposited at $\theta_{OAD} = 82°$, $r = 0.5$ nm/s and at substrate temperatures of 77 K and 300 K [LIE01]. To study the orientation of the crystallites, IPPF measurements are carried out and compared with the calculated IPPFs [161]. The samples are aligned in the XRD-goniometer so that the direction of the incoming particle flux corresponds to $\Phi = 0°$. For experimental measurement of the corresponding Al{111} and Al{200} pole figures, the Bragg reflections at $2\theta = 38.472°$ and $2\theta = 44.738°$ are used, respectively [190]. Figure 6.18 (a), (b) as well as (c), (d) depict the resulting stereographic projections for deposition at 77 K and 300 K, respectively. The Al(200) pole density maximum in Figure 6.18 (a), (c) indicate that the [100] directions of all Al crystallites are oriented similarly towards the incident flux direction. Figure 6.18 (b), (d) show four broadened, but separated pole density maxima at azimuthal angle $\Phi = 54.7°$. This experimentally observed angle is in good agreement with the expected angle between the Al(100) and Al(111) lattice planes in the fcc Al unit cell. The well-defined pole density distribution reveals the biaxial texture of the columnar Al thin films deposited at 77 K and 300 K. This contrasts with the columnar Ti thin films, which exhibit a fiber texture if deposited at 77 K ($T_H = 0.04$). The observation of a biaxial texture for deposition at 77 K is because Al exhibits an enlarged adatom mobility at 77 K ($T_H = 0.08$) compared to metals with higher melting points such as Ti, which has been discussed previously. A fiber texture contribution is indicated by the low-density ring connecting each two pole density maxima. In Figures 6.9 (e), (g), sharp peaks can be obtained that originate from the Si(100) substrate. An epitaxial relationship between the Al columns and the substrate is not expected due to the 800 nm thick thermal oxide layer atop of the Si(100) substrate.

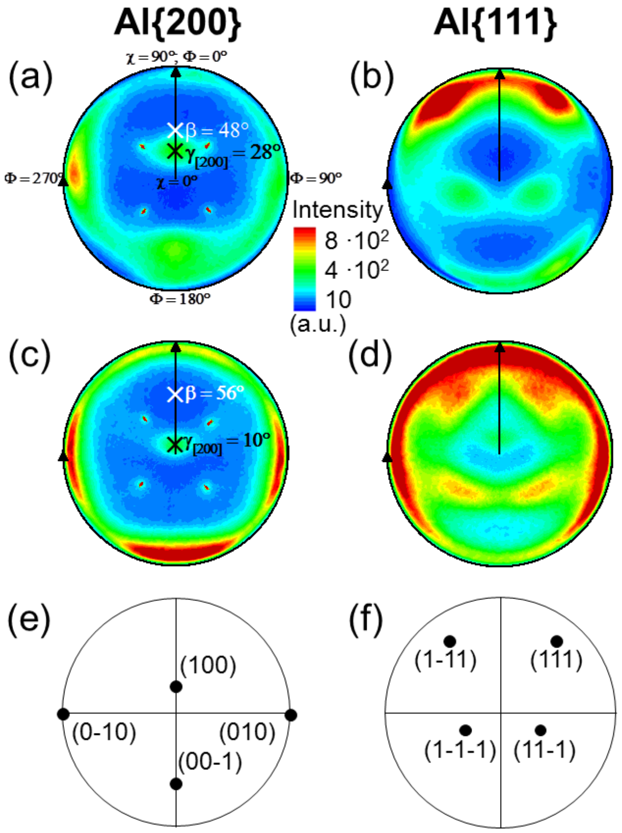

Figure 6.18: Measured in-plane pole figures for the cubic (a) Al{200} and (b) Al{111} planes in an obliquely ($\theta_{OAD} = 82°$) deposited thin film at 77 K. (c) Al{200} and (d) Al{111} planes in an obliquely ($\theta_{OAD} = 82°$) deposited thin film at 300 K. The [200] direction of the crystallites is tilted by $\gamma_{[200]}$ and the tilt angle of the columns is β, both measured with respect to the substrate normal. Intensity (a.u.) is depicted on a linear scale and applies for all measured in-plane pole figures ((a) – (d)). Calculated in-plane pole figures for the cubic (e) Al{200} and (f) Al{111} planes in an obliquely ($\theta_{OAD} = 82°$) deposited thin film.

A comparison between the calculated positions of the pole density maxima with the measured positions confirms that there is a good match. Besides, from Figure 6.18 (a) and (c) can be derived that the tilt of the [100] direction of the crystallites $\gamma_{[100]}$ is not equal to the tilt of the columns β. Precisely, this difference is $\Delta = \beta - \gamma_{[100]} = 48° - 28° = 20°$ for deposition at 77 K ($T_H = 0.08$) and $\Delta = 56° - 10° = 46°$ for deposition at 300 K ($T_H = 0.32$), meaning that the difference between both angles becomes significantly larger if the temperature is enlarged from $T_H = 0.08$ to $T_H = 0.32$. This observation suggests that the formation of a biaxial texture for columnar Al thin films is not correlated with a small difference Δ between β and $\gamma_{[100]}$.

In addition, polycrystalline Al thin films are fabricated by vertical deposition ($\theta_{OAD} = 0°$) at 77 K and 300 K. The θ-2θ scans (not shown here) reveal a preferred growth direction along Al(111) for deposition at 77 K, but a preferred growth direction along both [111] and [100] for deposition at 300 K. According to Wulff´s rule [14], the lowest surface energy plane of the fcc Al is the (111) plane, which is the plane with the highest surface diffusion. This plane finally develops to the faceted surface under equilibrium conditions. In summary, differences in the texture of the Al thin films are observed depending on the substrate temperature. Moreover, differences in the preferred growth directions for vertically and obliquely deposited Al thin films are observed. To conclude, the substrate temperature and in turn surface diffusion affect the crystalline texture of the columnar Al thin films.

6.4 Summary of results

The following conclusions can be drawn based on the structure analysis of the columnar metallic thin films:

Influence of the film thickness:

- RHEED measurements indicate that the Mo crystallites formed by oblique deposition at $\theta_{OAD} = 84°$ at RT on thermally oxidized Si(100) substrates are oriented randomly on the substrate surface at the beginning of the growth process (first 10 nm of thin film growth). For a film thickness of 40 nm, first breaks in the diffraction rings of the RHEED patterns can be obtained, indicating the beginning selective growth process. The breaks in the diffraction rings become successively more pronounced with increasing film thickness, implying an evolving texture of the Mo thin films.
- In the IPPFs, the first pole density maxima can be obtained for 70 nm thick columnar Mo thin films, meaning that the crystallites are not oriented random anymore. As the film thickness is enlarged from 70 nm up to 2.5 µm, these pole density maxima become more pronounced, and additional pole density maxima appear. For a 250 nm thick Mo film, a biaxial texture with fiber contribution could be detected. As the thickness is increased to 2.5 µm, the Mo thin film exhibits a nearly full biaxial texture with no or only minor fiber texture contribution.
- Preferentially oriented nucleation and post-deposition crystallization [11] can be excluded as factors that may introduce texture in the Mo thin films. Instead, the evolutionary or competitive selection of initially random nucleation is found to

cause the texture formation of the investigated films. The RHEED, IPPF, and SAED measurements show consistently that the competitive growth process is basically ceased after the columnar Mo thin film has reached a thickness of 2.5 μm.

- The measured IPPFs are in good agreement with the calculated pole figures.
- IPPF measurements are a suitable to determine the tilt angle of a given lattice direction of the crystallites in a metallic, obliquely deposited thin film (measured with respect to the substrate normal).
- The crystallites of the Mo columns grow along the thermodynamically favored [110] direction. The atoms of the [110] planes continuously become shadowed during the growth process so that the tilt angle β of the Mo columns is not equal to the tilt angle $\gamma_{[110]}$ of the [110] direction of the bcc Mo crystallites.
- A theoretical estimation is deduced that enables the prediction of the γ-angle that enables the fastest vertical growth of the crystallite, as already proposed by van der Drift [11]. The measured and the predicted γ-angle differ, because the estimation is based exclusively on geometrical considerations.
- Columnar Cr thin films deposited with similar conditions as the studied Mo thin films exhibit a biaxial texture as well. The columnar tilt angle β is not equal to the tilt angle $\gamma_{[110]}$ of the [110] direction of the bcc Cr crystallites.

Influence of the direction of the incoming particle flux:

- A biaxial texture with fiber contribution is observed for columnar Ti thin films with a thickness in the range of 2 μm deposited on thermally oxidized Si(100) substrates at RT with $\theta_{OAD} = 78°$ and $\theta_{OAD} = 84°$, respectively. The c-axes of the hcp Ti crystallites exhibit a preferred growth direction towards the incoming particle flux.
- For less oblique deposition geometries ($70° \leq \theta_{OAD} < 78°$), a fiber texture is found, and the preferred orientation of the c-axes of the crystallites towards the incoming flux direction vanishes, and numerous other growth directions appear. This can be explained by the evolutionary selection process that is driven by the shadowing effect. Less oblique deposition leads to a reduced shadowing effect, thereby the effective growth front of the film is increased. This results in a less competitive growth process among the developing columns so that a larger variety of growth directions can be obtained.
- In accordance with the observations made for the Mo thin films, the columnar tilt angle β of the Ti thin films is not equal to the tilt angle $\gamma_{[0001]}$ of the c-direction of the hcp Ti crystallites. Both angles show the tendency to become smaller for less oblique deposition geometries. The experimentally observed γ-angles are in good agreement with the predicted γ-angles for fastest vertical growth of the crystallite. Thus, the crystallites grow along the thermodynamically favored c-direction with

an angle $\gamma_{[0001]}$, but the columnar tilt angle β is formed as a result of shadowing (analogue discussion as for Mo thin films).

- For thin films composed of vertical Ti and Cr columns, a weak fiber texture is obtained.
- The θ-2θ X-ray diffraction pattern detected exemplarily for vertical Cr columns reveals a slightly preferred growth along the [110] direction. However, additional other growth directions of the bcc crystallites in the vertical Cr columns are present as well.

Influence of the substrate temperature:

- Columnar Ti thin films grown at 485 K ($T_H = 0.25$) and 679 K ($T_H = 0.35$) exhibit a biaxial texture with minor fiber contributions, but a fiber texture could be obtained for low substrate temperatures (77 K, $T_H = 0.04$) and for high substrate temperatures (873 K, $T_H = 0.45$).
- In the temperature range between $T_H = 0.04$ and $T_H = 0.45$, crystal components with the c-axes pointing away by an angle $27° < \gamma < 45°$ from the substrate normal and crystal components with the c-axes aligned nearly parallel to the substrate surface are obtained.
- The substrate temperature influences the orientation of the c-axis as well as the columnar tilt angle remarkably. The difference between both angles decreases from 26° to 3° as the substrate temperature is increased from 77 K to 485 K. For higher substrate temperatures, this difference is enlarged up to 41° for 873 K. Reasons that contribute to this observation are expected to be the competition between shadowing length and adatom diffusion length.
- Columnar Al thin film deposited obliquely at 77 K and 300 K exhibit a biaxial texture with fiber contribution. Columnar tilt angle and tilt of crystallites [100] direction are not equal. The difference between both angles becomes larger with increased substrate temperature.
- Vertically deposited Al thin films have a different preferred growth direction compared to columnar Al thin films, again implying that the direction of the incoming flux has an impact on the texture formation.

7 Summary and Conclusions

The present work is a systematic experimental study on the growth of metallic, columnar thin films fabricated by electron beam evaporation under the variation of different deposition parameters. For this purpose, metals have been chosen so that a large range of melting points (T_{Melt}(Al) = 933 K to T_{Melt}(Ta) = 3269 K) and crystal structures (bcc, fcc, hcp) is covered. The found experimental results are described, discussed, and compared, with the aim to gain a more general understanding of the growth of such metallic, columnar thin films.

The focus of first part in this work has been the analysis of the morphology of metallic, columnar thin films by SEM. To overcome the influence of surface self-diffusion that counteracts the shadowing effect, a liquid nitrogen cooled sample holder that enables cooling down the substrate temperature to 77 K has been designed and fabricated. Metallic columnar thin films of seven different metals (Al, Ni, Co, Ti, Cr, Mo, and Ta) could successfully be deposited at a substrate temperature of 77 K by using this sample holder. Although all thin films exhibit a similar overall columnar shape (high aspect ratio rods) at 77 K, differences in the columnar diameters as well as in the columnar tilt angles are obtained and discussed for varying substrate temperatures up to 987 K. The precise understanding of the surface self-diffusion has been found to be a crucial aspect to understand the β–θ_{OAD} relations for varying substrate temperatures. Depending on the incidence angle and on the substrate temperature, the film porosity has shown to be adjustable between $\sim 30\% \leq P \leq \sim 90\%$. Further, it has been demonstrated that tilted columns grow faster in height than spirals, screws, and vertical columns for identical deposition conditions. Based on geometrical considerations that take the different local deposition geometries of the columnar growth zones with respect to the incoming particle flux into account, an inequality could be derived that reflexes the tendency of tilted columns to grow faster than spirals, screws, and vertical columns. Additionally, the different local deposition geometries are the reason for the remarkably different tilt angles of arm 1 and 2 in Mo zigzag columns. Those tilt angles have shown the tendency to converge with increasing number of arms caused by the reduction and selection of developing zigzag structures as the competitive growth process proceeds.

In the second part, the structure of individual metallic columns has been examined by TEM, and in the third part the texture of the thin films has been investigated by XRD and RHEED measurements. By using HRTEM, the lattice planes of individual columns could be obtained directly, and partly with atomic-resolution. Exemplarily for Ti, the structure of individual columns deposited at 77 K has been examined by µP-STEM. Those columns are partly crystalline, partly amorphous, indicating that a fraction of the adatoms has sufficient energy to overcome the diffusion barrier so that even for such low temperatures adatom surface self-diffusion occurs. However, the adatom diffusion length is strictly limited so that the columnar growth is dominated by shadowing. Columns grow along the geometrically fastest vertical direction, and the competition between growing columns is induced by an anisotropy of the incoming particle flux. The low adatom mobility causes the formation of crystalline parts in the columns so that a fiber texture could be detected.

If deposited at RT under an highly oblique deposition angles $\theta_{OAD} > 80°$ with low working pressure ($p_{Work} \leq 10^{-8}$ mbar) on natively and thermally oxidized Si(100) substrates, tilted Ti, Cr, and Mo columns tend to grow with a single crystalline structure. The formation of single crystalline columns requires (i) an adatom mobility that allows the formation of single crystalline nuclei at substrate surface, and (ii) a low working pressure to prevent the incorporation of impurities. Besides, (iii) the shadowing length should be sufficiently large to ensure that developing columns do not bundle or coalesce during growth. Then, the initial single crystalline structure of nuclei will be preserved so that single crystalline nuclei can develop to single crystalline columns.

The Ti (hcp), Cr (bcc), and Mo (bcc) crystallites grow along the thermodynamically favored direction [0002] and [110], respectively. This contrasts with Al (fcc) crystallites, which have been observed to grow along the [100] direction, not along the thermodynamically favored [111] direction. The tilt angle of these crystal directions γ differs from the tilt angle of the corresponding column β by a difference $\Delta = \beta - \gamma > 0$. For varying incident angles, substrate temperatures and different deposited metals, it is observed that γ is smaller than β. Additionally, for equal deposition parameters, different γ-angles are obtained for different metals, indicating that γ also depends on the crystal structure and the material.

The observation that γ is smaller than β can be attributed to the fact that the layers in the columns grow in a direction that ensures a maximal vertical growth (γ-angle), but those layers are continuously shadowed during growth, thereby defining the columnar tilt angle β. The vertical growth component of a column becomes approximately maximized if the product ($\cos(\gamma) \cdot \cos(\theta_{OAD} - \gamma)$) becomes maximal, indicating that $\gamma = \frac{1}{2} \cdot \theta_{OAD}$ [11]. This is a rough estimation based exclusively on geometrical considerations. Nevertheless, it could be shown that this deviation is suitable to predict approximately the γ-angles that ensure a maximized growth.

Among initially random oriented, single crystalline nuclei, those are selected that exhibit their lowest surface energy planes inclined by an angle γ towards the incoming particle flux so that a maximal amount of material can be captured. This ensures a maximized vertical growth component so that nuclei (columns) with less preferential orientation towards the incoming flux direction are shadowed by faster growing columns. Consequently, the distribution of crystal orientations of the growing columnar thin film is reduced. This selection process intrinsically proceeds with increasing film thickness, which has been examined for columnar Mo thin films deposited at RT. In general, such a process requires an adatom mobility high enough to allow the formation of crystalline nuclei, but the adatom diffusion must also be restricted so that it is not possible for the adatom to reach other columns (nuclei) during growth. Thus, the formation of a biaxial textured metallic thin films requires adequate shadowing length as well as an adequate adatom diffusion length. Exemplarily for columnar Ti thin films, a biaxial texture could be obtained for 300 K ≤ T_{Sub} ≤ 485 K. In addition, biaxial textured thin films have been observed for columnar Cr and Mo thin films deposited at RT and for columnar Al thin films deposited at 77 K and RT.

If the adatom mobility becomes so large that adatoms can move to other crystal planes or columns, the selection of the crystal orientations according to the γ-angles that ensure the maximized vertical growth cannot be applied anymore. Then, the adatoms move to their thermodynamically favored position according to their crystal habit, thereby forming large columns with single crystalline structure, and the occurrence of columnar thin films vanishes. As a result, the biaxial texture is transformed to a fiber texture as the adatom mobility enlarges and the shadowing length decreases.

To draw a conclusion, the growth and structure formation of obliquely deposited metallic thin films is the result of a complex interplay between shadowing and adatom surface self-diffusion. The present study has demonstrated that comparing the growth characteristics of columnar thin films made of metals with different melting points and crystal structures is a suitable approach to deduce a more general knowledge concerning the growth process of metallic OAD and GLAD thin films.

8 List of Literature

1. Srivastava, S.K., Shalabney, A., Khalaila, I., Grüner, C., Rauschenbach, B. and Abdulhalim, I., *SERS Biosensor Using Metallic Nano-Sculptured Thin Films for the Detection of Endocrine Disrupting Compound Biomarker Vitellogenin.* Small, 2014. **10**(17): p. 3579-3587.
2. Abdulhalim, I., *Plasmonic Sensing Using Metallic Nano-Sculptured Thin Films.* Small, 2014. **10**(17): p. 3499-3514.
3. Srivastava, S.K., Grüner, C., Hirsch, D., Rauschenbach, B. and Abdulhalim, I., *Enhanced intrinsic fluorescence from carboxidized nano-sculptured thin films of silver and their application for label free dual detection of glycated hemoglobin.* Opt. Express, 2017. **25**(5): p. 4761-4772.
4. Grüner, C., Abdulhalim, I. and Rauschenbach, B., *Glancing Angle Deposition for Biosensing Applications* in *Encyclopedia of Interfacial Chemistry: Surface Science and Electrochemistry*, Wandelt, K., Editor. 2018, Elsevier. p. 129-137.
5. Kundt, A., *Über Doppelbrechung des Lichtes in Metallschichten, welche durch Zerstäuben einer Kathode hergestellt sind.* Ann. Phys., 1886. **263**(1): p. 59-71.
6. Hawkeye, M.M., Taschuk, M.T. and Brett, M.J., *Introduction: Glancing Angle Deposition Technology*, in *Glancing Angle Deposition of Thin Films*. 2014, John Wiley & Sons, Ltd: The Atrium, Southern Gate, Chichester, West Sussex, PO19 8SQ, United Kingdom. p. 1-30.
7. Tait, R.N., Smy, T. and Brett, M.J., *Modelling and characterization of columnar growth in evaporated films.* Thin Solid Films, 1993. **226**(2): p. 196-201.
8. Kashchiev, D., *Nucleation: Basic Theory with Applications*. Vol. 1. 2000, Linacre Home, Jordan Hill, Oxford OX2 8DP: Elsevier Ltd. 544.
9. Venables, J.A., Spiller, G.D.T. and Hanbucken, M., *Nucleation and growth of thin films.* Rep. Prog. Phys., 1984. **47**(4): p. 399.
10. König, H. and Helwig, G., *Über die Struktur schräg aufgedampfter Schichten und ihr Einfluss auf die Entwicklung submikroskopischer Oberflächenrauhigkeiten* Optik, 1950. **6**(2): p. 111-124.
11. van der Drift, A., *Evolutionary selection, a principle governing growth orientation in vapour-deposited layers.* Philips Res. Rep., 1967. **22**: p. 267-288.
12. Steele, J.J. and Brett, M.J., *Nanostructure engineering in porous columnar thin films: recent advances.* J. Mater. Sci. - Mater. Electron., 2007. **18**(4): p. 367-379.
13. Smith, D.O., Cohen, M.S. and Weiss, G.P., *Oblique-Incidence Anisotropy in Evaporated Permalloy Films.* J. Appl. Phys., 1960. **31**(10): p. 1755-1762.
14. Wulff, G., *Zur Frage der Geschwindigkeit des Wachstums und der Auflösung der Kristallflächen.* Z. Kristallogr. Cryst. Mater., 1901. **34**: p. 449-530.
15. Herring, C., *The Use of Classical Macroscopic Concepts in Surface-Energy Problems*, in *Structure and Properties of Solid Surfaces*, Gombr, R. and Smith, C.S., Editors. 1953, The University of Chicago Press: 5750 Ellis Avenue, Chicago 37, Illinois.
16. Sadeghi-Khosravieh, S. and Robbie, K., *Morphology and crystal texture in tilted columnar micro-structured titanium thin film coatings.* Thin Solid Films, 2017. **627**: p. 69-76.
17. Khudhayer, W.J., Kariuki, N.N., Wang, X.P., Myers, D.J., Shaikh, A.U. and Karabacak, T., *Oxygen Reduction Reaction Electrocatalytic Activity of Glancing*

Angle Deposited Platinum Nanorod Arrays. J. Electrochem. Soc., 2011. **158**(8): p. B1029-B1041.

18. Messier, R., Giri, A.P. and Roy, R.A., *Revised structure zone model for thin film physical structure.* J. Vac. Sci. Technol. A, 1984. **2**(2): p. 500-503.
19. Nieuwenhuizen, J.M. and Haanstra, H.B., *Microfractography of thin films.* Philips Tech. Rev. , 1966. **27**: p. 87-91.
20. Zhao, Y., He, Y. and Brown, C., *Composition dependent nanocolumn tilting angle during the oblique angle co-deposition.* Appl. Phys. Lett., 2012. **100**(3): p. 033106.
21. Hara, K., Kamiya, M., Hashimoto, T., Okamoto, K. and Fujiwara, H., *Oblique-incidence anisotropy of the iron films evaporated at low substrate temperatures.* J. Magn. Magn. Mater., 1988. **73**(2): p. 161-166.
22. Abelmann, L. and Lodder, C., *Oblique evaporation and surface diffusion.* Thin Solid Films, 1997. **305**(1-2): p. 1-21.
23. Lichter, S. and Chen, J., *Model for columnar microstructure of thin solid films.* Phys. Rev. Lett., 1986. **56**(13): p. 1396-1399.
24. Tanto, B., Eyck, G.T. and Lu, T.M., *A model for column angle evolution during oblique angle deposition.* J. Appl. Phys., 2010. **108**(2): p. 026107.
25. Zhu, H., Cao, W., Larsen, G.K., Toole, R. and Zhao, Y., *Tilting angle of nanocolumnar films fabricated by oblique angle deposition.* J. Vac. Sci. Technol. B, 2012. **30**(3): p. 030606.
26. Grüner, C., Liedtke, S., Bauer, J., Mayr, S.G. and Rauschenbach, B., *Morphology of Thin Films Formed by Oblique Physical Vapor Deposition.* ACS Appl. Nano Mater., 2018. **1**(3): p. 1370-1376.
27. Okamoto, K. and Itoh, K., *Incidence Angle Dependences of Columnar Grain Structure and Texture in Obliquely Deposited Iron Films.* Jpn. J. Appl. Phys., 2005. **44**(3): p. 1382-1388.
28. Wassermann, G. and Grewen, J., *Texturen metallischer Werkstoffe*. 2 ed. 1939: Springer-Verlag Berlin Heidelberg GmbH.
29. Selvamanickam, V., Sambandam, S., Sundaram, A., Lee, S., Rar, A., Xiong, X., Alemu, A., Boney, C. and Freundlich, A., *Germanium films with strong in-plane and out-of-plane texture on flexible, randomly textured metal substrates.* J. Cryst. Growth, 2009. **311**(21): p. 4553-4557.
30. Taschuk, M.T., Hawkeye, M.M. and Brett, M.J., *Glancing Angle Deposition*, in *Handbook of Deposition Technologies for Films and Coatings: Science, Applications and Technology*, Peter Martin, W.A., Editor. 2010, Elsevier: Oxford, United Kingdom. p. 621-672.
31. Barranco, A., Borras, A., Gonzalez-Elipe, A.R. and Palmero, A., *Perspectives on oblique angle deposition of thin films: From fundamentals to devices.* Prog. Mater Sci., 2016. **76**: p. 59-153.
32. Mahieu, S., Ghekiere, P., Depla, D. and De Gryse, R., *Biaxial alignment in sputter deposited thin films.* Thin Solid Films, 2006. **515**(4): p. 1229-1249.
33. Xu, Y., Lei, C.H., Ma, B., Evans, H., Efstathiadis, H., Rane, M., Massey, M., Balachandran, U. and Bhattacharya, R., *Growth of textured MgO through e-beam evaporation and inclined substrate deposition.* Supercond. Sci. Technol., 2006. **19**(8): p. 835.
34. Paranthaman, M.P. and Izumi, T., *High-Performance YBCO-Coated Superconductor Wires.* MRS Bull., 2011. **29**(8): p. 533-541.
35. Gaire, C., Clemmer, P.C., Li, H.F., Parker, T.C., Snow, P., Bhat, I., Lee, S., Wang, G.C. and Lu, T.M., *Small angle grain boundary Ge films on biaxial CaF_2/glass substrate.* J. Cryst. Growth, 2010. **312**(4): p. 607-610.

36. Findikoglu, A.T., Choi, W., Matias, V., Holesinger, T.G., Jia, Q.X. and Peterson, D.E., *Well-Oriented Silicon Thin Films with High Carrier Mobility on Polycrystalline Substrates.* Adv. Mater., 2005. **17**(12): p. 1527-1531.
37. Teplin, C.W., Ginley, D.S. and Branz, H.M., *A new approach to thin film crystal silicon on glass: Biaxially-textured silicon on foreign template layers.* J. Non-Cryst. Solids, 2006. **352**(9): p. 984-988.
38. Young, N.O. and Kowal, J., *Optically Active Fluorite Films.* Nature, 1959. **183**: p. 104.
39. Robbie, K., Friedrich, L.J. and Dew, S.K., *Fabrication of thin films with highly porous microstructures.* J. Vac. Sci. Technol. A, 1995. **13**(3): p. 1032-1035.
40. Robbie, K., Brett, M.J. and Lakhtakia, A., *Chiral sculptured thin films.* Nature, 1996. **384**: p. 616.
41. Steele, J.J., van Popta, A.C., Hawkeye, M.M., Sit, J.C. and Brett, M.J., *Nanostructured gradient index optical filter for high-speed humidity sensing.* Sens. Actuators B Chem., 2006. **120**(1): p. 213-219.
42. Liu, C.L., Cohen, J.M., Adams, J.B. and Voter, A.F., *EAM study of surface self-diffusion of single adatoms of fcc metals Ni, Cu, Al, Ag, Au, Pd, and Pt.* Surf. Sci., 1991. **253**(1-3): p. 334-344.
43. Ratsch, C. and Scheffler, M., *Density-functional theory calculations of hopping rates of surface diffusion.* Phys. Rev. B, 1998. **58**(19): p. 13163-13166.
44. Suzuki, M., Nagai, K., Kinoshita, S., Nakajima, K., Kimura, K., Okano, T. and Sasakawa, K., *Vapor phase growth of Al whiskers induced by glancing angle deposition at high temperature.* Appl. Phys. Lett., 2006. **89**(13): p. 133103.
45. Suzuki, M., Nagai, K., Kinoshita, S., Nakajima, K., Kimura, K., Okano, T. and Sasakawa, K., *Morphological evolution of Al whiskers grown by high temperature glancing angle deposition.* J. Vac. Sci. Technol. A, 2007. **25**(4): p. 1098-1102.
46. Mukherjee, S. and Gall, D., *Anomalous scaling during glancing angle deposition.* Appl. Phys. Lett., 2009. **95**(17): p. 173106.
47. Khare, C., Patzig, C., Gerlach, J.W., Rauschenbach, B. and Fuhrmann, B., *Influence of substrate temperature on glancing angle deposited Ag nanorods.* J. Vac. Sci. Technol. A, 2010. **28**(4): p. 1002-1009.
48. Mukherjee, S. and Gall, D., *Power law scaling during physical vapor deposition under extreme shadowing conditions.* J. Appl. Phys., 2010. **107**(8): p. 084301.
49. Deniz, D. and Lad, R.J., *Temperature threshold for nanorod structuring of metal and oxide films grown by glancing angle deposition.* J. Vac. Sci. Technol. A, 2011. **29**(1): p. 011020.
50. Khare, C., W., G.J., Weise, M., Bauer, J., Höche, T. and Rauschenbach, B., *Growth temperature altered morphology of Ge nanocolumns.* Phys. Status Solidi A, 2011. **208**(4): p. 851-856.
51. Movchan, B.A. and Demchishin, A.V., *Structure and properties of thick condensates of Nickel, Titanium, Tungsten, Aluminium oxides, and Zirconium dioxide in vacuum.* Fiz. Metal. Metalloved., 1969. **28**: p. 653-660.
52. Mukherjee, S. and Gall, D., *Structure zone model for extreme shadowing conditions.* Thin Solid Films, 2013. **527**: p. 158-163.
53. Thornton, J.A., *Influence of apparatus geometry and deposition conditions on the structure and topography of thick sputtered coatings.* J. Vac. Sci. Technol., 1974. **11**(4): p. 666-670.
54. Askill, J. and Tomlin, D.H., *Self-diffusion in chromium.* Philos. Mag., 1965. **11**(111): p. 467-474.

55. Flahive, P.G. and Graham, W.R., *Pair potential calculations of single atom self-diffusion activation energies.* Surf. Sci., 1980. **91**(2): p. 449-462.
56. Hok, S. and Drechsler, M., *A measurement of the surface self-diffusion of tantalum.* Surf. Sci. Lett., 1981. **107**(2): p. L362-L366.
57. Mundy, J.N., Hoff, H.A., Pelleg, J., Rothman, S.J., Nowicki, L.J. and Schmidt, F.A., *Self-diffusion in chromium.* Phys. Rev. B, 1981. **24**(2): p. 658-665.
58. Prasad, J.J.B. and Reddy, K.V., *Self diffusion studies on cobalt thin films.* Bull. Mater. Sci., 1985. **7**(1): p. 15-20.
59. Feibelman, P.J., *Diffusion path for an Al adatom on Al(001).* Phys. Rev. Lett., 1990. **65**(6): p. 729-732.
60. Stumpf, R. and Scheffler, M., *Ab initio calculations of energies and self-diffusion on flat and stepped surfaces of Al and their implications on crystal growth.* Phys. Rev. B, 1996. **53**(8): p. 4958-4973.
61. Dabrowski, A.M., Biernat, T., Beben, J. and Gubernator, W., *Investigation of self-diffusion of titanium by fluctuation autocorrelation method.* Acta Phys. Pol. A, 1997. **91**(6): p. 1091-1095.
62. Li, J.M., Zhang, P.H., Yang, J.L. and Liu, L., *Theoretical study of adatom self-diffusion on metallic fcc {001} surfaces.* Chin. Phys. Lett., 1997. **14**(10): p. 768-771.
63. Gorshkov, A.V., *Empirical relation for the activation energy of diffusion in elemental substances.* Inorg. Mater., 2000. **36**(1): p. 22-23.
64. Kong, L.T. and Lewis, L.J., *Transition state theory of the preexponential factors for self-diffusion on Cu, Ag, and Ni surfaces.* Phys. Rev. B, 2006. **74**(7).
65. Mattsson, T.R., Sandberg, N., Armiento, R. and Mattsson, A.E., *Quantifying the anomalous self-diffusion in molybdenum with first-principles simulations.* Phys. Rev. B, 2009. **80**(22).
66. Sushko, G.B., Verkhovtsev, A.V., Yakubovich, A.V., Schramm, S. and Solov'yov, A.V., *Molecular dynamics simulation of self-diffusion processes in titanium in bulk material, on grain junctions and on surface.* J. Phys. Chem. A, 2014. **118**(33): p. 6685-91.
67. Khudhayer, W.J., Shaikh, A.U. and Karabacak, T., *Platinum Nanorod Arrays with Preferred Morphological and Crystal Properties for Oxygen Reduction Reaction.* Adv. Sci. Lett., 2011. **4**(11-12): p. 3551-3559.
68. Khudhayer, W.J., Shaikh, A.U. and Karabacak, T., *Periodic Pt Nanorod Arrays with Controlled Porosity for Oxygen Reduction Reaction.* Nanosci. Nanotechnol. Lett., 2012. **4**(10): p. 999-1007.
69. Khudhayer, W.J., Begum, M., Nasini, U.B., Cansizoglu, M.F., Yurukcu, M., Shaikh, A.U. and Karabacak, T., *Oxygen reduction reaction electrocatalytic activity of tilted Pt nanorod arrays fabricated by glancing angle deposition.* J. Appl. Electrochem., 2015. **45**(10): p. 1-9.
70. Sharma, S.K., Kim, M.-S., Kim, D.Y. and Yu, J.-S., *Al nanorod thin films as anode electrode for Li ion rechargeable batteries.* Electrochim. Acta, 2013. **87**: p. 872-879.
71. Kesapragada, S.V., Victor, P., Nalamasu, O. and Gall, D., *Nanospring Pressure Sensors Grown by Glancing Angle Deposition.* Nano Lett., 2006. **6**(4): p. 854-857.
72. Khedir, K.R., Kannarpady, G.K., Ishihara, H., Woo, J., Ryerson, C. and Biris, A.S., *Design and Fabrication of Teflon-Coated Tungsten Nanorods for Tunable Hydrophobicity.* Langmuir, 2011. **27**(8): p. 4661-4668.
73. Fujii, T., Aoki, Y. and Habazaki, H., *Fabrication of Super-Oil-Repellent Dual Pillar Surfaces with Optimized Pillar Intervals.* Langmuir, 2011. **27**(19): p. 11752-11756.

74. Fujii, T., Sato, H., Tsuji, E., Aoki, Y. and Habazaki, H., *Important Role of Nanopore Morphology in Superoleophobic Hierarchical Surfaces.* J. Phys. Chem. C, 2012. **116**(44): p. 23308-23314.
75. Chenyu, X., Zhen, C., Junhong, D., Zhifeng, H., Zheng, X., Junxue, F. and Levent, Y., *Microfluidic-based metal enhanced fluorescence for capillary electrophoresis by Ag nanorod arrays.* Nanotechnology, 2014. **25**(22): p. 225502.
76. Shalabney, A. and Abdulhalim, I., *Sensitivity-enhancement methods for surface plasmon sensors.* Laser Photonics Rev., 2011. **5**(4): p. 571-606.
77. Fu, J.X., Collins, A. and Zhao, Y.P., *Optical Properties and Biosensor Application of Ultrathin Silver Films Prepared by Oblique Angle Deposition.* J. Phys. Chem. C, 2008. **112**(43): p. 16784-16791.
78. Zhang, N., Su, X., Free, P., Zhou, X., Neoh, K.G., Teng, J. and Knoll, W., *Plasmonic metal nanostructure array by glancing angle deposition for biosensing application.* Sens. Actuators B Chem., 2013. **183**: p. 310-318.
79. Abdulhalim, I., Karabchevsky, A., Patzig, C., Rauschenbach, B., Fuhrmann, B., Eltzov, E., Marks, R., Xu, J., Zhang, F. and Lakhtakia, A., *Surface-enhanced fluorescence from metal sculptured thin films with application to biosensing in water.* Appl. Phys. Lett., 2009. **94**(6): p. 063106.
80. Singh, J.P., Lanier, T.E., Zhu, H., Dennis, W.M., Tripp, R.A. and Zhao, Y., *Highly Sensitive and Transparent Surface Enhanced Raman Scattering Substrates Made by Active Coldly Condensed Ag Nanorod Arrays.* J. Phys. Chem. C, 2012. **116**(38): p. 20550-20557.
81. Maher, R.C., *Raman Spectroscopy for Nanomaterials Characterization*, in *SERS Hot Spots*. 2012, Springer-Verlag Berlin Heidelberg.
82. Zhou, Q., He, Y., Abell, J., Zhang, Z. and Zhao, Y., *Surface-enhanced Raman scattering from helical silver nanorod arrays.* Chem. Commun., 2011. **47**(15): p. 4466-4468.
83. Karabchevsky, A., Tsapovsky, L., Marks, R.S. and Abdulhalim, I. *Optical immunosensor for endocrine disruptor nanolayer detection by surface plasmon resonance imaging*. in *SPIE NanoScience and Engineering*. 2011. SPIE.
84. Karabchevsky, A., Abdulhalim, I., Khare, C. and Rauschenbach, B. *Microspot sensing based on surface-enhanced fluorescence from nanosculptured thin films*. 2012. SPIE.
85. Aslan, K., Gryczynski, I., Malicka, J., Matveeva, E., Lakowicz, J.R. and Geddes, C.D., *Metal-enhanced fluorescence: an emerging tool in biotechnology.* Curr. Opin. Biotechnol., 2005. **16**(1): p. 55-62.
86. Textor, M., Sittig, C., Frauchiger, V., Tosatti, S. and Brunette, D.M., *Titanium in Medicine*. 1 ed. Properties and biological significance of natural oxide films on titanium and its alloys, ed. Brunette, D.M., Tengvall, P., Textor, M. and Thomsen, P. 2001, Berlin: Springer-Verlag Berlin Heidelberg.
87. Lampin, M., Warocquier, C., Legris, C., Degrange, M. and Sigot-Luizard, M.F., *Correlation between substratum roughness and wettability, cell adhesion, and cell migration.* J. Biomed. Mater. Res., 1997. **36**(1): p. 99-108.
88. Zhou, W., Zhong, X., Wu, X., Yuan, L., Zhao, Z., Wang, H., Xia, Y., Feng, Y., He, J. and Chen, W., *The effect of surface roughness and wettability of nanostructured TiO_2 film on TCA-8113 epithelial-like cells.* Surf. Coat. Technol., 2006. **200**(20): p. 6155-6160.
89. Jiang, X., Bruzewicz, D.A., Wong, A.P., Piel, M. and Whitesides, G.M., *Directing cell migration with asymmetric micropatterns.* Proc. Natl. Acad. Sci. U. S. A., 2005. **102**(4): p. 975-978.

90. Park, J., Bauer, S., von der Mark, K. and Schmuki, P., *Nanosize and Vitality: TiO_2 Nanotube Diameter Directs Cell Fate.* Nano Lett., 2007. **7**(6): p. 1686-1691.
91. Vetrone, F., Variola, F., de Oliveira, P.T., Zalzal, S.F., Yi, J.-H., Sam, J., Bombonato-Prado, K.F., Sarkissian, A., Perepichka, D.F., Wuest, J.D., Rosei, F. and Nanci, A., *Nanoscale Oxidative Patterning of Metallic Surfaces to Modulate Cell Activity and Fate.* Nano Lett., 2009. **9**(2): p. 659-665.
92. Lavenus, S., Ricquier, J.-C., Louarn, G. and Layrolle, P., *Cell interaction with nanopatterned surface of implants.* Nanomedicine, 2010. **5**(6): p. 937-947.
93. Tan, A.W., Pingguan-Murphy, B., Ahmad, R. and Akbar, S.A., *Review of titania nanotubes: Fabrication and cellular response.* Ceram. Int., 2012. **38**(6): p. 4421-4435.
94. Durmus, N.G. and Webster, T.J., *Nanostructured titanium: the ideal material for improving orthopedic implant efficacy?* Nanomedicine, 2012. **7**(6): p. 791-793.
95. Variola, F., Brunski, J., Orsini, G., de Oliveira, P.T., Wazen, R. and Nanci, A., *Nanoscale surface modifications of medically-relevant metals: state-of-the art and perspectives.* Nanoscale, 2011. **3**(2): p. 335-353.
96. Nair, L.S. and Laurencin, C.T., *Nanofibers and nanoparticles for orthopaedic surgery applications.* J. Bone Joint Surg. Am., 2008. **90 Suppl 1**: p. 128-31.
97. Dolatshahi-Pirouz, A., Pennisi, C.P., Skeldal, S., Foss, M., Chevallier, J., Zachar, V., Andreasen, P., Yoshida, K. and Besenbacher, F., *The influence of glancing angle deposited nano-rough platinum surfaces on the adsorption of fibrinogen and the proliferation of primary human fibroblasts.* Nanotechnology, 2009. **20**(9): p. 095101.
98. Pennisi, C.P., Dolatshahi-Pirouz, A., Foss, M., Chevallier, J., Fink, T., Zachar, V., Besenbacher, F. and Yoshida, K., *Nanoscale topography reduces fibroblast growth, focal adhesion size and migration-related gene expression on Platinum surfaces.* Colloids Surf. B, 2011. **85**(2): p. 189-197.
99. Murarka, S.P. and Fraser, D.B., *Thin film interaction between Titanium and polycrystalline Silicon.* J. Appl. Phys., 1980. **51**(1): p. 342-349.
100. Nemanich, R.J., Fulks, R.T., Stafford, B.L. and Vander Plas, H.A., *Initial reactions and silicide formation of titanium on silicon studied by Raman spectroscopy.* J. Vac. Sci. Technol. A, 1985. **3**(3): p. 938-941.
101. del Giudice, M., Joyce, J.J., Ruckman, M.W. and Weaver, J.H., *Silicide formation at the Ti/Si(111) interface: Room-temperature reaction and Schottky-barrier formation.* Phys. Rev. B, 1987. **35**(12): p. 6213-6221.
102. Mizutani, T., *Correct substrate temperature monitoring with infrared optical pyrometer for molecular-beam epitaxy of III–V semiconductors.* J. Vac. Sci. Technol. B, 1988. **6**(6): p. 1671-1677.
103. (NIST), N.I.o.S.a.T. *NIST Data Home Page ITS-90 Thermocouple Main Page* 2000 04/17/2008 [cited 2018 21/08/2018]; Available from: https://srdata.nist.gov/its90/type_k/kcoefficients_inverse.html.
104. Everhart, T.E. and Thornley, R.F.M., *Wide-band detector for micro-microampere low-energy electron currents.* J. Sci. Instrum., 1960. **37**(7): p. 246.
105. Rasband, W.S. *ImageJ.* 2018 [cited 2018; Available from: http://imagej.nih.gov/ij/.
106. De Broglie, L., *Recherche sur la théorie des quanta.* Ann. Phys. (Paris), 1925. **3**: p. 22-128.
107. Pennycook, S.J. and Boatner, L.A., *Chemically sensitive structure-imaging with a scanning transmission electron microscope.* Nature, 1988. **336**: p. 565-567.

108. Nellist, P.D. and Pennycook, S.J., *The principles and interpretation of annular dark-field Z-contrast imaging*, in *Advances in Imaging and Electron Physics*, Hawkes, P.W., Editor. 2000, Elsevier. p. 147-203.
109. Egerton, R.F., Li, P. and Malac, M., *Radiation damage in the TEM and SEM.* Micron, 2004. **35**(6): p. 399-409.
110. Lotnyk, A., Poppitz, D., Ross, U., Gerlach, J.W., Frost, F., Bernütz, S., Thelander, E. and Rauschenbach, B., *Focused high- and low-energy ion milling for TEM specimen preparation.* Microelectron. Reliab., 2015. **55**(9): p. 2119-2125.
111. *GatanDigitalMicrograph*. 2018 [cited 2017 30/03/2017]; Available from: http://www.gatan.com/products/tem-analysis.
112. Nagao, K. and Kagami, E., *X-ray thin film measurement techniques: VII. Pole figure measurement.* Rigaku Journal, 2011. **27**(2): p. 6-14.
113. Raman, C.V. and Krishnan, K.S., *A New Type of Secondary Radiation.* Nature, 1928. **121**: p. 501-502.
114. Zhang, S.-L., *Raman Spectroscopy and its Application in Nanostructures*. Vol. 1. 2012, Peking University, Beijing: John Wiley & Sons. 256.
115. Brillouin, L., *Diffusion de la lumière et des rayons X par un corps transparent homogène.* Ann. Phys. (Paris), 1922. **9**(17): p. 88-122.
116. Hawkeye, M.M., Taschuk, M.T. and Brett, M.J., *Engineering Film Microstructure with Glancing Angle Deposition*, in *Glancing Angle Deposition of Thin Films*. 2014, John Wiley & Sons, Ltd: The Atrium, Southern Gate, Chichester, West Sussex, PO19 8SQ, United Kingdom. p. 31-80.
117. Ramanlal, P. and Sander, L.M., *Theory of Ballistic Aggregation.* Phys. Rev. Lett., 1985. **54**(16): p. 1828-1831.
118. Müller, K.-H., *Ion-beam-induced epitaxial vapor-phase growth: A molecular-dynamics study.* Phys. Rev. B, 1987. **35**(15): p. 7906-7913.
119. Poxson, D.J., Mont, F.W., Schubert, M.F., Kim, J.K. and Schubert, E.F., *Quantification of porosity and deposition rate of nanoporous films grown by oblique-angle deposition.* Appl. Phys. Lett., 2008. **93**(10): p. 101914.
120. Dick, B., Brett, M.J. and Smy, T., *Investigation of substrate rotation at glancing incidence on thin-film morphology.* J. Vac. Sci. Technol. B, 2003. **21**(6): p. 2569-2575.
121. Zhou, C.M. and Gall, D., *Development of two-level porosity during glancing angle deposition.* J. Appl. Phys., 2008. **103**(1): p. 014307.
122. Jen, Y.J., Chan, S., Huang, J.W., Jheng, C.Y. and Liu, W.C., *Self-Shadowing Deposited Pure Metal Nanohelix Arrays and SERS Application.* Nanoscale research letters, 2015. **10**(1): p. 498.
123. Jen, Y.-J., Huang, J.-W., Liu, W.-C., Chan, S. and Tseng, C.-H., *Glancing angle deposited gold nanohelix arrays on smooth glass as three-dimensional SERS substrates.* Opt. Mater. Express, 2016. **6**(3): p. 697.
124. Jen, Y.J., Huang, Y.J., Liu, W.C. and Lin, Y.W., *Densely packed aluminum-silver nanohelices as an ultra-thin perfect light absorber.* Sci. Rep., 2017. **7**: p. 39791.
125. Barabási, A.L. and Stanley, H.E., *Fractal Concepts in Surface Growth*. 1995, Cambridge: Cambridge University Press.
126. Fink, H.-W. and Ehrlich, G., *Lattice steps and adatom binding on W(211).* Surf. Sci., 1984. **143**(1): p. 125-144.
127. Valkealahti, S. and Manninen, M., *Diffusion processes and growth on aluminum cluster surfaces.* Z. Phys. D, 1997. **40**(1): p. 496-502.

128. van Oosterhout, G.W. and van de Waterbeemd, J.G.W., *Effect on the mobility of metal atoms on the structure of thin films deposited at oblique incidence.* Philips Res. Rep., 1967. **22**: p. 375-387.
129. Hergt, R. and Pfeiffer, H., *On Texture Formation in Metallic Films.* Phys. Status Solidi A, 1985. **92**(2): p. K89-K92.
130. Davydov, S.Y., *Calculation of the activation energy for surface self-diffusion of transition-metal atoms.* Phys. Solid State, 1999. **41**(1): p. 8-10.
131. Kellogg, G.L., *Field ion microscope studies of single-atom surface diffusion and cluster nucleation on metal surfaces.* Surf. Sci. Rep., 1994. **21**(1-2): p. 1-88.
132. Kellogg, G.L. and Feibelman, P.J., *Surface self-diffusion on Pt(001) by an atomic exchange mechanism.* Phys. Rev. Lett., 1990. **64**(26): p. 3143-3146.
133. Brown, A.M. and Ashby, M.F., *Correlations for diffusion constants.* Acta Metallurgica, 1980. **28**(8): p. 1085-1101.
134. Mehrer, H., *Diffusion in Solids: Fundamentals, Methods, Materials, Diffusion-Controlled Processes*, ed. Cardona, M., Fulde, P., von Klitzing, K., Merlin, R., Queisser, H.-J. and Stoermer, H. Vol. 1. 2007: Springer-Verlag Berlin Heidelberg. 651.
135. Adda, Y. and Philibert, J., *La diffusion dans les solids*. Vol. 2. 1966, Paris, France: Press Universitaires de France.
136. McLean, M. and Hirth, J.P., *Surface self-diffusion on gold.* Surf. Sci., 1968. **12**(2): p. 177-188.
137. Bonzel, H.P. and Gjostein, N.A., *Surface self-diffusion measurements on copper.* Phys. Status Solidi B, 1968. **25**(1): p. 209-222.
138. Campbell, J.L. and Schulte, C.W., *Positron trapping and self-diffusion activation-energies in chromium.* Appl. Phys., 1979. **19**(2): p. 149-152.
139. Odishariya, G.A., *Field emission microscope study of niobium surface diffusion in a high electric field: G A Odishariya,fiz tverd tela, 10 (5), May 1968, 1425–1432 (in Russian).* Vacuum, 1968. **18**(10): p. 573.
140. Binh, V.T., Uzan, R. and Drechsler, M., *Une détermination du coefficient d'auto-diffusion de surface du molybdène.* Surf. Sci., 1976. **57**(1): p. 118-124.
141. Bettler, P.C., AFOSR report No. 62, 1965. **297**.
142. Warner, H.R. 1967, Pittsburgh University: Carnegie Institute of Technology.
143. Piquet, A., Roux, H., Binh, V.T., Uzan, R. and Drechsler, M., *Une détermination du coefficient d'auto-diffusion de surface avec des pointes à émission de champ (tungstène).* Surf. Sci., 1974. **44**(2): p. 575-584.
144. Xi, J.Q., Schubert, M.F., Kim, J.K., Schubert, E.F., Chen, M., Lin, S.-Y., Liu, W. and Smart, J.A., *Optical thin-film materials with low refractive index for broadband elimination of Fresnel reflection.* Nat. Photon., 2007. **1**: p. 176.
145. Sumigawa, T., Tanie, H., Sakurai, A., Iwata, K., Chen, S. and Kitamura, T., *Substrate temperature control for the formation of metal nanohelices by glancing angle deposition.* J. Vac. Sci. Technol. A, 2015. **33**(6): p. 060609.
146. Knudsen, M., *Die Gesetze der Molekularströmung und der inneren Reibungsströmung der Gase durch Röhren.* Ann. Phys., 1909. **333**(1): p. 75-130.
147. Harris, K.D., Vick, D., Smy, T. and Brett, M.J., *Column angle variations in porous chevron thin films.* J. Vac. Sci. Technol. A, 2002. **20**(6): p. 2062.
148. Dick, B., Brett, M.J., Smy, T.J., Freeman, M.R., Malac, M. and Egerton, R.F., *Periodic magnetic microstructures by glancing angle deposition.* J. Vac. Sci. Technol. A, 2000. **18**(4): p. 1838-1844.
149. Frederick, J.R. and Gall, D., *Nanostaircases: An atomic shadowing instability during epitaxial CrN(001) layer growth.* Appl. Phys. Lett., 2005. **87**(5): p. 053107.

150. Wang, J., Huang, H., Kesapragada, S.V. and Gall, D., *Growth of Y-Shaped Nanorods through Physical Vapor Deposition.* Nano Lett., 2005. **5**(12): p. 2505-2508.
151. Kesapragada, S.V. and Gall, D., *Anisotropic broadening of Cu nanorods during glancing angle deposition.* Appl. Phys. Lett., 2006. **89**(20): p. 203121.
152. Choi, W.K., Li, L., Chew, H.G. and Zheng, F., *Synthesis and structural characterization of germanium nanowires from glancing angle deposition.* Nanotechnology, 2007. **18**(38): p. 385302.
153. Li, L., Fang, X., Chew, H.G., Zheng, F., Liew, T.H., Xu, X., Zhang, Y., Pan, S., Li, G. and Zhang, L., *Crystallinity-Controlled Germanium Nanowire Arrays: Potential Field Emitters.* Adv. Funct. Mater., 2008. **18**(7): p. 1080-1088.
154. Tang, F., Parker, T., Li, H.-F., Wang, G.-C. and Lu, T.-M., *Unusual Magnesium Crystalline Nanoblades Grown by Oblique Angle Vapor Deposition.* J. Nanosci. Nanotechnol., 2007. **7**: p. 3239-3244.
155. Wang, H.-H., Shi, Y.-J., Chu, W. and Blum, Y., *Strong Surface Diffusion Mediated Glancing-Angle Deposition: Growth, Recrystallization and Reorientation of Tin Nanorods.* Chin. Phys. Lett., 2008. **25**(1): p. 234-337.
156. He, Y., Zhao, Y. and Wu, J., *The effect of Ti doping on the growth of Mg nanostructures by oblique angle codeposition.* Appl. Phys. Lett., 2008. **92**(6): p. 063107.
157. Morrow, P., Tang, F., Karabacak, T., Wang, P.-I., Ye, D.-X., Wang, G.-C. and Lu, T.-M., *Texture of Ru columns grown by oblique angle sputter deposition.* J. Vac. Sci. Technol. A, 2006. **24**(2): p. 235-245.
158. Karabacak, T., Mallikarjunan, A., Singh, J.P., Ye, D., Wang, G.-C. and Lu, T.-M., *β-phase tungsten nanorod formation by oblique-angle sputter deposition.* Appl. Phys. Lett., 2003. **83**(15): p. 3096-3098.
159. Singh, J.P., Tang, F., Karabacak, T., Lu, T.-M. and Wang, G.-C., *Enhanced cold field emission from 〈100〉 oriented β–W nanoemitters.* J. Vac. Sci. Technol. B, 2004. **22**(3): p. 1048-1051.
160. Teki, R., Parker, T.C., Li, H., Koratkar, N., Lu, T.-M. and Lee, S., *Low temperature synthesis of single crystalline ZnO nanorods by oblique angle deposition.* Thin Solid Films, 2008. **516**(15): p. 4993-4996.
161. Boudias, C. and Monceau, D. *CaRIne Crystallography Divergent S. A.* 2005 [cited 2017; Available from: http://carine.crystallography.pagesperso-orange.fr/
162. Frank, O., Zukalova, M., Laskova, B., Kurti, J., Koltai, J. and Kavan, L., *Raman spectra of titanium dioxide (anatase, rutile) with identified oxygen isotopes (16, 17, 18).* PCCP, 2012. **14**(42): p. 14567-14572.
163. Motemani, Y., Greulich, C., Khare, C., Lopian, M., Buenconsejo, P.J.S., Schildhauer, T.A., Ludwig, A. and Koller, M., *Adherence of human mesenchymal stem cells on Ti and* TiO_2 *nano-columnar surfaces fabricated by glancing angle sputter deposition.* Appl. Surf. Sci., 2014. **292**: p. 626-631.
164. Izquierdo-Barba, I., García-Martín, J.M., Álvarez, R., Palmero, A., Esteban, J., Pérez-Jorge, C., Arcos, D. and Vallet-Regí, M., *Nanocolumnar coatings with selective behavior towards osteoblast and Staphylococcus aureus proliferation.* Acta Biomater., 2015. **15**(Supplement C): p. 20-28.
165. Holmwood, R.A. and Glang, R., *Vacuum Deposited Molybdenum Films.* J. Electrochem. Soc., 1965. **112**(8): p. 827-831.
166. Hagemeyer, A., Richter, H.J., Hibst, H., Maier, V. and Marosi, L., *Crystallographic texture and morphology of obliquely deposited Co-Cr magnetic thin films on flexible polymeric substrates.* Thin Solid Films, 1993. **230**(2): p. 199-202.

167. Moon, K.S. and Shin, S.C., *Dependence of structural and magnetic properties on deposition angle in electron-beam evaporated Co/Pt multilayer thin films.* J. Appl. Phys., 1996. **79**(8): p. 4991-4993.
168. Tang, F., Karabacak, T., Morrow, P., Gaire, C., Wang, G.C. and Lu, T.M., *Texture evolution during shadowing growth of isolated Ru columns.* Phys. Rev. B, 2005. **72**(16): p. 165402.
169. Tang, F., Gaire, C., Ye, D.X., Karabacak, T., Lu, T.M. and Wang, G.C., *AFM, SEM and in situ RHEED study of Cu texture evolution on amorphous carbon by oblique angle vapor deposition.* Phys. Rev. B, 2005. **72**(3): p. 035430.
170. Itoh, K., Ichikawa, F., Takahashi, Y., Tsutsumi, K., Noguchi, Y., Okamoto, K., Uchiyama, T. and Iguchi, I., *Columnar Grain Structure in Cobalt Films Evaporated Obliquely at Low Substrate Temperatures.* Jpn. J. Appl. Phys., 2006. **45**(4A): p. 2534-2538.
171. Tang, F., Parker, T., Wang, G.C. and Lu, T.M., *Surface texture evolution of polycrystalline and nanostructured films: RHEED surface pole figure analysis.* J. Phys. D: Appl. Phys., 2007. **40**(23): p. R427-R439.
172. Drüsedau, T.P., Klabunde, F., Lohmann, M., Hempel, T. and Bläsing, J., *Turnover of Texture in low rate Sputter-Deposited Nanocrystalline Molybdenum Films.* MRS Proceedings, 2011. **472**: p. 33.
173. Chen, L., Lu, T.M. and Wang, G.C., *Biaxially textured Mo films with diverse morphologies by substrate-flipping rotation.* Nanotechnology, 2011. **22**(50): p. 505701.
174. Krishnan, R., Riley, M., Lee, S. and Lu, T.-M., *Formation of biaxially textured molybdenum thin films under the influence of recrystallization conditions.* Thin Solid Films, 2011. **519**: p. 5429-5432.
175. Krishnan, R., Riley, M., Lee, S. and Lu, T.-M., *Vertically aligned biaxially textured molybdenum thin films.* J. Appl. Phys., 2011. **110**: p. 064311.
176. Chen, L., Lu, T.M. and Wang, G.C., *Incident flux angle induced crystal texture transformation in nanostructured molybdenum films.* J. Appl. Phys., 2012. **112**: p. 024303.
177. Deng, R., Muralt, P. and Gall, D., *Biaxial texture development in aluminum nitride layers during off-axis sputter deposition.* J. Vac. Sci. Technol. A, 2012. **30**(5): p. 051501.
178. LaForge, J.M., Ingram, G.L., Taschuk, M.T. and Brett, M.J., *Flux Engineering To Control In-Plane Crystal and Morphological Orientation.* Cryst. Growth Des., 2012. **12**(7): p. 3661-3667.
179. Shetty, A.R. and Karimi, A., *Texture mechanisms and microstructure of biaxial thin films grown by oblique angle deposition.* Phys. Status Solidi B, 2012. **249**(8): p. 1531-1540.
180. Chen, L., Shimpi, P., Lu, T.M. and Wang, G.C., *Fiber texture of sputter deposited molybdenum films and structural zone model.* Mater. Chem. Phys., 2014. **145**(3): p. 288-296.
181. Wang, G.C. and Lu, T.M., *RHEED Transmission Mode and Pole Figures*. 1 ed. Thin Film and Nanostructure Texture Analysis. 2014, New York, NY: Springer.
182. Spieß, L., Teichert, G., Schwarzer, R., Behnken, H. and Genzel, C., *Moderne Röntgenbeugung*. Vol. 2. 2009, GWV Fachverlage GmbH, Wiesbaden: Vieweg und Teubner. 564.
183. Schreiner, W., *PDF (Powder Diffraction File) No. 42-1120*. 1991, Intelligent Controls Inc.: Amawalk, NY, USA.

184. Swanson, *PDF (Powder Diffraction File) No 06-0694*. 1955: Natl. Bur. Stand. (U.S.), Circ. 539, V, 20.

185. Palmero, A., Rudolph, H. and Habraken, F.H.P.M., *Generalized Keller-Simmons formula for nonisothermal plasma-assisted sputtering depositions*. Appl. Phys. Lett., 2006. **89**(21): p. 211501.

186. Alvarez, R., Garcia-Martin, J.M., Garcia-Valenzuela, A., Macias-Montero, M., Ferrer, F.J., Santiso, J., Rico, V., Cotrino, J., Gonzalez-Elipe, A.R. and Palmero, A., *Nanostructured Ti thin films by magnetron sputtering at oblique angles*. J. Phys. D: Appl. Phys., 2016. **49**(4): p. 045303.

187. Sailer, R. and McCarthy, G., *PDF (Powder Diffraction File) No. 441294*. 1993: North Dakota State University, Fargo, North Dakota, USA.

188. Alouach, H. and Mankey, G.J., *Texture orientation of glancing angle deposited copper nanowire arrays*. J. Vac. Sci. Technol. A, 2004. **22**(4): p. 1379-1382.

189. Alouach, H. and Mankey, G.J., *Erratum: "Texture orientation of glancing angle deposited copper nanowire arrays" [J. Vac. Sci. Technol. A 22, 1379 (2004)]*. J. Vac. Sci. Technol. A, 2005. **23**(2): p. 366-366.

190. Swanson and Tatge, *PDF (Powder Diffraction File) No 04-0787*. 1953: Natl. Bur. Stand. (U.S.), Circ. 539, I, 11.

9 List of Abbreviations

In the following, the abbreviations used in the text are listed:

ABF	Annual bright field
bcc	Body-centered cubic
BF	Bright field
BSE	Back-scattered electron
DC	Direct current
DF	Dark field
DHL	Divergence height limiting
EB	Electron beam
EDX	Energy dispersive X-ray spectroscopy
EELS	Electron energy loss spectroscopy
fcc	Face-centered cubic
FIB	Focused ion beam
FWHM	Full width at half maximum
GLAD	Glancing angle deposition
HAADF	High angle angular dark field
hcp	Hexagonal closed packed
HIPIMS	High power impulse magnetron sputtering
HRTEM	High resolution transmission electron microscopy
IPPF	In-plane pole figure
LN_2	Liquid nitrogen
MD	Molecular dynamics
NBED	Nano-beam electron diffraction
OAD	Oblique angle deposition
PDF	Powder diffraction file
PLD	Pulsed laser deposition
PSA	Parallel slit analyzer
PSC	Parallel slit collimator
PVD	Physical vapor deposition
QCM	Quartz crystal microbalance
RF	Radio frequency

RHEED	Reflection high-energy electron diffraction
RT	Room temperature
SAED	Selected area electron diffraction
SE	Secondary electron
SEM	Scanning electron microscopy
SERS	Surface-enhanced Raman scattering
SF	Scaling factor
STEM	Scanning transmission electron microscopy
SZM	Structure zone model
TC	Thermocouple
TEM	Transmission electron microscopy
TF	Tooling factor
UHV	Ultra-high vacuum
XRD	X-ray diffraction
µP-STEM	Micro-probe STEM

10 List of Variables and Constants

This list summarizes the variables and constants used in the text:

A	Area
c	Speed of light
C	Concentration
d	Columnar diameter
d_{Col}	Collision radius
d_{hkl}	Lattice distance
D	Bulk density
D_S	Diffusivity, Diffusion coefficient
D_0	Proportionality constant
e	Elementary charge
E	Energy
E_A	Activation energy
E_{Therm}	Thermal energy
G	Free enthalpy
h	Planck constant
h_i	Height of nucleus or column
hkl	Miller indices
J	Incident vapor flux deposition rate
J_N	Particle flux
k_B	Boltzmann constant
l	Length of column
l_{Shadow}	Shadowing length
L	Mean free path
m	Slope
m_{Dep}	Deposited mass
m_{Evap}	Evaporated mass
m_{Mol}	Mass of the residual gas particles
m_0	Electron mass
M	Mass of evaporated element
n	Positive integer

N	Atomic area density
p	Momentum
p_{Base}	Vacuum base pressure
p_J	Jump frequency
p_{Work}	Vacuum working pressure
P	Porosity
r	Deposition rate
R	Impingement rate
s	Distance between evaporation source and sample surface during deposition
t	Film thickness
t_{Dep}	Deposition time
$t_{measured}$	Measured film thickness
t_{preset}	Preset film thickness created by the instrument
t_{Tilt}	Thickness of film composed of tilted columns
t_0	Thickness of film composed of vertical columns
T	Temperature
T_H	Homologous temperature
T_{Melt}	Melting point of material
T_{Sub}	Substrate temperature
u	Diffraction vector
U	Thermoelectric voltage
U_B	Acceleration voltage
V	Volume
α	Angle of incidence between incoming particle flux and normal of the growth zone for a tilted column
β	Tilt angle of a column with respect to the substrate normal
$\beta_{\theta=90^\circ}$	Linear extrapolated tilt angle of a column expected at $\theta_{OAD} = 90^\circ$
γ	Tilt angle between a given lattice direction and the substrate normal
Δ	Difference between columnar tilt angle β and tilt angle of lattice direction γ
ΔE_{Raman}	Raman energy shift
Δf_{Raman}	Raman frequency shift
ε	Revolution angle for azimuthal substrate rotation
θ	Bragg angle

θ_{OAD}	Angle of the incoming particle flux with respect to the substrate normal
λ	Wavelength
λ_B	De Broglie wavelength
Λ	Self-diffusion length of an adatom
υ	Ratio of deposition rate r and substrate rotation frequency ω
ρ	Film density of deposited material
Σ	Free surface energy
τ_M	Mobility lifetime
Φ	Azimuthal angle in stereographic projection of pole figure
Φ_{Fan}	Fan angle
Φ_{Flux}	Particle flux
$\Phi_{Parallel}$	Particle flux arriving at growth zone of vertical column
Φ_{Tilt}	Particle flux arriving at growth zone of tilted column
χ	Polar angle in stereographic projection of pole figure
ψ	Characteristic atomic oscillation frequency
Ω	Atomic volume

11 Acknowledgements

First of all, I thank Prof. Dr. Dr. h. c. Rauschenbach for given me the opportunity to prepare my dissertation at the Leibniz Institute of Surface Engineering (IOM). I thank especially for the continuously authentic and honest supervision and for the always constructive discussions.

I thank Mr. Grüner for introducing me to the concept of OAD and GLAD, for making me familiar with the deposition of OAD and GLAD thin films, and for technical support. I thank Ms. Mill and Mr. Hirsch for instructions concerning working with the FIB and SEM. Further, I would like to thank Dr. Gerlach and Mr. Mensing for introducing me in the XRD measurements. I also thank Mr. Grüner, Mr. Gerlach, and Dr. Lotnyk for valuable discussions.

I thank Dr. Lotnyk for collecting the TEM data and Ms. Mill for preparing the FIB lamellae. I thank Mr. Mensing and Mr. Schumacher for collecting the RHEED data and Mr. Lehnert for collecting the Raman spectra.

I thank the workshop of the IOM for fabricating the steal sample holder as well as the liquid nitrogen cooled sample holder.

Publication list

This dissertation contains experimental results of the author that have already been published, are under review or are submitted to peer-reviewed journals or are in preparation:

[LIE01] **S. Liedtke**, C. Grüner, A. Lotnyk, B. Rauschenbach, Glancing angle deposition of sculptured thin metal films at room temperature, Nanotechnology 28 (38), 385604, 2017, DOI:10.1088/1361-6528/aa7a79.
Contribution: Performance of experimental work (Sample preparation, SEM), data analysis, writing of manuscript.

[LIE02] **S. Liedtke**, C. Grüner, J.W. Gerlach, B. Rauschenbach, Comparative study of sculptured metallic thin films deposited by oblique angle deposition at different temperatures, Beilstein J. Nanotechnol. 9 (2018) 954-962, DOI: 10.3762/bjnano.9.89.
Contribution: Performance of experimental work (sample preparation, SEM, IPPF, XRD), data analysis and interpretation, writing of manuscript.

[LIE03] **S. Liedtke**, C. Grüner, J.W. Gerlach, A. Lotnyk, B. Rauschenbach, Crystalline Ti-Nanostructures Prepared by Oblique Angle Deposition at Room Temperature, J. Vac. Sci. Technol. B 36 (3), 031804, 2018, DOI 10.1116/1.5025013.
Contribution: Performance of experimental work (sample preparation, SEM, IPPF, XRD), data analysis and interpretation, writing of manuscript.

[LIE04] **S. Liedtke-Grüner**, C. Grüner, A. Lotnyk, J.W. Gerlach, M. Mensing, P. Schumacher, B. Rauschenbach, Crystallinity and texture of nanostructured molybdenum thin films obliquely deposited at room temperature, submitted to Thin Solid Films.
Contribution: Performance of experimental work (sample preparation, SEM, IPPF, XRD), data analysis and interpretation, writing of manuscript.

[LIE05] **S. Liedtke-Grüner**, C. Grüner, A. Lotnyk, J.W. Gerlach, and B. Rauschenbach, Structural and texture analysis of columnar Ti thin films obliquely deposited at various substrate temperatures, in preparation.
Contribution: Performance of experimental work (sample preparation, SEM, IPPF, XRD), data analysis and interpretation, writing of manuscript.

Further co-author articles have been published in peer-reviewed journals or are under review with content relevant for this dissertation:

- C. Grüner, **S. Liedtke**, J. Bauer, S.G. Mayr, B. Rauschenbach, Morphology of Thin Films Formed by Oblique Physical Vapor

Deposition, ACS Appl. Nano Mater., 2018, 1 (3), pp 1370–1376, DOI: 10.1021/acsanm.8b00124.
Contribution: Assistance in performance of sample preparation, helped with developing the basic concept, assistance in writing of manuscript.

- C. Grüner, P. Reeck, P.-P. Jacobs, **S. Liedtke**, A. Lotnyk, B. Rauschenbach, Gold Coated Metal Nanostructures Grown by Glancing Angle Deposition and Pulsed Electroplating, Physics Letters A 382 (19), 1287 – 1290, 2018, https://doi.org/10.1016/j.physleta.2018.03.010.
  Contribution: Assistance in performance of sample preparation, assistance in writing of manuscript.

- C. Grüner, **S. Liedtke**, S.G. Mayr, B. Rauschenbach, Avoiding anisotropies in on-lattice simulations of ballistic deposition, submitted to Computer Physics Communications, under review.
  Contribution: Helped with data interpretation, assistance in writing of manuscript.

The author has presented contents of this dissertation during the following national and international conferences:

26. – 28.09.2018	**Materials Science Engineering Congress**, Darmstadt, Germany (Oral presentation)
17. – 22.06.2018	**15th European Vacuum Conference**, Geneva, Switzerland (Oral presentation)
11. – 16.03.2018	**Frühjahrstagung der Deutschen Physikalischen Gesellschaft (DPG Spring Meeting)**, Berlin, Germany (Oral presentation)
28. – 30.06.2017	**Nanotech France**, Paris, France (Oral presentation)
19. – 24.03.2017	**Frühjahrstagung der Deutschen Physikalischen Gesellschaft (DPG Spring Meeting)**, Dresden, Germany (Oral presentation)
06. – 07.03.2017	**Annual BuildMoNa Conference**, Leipzig, Germany (Oral presentation)
19. – 21.10.2016	**European Conference on Nanofilms**, Bizkaia Aretoa of Bilbao, Spain (Oral presentation) **S. Liedtke**, C. Grüner, M. Mensing, J.W. Gerlach, B. Rauschenbach, Metallic Nanostructures Prepared by Glancing Angle Deposition, European Conference on Nanofilms, Proceedings, Bilbao, Spain, 116-117, 21.10.2016.
06. – 11.03.2016	**Frühjahrstagung der Deutschen Physikalischen Gesellschaft (DPG Spring Meeting)**, Regensburg, Germany (Poster)
14. – 15.03.2016	**Annual BuildMoNa Conference**, Leipzig, Germany (Poster)

Selbstständigkeitserklärung

Hiermit versichere ich, dass ich die vorliegende Arbeit ohne unzulässige Hilfe und ohne Benutzung anderer als der angegebenen Hilfsmittel angefertigt und dass die aus fremden Quellen direkt oder indirekt übernommenen Gedanken in der Arbeit als solche kenntlich gemacht wurden.

Ich versichere, dass alle Personen, von denen ich bei der Auswahl und Auswertung des Materials sowie bei der Herstellung des Manuskripts Unterstützungsleistungen erhalten habe, in der Danksagung der vorliegenden Arbeit aufgeführt sind.

Ich versichere, dass – außer in der Danksagung genannten – weitere Personen bei der geistigen Herstellung der vorliegenden Arbeit nicht beteiligt waren. Insbesondere versichere ich, nicht die Hilfe eines Promotionsberaters in Anspruch genommen zu haben und weitere Personen von mir oder meinem Auftrag weder unmittelbar noch mittelbar geldwerte Leistungen für Arbeiten erhalten haben, die im Zusammenhang mit dem Inhalt der vorgelegten Dissertation stehen.

Ich versichere, dass die vorgelegte Arbeit oder Teile daraus weder im Inland noch im Ausland in gleicher oder in ähnlicher Form einer anderen Prüfungsbehörde zum Zwecke einer Promotion oder eines anderen Prüfungsverfahrens vorgelegt wurden.

Ich teile mit, dass keine früheren erfolglosen Promotionsversuche stattgefunden haben.

Leipzig, den 18. Oktober 2018 Susann Liedtke-Grüner